Ion-electron coincidence studies of femtosecond dynamics triggered by extreme ultraviolet photoionization of atoms and molecules

by

Seyyed Javad Robatjazi

B.S. Shiraz University, 2008

M.S. Shahid Beheshti University, 2012

AN ABSTRACT OF A DISSERTATION

submitted in partial fulfillment of the
requirements for the degree

Doctor of Philosophy

Department of Physics
College of Arts and Sciences

KANSAS STATE UNIVERSITY
Manhattan, Kansas

2021

Abstract

Photoelectron spectroscopy employing X-ray and extreme ultraviolet (XUV) radiation is one of the most important experimental methods to study the electronic structure of atoms, molecules, and solids. Recent developments of XUV and X-ray sources with ultrashort pulse durations, like free-electron lasers (FELs) and high-order harmonics of infrared lasers, enabled combining this approach with a concept of a time-resolved measurement, where a pair of synchronized short light pulses is used to initiate and observe a physical or chemical process of interest. Among other advances, such combination turned out to be particularly useful for atomic physics and gas-phase femtochemistry, where femtosecond or even sub-femtosecond short-wavelength radiation can be used to trigger the dynamics in high-lying states previously inaccessible for time-resolved measurements and offers a variety of novel schemes to probe light-induced electronic and nuclear motion. One of the key challenges for time-domain studies employing short-pulsed radiation sources is that they are necessarily broadband and, thus, typically populate a broad range of atomic of molecular states. The main goal of this thesis is to develop an experimental approach that enables state-selective analysis of the dynamics induced by such broadband femtosecond pulses in the XUV domain, and to apply it to study several exemplary reactions in photoionized molecules. Since reducing the bandwidth of the XUV pulse would ultimately limit the achievable temporal resolution, in this work the challenge of state selectivity is addressed by employing photoelectron-photoion and photoion-photoion coincident measurements. In the experimental apparatus developed as a part of this thesis, a double-sided velocity map imaging (VMI) spectrometer for coincident detection of electrons and ions is combined with a femtosecond pump-probe setup that includes a near-infrared (NIR) laser and a fiber-based

XUV source based on high-order harmonics generation. This instrument has been commissioned, characterized, and applied to several time-resolved experiments on atomic and molecular targets. More specifically, this thesis describes three different sets of experiments. First, a brief overview of several XUV-NIR pump-probe measurements addressing two-color single, double or triple ionization of atoms is presented. Here, the main focus is set on capturing generic characteristic features of the corresponding two-color signals, and on revealing physical mechanisms determining their "transient" or "steady" behavior with respect to the time delay between the XUV and NIR pulses. The second series of experiments focuses on exploring coupled electronic and nuclear dynamics in XUV-ionized CO_2 molecule probed by the synchronized NIR pulse. This study, which constitutes the central part of the thesis, relies on the detection of the photoelectron that reveals which electronic state is initially populated, in coincidence with ionic fragments, which provide information on the specific dissociation channel of the molecular ion after the interaction with both pulses. Here, we observe signatures of an electron-hole wave packet motion near a conical intersection of two low-lying cationic states, trace rotational dynamics determined by the dependence of the state-specific XUV photoionization cross section on molecular orientation, and disentangle the contributions of individual states to different dissociation pathways. The third series of experiments aims at studying nuclear dynamics in XUV-ionized alcohol molecules, focusing on the channels involving ultrafast hydrogen motion. Here, ion mass spectrometry measurements on methanol and its deuterated isotopologue (CH_3OH and CD_3OH) show that, depending on a specific XUV wavelength, the formation of molecular hydrogen or trihydrogen cations can be either dominated by the channels combining the hydrogen from the oxygen site with one or two hydrogens from the methyl carbon, or by the ejections of all hydrogen atoms from the methyl group. Coincident electron spectra for specific ionic fragments enable linking these channels to the calculated dissociation pathways leading to H_2^+ or H_3^+ formation. Finally, we present the results of XUV-NIR pump-probe experiments on ethanol, where a transient enhancement of particular dissociation channels has been ob-

served. The experimental methodology presented in this work can be readily extended to a broad range of molecular systems, including both, molecular ions and high-lying excited states of the neutral molecules. At the same time, highly-differential data on small polyatomic molecules like CO_2, methanol, and ethanol presented here, can be used to benchmark theoretical models for XUV ionization of these prototypical systems, improving our general understanding of light-induced molecular dynamics.

Ion-electron coincidence studies of femtosecond dynamics triggered by extreme ultraviolet photoionization of atoms and molecules

by

Seyyed Javad Robatjazi

B.S. Shiraz University, 2008

M.S. Shahid Beheshti University, 2012

A DISSERTATION

submitted in partial fulfillment of the
requirements for the degree

Doctor of Philosophy

Department of Physics
College of Arts and Sciences

KANSAS STATE UNIVERSITY
Manhattan, Kansas

2021

Approved by:

Major Professor
Dr. Artem Rudenko

Copyright

Abstract

Photoelectron spectroscopy employing X-ray and extreme ultraviolet (XUV) radiation is one of the most important experimental methods to study the electronic structure of atoms, molecules, and solids. Recent developments of XUV and X-ray sources with ultrashort pulse durations, like free-electron lasers (FELs) and high-order harmonics of infrared lasers, enabled combining this approach with a concept of a time-resolved measurement, where a pair of synchronized short light pulses is used to initiate and observe a physical or chemical process of interest. Among other advances, such combination turned out to be particularly useful for atomic physics and gas-phase femtochemistry, where femtosecond or even sub-femtosecond short-wavelength radiation can be used to trigger the dynamics in high-lying states previously inaccessible for time-resolved measurements and offers a variety of novel schemes to probe light-induced electronic and nuclear motion. One of the key challenges for time-domain studies employing short-pulsed radiation sources is that they are necessarily broadband and, thus, typically populate a broad range of atomic of molecular states. The main goal of this thesis is to develop an experimental approach that enables state-selective analysis of the dynamics induced by such broadband femtosecond pulses in the XUV domain, and to apply it to study several exemplary reactions in photoionized molecules. Since reducing the bandwidth of the XUV pulse would ultimately limit the achievable temporal resolution, in this work the challenge of state selectivity is addressed by employing photoelectron-photoion and photoion-photoion coincident measurements. In the experimental apparatus developed as a part of this thesis, a double-sided velocity map imaging (VMI) spectrometer for coincident detection of electrons and ions is combined with a femtosecond pump-probe setup that includes a near-infrared (NIR) laser and a fiber-based

XUV source based on high-order harmonics generation. This instrument has been commissioned, characterized, and applied to several time-resolved experiments on atomic and molecular targets. More specifically, this thesis describes three different sets of experiments. First, a brief overview of several XUV-NIR pump-probe measurements addressing two-color single, double or triple ionization of atoms is presented. Here, the main focus is set on capturing generic characteristic features of the corresponding two-color signals, and on revealing physical mechanisms determining their "transient" or "steady" behavior with respect to the time delay between the XUV and NIR pulses. The second series of experiments focuses on exploring coupled electronic and nuclear dynamics in XUV-ionized CO_2 molecule probed by the synchronized NIR pulse. This study, which constitutes the central part of the thesis, relies on the detection of the photoelectron that reveals which electronic state is initially populated, in coincidence with ionic fragments, which provide information on the specific dissociation channel of the molecular ion after the interaction with both pulses. Here, we observe signatures of an electron-hole wave packet motion near a conical intersection of two low-lying cationic states, trace rotational dynamics determined by the dependence of the state-specific XUV photoionization cross section on molecular orientation, and disentangle the contributions of individual states to different dissociation pathways. The third series of experiments aims at studying nuclear dynamics in XUV-ionized alcohol molecules, focusing on the channels involving ultrafast hydrogen motion. Here, ion mass spectrometry measurements on methanol and its deuterated isotopologue (CH_3OH and CD_3OH) show that, depending on a specific XUV wavelength, the formation of molecular hydrogen or trihydrogen cations can be either dominated by the channels combining the hydrogen from the oxygen site with one or two hydrogens from the methyl carbon, or by the ejections of all hydrogen atoms from the methyl group. Coincident electron spectra for specific ionic fragments enable linking these channels to the calculated dissociation pathways leading to H_2^+ or H_3^+ formation. Finally, we present the results of XUV-NIR pump-probe experiments on ethanol, where a transient enhancement of particular dissociation channels has been ob-

served. The experimental methodology presented in this work can be readily extended to a broad range of molecular systems, including both, molecular ions and high-lying excited states of the neutral molecules. At the same time, highly-differential data on small polyatomic molecules like CO_2, methanol, and ethanol presented here, can be used to benchmark theoretical models for XUV ionization of these prototypical systems, improving our general understanding of light-induced molecular dynamics.

Table of Contents

List of Figures

List of Tables

Acknowledgments

This thesis would not be possible without the dedication and support of all my instructors, colleagues, friends, and family acknowledged here. I would firstly like to thank my thesis advisor, Professor Artem Rudenko. Only with his knowledge, experience, and diligence were the projects within in this thesis came to fruition. He was always supportive with advice on experimental problem solving, financing our complex experimental setups, and helping me navigate the complexities of scientific writing and communication. The contributions of Professor Daniel Rolles to the projects within this thesis were also of significant importance. His comments, suggestions, and questions during all steps of my PhD works always provided additional insight. Next, I would like to thank the commitment to the members of my PhD committee: Professors of the Physics department Uwe Thumm and Vinod Kumarrapan, Shuting Lei of the engineering department, and the external member Professor Caterina Scoglio. I appreciate the time and attention they dedicated to assuring the quality and rigor of my work. I am very lucky and grateful to have worked with the graduate students and postdocs belonging to the collaborative group of Professors Rudenko and Rolles. Special thanks goes Shashank Pathak for his tireless efforts on helping me build the KAMP setup that are discussed in this work (even multiple times doing so). Great knowledge and skills were instilled in me when working with Doctor Lee Pearson from the onset of my graduate career, I am elated that the hard work and time he dedicated to the XUUS- HHG source have proven to successful. The knowledge I learned about VMI spectroscopy techniques from Dr. Jeff Powell while he was a graduate student under the guidance of Artem Rudenko, I hope that he continues to have great success as a postdoctoral researcher at INRS-EMT. I would like to thank the assistance in Doctor Enliang Wang whose theoretical knowledge provided key understandings to our experimental results. I look forward to working with you further in further improving our setups on the new laser

sources. Inarguably, none of these experimental results would be possible without the tireless and careful work of Doctor Charles Fehrenbach and Doctor Kanaka Raju Pandiri, their help with laser characterization and optical maintenance on the PULSAR system have been immeasurable. In a similar nature was the help from Professor Kevin Carnes. I am grateful for his advice, instruction, and work on developing the robust data acquisition hardware and complex sorting codes thoroughly used in our experiments. Furthermore, I would like to thank JRM research technologist members Chris Aikens and Justin Millette. Their logistical knowledge and experience on all the experimental apparatuses helped research always move quickly and effectively. They helped on everything from intricate measurements and design, to helping move bulky equipment. I would like to thank the work and guidance of the scientists Scott Chainey, whom always helped with electronics design for our DAQ systems, and Vincent Needham, his help navigating all the software required for our experiments cannot be overstated.

Additional thanks is dedicated to graduate students and postdocs that provided help, support, and insight on this PhD work, through discussions, sharing their equipment and programs, or just small favors. This currently includes Farzaneh Ziaee, Erfan Saydanzad, Kurtis Borne, and Keyu Chen. I wish them the best on their pursuit. Additional thanks to previous group members of the Rudenko and Rolles group, including Utuq Ablikim and Yubaraj Malakar.

Of course there are dozens, if not hundreds of others that helped me in the several years of my graduate studies, and as for everyone, I wish all the best.

Dedication

This thesis is dedicated to my parents

For their endless love, support and

encouragement

Preface

Chapter 1

Introduction

A large portion of our knowledge of the structure of matter was obtained by using short-wavelength light. For example, we can directly "see" bones in a human body [1] or determine the microscopic structure of such complicated molecules as DNA [2] using X-ray radiation. X-ray and extreme ultraviolet radiation also proved to be a unique tool for studying the electronic structure of matter and its chemical composition. In particular, photoelectron spectroscopy employing X-ray and extreme ultraviolet radiation is one of the most important experimental methods to study the electronic structure of atoms, molecules, and solids [3,4].

This work focuses on applications employing light pulses in the extreme ultraviolet spectral range. Extreme ultraviolet radiation, known as EUV or XUV, is a form of radiation with photon energies between 10 eV up to 124 eV (corresponding to 124nm down to 10nm wavelengths). Throughout this work, we use the abbreviation "XUV". There are intense natural sources of XUV light, like stellar corona (an aura of plasma surrounding a star). Today, many different types of man-made XUV sources are available, such as discharge lamps [5], synchrotron radiation facilities [6], free-electron lasers (FELs) [7; 8] or sources based on high-order harmonic generation (HHG) [9,10]. Since XUV light is efficiently absorbed by outer-valence and inner-valence orbitals of atoms and molecules, its transmission requires a high-vacuum environment.

Recent developments of XUV and X-ray sources with ultrashort pulse durations, like FELs and high-order harmonics of infrared lasers, enabled combining photoelectron spectroscopy with the concept of a time-resolved measurement where a pair of synchronized short light pulses is used to initiate and observe a physical or chemical process of interest. Among other advances, such a combination turned out to be particularly useful for atomic physics and gas-phase femtochemistry [11], where femtosecond or even sub-femtosecond short-wavelength radiation can be used to trigger the dynamics in high-lying states previously inaccessible for time-resolved measurements and offer a variety of novel schemes to probe light-induced electronic and nuclear motion [12,13]. One of the key challenges for time-domain studies employing short-pulse radiation sources is that they are necessarily broadband and, thus, typically populate a broad range of atomic or molecular states.

The main goal of this thesis is to develop an experimental approach that enables state-selective analysis of the dynamics induced by such broadband femtosecond pulses in the XUV domain and to apply it to study several exemplary reactions in photoionized molecules. Since reducing the bandwidth of the XUV pulse would ultimately limit the achievable temporal resolution [14], in this work, the challenge of state selectivity is addressed by employing photoelectron-photoion and photoion-photoion coincident measurements. In the experimental apparatus developed as a part of this thesis, a double-sided velocity map imaging (VMI) spectrometer for coincident detection of electrons and ions is combined with a femtosecond pump-probe setup that includes a near-infrared (NIR) laser and a fiber-based XUV source based on high-order harmonic generation. This instrument has been commissioned, characterized, and applied to several time-resolved experiments on atomic and molecular targets. Three basic groups of experiments discussed in this work include two-color pump-probe experiments on single and multiple ionization of atoms, a coincident study of ultrafast electronic and nuclear dynamics in XUV-ionized CO_2 molecules, and a set of similar experiments on alcohol molecules, with the focus on tracing ultrafast hydrogen dynamics. These studies provide a new perspective on several aspects of our current view of ionization-induced molec-

ular dynamics, and yield benchmark data on such prototypical systems as carbon dioxide and methanol molecules.

The thesis document is structured as follows: In chapter 2, a brief overview of the theoretical background needed for this work is given. Chapter 3 provides a detailed description of the experimental setup, including the XUV source and its major components and the electron-ion coincident spectrometer. In chapter 4, an overview of several typical two-color XUV-NIR measurements on atoms and molecules is presented. It includes sideband measurements, NIR ionization of neutral and cationic excited states prepared by the XUV pulse, a measurement on inner-shell ionization of xenon, and an example of two-color double ionization of molecules. The main focus of this chapter is studying physical mechanisms leading to steady and transient behavior of these two-color signals. In chapter 5, photoelectron-photoion coincidence results of the XUV pump - NIR probe experiment on the CO_2 molecule are presented. The focus of this chapter is on exploring coupled electronic and nuclear dynamics in XUV-ionized CO_2 probed by a synchronized NIR pulse. This coincidence study reveals which electronic state is initially populated, providing information on the specific dissociation channels of the molecular ion after the interaction with both pulses. In particular, a detailed analysis of a coherent electron hole wave packet evolution near the conical inter-section of the two low-lying states of CO_2^+ is presented here. In chapter 6, H_2^+ and H_3^+ formation pathways from methanol and its deuterated isotopologue (CH_3OH and CD_3OH) ionized by a single XUV photon are explored. A combination of XUV wavelengths, electron-ion coincidence measurements, and a deuterated sample enabled the first reliable observation of tri-hydrogen ejection from methanol monocations and disentangling contributions from "local" and "extended" formation mechanisms. This chapter is concluded with a brief overview of exploratory XUV-NIR pump-probe experiments on methanol and ethanol. Finally, a brief summary of the obtained results and future perspectives is given in chapter 7.

Chapter 2

Theoretical Background

In this chapter, a brief overview of basic physical processes, theoretical background and terminology needed for explaining the results of this work will be presented. It includes a brief discussion of different laser ionization regimes, basic principles of the high harmonic generation process and phase matching, and the fundamentals of single-photon ionization and related phenomena. The chapter ends with a short introduction to molecular physics, including the Born-Oppenheimer approximation, the structure of molecular orbitals and selection rules for single-photon transitions.

2.1 Strong-field ionization

In the presence of an intense laser field, atoms and molecules can be ionized. Based on the laser intensity, wavelength and target binding energy, strong-field ionization is often categorized into three different regimes: multiphoton ionization, tunneling ionization, and over-the-barrier ionization. The transition between the multiphoton and tunneling regimes can be defined by the Keldysh parameter [15]. The Keldysh parameter (γ) is defined by:

$$\gamma = \sqrt{\frac{I_p}{2U_p}} \tag{2.1}$$

where I_p is the ionization potential and U_p is the ponderomotive energy, i.e., the quiver energy of a free electron in the oscillating laser field. In atomic units it is given by $U_p = E_0^2/4\omega_0^2$, where E_0 is the peak intensity of the laser field and ω_0 is its frequency. Thus, the Keldyish parameter decreases with increasing intensity or wavelength, and increases for larger binding energies.

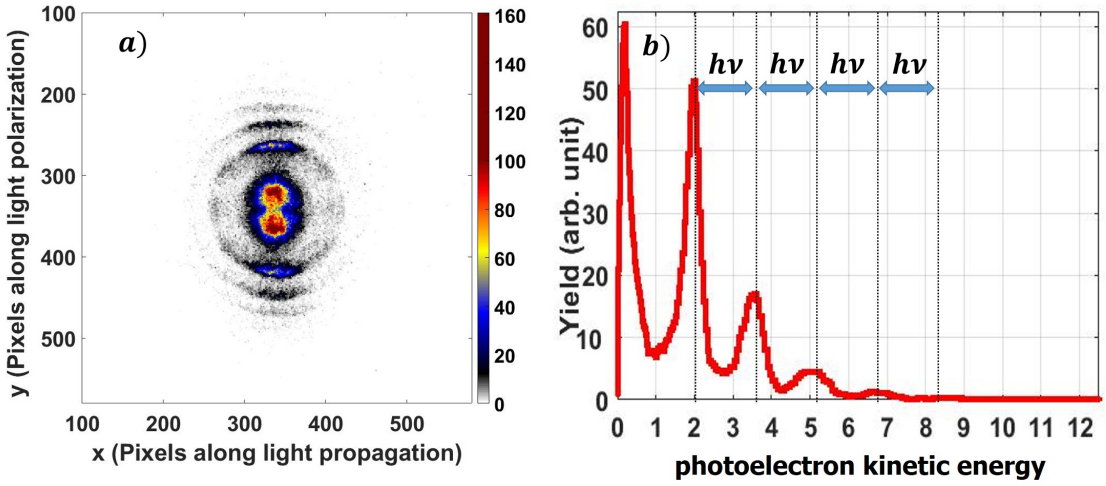

Figure 2.1: *Typical VMI image and photoelectron energy spectrum for single ionization of Xe by 800 nm, 25 fs laser pulses.*

2.1.1 Multiphoton ionization

If the Keldysh parameter is larger than 1 ($\gamma > 1$), the ionization process can be considered as a result of multiphoton absorption. Multiphoton ionization can be described by perturbation theory, where n-photon absorption corresponds to n^{th} order perturbation. Therefore, the multiphoton ionization rate is given by:

$$W_n^{ab} = \sigma_n I^n \tag{2.2}$$

where ab indicates a transition from the a to b state, σ_n is the n^{th} order generalized cross section, and I is the laser intensity. $log(W_n^{ab})$ as a function of intensity is linear and propor-

tional to the number of photons absorbed, at least at low laser intensities. At higher laser intensities, equation 2.2 typically overestimates the ionization rate.

The number of absorbed photons can often exceed the minimum number of photons required to overcome the atom's ionization potential. In this case, the excess photon energy is transferred to electrons ejected from the atom. Therefore, peaks with one photon energy spacing between them are observed in the photoelectron energy spectrum. This phenomenon is called above threshold ionization (ATI). An example of a photoelectron image on the detector and the corresponding photoelectron energy spectrum in the ATI regime is shown in Fig. 2.1 for single ionization of Xe by 25 fs, 800 nm laser pulses.

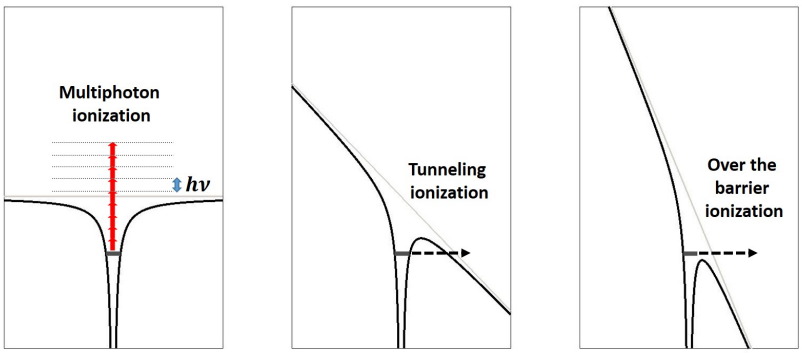

Figure 2.2: *Schematic representation of multiphoton, tunneling and over-the-barrier ionization. For a given laser wavelength, the intensity grows from left to right.*

2.1.2 Tunneling and over-the-barrier ionization

In this regime, the Keldysh parameter is smaller than 1 ($\gamma < 1$), and the laser field strength is comparable to the atomic potential. Therefore, the atomic potential is tilted, and the electron tunnels through the Coulomb barrier. At even higher intensities, the atom's Coulomb barrier is suppressed to a level that the electron is essentially in the continuum, and no tunneling is needed for it to escape. Fig 2.2 shows a schematic picture of all three ionization regimes. The minimum laser field strength required for over-the-barrier ionization (OBI) is given by

	Laser intensity (W/cm^2)	$I_p(eV)$	γ
HHG generation			
$Argon$	4.0e14	15.76	0.58
$Neon$	1.2e15	21.55	0.39
NIR probe			
$Xenon$	2.0e13	12.13	2.28
$Krypton$	3.0e13	14.00	2.00
$Neon$	3.0e13	21.55	2.48
CO_2	4.0e13	13.78	1.72
$Methanol$	2.0e13	10.84	2.16
$Ethanol$	2.0e13	10.81	2.11

Table 2.1: *Keldysh parameter for different intensities relevant to the experiments discussed in the following chapters*

$$E_{critical} \approx \frac{Z^3}{16n^{*2}} \tag{2.3}$$

where Z is the ion charge, and $n^* = \frac{Z}{\sqrt{2I_p}}$ is the orbital's effective principal quantum number [16].

The values of the Keldysh parameter for gas targets and intensities typically used in experiments carried out as a part of this thesis work are listed in table 2.1. For high harmonic generation, tunneling ionization plays the most crucial role. However, in XUV pump - NIR probe experiments, multiphoton ionization is the dominant ionization process for the NIR probe. The strong-field ionization regimes mentioned here cannot be entirely separated from each other. First, there is no sharp transition at the Keldysh parameter value of 1, and the ionization process in this regime can manifest both multiphoton or tunneling signatures. Second, for gas-phase targets, an atom or a molecule may experience lower or higher intensities depending on their position with respect to the center of the laser focus. Therefore, contributions from all of these regimes can be present in the experiment performed at a given intensity, provided its peak value is high enough to enter the OBI regime.

2.2 High harmonic generation

When atoms or molecules are exposed to intense linearly polarized laser pulses, photons with energies corresponding to integer multiplies of fundamental laser frequency can be emitted, which is called high-order harmonic generation (HHG). The generated harmonics are highly coherent in both the space and time domain [17,18,19,20]. The nonlinear frequency conversion of the fundamental laser frequency can be extended to soft X-ray and XUV regimes. HHG sources are typically compact and tabletop. Thus, they are an excellent substitute for much more expensive synchrotron radiation sources, although generally providing lower photon flux and less tunability. The spectrum of such high harmonics contains a plateau where their intensity is nearly constant. A sharp cutoff follows the plateau, with the cutoff photon energy given by:

$$h\nu_{cut-off} = I_P + 3.2U_p \tag{2.4}$$

where U_p is the pondermotive energy of atoms or molecules used to generate harmonics. As mentioned above, the pondermotive energy in atomic units is given by $U_p = E_0^2/4\omega_0^2$. In units of eV it can be calculated as $U_p = 9.337 * 10^{-14}(\mathrm{I})(\lambda^2)$, where intensity is in (W/cm^2) and wavelength in (μm). High harmonic generation is one of the most important topics in the field of laser-matter interactions. The advances in HHG have opened a new sub-field in nonlinear optics and paved the way toward attosecond spectroscopy in the XUV and soft X-ray regimes [10].

2.2.1 Semiclassical three-step model

A rather simple semiclassical three-step model can qualitatively explain many features of the HHG process [21]. In the first step, in the presence of an external laser field, electrons tunnel out of the atom into the continuum with no kinetic energy. In the second step, electrons propagate classically under the influence of the external oscillating laser field. In

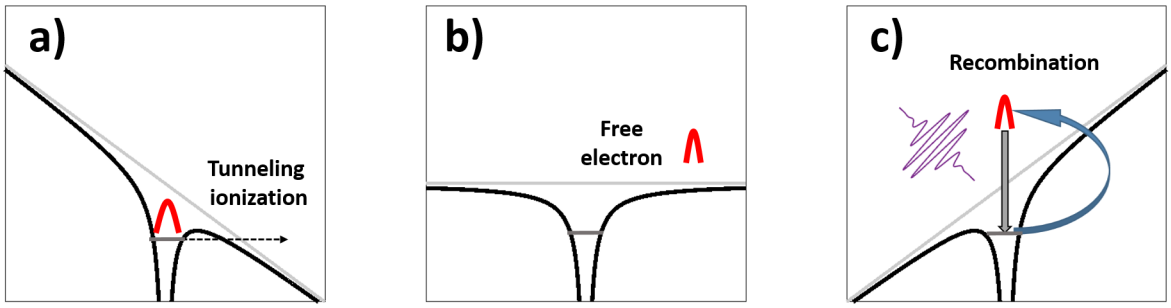

Figure 2.3: *Schematic representation of a three-step process leading to high harmonic generation.*

the third step, electrons can, with a certain probability, recombine with the parent ion and emit a high-energy photon. Thus, within this model, electrons in the first and third steps are treated quantum mechanically, whereas the dynamics of the electron driven by the laser field in the second step are treated classically. The energy of the emitted photon equals energy gained by the electron in the laser field plus the ionization potential.

Let us assume that the electron is born at t=t_0 with x(t_0)=$x^{'}(t_0)$=0 and is propagating under the influence of the electric field of the laser $E(t)$=$E_0 cos(\omega t)$, which is linearly polarized in the x direction. By solving the equations of motion with the initial conditions mentioned above, the position and velocity of the electron in a.u at any given time $t > t_0$ is given by:

$$x(t) = -\frac{E_0}{\omega^2}(cos(\omega t_0) - cos(\omega t) + (\omega t_0 - \omega t)sin(\omega t_0)) \tag{2.5}$$

$$x^{'}(t) = -\frac{E_0}{\omega}(sin(\omega t_0) - sin(\omega t)) \tag{2.6}$$

the kinetic energy of the electron at any given time $t > t_0$ is given by:

$$KE_{electron}(t) = \frac{E_0^2}{2\omega^2}(sin(\omega t_0) - sin(\omega t))^2 = 2U_p(sin(\omega t_0) - sin(\omega t))^2 \tag{2.7}$$

the recombination time can be found by solving x(t_r)=0, and the kinetic energy of the

electron upon recombination is given by equation 2.7. The emitted HHG photon energy is equal to E_{HHG}=I_P+$KE_{electron}(t_r)$, where I_P is the ionization potential of the atomic or molecular target. Here, we only consider single recollision events and neglect multiple recollisions since the electron wave packet expands over time and contributions from multiple recollision are expected to be rather small.

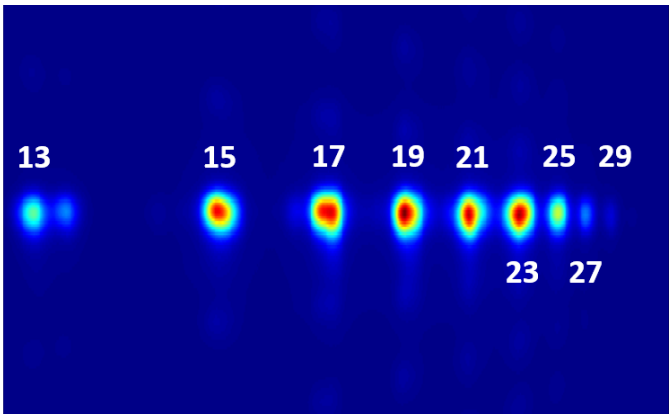

Figure 2.4: *A HHG spectrum generated by XUUS.*

For ωt_0 between 0 and $\pi/2$, two solutions for x(t_r)=0 can be found, meaning that the electron can recombine with the parent ion in two different trajectories. However, for ωt_0 between $\pi/2$ to π, no solution for x(t_r)=0 can be found, which means that the electron never returns to the parent ion. In the same manner, electron recombination is possible for ωt_0 between π to $3\pi/2$ and not possible for ωt_0 between $3\pi/2$ to 2π. This means that the recombination and, thus, HHG emission happens every half of the optical cycle for any given kinetic energy. Therefore, a pulse train with a period of a half-cycle of the optical laser field is generated. The phase of every adjacent HHG pulse is different by π, and the Fourier transform of the pulse train ensures that only odd multiples of the fundamental optical angular frequency are non-zero. This explains why only odd-order harmonics are usually observed. A high harmonic spectrum generated in our experimental hollow-core fiber, filled by argon and filtered by an Al foil, is shown in Fig 2.4. As expected, only the odd-order harmonics are present in the spectrum.

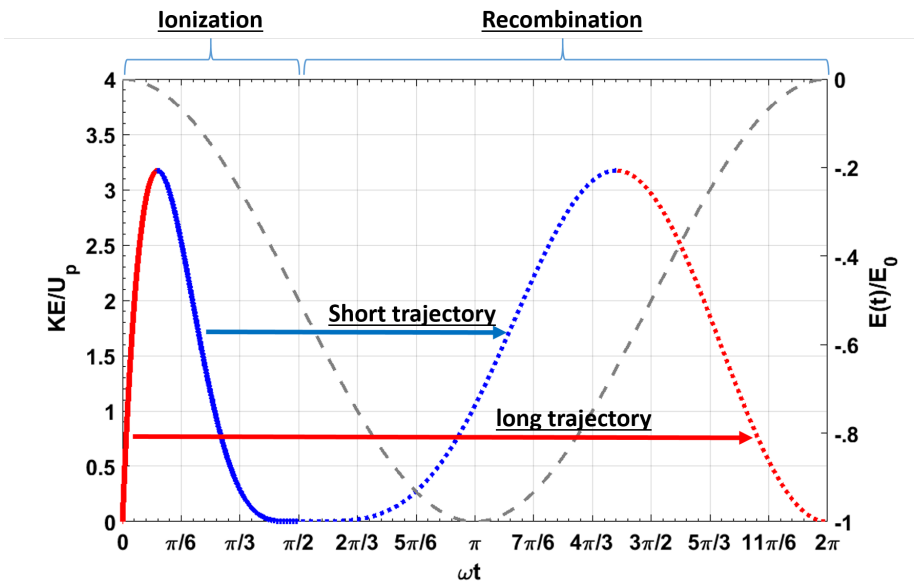

Figure 2.5: *Kinetic energy of electron upon recombination as a function of* ωt.

For ωt_0 between 0 and $\pi/2$, the kinetic energy of the electron upon recombination as a function of its birth time and return time is plotted in Fig 2.5. The maximum kinetic energy of the electron occurs at the birth time $\omega t_0 = 17^o$ or return time $\omega t_r = 255^o$, with a KE_{max} equal to $3.17U_p$. This is in good agreement with the harmonic cutoff energy (equation 2.4). If the electron is born within $0 < \omega t_0 < 17^o$ (solid red line), it follows a long trajectory (dashed red line), and if it is born within $17^o < \omega t_0 < 90^o$ (solid blue line), it will experience a short trajectory (dashed blue line). Two arrows in Fig 2.5 indicate short and long trajectories.

The semiclassical three-step model nicely describes electron trajectories in the continuum, and such characteristic HHG features as chirp, HHG spectrum dependence on laser polarization, and cut-off energy. However, it fails to address essential aspects of HHG, such as the phase and amplitude of high harmonics and the conversion efficiency of the HHG process. Thus, more rigorous theoretical models, like, for example, solving the TDSE for calculating high harmonic generation, are needed. In the following section, we briefly discuss the solution of the TDSE for an atom exposed to an intense laser field.

2.2.2 TDSE solution for HHG

This section is adapted from Chapter 5 of the book "Attosecond and Strong-Field Physics Principles and Applications" by C. D. Lin [22]. The time-dependent Hamiltonian of an atom exposed to an intense laser field in the length gauge is given by:

$$H(t) = -\frac{1}{2}\nabla^2 + V(r) + r.E(t) \tag{2.8}$$

The induced time-dependent dipole radiates. It can be calculated by solving the time-dependent Schrödinger equation (TDSE) $\mathrm{i}\frac{\partial}{\partial t}\ |\Psi(r,t)>=H(t)\ |\Psi(r,t)>$ for the Hamiltonian mentioned above. The dipole is given by:

$$\mathbf{D}(t) =< \Psi(t)|\mathbf{r}|\Psi(t) > \tag{2.9}$$

The emission of high harmonics can be calculated by evaluating the Fourier transform of $D(t)$. Thus, the power spectrum will be proportional to $\omega^4\ |D_i(\omega)|^2$, where i is along the harmonic's polarization direction. Numerical calculations such as time-dependent density functional theory (TDDFT) can be carried out to describe the HHG in atoms and molecules. If, however, phase matching is considered, the direct TDDFT calculation will become slow and inefficient. At different steps, the HHG calculation can be simplified by a series of approximations. One of the popular and efficient approximations for modelling HHG is briefly outlined below.

2.2.3 The Lewenstein Model

This model was first developed by Lewenstein in 1994 [23,24]. He made a series of assumptions based on the second-order strong-field approximation. a) The ground state depletion is not significant and can be ignored. b) The excited states do not contribute to ionization. c) The electrons propagate in the continuum without being affected by the atomic potential.

The time-dependent dipole moment based on the assumptions above can be written as:

$$D(t) = -i \int_{-\infty}^{t} dt^{'} \int d^3p \; \mathbf{d}^*(\mathbf{p} + \mathbf{A}(t)) exp(-iS(\mathbf{p}, t, t^{'})) \mathbf{E}(t^{'}) \cdot \mathbf{d}(\mathbf{p} + \mathbf{A}(t^{'})) + c.c. \quad (2.10)$$

where $\mathbf{d}(p)$ is the dipole transition matrix element, $\mathbf{A}(t)$ is the vector potential, and $\mathbf{p}$ is the canonical momentum. The action function S is given by:

$$S(\mathbf{p}, t, t^{'}) = \int_{t'}^{t} dt^{''} [\frac{1}{2}(\mathbf{p} + \mathbf{A}(t^{''}))^2 + I_p] \quad (2.11)$$

The Fourier transform of $D(t)$ is given by:

$$\begin{aligned} \mathbf{D}(w) &= \int_{-\infty}^{\infty} dt \mathbf{D}(t) \; exp(i\omega t) \\ &= -i \int_{-\infty}^{\infty} dt \int_{-\infty}^{t} dt^{'} \int d^3p \; \mathbf{d}^*(\mathbf{p} + \mathbf{A}(t)) exp(i\omega t - iS(\mathbf{p}, t, t^{'})) \mathbf{E}(t^{'}) \cdot \mathbf{d}(\mathbf{p} + \mathbf{A}(t^{'})) + c.c. \end{aligned} \quad (2.12)$$

The equation 2.10 has a straightforward interpretation that corresponds to the semiclassical three step model. The term $\mathbf{E}(t^{'}) \cdot \mathbf{d}(\mathbf{p} + \mathbf{A}(t^{'}))$ shows that ionization happens at a time $t^{'}$, the electron's instantaneous velocity at a time t is $\mathbf{p} + \mathbf{A}(t)$, the term $exp(-iS(\mathbf{p}, t, t^{'}))$ corresponds to electron propagation from time $t^{'}$ to t, and the term $\mathbf{d}^*(\mathbf{p} + \mathbf{A}(t))$ indicates that recombination occurs at time t. Saddle-point analysis is typically used to evaluate the integral over the momentum $\mathbf{p}$ in equation 2.12. The complete mathematical calculation, using the saddle-point approximation, can be found in Ref. [22,25].

2.2.4 HHG Phase matching in hollow core fiber

The equations for this section are adapted from the article "Phase matching of high harmonics in hollow waveguide" [26]. Phase matching in an experimental configuration where the laser beam is focused in a gas jet is usually dominated by the Guoy phase shift. Typically, shifting the focus outside of the interaction region would enhance the harmonic generation

efficiency. However, this method is limited by the length of interaction, and also, typically, a higher laser energy per pulse is required. This section will show that by using a hollow waveguide, the restrictions mentioned above can be resolved. In this method, the laser beam is focused into a hollow core waveguide filled by a target gas. The anomalous dispersion of the target gas can be compensated by the dispersion of free electrons and also the ordinary dispersion of the fiber in the considerably longer interaction length.

In a hollow-core waveguide, the propagation constant is given by:

$$k^2 = (nk_0)^2 - \frac{{u_{mn}}^2}{a^2} \tag{2.13}$$

where k_0, u_{mn}, and a are the wavenumber in vacuum, a constant which corresponds to the mode of propagation in the waveguide, and the radius of the fiber, respectively. The index of refection depends on the pressure (p), the number density (N_a), the nonlinear refractive index(n_2), the ionization fraction (η), the intensity of the laser pulse (I), and the natural gas dispersion ($\delta(\lambda)$). The effect of the nonlinear refractive index is small compared to gas dispersion and can be neglected. Thus, the refractive index can be written as:

$$n = 1 + P(1-\eta)\delta(\lambda) - \eta P N_a r_e \frac{\lambda^2}{2\pi} \tag{2.14}$$

By substituting equation 2.14 into 2.13, the propagation constant can be written as:

$$k \approx \frac{2\pi}{\lambda} + \frac{2\pi\delta(\lambda)N_a}{\lambda} - \lambda r_e N_e - \frac{\lambda u_{mn}^2}{4\pi a^2} \tag{2.15}$$

where the term $\frac{2\pi}{\lambda}$ corresponds to propagation in vacuum, the term $\frac{2\pi\delta(\lambda)N_a}{\lambda}$ is the dispersion in the neutral gas, the term $\lambda r_e N_e$ is the dispersion in plasma (where N_e=$P\eta N_a$ is the plasma or electron density), and the term $\frac{\lambda u_{mn}^2}{4\pi a^2}$ corresponds to the dispersion of the fiber. A phase mismatch between the NIR pulse and the XUV pulse is given by:

$$\begin{aligned}\Delta k &= k_{XUV} - qk_{IR} \\ &\approx -\frac{2\pi N_a}{\lambda_{XUV}}(\delta(\lambda_{IR}) - \delta(\lambda_{XUV})) + r_e N_e(q\lambda_{IR} - \lambda_{XUV}) + q\frac{u_{mn}^2 \lambda_{IR}}{4\pi a^2}\end{aligned} \tag{2.16}$$

where q is the order of the harmonic (XUV). The phase matching holds if Δk=0. Parameters that can be adjusted to achieve phase matching are:

- The wavelength.
- Gas type.
- Gas pressure.
- Laser intensity.
- The waveguide size.
- The spatial mode.

As discussed above, there are three dispersion types, the dispersion from (a) neutral atoms, (b) plasma, and (c) the waveguide. The balance between these three terms depends on NIR intensity and the fractional ionization rate. In a low NIR intensity regime, the plasma density is low and plasma dispersion can be neglected. In this regime, we only consider neutral gas dispersion and waveguide dispersion, and the gas pressure plays an important role in phase matching. For a specific harmonic and a given intensity, the optimum gas pressure depends on how dispersive the target gas is. If the target gas is less dispersive, higher gas pressure is required, and if the target gas is more dispersive, lower gas pressure is required for proper phase matching. For example, for a given harmonic such as Harmonic 25, using Xe, Kr, Ar, Ne, or He, the optimum pressure for phase matching would be $P_{Xe} < P_{Kr} < P_{Ar} < P_{Ne} < P_{He}$ since the gas dispersion of Xe is highest among all of the atoms mentioned above. At higher IR intensities, the plasma dispersion can no

longer be neglected, and it is equally important. Thus, both plasma and waveguide dispersion should be considered to compensate for gas dispersion. In this regime, the ionization fraction η increases (N_e increases), and gas pressure should increase (N_a should increase) to achieve phase matching. At very high NIR intensities, the dispersion is dominated by the plasma dispersion. Thus, the phase matching condition can not be satisfied anymore, and the HHG phase matching efficiency drops significantly. Critical ionization can be defined as an ionization fraction η_{cr} where the gas dispersion and the plasma dispersion are equal. Phase matching is considered to be efficient if, for a given harmonic, the ionization rate is below η_{cr}.

Non-collinear phase matching occurs when high harmonic radiation is emitted at an angle θ with respect to the IR laser field propagation. In this case, the phase condition is equal to $\Delta k = k_{XUV} cos(\theta) - q k_{IR}$. This type of phase matching is called Cerenkov phase matching. It is not an efficient way to achieve phase matching since the HHG signal can not coherently increase over a long distance, and it quickly goes out of the source region.

To achieve phase matching, it is important to consider absorption by the medium. The absorption coefficient α depends on HHG energy and gas type. The HHG signal strength depends on both the coherence length ($\frac{1}{\Delta k}$) and absorption depths ($\frac{1}{2\alpha}$). If, for a given harmonic, the absorption coefficient α is high, the absorption depth is smaller than the coherence length, and HHG can not efficiently build up over the length of the waveguide even though Δk is pretty small.

2.3 XUV photoionization

The central NIR photon energy of laser pulses used in this work is 1.57 eV, corresponding to a 790 nm wavelength. In order to photoionize atoms or molecules using an NIR pulse, multiple photons need to be absorbed. Valence shell electrons are the first electrons that are removed by NIR pulses. To remove an inner-valence or core-shell electron, the least

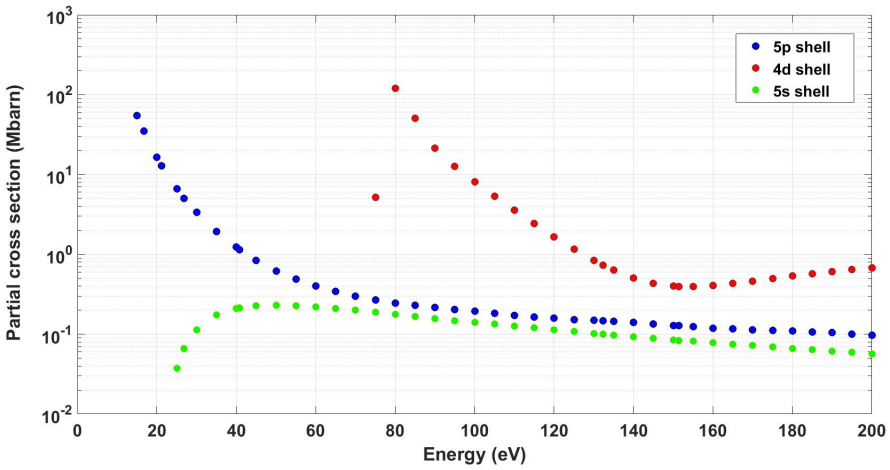

Figure 2.6: *Partial photo-ionization cross section of xenon atom, for 4d, 5s, and 5p levels, adapted from [27].*

bound electrons are usually removed first by NIR. XUV and X-ray photon energies are typically higher than the electron binding energy in atoms, such that the absorption of a single photon normally results in ionization. Using XUV light, an inner-valence shell or core-shell ionization can occur without ionizing outer-valence shells first.

The photoionization cross section depends on the photon energy and, above a particular absorption edge, usually decreases with increasing photon energy. However, photoionization increases significantly at photon energies approaching an absorption edge (absorption edges are typically energies corresponding to the ionization potential of a specific shell). For heavier atoms, the cross section is typically higher than for lighter atoms at a given energy.

The atomic absorption coefficient away from absorption edges is expressed by the empirical Victoreen equation:

$$\mu_0/\rho = c\lambda^3 + d\lambda^4 \tag{2.17}$$

where ρ is the density of final states and c and d are constants that are atom and shell specific [28]. The partial cross section of the 5p, 5s, and 4d shells of Xenon are plotted in Fig. 2.6. At photon energies between 80 and 90 eV, XUV light mainly ionizes 4d shell of

Xenon.

In one-electron atoms, within the dipole approximation (which states that the electric field and vector potential only depend on time, and a contribution from the magnetic field is neglected, such that $kr << 1$ or $r << \lambda$), the ionization rate per unit energy for linearly polarized light along the z direction is given by [22]:

$$\frac{dW}{dE} = \frac{4\pi^2 I(\omega_{Ei})}{c} |D_{Eiz}|^2 \rho(E) \tag{2.18}$$

where D_{Ei} is the electric dipole moment ($D_{Eiz} = - < E|z|i >$), ω_{Ei} is the energy difference between the continuum state and the bound state, and $\rho(E)$ is the density of the final state. Therefore, the photoionization cross section from a bound state $|i >$ to a continuum state $|f >$ is expressed by:

$$\sigma_{fi} = \frac{4\pi^2 \omega_{fi}}{c} | < f|z|i > |^2 \tag{2.19}$$

The continuum state f and the bound state i can be written in spherical coordinates, and after some intermediate calculations, the photoionization differential cross section can be written as:

$$\frac{d\sigma}{d\Omega} = \frac{\sigma_T}{4\pi}(1 + \beta P_2(cos(\theta))) \tag{2.20}$$

where β is the asymmetry parameter and $P_2(cos(\theta)) = \frac{3cos^2(\theta)-1}{2}$ is the second Legendre polynomial. This equation is widely used to describe the angular distribution of the photoelectrons resulting from the photoionization process. The β value can lie between -1 and 2. For positive values, the electron angular distribution is peaked along the light polarization (for example, for $\beta = 2$, the angular dependence is proportional to $cos^2(\theta)$), for values near zero the distribution is uniform, and for negative values the electrons are mostly emitted along the direction perpendicular to light polarization (for example, for $\beta = -1$, the angular dependence is proportional to $sin^2(\theta)$). Polar plots of a photoelectron differential cross

section for four asymmetry parameters are plotted in Fig.2.7 ($\frac{d\sigma}{d\Omega}/\frac{\sigma_T}{4\pi}$ is plotted) .

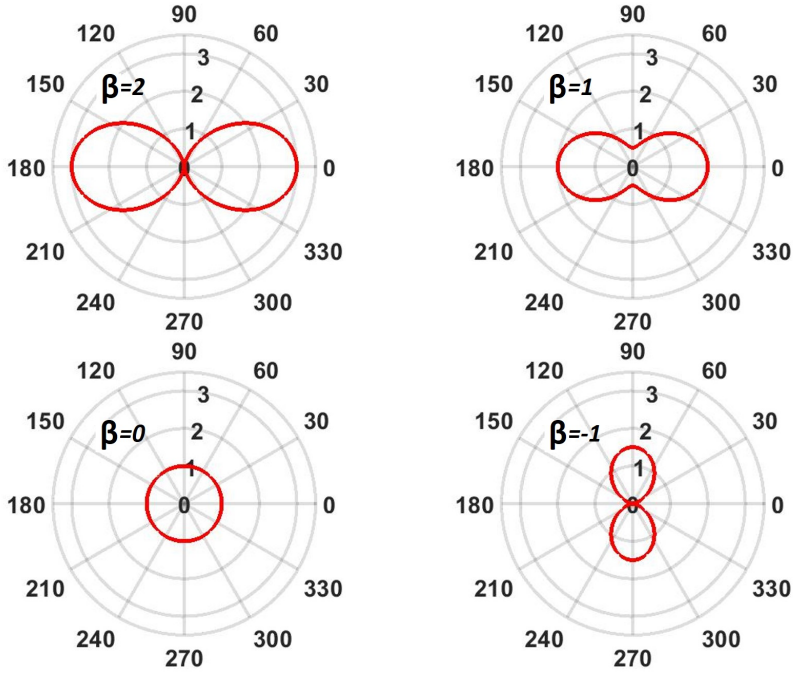

Figure 2.7: *Photoelectron differential cross section, θ is the angle between the velocity vector of the electron and the light polarization. For $\beta = 2$ and 1, photoelectrons are emitted mostly along the light polarization, for $\beta = 0$ the distribution is uniform, and for $\beta = -1$ photoelectrons are mostly emitted perpendicular to the light polarization.*

2.3.1 Relaxation, shake-up and shake-off processes

As mentioned above, XUV photons can have energies much higher than the binding energy of the least-bound electron(s) in an atom or a molecule. The excess energy can be shared with another electron, leaving the ion in an excited state (shake-up), or even emitting a second electron (shake-off). If an inner-valence or core-shell electron is ionized, creating an inner hole, an atom or a molecule is left in an energetically unfavorable, highly excited state. An electron from the outer shell can fill the inner hole. If this happens, the energy difference between the binding energy of the outer-shell electron and the inner hole can be released as a photon (fluorescence) or exchanged between electrons (Auger decay).

2.3.2 Fluorescence

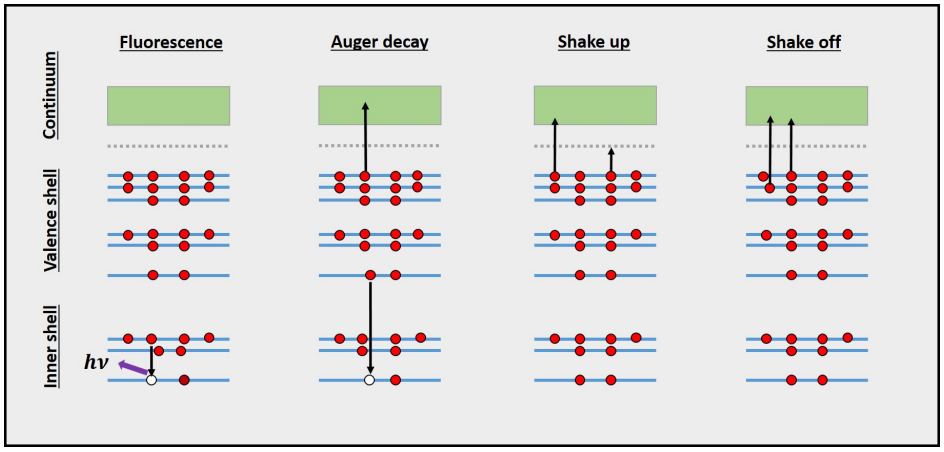

Figure 2.8: *Schematic of fluorescence, Auger decay, shake-up, and shake-off processes.*

In fluorescence decay, a photon is emitted when an outer-shell electron fills the inner-shell hole. In this process, the charge state of an atom does not change since no further electron is ejected. The energy of the emitted photon is equal to the binding energy difference between two levels ($E_{radiation} = E_{innershell} - E_{outershell}$). Fluorescence decay is a spontaneous emission process. In one-electron systems, within the dipole approximation, spontaneous emission rate is expressed by[22]:

$$W^s_{ab} = \frac{4\omega^3_{ab}}{3c^3}|D_{ba}|^2 \tag{2.21}$$

where $D_{ba} = - < b|r|a >$ is the electric dipole moment. For one-electron systems, $< r >$ and ω_{ba} are proportional to $\frac{1}{Z}$, and Z^2, respectively. Thus, the transition probability is proportional to Z^4. The relative fluorescence yield values for the K, L, and M shells of a few elements are presented in table 2.2. Fluorescence emission for the L and M shells of light atoms (low Z value) is very unlikely. However, for heavy atoms, the spontaneous emission rate is more likely, becoming the dominant decay process for K shell).

element	Z number	K shell	L shell	M shell
Ar	18	0.12	0.0015	0
Zn	30	0.49	0.01	1e-4
Kr	36	0.65	0.02	4e-4
Xe	54	0.89	0.088	3.6e-3
Hg	80	0.96	0.34	0.026

Table 2.2: *Fluorescence yield value for K, L and M shell of few elements,adapted from[29]*

2.3.3 Auger decay

In this process, the inner-shell hole created by photoionization is filled with an outer-shell electron, and the energy difference between the binding energy of the hole and the outer-shell electron is transmitted to another electron through Coulomb interaction. Thus, the second electron (Auger electron) is ejected, and the charge state of the atom increases by one. The energy of a photoelectron and an Auger electron are given by $E_{e1} = h\nu - |E_{inner-shell}|$, and $E_{e2} = |E_{inner-shell}| - |E_{outer-shell}| - |E_2|$, respectively. Here, $E_{inner-shell}$ is the binding energy of the photoelectron, $E_{outer-shell}$ is the binding energy of the electron filling the hole, and E_2 is the binding energy of the Auger electron. The Auger electron's energy does not depend on the photon energy and, for a specific Auger decay path, is always fixed. A double Auger decay can occur when the energy difference is enough to simultaneously ionize two outer electrons, increasing the charge state by two. We will discuss an example of Auger decay in chapter 3, where photoionization creates a hole in the 4d shell of Xe, and two Auger decays in a row increase the charge state of Xe to three plus.

Using the Fermi Golden rule of perturbation theory, the transition rate of Auger processes can be expressed as:

$$W_{if} = 2\pi| < \psi_f(\mathbf{r}_1, \mathbf{r}_2)|H^{'}(\mathbf{r}_1, \mathbf{r}_2)|\psi_i(\mathbf{r}_1, \mathbf{r}_2) > |^2 \rho(E_f) \tag{2.22}$$

here, the perturbation $H^{'} = \frac{1}{\mathbf{r}_1 - \mathbf{r}_2}$ is the Coulomb interaction between two electrons. The $< \frac{1}{r} >_{nlm}$ is proportional to Z, thus the probability is proportional to Z^2. If energetically

allowed, Auger decay from the same shell is more probable than Auger decay from a different shell because the overlap with the wave function of the electron from the same shell is higher. As we have seen in the previous section, fluorescence is the primary decay mechanism for heavy atoms, especially for the K shell. However, Auger decay is the primary relaxation process for light atoms.

2.3.4 Shake-up and shake-off processes

The initial direct photoionization, as well as every relaxation process, can be accompanied by excitation or emission of additional electrons whenever energetically allowed. For example, in the Auger decay process, the Auger electron carries the entire excess binding energy. However, the electron-electron interaction between the photoelectron or Auger electron and valence electrons can put a valence electron into the continuum or an unoccupied excited state. If the valence electron is excited to an unoccupied state, the process is called shake-up, and if the valence electron is excited to the continuum, the process is called shake-off. In shake-up (or shake-off), the energy of the absorbed photon is shared with a second electron to excite it (or ionize it). If no Auger process is involved, the energy sum of both the photoelectron and the shake-off electron is equal to $h\nu - E_{inner-shell}$ (or in shake-up process, the energy of the photoelectron is $h\nu - E_{inner-shell} - E_{excitation}$), where $E_{excitation}$ is the excitation energy of the shake-up electron.

2.4 Sidebands

A photoionization process can be significantly modified in the presence of a second, longer-wavelength light field (e.g., NIR). Several methods for XUV and X-ray pulse characterization rely on such two-color effects, where the energy (momentum) of an electron created by XUV / X-ray photoionization is modified by an overlapping visible or NIR laser field. If the effective duration of the XUV / X-ray pulse is shorter than the oscillation period of a

long-wavelength laser field, the latter results in the periodic change of the momentum (and energy) of the created electron, which depends on the instantaneous electric field of the long-wavelength pulse at the time of photoionization and, thus, on the exact phase relation between the two pulses. Based on this, both the chirp and the temporal duration of a single XUV or X-ray pulse can be determined [30].

In the opposite limit, when the XUV / X-ray pulse is longer than one optical cycle of a visible / NIR pulse, the photoelectron spectrum exhibits so-called "sidebands", the peaks appearing at energies shifted by ± one photon energy compared to the single-color XUV / X-ray ionization. In other words, the sidebands emerge with even-order harmonic frequencies between adjacent harmonics. Two different pathways can create sidebands, by absorption of a photon from a harmonic and absorption of a photon from the NIR field, or by absorption of a photon from the next harmonic and emission of a photon from the IR field. These two different quantum pathways interfere with each other. If the XUV pulse is in fact a train of attosecond pulses, which is almost always the case for HHG, this interference causes the sideband signal to oscillate periodically as a function of XUV-NIR delay. This oscillation can be used to characterize the temporal profile of individual pulses in the train. This technique is known as "Reconstruction of Attosecond harmonic Beating By Interference of Two-photon Transitions" (RABBITT) [31]. In addition, information about the gas target can be obtained by studying the phase of this oscillation [32].

Sidebands can be used to study the polarization dependence of rare gas photoionization [33]. Even without resolving the RABBITT-type oscillations, they can be used to characterize the XUV pulse duration or to obtain information on the relative phase of high harmonics. The sideband intensity is very sensitive to temporal and spatial overlap between the XUV and NIR pulses. We frequently use sidebands to characterize the XUV pulse duration or to obtain exact time-zero positions in pump-probe experiments throughout this work. Examples of sideband structures in argon, neon, CO_2, and alcohol molecules are presented in chapter 4, 5, and 6.

2.5 Molecular dynamics

A molecule is a group of atoms bound together. Because of additional degrees of freedom, molecules are harder to understand than atoms. The motion of atomic nuclei is typically significantly slower than the motion of the electrons. Therefore, the associated energy of these motions is significantly different as well. The so-called Born-Oppenheimer approximation can be used to understand the molecular structure better. [22]

2.5.1 Born-Oppenheimer approximation

Since the time scales of electronic and nuclear motion are remarkably different, the molecular wave function can be written as two separate parts, the electronic wave function and the nuclear wave function. The nuclei are slower than the electrons (they are much heavier), thus for the electronic wave function calculation, the nuclear distance can be considered fixed. The total Hamiltonian of a molecule is given by:

$$\begin{aligned} H &= \sum_i \frac{P_i^2}{2M_i} + \sum_j p_j^2 - \sum_{i,j} \frac{Z_i}{|\mathbf{r}_j - \mathbf{R}_i|} + \sum_{j>k} \frac{1}{r_{jk}} + \sum_{i>m} \frac{Z_i Z_m}{R_{im}} \\ &= \sum_i \frac{P_i^2}{2M_i} + H_{el}(\mathbf{r}, \mathbf{R}) \end{aligned} \tag{2.23}$$

For a fixed nuclear coordinate $\mathbf{R}$, we can solve the electronic part of the Schrödinger equation $\hat{H}_{el}\Phi_n(\mathbf{r}, \mathbf{R}) = E_n\Phi_n(\mathbf{r}, \mathbf{R})$. The electronic eigenfunctions $\Phi_n(\mathbf{r}, \mathbf{R})$ form a complete basis set. We may write the total wave function $\Psi(\mathbf{r}, \mathbf{R})$ as an expansion of $\Phi_n(\mathbf{r}, \mathbf{R})$ basis sets:

$$\Psi(\mathbf{r}, \mathbf{R}) = \sum_n \psi_n(\mathbf{R})\Phi_n(\mathbf{r}, \mathbf{R}) \tag{2.24}$$

here, $\psi_n(\mathbf{R})$ is the nuclear wavefunction. By substituting the expansion 2.24 into the Schrödinger equation, and for nuclear coordinates where the energy gap between electronic energy states n and n' is not small, the nuclear eigenvalue problem is given by:

$$(\sum_i \frac{P_i^2}{2M_i} + E_n)\psi_n(\mathbf{R}) = E_{\psi,n}(\mathbf{R}) \tag{2.25}$$

The Born-Oppenheimer approximation breaks down near a conical intersection of two electronic states, where their energies are degenerate.

To solve the electronic eigenvalue problem, one may use the independent particle model. Applying this approximation to the equation $\hat{H}_{el}\Phi_n(\mathbf{r},\mathbf{R}) = E_n\Phi_n(\mathbf{r},\mathbf{R})$ leads to the Hartree-Fock equation. This equation is solved to get molecular orbitals. A linear combination of atomic orbitals can be used to form molecular orbitals. MO's are filled based on the Aufbau principle. To improve the approximation, many-body perturbation theory, the configuration interaction approach, or the MCHF method can be employed.

The electronic structure of molecules is far more complicated than that of atoms. The molecular symmetry property can be taken into account to simplify the interpretation of the electronic structure.

There is cylindrical symmetry along the molecular axis for diatomic molecules, which means the total orbital angular momentum's ($|M|$) projection on the molecular axis is a constant of motion. The molecular orbitals are shown by the projection of their orbital angular momentum on the molecular axis($|m|$). The notations σ, π, and δ are used for $|m|$ equals 0, 1, and 2 respectively. If applicable, the parity notation g and u can be used for even and odd molecular orbital functions. For example δ_u means $|m| = 2$ and an odd function.

We often see terms such as $X^3\Sigma_g^-$, $a^1\delta_g$, $B^3\Sigma_u^-$, ... for electronic states of diatomic and linear polyatomic molecules. Let us decode what these molecular terms mean. The molecular term is written by a letter accompanied by a term ($^{2S+1}\Lambda_{\Omega,(g/u)}^{(+/-)}$). For the ground state, the letter is X. For excited states, the letter is either (A, B, C,...,) if the spin of the ground state is the same as the excited state, or (a,b,c,...) if the spin of the ground state is different than the excited state. The term 2S+1 is the spin multiplicity, where S is the total spin of the electron. The term Λ is the total electron orbital angular momentum $|M|$ along

the molecular axis. Notation Σ, Π, and Δ are used for $|M|$ equals 0, 1, and 2 respectively. If a molecule has a center of symmetry, the term g or u is used for even and odd parity of the total electronic wavefunction (inversion with respect to the center of symmetry). The term Ω is the projection on the molecular axis of total spin and electron angular momentum. Also, $+/-$ is used for positive and negative symmetry of reflection of the wavefunction with respect to the molecular plane.

In diatomic molecules, the nuclear eigenvalue problem 2.25 can be solved by separating rotational and vibrational motions in order to find rotational and vibrations energy levels and wavefunctions. The rotational wave function is a spherical harmonic Y_{JM}, where J is the nuclear angular momentum. The rotational energies are given by $E_{rot} = B_e J(J+1)$, where B_e is the rotational constant.

Vibrational motions are typically studied near equilibrium. By expanding the electronic potential E_n near the equilibrium coordinate, $E_n(R) = E_n(R_e) + \frac{1}{2}k(R-R_e)^2$, one can show that the vibrational wavefunctions are a solution of the harmonic oscillator Schrödinger equation. Therefore, the wave functions are Hermite functions, and vibrational energies are given by $E_{n,\nu} = (\nu + \frac{1}{2})\omega$.

In linear triatomic molecules such as the CO_2 molecule, the rotational energies are given by the same equation as used for diatomic molecules. For vibrational energies, one may expand the potential energy surface near equilibrium. Therefore, the total vibrational energy can be given by:

$$E_{\nu_1,\nu_2,\nu_3} = \sum_{i=1}^{3}(\nu_i + \frac{1}{2})\omega_i \tag{2.26}$$

2.5.2 Single-photon transitions in molecules and selection rules

In this section, we discuss single-photon absorption and radiation transitions in molecules. In diatomic molecules, if the final and initial transition states are lying in the same electronic state, we only have vibrational and rotational transitions. The intensity of a transition

within the same electronic state can be given by:

$$I \propto | < \Psi_{n,\nu',J',M'_J} | \boldsymbol{\mu}(Q) | \Psi_{n,\nu,J,M} > |^2 \tag{2.27}$$

the term $\boldsymbol{\mu}(Q)$ is the dipole moment of the molecule for the same electronic state $\phi_n(\mathbf{r}, \mathbf{R})$.

Due to symmetry, the dipole moments of homonuclear diatomic molecules such as H_2, O_2, and N_2 are zero. Therefore, vibrational-rotational dipole transitions within the same electronic state in homonuclear diatomic molecules are not allowed. However, in heteronuclear diatomic molecules such as HF, HCL, CO, ... the dipole moments don't vanish, and vibrational-rotational dipole transitions are allowed. For rotation-only transition, the selection rule is:

$$\triangle J = \pm 1, \quad \triangle M = 0, \pm 1 \tag{2.28}$$

For pure vibrational transition the selection rule is given by:

$$\triangle \nu = \pm 1 \tag{2.29}$$

For both vibrational and rotational transitions together, the selection rule is given by:

$$\begin{aligned} \triangle J = \pm 1, \quad \triangle \nu = \pm 1 \quad for \quad \Lambda = 0 \\ \triangle J = 0, \pm 1, \quad \triangle \nu = \pm 1 \quad for \quad \Lambda \neq 0 \end{aligned} \tag{2.30}$$

$$\triangle J = \pm 1, \quad \triangle M = 0, \pm 1 \tag{2.31}$$

The rotational transitions are typically in microwave wavelengths, and vibrational transitions are in infrared to mid-infrared wavelengths. However, the electronic transitions are in near-infrared to UV wavelengths because the energy differences between different electronic states are on the order of few eV or higher. For a dipole transition between different

electronic states to be allowed, the dipole of the electronic transition cannot vanish. This dipole can be given by:

$$\mathbf{D}_{e,n'n} =< \Phi_{n'}|\hat{\mu}|\Phi_n > \tag{2.32}$$

The most important selection rules for electronic dipole transitions in diatomic molecules are:

- ☐ For parallel transitions, $\triangle\Lambda = 0$; transitions such as Σ to Σ, Π to Π, and $\triangle$ to $\triangle$ are allowed.
- ☐ For perpendicular transitions, $\triangle\Lambda = \pm 1$; transitions such as Σ to Π, Π to $\triangle$, and Π to Σ are allowed.
- ☐ Singlet to triplet and vice versa are not allowed, $\triangle S = 0$.
- ☐ Parity should be different, from g to u or u to g.

For parallel transitions, the molecular axis is along the light polarization, and for perpendicular transitions, it is perpendicular. The above conditions are only valid if the motion of the nuclei is not considered. However, if we consider nuclear motion, transitions between vibrational states also should be considered. These simultaneous electronic and vibrational transitions are called vibronic transitions.

Franck – Condon Principle: Vibrational transitions occur on a much longer time scale than electronic transitions. Compared to nuclear motion, the electronic transitions can be considered instantaneous. Therefore, the new vibrational state should be compatible with the old vibrational state. This principle is called the Franck-Condon principle. We can show this principle is quantitatively true if we write down the vibronic transition dipole and consider that the electronic transition dipole is independent of inter-nuclear coordinates:

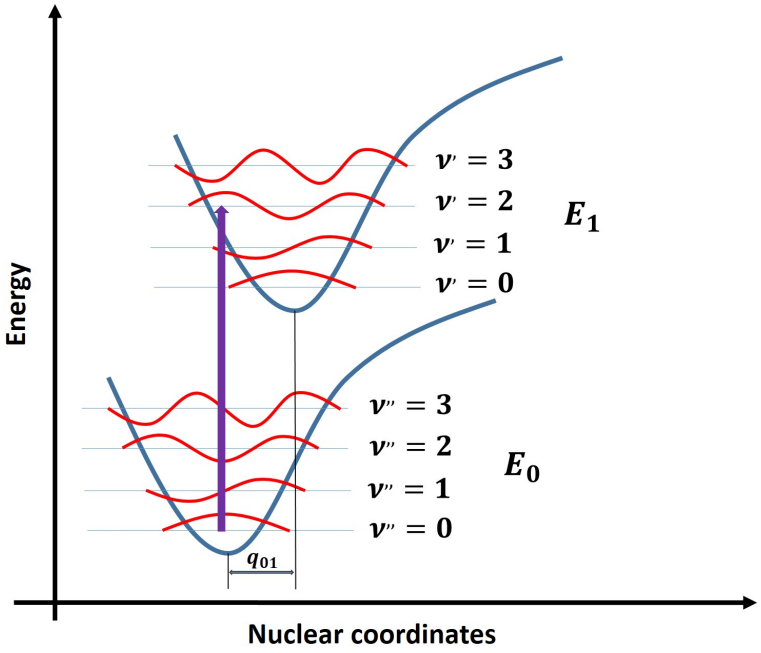

Figure 2.9: *Schematic of the Franck-Condon principle. Electronic transitions with a minimal change in the nuclear coordinates are more favorable, i.e., vertical transitions.*

$$\begin{aligned} \mathbf{D}_{e,n'n,\nu'\nu} &= \int\int \Phi_{n'}\Psi_{n',\nu'}\hat{\mu}\Psi_{n,\nu}\Phi_n \, dr_e dR \\ &= \mathbf{D}_{e,n'n}\int \Psi_{n',\nu'}\Psi_{n,\nu}\, dR \end{aligned} \tag{2.33}$$

The term $\int \Psi_{n',\nu'}\Psi_{n,\nu}\, dR$ is called the Franck-Condon factor. The intensity of a vibronic transition is proportional to the square of the Franck-Condon factor. For a vibronic transition, a transition between vibrational levels with large overlap is more probable. The schematic of the Franck-Condon principle is shown in Fig. 2.9. The Franck-Condon principle can be expanded to polyatomic molecules as well.

Chapter 3

Experimental setup

The experimental setup used in this work combines a femtosecond, high repetition rate pump-probe arrangement, consisting of a Ti:Sapphire NIR laser system and an XUV radiation source based on HHG, with a double-sided Velocity Map Imaging (VMI) spectrometer for coincident charged particle detection. The HHG source is built around a fiber-based commercial device called **XUUS**, which stands for *e***X***treme* **U***ltraviolet* **U***ltrafast* **S***ource*. Assembling and commissioning XUUS was the first part of my Ph.D. project. The VMI spectrometer, **KAMP** (an abbreviation for **K***ansas* **A***tomic* and **M***olecular* **P***hysics* apparatus), is an instrument designed to record times of flight and momentum images of electrons and ions, either separately or in coincidence mode, which enables performing photoion-photoion coincidence (PIPICO), photoelectron-photoion coincidence (PEPICO), and photoelectron-photoion-photoion coincidence (PEPIPICO) measurements. Designing, building, and commissioning KAMP and connecting it to the XUUS setup for pump-probe experiments was the second technical part of my Ph.D. project.

In the following two sections, basic elements of both the XUUS and KAMP instruments will be presented.

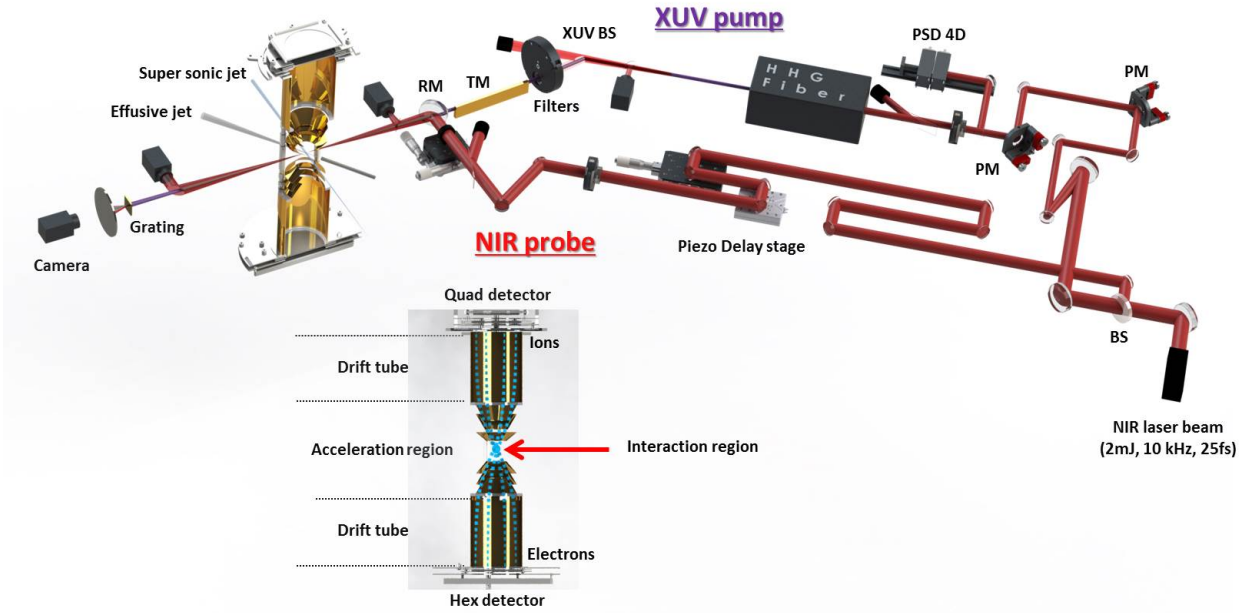

Figure 3.1: *Scheme of the experimental setup. The XUV pulses are generated by the high harmonic generation process in XUUS. The XUV pump and NIR probe pulses are collinearly combined and focused into the interaction region of a VMI spectrometer. In the VMI, both the position and time of flight of photoions and photoelectrons, created by laser interaction with the gas jet, are measured with a quad-anode and a hex-anode detector respectively.*

3.1 XUUS experimental setup

3.1.1 PULSAR laser system

As discussed in chapter 2, high harmonics are generated in atoms or molecules exposed to a strong laser field. Femtosecond lasers are capable of delivering ultrashort and intense laser pulses. The femtosecond laser used in this thesis is called PULSAR (**P**rairie **U**ltrafast **L**aser **S**ource for **A**ttosecond **R**esearch). It is a commercial laser from **KM L**abs, specifically designed for Kansas State University based on a version of a standard Red Dragon system. In brief, the PULSAR laser is able to produce Fourier Transform Limited (FTL) pulses with

Full Width Half-Maximum (FWHM) temporal duration of 21-23 fs. The laser output power is 20 W at a repetition rate of 10 kHz, corresponding to 2 mJ energy per pulse. The system consists of an oscillator and two amplification stages. In the oscillator, a Ti:Sapphire (Ti:Sa) crystal is pumped with a CW laser (with a wavelength of 532nm) to generate femtosecond pulses with high repetition rate (75.2 MHz) and rather low energy per pulse (4 nJ). In the next step, light amplification is performed based on the so-called chirped pulse amplification technique [34]. In this approach, the laser pulse is first stretched from femtoseconds to picoseconds. The pulses are stretched to minimize damage to the Ti:Sa crystal in the amplification stages. Second, a Pockels cell is used to block the majority of pulses and only transmit 10000 or 20000 of pulses per second. Thus, the repetition rate of the laser can be tuned to 10 kHz or 20 kHz based on the Pockels cell settings. Next, stretched pulses are amplified in a two-stage amplification system pumped with green diode lasers at 532 nm. Later, the amplified pulses are compressed again using a pair of reflective gratings. A more detailed description of the PULSAR laser system is given in Ref. [35].

3.1.2 HHG source and XUV beamline

The experimental room is next to the laser room. The laser pulse is transported to the experimental room inside a tube. A schematics of whole experimental setup is shown in Fig. 3.1. A 20% reflective, 80% transmissive beam splitter (BS) is used to split the PULSAR beam into 0.4 mJ and 1.6 mJ pulses. The 1.6 mJ pulse is guided into the XUUS hollow core to generate high-order harmonics. The XUUS is a commercial product from KM labs employed as a high harmonic generation source for XUV and soft X-Ray experiments [36]. The XUUS setup has three main components: (1) a breadboard with a hollow-core waveguide; (2) a differential pumping manifold and pressure control system; and (3) an XUV transport module, including flipper mirror, XUV-NIR beam splitter, a filter wheel with holders for filter foils, and a focusing torodial mirror. A layout of major XUUS components is shown in Fig. 3.2

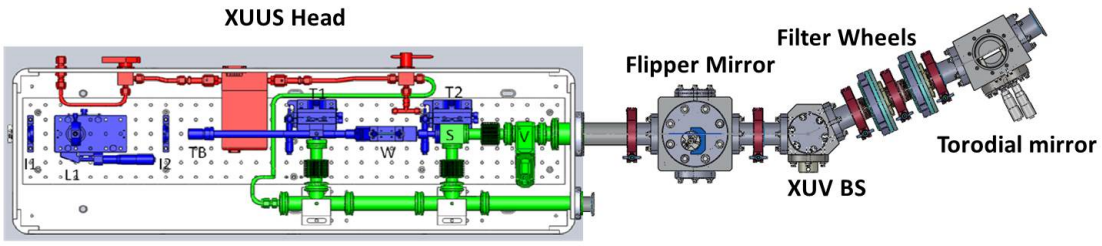

Figure 3.2: *Layout of XUUS head and XUV transport module. The XUUS head consists of a pressure control system (in red), a hollow-core fiber with focusing optics (in blue), and a differential pumping system (in green). The XUV transport module comprises a XUV beam splitter to remove residual IR from the high harmonic generation process, metal-foil filters to isolate specific or a narrow band of XUV wavelengths, and a toroidal mirror to focus the beam at the interaction region in the VMI.*

The XUUS's hollow-core fiber (wave-guide) has an inner diameter of 150 microns and a length of 5 cm. In order to avoid any damage to the fiber due to beam position drift, the Aligna/Beamlock 4D stabilization unit from TEM Messtechnik is employed. This system is meant to compensate for any laser beam pointing drift. Two position-sensitive detectors in the PSD 4D unit measure beam positions in X, Y, and two angles. Any deviation between the reference and real-time beam position values is corrected by two 2D movable mirrors equipped with 2 piezo-actuators each. The NIR focused beam waist at the fiber entrance should be close to 100 microns for obtaining the maximum coupling efficiency. We routinely achieved a coupling efficiency of 65 percent or higher. After the laser beam is successfully coupled into the waveguide, the hollow-core fiber is filled with a noble gas, and the gas pressure inside the fiber is precisely controlled for obtaining maximum phase matching efficiency. Gas pressure, gas type, and the laser input power are key factors in determining the HHG spectrum. For example, if we plan to generate low-order harmonics, 3W to 5W NIR beam power (corresponding to 0.3 mJ to 0.5 mJ energy per pulse) is coupled into the fiber, and the fiber is filled with argon gas at 30 torr. If we plan to generate very high order harmonics, 10W to 12W NIR beam power (corresponding to 1.0 mJ to 1.2 mJ energy per

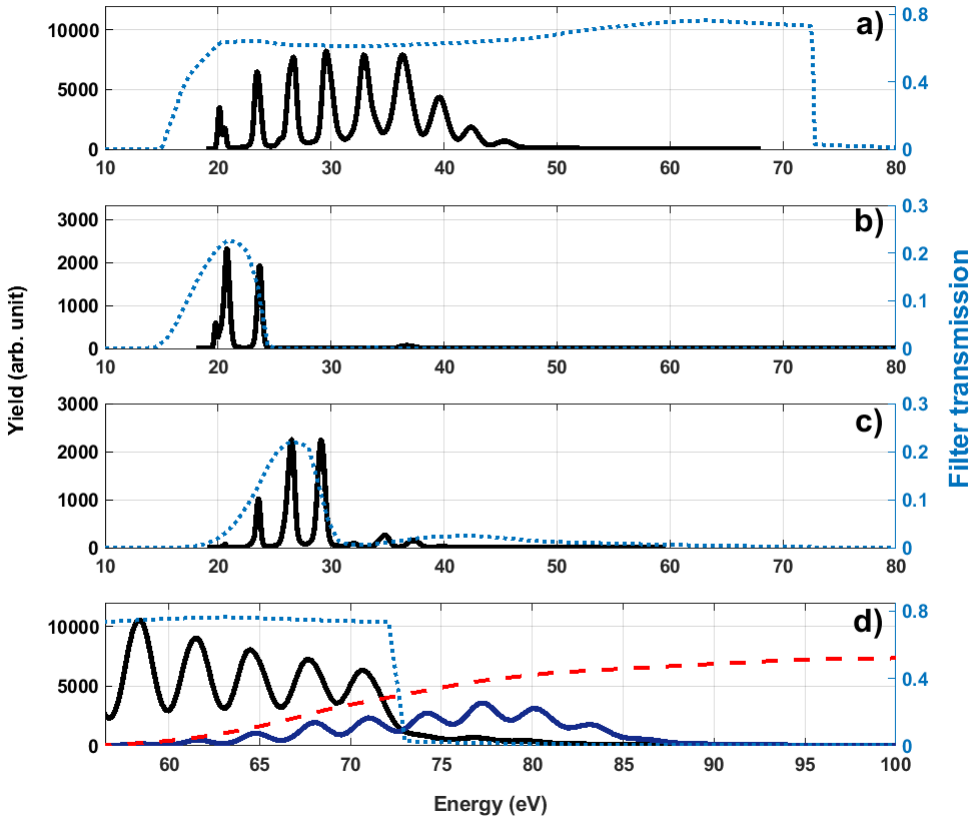

Figure 3.3: *Typical HHG spectra generated by XUUS:The solid black lines are measurements of the HHG spectra generated by coupling NIR pulses at different energies in the XUUS fiber filled with argon (a, b, and c) or neon (d) gas under different pressures and filtered with the following metal-foil filters: a) Al filter, b) Sn filter, c) Al+Ge filters, and d) Al filter (black line), Zr filter(blue line). The transmission curves of the metal-foil filters are shown in blue dotted lines. The blue dotted and red dashed lines in (d) are transmission curves of the Al and Zr filters respectively.*

pulse) is coupled into the fiber, and the fiber is filled with neon gas at 60 to 90 torr. Overall, a train of harmonics with energies between 19 eV up to 100 eV can be generated. The HHG cutoff energy is given by E_c=3.17U_p+I_p, where I_p is the ionization energy of the gas inside the fiber. The U_p is the ponderomotive energy (the electron's cycle-averaged quiver energy in presence of a laser field), which varies linearly with laser intensity. Higher order harmonics can be generated if the laser intensity is increased. However, excessive plasma

density inside the fiber is a limiting factor in how efficiently higher-order harmonics can be phase-matched. Therefore, higher order harmonics are generated by gases with relatively high ionization energy such as He or Ne. In the experiments described in this thesis, we use several gases to generate different ranges of energies such as Ar (for a lower-energy HHG spectrum) or Ne (for a higher-energy HHG spectrum). A combination of an XUV-NIR beam splitter and filter foils is used to remove the residual NIR from the high harmonic generation process. The XUV-NIR beam splitter is based on a Si substrate with a ZrO_2 coating. It operates at 12.5^o grazing angle (Brewster's angle for NIR), and the operation region is up to 100 eV. Filters are mounted into two filter wheels placed in a row. They can be employed to filter only a specific region of the photon energy spectrum. We typically use several filters such as Al, Sn, Ge, and Zr metal foil filters, depending on the experiment's requirements.

In Fig. 3.3 the transmission curves of the metal-foil filters are shown in blue dotted lines, and the corresponding HHG spectra are shown in black lines. The Al filter is the most common filter. It has descent transmission for energies between 19 to 73 eV. Sn and Ge filters have rather narrow transmission energy ranges, and they are extremely useful for selecting just one or two harmonic orders from a train of harmonics. A Zr filter (red dotted line in Fig. 3.3d) is used for inner-valence or inner-shell experiments, where high photon energies are needed.

Monochromators are often used to select specific harmonics. However, they often result in significant time broadening and considerable intensity reduction. Thus, in our setup, we use metallic transmission filters for selecting a portion of the HHG spectrum. Filter transmission depends on the material and thickness of the filters (as seen in Fig. 3.3). As shown in the next chapter, a proper selection of filters can result in a selection of a few harmonics with insignificant time broadening. Avoiding time broadening is especially crucial in studying time-resolved ultrafast molecular dynamics. A toroidal mirror with a focal length of roughly 100 cm and a grazing angle of 4 degrees is used to focus the XUV beam into the interaction region. The XUV beam size at focus is about 200 microns,

estimated from the beam parameters and the measurement of the focal spot for the residual NIR beam passing through the same beamline optics.

In XUV-NIR pump-probe experiments, about 0.4 mJ of NIR pulse energy from the other laser arm is guided through a movable delay stage equipped with a piezo motor. A precisely controlled delay between NIR and XUV pulses can be set by moving the delay stage accordingly. A LabVIEW program controls the delay stage movement. We typically use a certain number of delay steps, and the stage stays in a specific delay step for a certain amount of time. In order to minimize laser intensity fluctuations, pump-probe experiments are performed by consecutively repeating many delay scan loops. A lens with a focal length of 100 cm is employed to focus the NIR pulse. The delayed NIR pulses are combined with XUV inside the vacuum by using a 2-inch silver mirror with a 5 mm diameter hole drilled in the mirror's center. A CCD camera and a beam viewer are used to coarsely find spatial and temporal overlap between the XUV and NIR pulses. In this case, filters are removed from the beamline, and the residual NIR beam propagating collinearly with the XUV from the fiber is overlapped with the NIR pulse from the other arm to find spatial and temporal overlap. The interference pattern between the residual NIR coming from the waveguide and the NIR probe arm is detected as a coarse signature of temporal overlap.

3.2 KAMP: a double-sided Velocity Map Imaging spectrometer for electron-ion coincidence measurements

3.2.1 General layout and vacuum arrangement

The pairs of XUV and NIR pulses produced by the optical setup described in the previous sections are both focused on a gas target inside a dedicated charged-particle spectrometer. This instrument is a double-sided velocity map imaging (VMI) apparatus dubbed KAMP (for Kansas Atomic and Molecular Physics). The KAMP instrument is designed based on

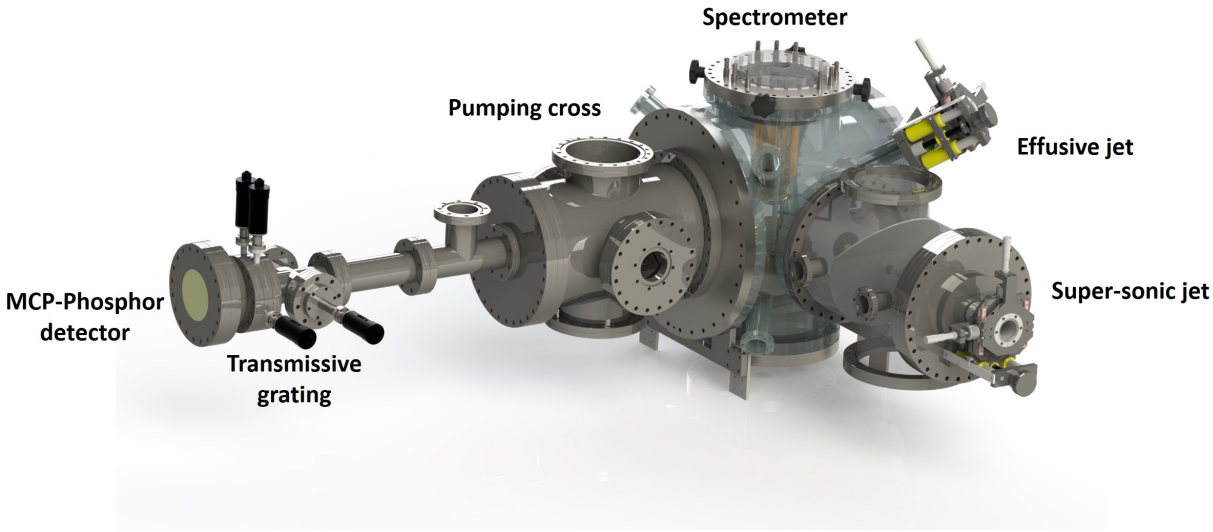

Figure 3.4: *3D layout of the KAMP instrument. It consists of a main vacuum chamber hosting the VMI spectrometer, a pumping cross for turbo-molecular pumps (not shown) to generate* $\sim 10^{-10}$ *torr vaccum, a super-sonic jet to deliver a cold molecular beam, an effusive jet assembly to deliver a molecular target with higher density and transmission grating with an MCP-phosphor detector to measure the spectra of the XUV pulses.*

CAMP [37,38] and LAMP [39] apparatuses developed for experiments at FEL facilities. The CAMP setup was initially developed by the Max Plank Advanced Study Group in Hamburg. It is a versatile apparatus, compatible with reaction microscope or velocity map imaging spectrometers, as well as X-ray photon detection [37]. In the current configuration in our lab, it is equipped with a double-sided VMI spectrometer, a supersonic jet target, an effusive jet target, a pumping cross on the backside of the main chamber with three turbo-molecular pumps (two 700 l/s, and one 1000 l/s) for pumping the main chamber, an extension tube on the back to reduce the stray light/electron signal. In addition, a combination of a transmissive grating, an MCP + phosphor screen detector, and an integrating camera is installed on the back of KAMP for HHG spectrum characterization.

The supersonic jet is installed in a horizontal direction on a DN250CF flange. It consists of two stages. In the first stage, a target gas is ejected into the vacuum by a nozzle with

30 μm diameter. The nozzle is mounted on an XYZ manipulator. A skimmer with the diameter of 500 μm is mounted in the first stage. The movable nozzle is placed less than 5 mm from the skimmer. A turbo-molecular pump with a pumping speed of 1000 l/s is used in the first stage. In the second stage, a gasket with a 1 mm hole is mounted, further collimating the gas target. This stage is pumped with a 700 l/s pump. A two-stage catcher is installed on the DN250CF flange on the opposite side of the supersonic jet for capturing most of the gas load coming from the supersonic jet. During supersonic jet operation, the pressure in the first stage reaches 10^{-4} torr, while the second stage is at 10^{-7} torr, the main chamber at mid 10^{-10} torr, and the catcher at 10^{-9} torr. There are in total eight DN40CF flanges on the main chamber at 53° with respect to horizontal. These ports can be used to add extra equipment to the main chamber. The effusive jet is installed on a DN40CF flange and is mounted on an XYZ manipulator. This configuration allows us to move the needle in or out of the spectrometer's interaction region, depending on the mode of operation. When using the supersonic jet, the needle is fully moved out of the spectrometer region. During effusive gas jet operation, the pressure in the main chamber is $\sim 10^{-6}$ and 10^{-10} torr with and without target gas, respectively.

3.2.2 Double-sided velocity map imaging spectrometer

The VMI spectrometer used in this work is identical to the ones used in the CAMP apparatus. (In fact, the spectrometer electrodes currently used in KAMP were initially manufactured for CAMP). The 3D model of KAMP's double sided VMI spectrometer is shown in Fig. 3.5. The spectrometer is compatible with 80mm MCP detectors. The length of each side of the spectrometer is 20 cm. The opening in the interaction region is 3.5 cm wide and 3.5 cm long. The length of the drift tube on each side is 12.5 cm. There are, in total, six conical electrodes. This configuration provides the possibility of simultaneous detection of ions, electrons, and scattered or fluorescent photons. However, due to the spectrometer's large opening in the middle and the conical shape of its electrodes, simultaneous focusing

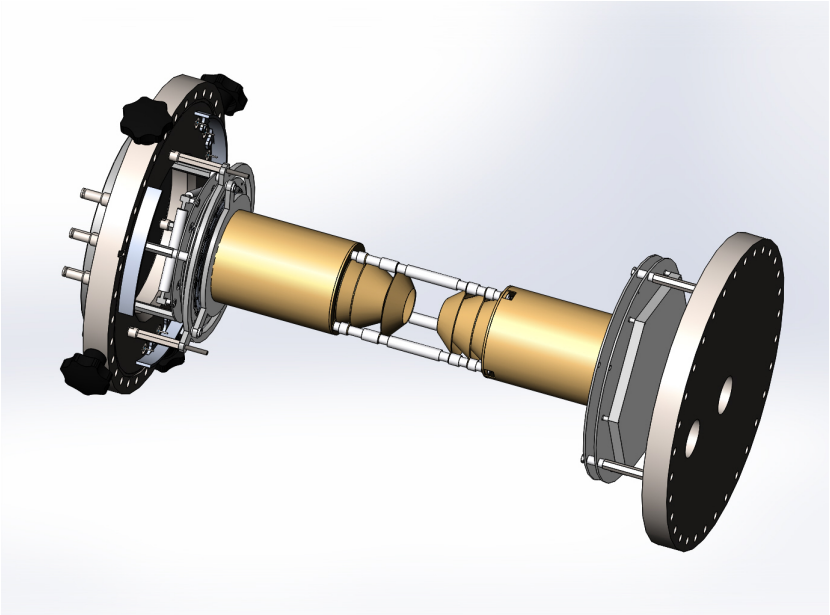

Figure 3.5: *Layout of the double sided velocity map imaging spectrometer. The VMI consists of gold-plated conical electrodes and drift tubes to extract and focus the charged particles generated, as well as quad and hex anode detectors to measure the position and time-of-flight of the particles.*

of electrons and ions is challenging and sensitively depends on the exact interaction region's position with respect to the central electrodes. We typically operate the spectrometer at voltages of -4000 V (ion's drift tube),-1727 V,-640 V,+550 V,+2276 V, and +4000 V (electron's drift tube). There is a mesh at each end of each drift tube to prevent field penetration. However, we have slight field penetration on the ion side due to the ion's mesh being kept at a lower voltage than the drift tube (due to a voltage threshold limit on the voltage-divider box). A set of simulated ion and electron trajectories for the KAMP spectrometer is shown in Fig. 3.6. Electrons with energies up to 65 eV can be imaged in full 4π solid angle.

The KAMP instrument is currently equipped with a time- and position-sensitive MCP/quad delay-line detector for ion detection and a time- and position-sensitive MCP/hexagonal delay-line detector for electron detection (Fig. 3.7).

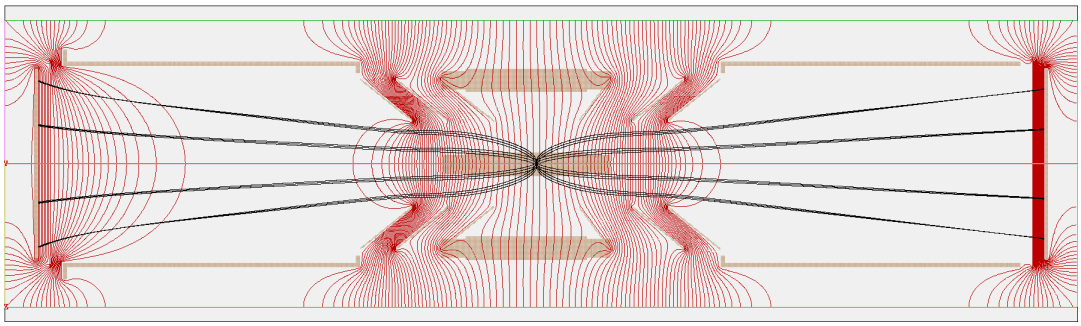

Figure 3.6: *A simulated set of ion and electron trajectories for the double-sided VMI spectrometer. The ion detector (quad) is on the left side and the electron detector (hex) is on the right. Electrons and ions are created at source positions (0,0,0), (0,0,1mm), and (0,0,-1mm). Their kinetic energies are assumed to be 10 and 50 eV, in the $\hat{z}$ and $-\hat{z}$ directions, respectively. The field penetration on the ion side is due the to the ion's mesh being at a lower voltage than the drift tube. The simulation is done using SIMION 8.0.4 (2008) package.*

3.2.3 Data acquisition and analysis

In the quad and hex delay-line anodes, the position of the particles hitting the detector is calculated based on the difference between the signal propagation times toward two different ends of a wire wrapped along a particular direction. For each coordinate, a separate pair of wires is used to build a differential signal. For a quad detector, two layers (i.e., two pairs of wires) are used, one each for the X and Y direction. For the hex delay-line anode, a third layer is used to reduce the dead time of the detector and improve its multi-hit capabilities.

The digital encoding for acquire a 2D image is given by:

$$\begin{aligned} X &= x1 - x2 + (Offset)_x \\ Y &= y1 - y2 + (Offset)_y \end{aligned} \tag{3.1}$$

where propagation time for each signal (i.e., to each corner of the detector) is given by x1, x2, y1, and y2. For the quad **DLD80** detector, the single pitch propagation time is 1 ns for 1 mm. Therefore, the relation between relative time delay in 2D image and 1mm position distance is twice the single propagation time (2 ns for 1 mm).

For the hex **Hex100**, the single pitch propagation time (ns per mm) is slightly different

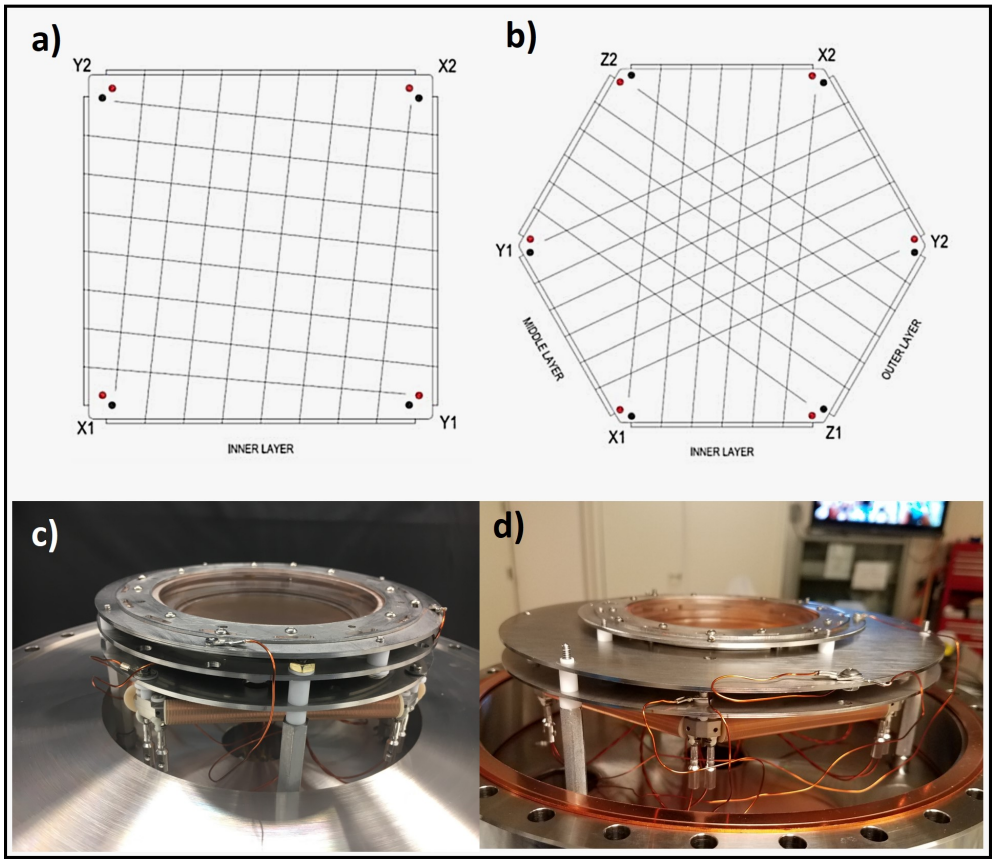

Figure 3.7: *Quad and hex detectors. a) and b): Schematic of the wiring pattern, and terminal pairs in each corner of Quad and Hex delay-line anodes respectively[adapted from 40]. c) and d): MCP-Quad, and MCP-Hex detectors fully assembled.*

for each layer. The values can be calculated by a self-calibration routine. The positions u, v, and are expressed by(in hexagonal coordinates):

$$\begin{aligned} u &= (x1 - x2) * d_1 \\ v &= (y1 - y2) * d_2 \\ w &= (z1 - z2) * d_3 + offset \end{aligned} \tag{3.2}$$

where d_1, d_2, and d_3 are conversion constants

For determining the X and Y positions, only two pairs of hexagonal coordinates (u, v, and w) are needed. Any combination of u,v, and w can be used. This is an important

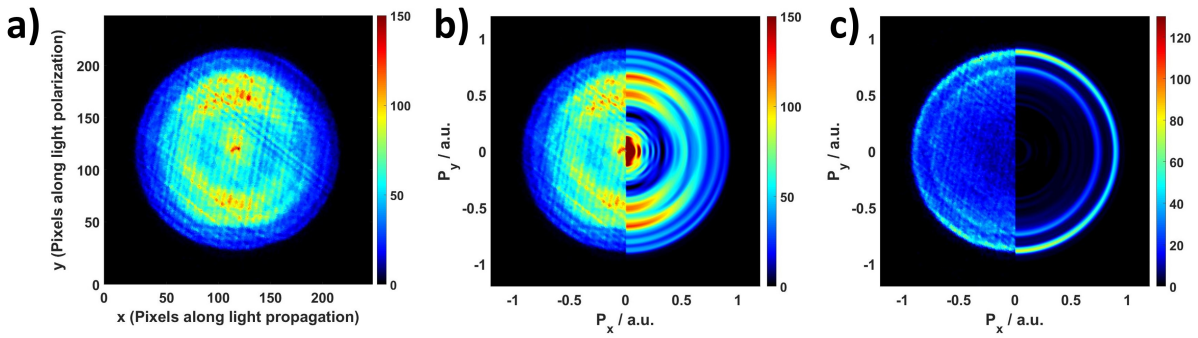

Figure 3.8: *CH_3OH molecule ionized by H13-15. a) Raw image of all detected photoelectrons. b) Raw vs inverted photoelectron image of all fragments combined. c) Raw vs inverted photoelectron detected in coincidence with CH_3OH^+.*

advantage of a hex delay-line compared to a quad delay-line. For example, if a pair of signals in one layer in a quad detector is missing, the image reconstruction can not occur. However, if a pair of signals in the u layer in the hex detector is missing, the image can still be reconstructed using the signals from the v and w layers. There are in total thirteen analog signals, five analog signals from the MCP/quad delay-line detector, seven analog signals from the MCP/hex delay-line detector, and one signal from a photodiode detector for a time zero gating. The amplitudes of these analog signals, except the photodiode signal, are very small (few millivolts). They are amplified using two eight-channel Octal Fast Timing Amplifiers (FTA820A). The amplified signals are processed by four Ortec 935 QUAD CFDs (constant fraction discriminators). The analog signals are converted to digital signals using a 16-channels CAEN V1290N TDC (time-to-digital converter) and recorded by the data acquisition setup. The signal from the photodiode triggers the TDC.

This geometry allows us to perform coincident photoelectron-photoion spectroscopy. For ions, a full 3D momentum reconstruction can be performed from measured ion hit positions and TOF, as will be illustrated below. However, since the electrostatic field's amplitude is high, electrons are accelerated toward detectors within a very short time. The electron TOF is typically within a few nanoseconds. Therefore, the achievable momentum resolution along the spectrometer axis is not sufficient for accurate 3D electron momentum reconstruction.

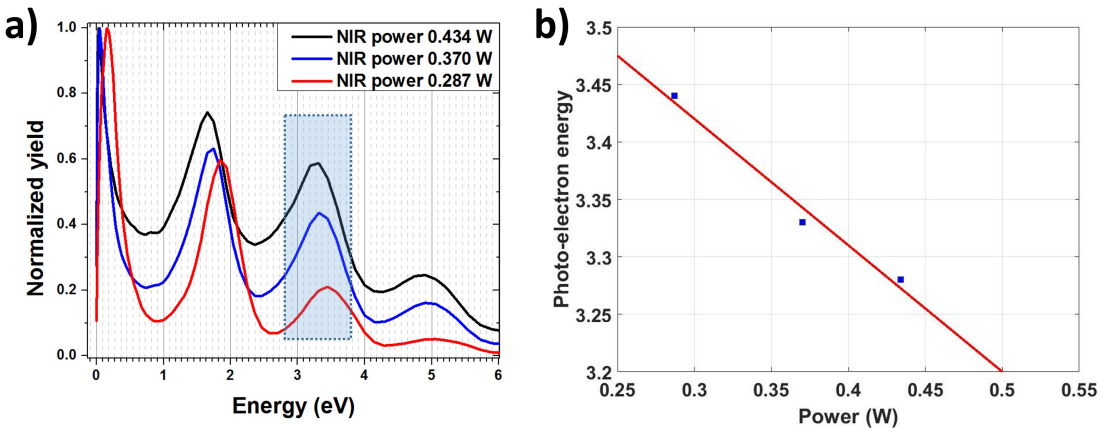

Figure 3.9: *a) ATI photoelectron energy spectra of a Xe atom from multi-photon NIR ionization, measured at different NIR laser average powers. b) Shift in photoelectron peak energy, in the peaks between 3-4 eV (shaded area in the left panel), as a function of the NIR average power.*

Thus, for electrons, 3D momentum reconstruction can not be directly performed since the electron TOF is too short for any meaningful reconstruction. However, slices through a 3D momentum distribution can be obtained by using standard VMI inversion methods [41,42,43]. A raw and inverted photoelectron image from methanol molecules singly ionized by H13 is shown in Fig. 3.8. The left-hand side of the image is a raw photoelectron image, and the right-hand side is a slice through an inverted image using a conventional inverse Abel transformation. Any angular distortion can significantly impact the quality of the electron kinetic energy resolution. For an ideal case of monochromatic light, the angular distribution of electrons should be a flat horizontal line (in a radius vs angle spectrum). Before any inversion transformation, we perform a circularization procedure to eliminate distortion effects and increase kinetic energy resolution. For low-statistics photoelectron images, appropriate inversion is not feasible. In this case, a (modified) analogue of the photoelectron energy spectrum is extracted from the radial distribution of non-inverted image. In the case of double or multiple ionization, where two or more electrons are ejected, only information from one of the electrons can be registered since the time difference between two electrons hitting the detector is shorter or comparable to the single pitch propagation

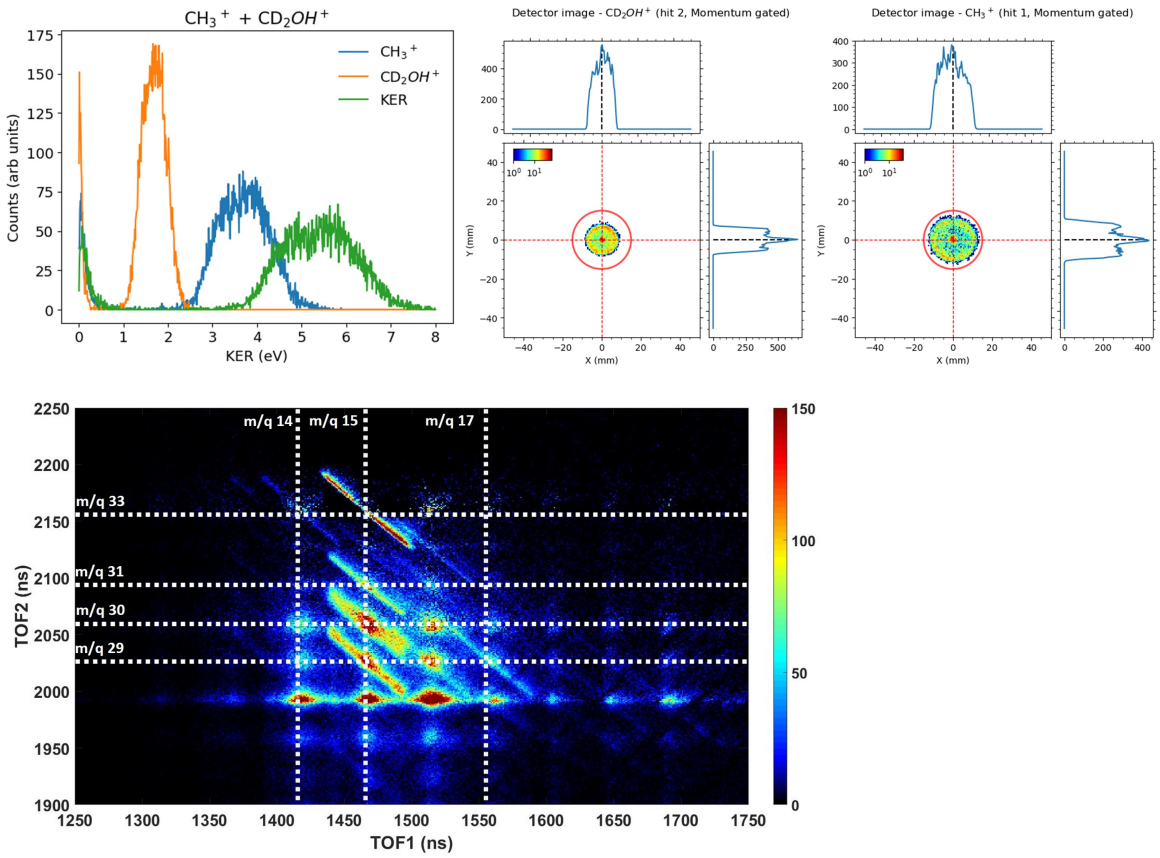

Figure 3.10: *The Kinetic energy release distribution, photo-ion images of $CH_3^+ + CD_2OH^+$ coincidence channel, and photoion-photoion coincidence (PIPICO) spectrum of double ionization of CH_3CD_2OH molecule by a train of high harmonics.*

time of the delay-line signals, and two electrons can not be resolved as two separate hits in the MCP signal.

The electron energy is assumed to be proportional to the square of the hit distance with respect to the detector center. The factor of proportionality is obtained from an energy calibration experiment. Above-threshold ionization (ATI) peaks from the Xe atom ionized by a NIR pulse are used to obtain the calibration factor. The calibration factor is adjusted until energy spacings between the adjacent ATI peaks exactly match one NIR photon energy (For the central wavelength of 790nm, this spacing should be 1.57eV). An example of ATI peaks from Xenon is shown in Fig. 2.1. The ATI peaks can be used to estimate the intensity of the NIR beam at focus as well. The spacing between the adjacent ATI peaks

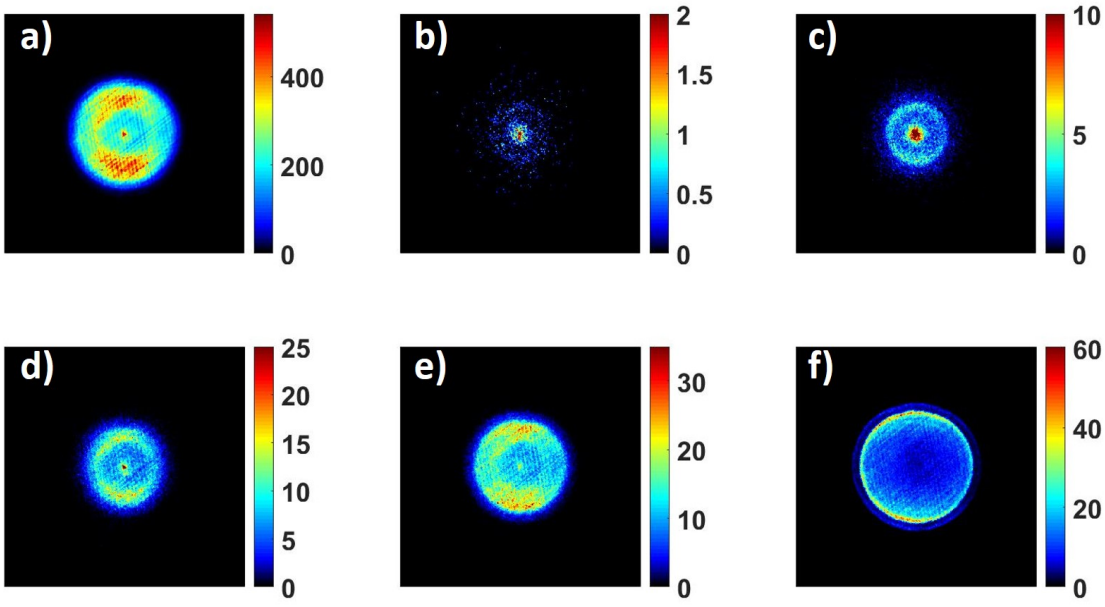

Figure 3.11: *The photoelectron images for different ionic fragments of CH_3CD_2OH molecule ionized by H13 obtained by gating on ion's time of flight. a) all detected photoelectrons, b) D^+/H_2^+, c) CH_3^+/CDH^+, d) $C_2H_3^+/C_2DH^+$, e) $CDOH^+/CH_3O^+$, f) $CH_3CD_2OH^+$.*

is fixed for moderate intensities, but the absolute energy of the peaks shift linearly with intensity. The energy shift is equal to the pondermotive energy change. Therefore, for intensity calibration, the ATI photoelectron images are recorded for multiple different input powers, and the energy shifts as a function of input powers are plotted (see an example in Fig. 3.9)). The plot's slope is used as a constant factor (C_0) to calibrate the in-situ experimental intensity on the target. The intensity for a given power is then estimated by $I(P) = |C_0|P/(9.337 * 10^{-14}\lambda^2)$, where P is input power in watt and λ is central wavelength in micron.

In a reaction microscope spectrometer [44], the electrostatic field is homogeneous, and one can find an analytical equation to reconstruct the 3D momentum of photoions from x, y hit positions, and TOF. However, in VMI-type spectrometers, the electrostatic field is inhomogeneous, and the analytical equation can not be found from x, y hit positions

and TOF. In order to reconstruct the 3D momentum of photoion, we simulate the x, y hit positions and TOF of ions generated in the interaction region with different initial velocities and angles. The simulation is done using the SIMION 8.0.4 (2008) package. For example, the kinetic energy release of the $CH_3^+ + CD_2OH^+$ channel of the CH_3CD_2OH molecule ionized by H13 is plotted in Fig. 3.10.

In every ionization event, the positions and TOFs of both ions and electrons are recorded. Photoelectrons in coincidence with different ionic fragmentation are separated from each other by appropriately gating on TOF and the position of corresponding photoions. In Fig. 3.11, a selection of photoelectron images of the CH_3CD_2OH molecule ionized by H13-15 is plotted. All photoelectrons are coming from singly ionized dissociation channels. In non-coincident measurements, only photoelectron images integrated over all channels can be observed (Fig. 3.11a). However, by performing a coincident measurement, we are able to detect and record photoelectron images of even very weak dissociation channels such as the D^+ ionic fragment in Fig. 3.11b).

Chapter 4

Steady and transient two-color signals in XUV-IR pump-probe experiments on atomic and molecular photoionization

4.1 Introduction

The development of new short-pulsed XUV and X-ray radiation sources, like free-electron lasers (FELs) [8,45,46,47,48] and high-order harmonics of infrared lasers [9,49], enabled numerous advances in our understanding of basic light-matter interactions. Specific examples include, among others, visualizing correlated electron dynamics in atoms [50], understanding the coupling between the electronic and nuclear degrees of freedom in molecules beyond the Born-Oppenheimer approximation [51,52], tracing the motion of individual atoms in photochemical reactions [53,54,55], and exploring the dynamics of previously inaccessible highly-excited states [56,57]. Many of these advances exploit photoionization processes

driven by the light of two different wavelengths, where the absorption of an XUV or X-ray photon is combined with the interaction with a visible or infrared pulse. This arrangement is often applied to probe the dynamics triggered by a short-wavelength photon [58] or to characterize the temporal profile of XUV or X-ray light pulses, which often represents a challenge for conventional optical techniques [59]. Therefore, understanding the details of the interactions of atoms and molecules with such two-color light fields is important for various novel XUV and X-ray applications.

A number of commonly used schemes for robust characterization of femtosecond or even sub-femtosecond XUV and X-ray pulses rely on the detection of a photoelectron emitted in the presence of a second light pulse of a much longer wavelength. As discussed in Section 2.4, if the effective duration of the XUV / X-ray pulse is shorter than an oscillation period of a long-wavelength light pulse (e.g., visible or infrared), the latter results in the change of the momentum (and energy) of the created electron, which depends on the instantaneous electric field of the long-wavelength pulse at the time of photoionization and, thus, on the exact phase relation between the two pulses. This phenomenon, often dubbed "photoelectron streaking", can be exploited for a detailed characterization of the temporal profile of sub-femtosecond XUV / X-ray pulses, to resolve in time X-ray induced processes like Auger decay on a few-fs time scale, or to study attosecond time delays in photoemission [60]. In the opposite limit, when the XUV / X-ray pulse is longer than one optical cycle of a longer wavelength, the photoelectron spectrum exhibits so-called "sidebands", the peaks appearing at energies shifted by $\pm$ one photon energy compared to the single-color XUV / X-ray ionization. These sidebands, which result from free-free transitions induced by the "dressing" of visible or infrared light [61], are often used to characterize the time structure of HHG, FEL or synchrotron radiation pulses in pulse duration ranges from a few femtoseconds to picoseconds [62,31,61]. Sideband photoelectron peaks also can appear as unwanted artifacts in some two-color pump-probe experiments (e.g., in adiabatic alignment of molecules [63]).

Despite the generality and robustness of the sideband approach, it has a couple of limita-

tions which restrict its usage for certain applications. First, it requires an electron spectrometer, which is not always compatible with a particular HHG or FEL experimental setup. This limitation can be resolved if comparable information can be retrieved from the ion time-of-flight measurement, which is often easier to combine with a complementary (e.g., photon imaging) experiment [64,65] and is less sensitive to the environment (e.g., the local magnetic field created by nearby equipment). Second, the sideband signal appears only if the two pulses directly overlap in time. While this is normally not an issue for most of the HHG-based setups, where the harmonic pulse is inherently synchronized with its driving laser beam, a portion of which can be used for pump-probe experiments, the situation is different at FEL facilities, especially those based on the Self-Amplified Spontaneous Emission (SASE) process. There, the synchronization with the external laser is much more difficult to establish and is typically limited to a couple of hundred femtoseconds. Correspondingly, for many pump-probe experiments at FELs, even the initial search of an exact "time zero", i.e., the time delay between the FEL pulse and the external optical laser pulse at which their peaks overlap, sometimes represents a technical challenge and needs to rely on a signal from the experiment itself, which then can be linked to some external FEL – laser cross-correlation setup [8,45,46,66]. This procedure strongly benefits from a two-color signal that exists in a time window much broader than the temporal overlap of both pulses, which can be as short as a couple of tens of femtoseconds (or even shorter).

Motivated by the above considerations, in this chapter a series of examples of cross-correlation signals for pump-probe experiments employing XUV pulses from the HHG source described in Section 3.1 and moderately intense NIR pulses (790 nm central wavelength, 25 fs pulse duration, intensities $\leq 10^{13}\ cm^2$) is presented. Here, we make use of the capabilities of the double-sided VMI spectrometer, which enables coincident detection of both electrons and ions resulting from light-matter interactions. Starting with the characterization of the XUV pulse duration and overlap position using a sideband signal, we then compare it with long-lived electron and ion signals from the XUV-excitation of atomic Rydberg states and

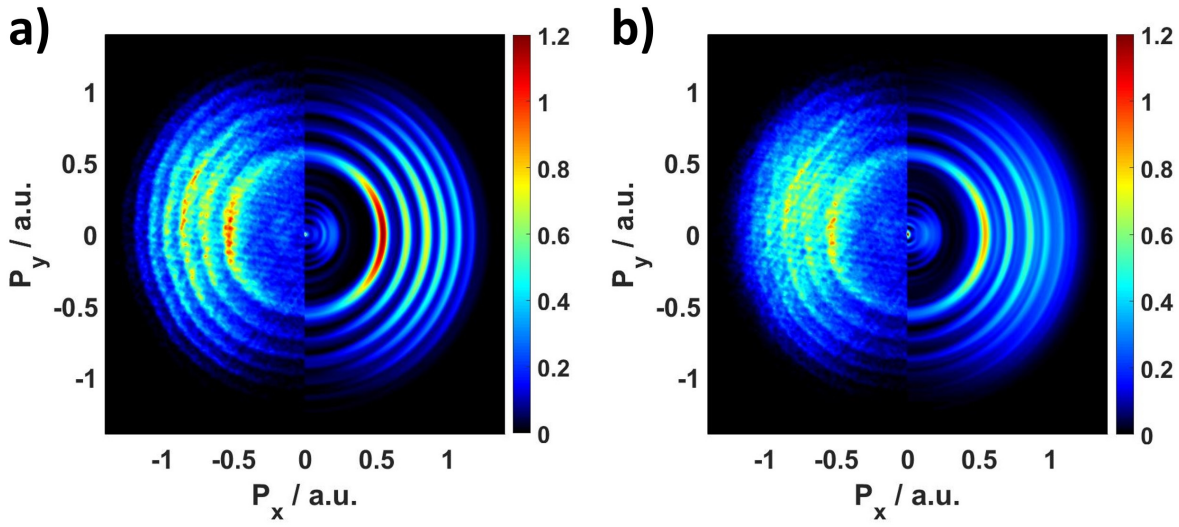

Figure 4.1: *a) Ar^+ photoelectron image (raw vs inverted) for NIR pulses arriving 150 fs before XUV pulses. b) Ar^+ photoelectron image (raw vs inverted) when both pulses overlap.*

subsequent ionization by the NIR pulse, and with the two-color signal from double ionization of atoms upon valence photoabsorption. It is followed by the example of a time-dependent two-color signal obtained from triple ionization of xenon atoms triggered by inner-shell photoabsorption and subsequent Auger decay. The chapter ends with the analysis of two-color double ionization of molecules, where the cross-correlation signal is influenced by both the temporal overlap of the XUV and NIR pulses and by the femtosecond dynamics of a highly excited molecular state. In all these examples, we analyze the basic mechanisms of the underlying physical processes using simultaneous detection of ions and electrons, as well as electron-ion and ion-ion coincidence capabilities, and characterize the temporal structure of the corresponding signals in comparison with the information obtained from the photoelectron sidebands.

4.2 Sideband measurements

As discussed above, we start the analysis of the delay-dependent XUV-NIR two-color signals with the measurement of the sidebands in the photoelectron spectra, which are known to

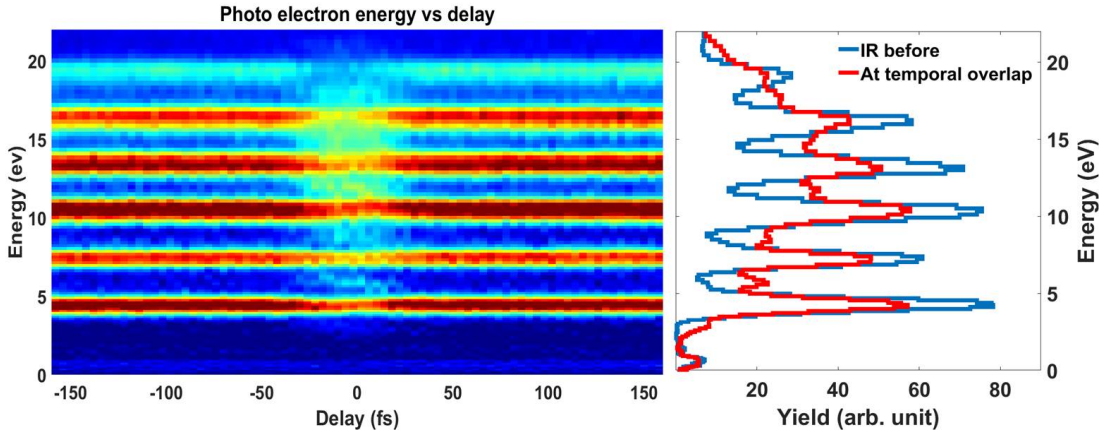

Figure 4.2: *Left panel: Ar^+ photoelectron energy spectrum vs delay between NIR and XUV pulses. Right panel: Photoelectron energy spectra for NIR arriving before XUV (red curve) and at overlap (blue curve).*

give a good representation of the cross-correlation between the XUV and NIR pulses. Here, we focus on a coarse characterization of the intensity envelope of the XUV pulse and ignore its temporal sub-structure. To perform the sideband experiment, we generate high harmonic radiation by coupling a 0.4 mJ NIR pulse into the fiber, which is filled with 30 torr of Ar (see section 3.1). The XUV beam passes through the Al filter, which, in combination with the transmission of the other beamline elements, results in an HHG spectrum covering $\sim$ 20 - 45 eV (harmonics, 13-29 see Fig. 3.3a). The absorption of an XUV photon predominantly results in single ionization of Ar atoms, with a small contribution from double ionization (which has a 43.39 eV threshold). By gating on the TOF of Ar^+ ions, the electrons resulting from single ionization of Ar are selected, suppressing all background contributions. The NIR intensity is restricted to $3 * 10^{12}\ W/cm^2$, such that the contribution to Ar^+ ionization from the NIR pulse itself is negligible.

Fig. 4.1 shows the VMI image of the photoelectrons detected in coincidence with Ar^+ ions produced by a combination of XUV and NIR pulses at two different delays between them. In Fig. 4.1a, the NIR pulse arrives 150 fs before the XUV, whereas in Fig. 4.1b the pulses overlap. Throughout this chapter, NIR polarization is kept parallel to XUV polarization. The polarization direction, in all photoelectron images in this chapter, is

along the X direction. While the overlap of the two pulses is initially adjusted by finding the interference pattern of the NIR probe pulse with the part of the NIR beam used for HHG, with the Al filter removed, the "time zero" for the experiment is set by the maximum of the delay-dependent signal of "sideband 14", as shown in Fig. 4.2 and 4.3. (Here a sideband labeled 2m corresponds to the photoelectrons produced by harmonic 2m-1 with the absorption of one NIR photon, or by harmonic 2m+1 with the emission of 1 NIR photon). As can be seen in Fig. 4.1b, when XUV and NIR pulses overlap, the sideband rings emerge between adjacent harmonics. The measured photoelectron spectrum is shown in the left panel of Fig. 4.2 as a function of XUV-NIR delay, while the spectra obtained at fixed delays corresponding to Fig. 4.1a (-150 fs) and 4.1b (0 fs, overlapping pulses) are shown in the right panel as blue and red lines, respectively. As can be seen from the figure, when the pulses are not overlapping in time, no sideband signal is generated. In the overlap region, the sidebands emerge in between the "main" photoelectron peaks from individual harmonics, while the main peaks decrease. Since at low NIR intensity the sideband signal results from the absorption of 1 XUV photon accompanied by either absorption or emission of 1 NIR photon, the sideband yield recorded as a function of XUV-NIR delay can be used as a convenient cross-correlation signal to measure the width of the XUV pulse envelope if the NIR pulse duration is known.

Fig. 4.3 shows the yield of sidebands 12 through 22 as a function of delay, with red lines displaying Gaussian fits to the data. The "zero delay" for each of these graphs is set by the maximum of the Gaussian fit for sideband 14. The maxima of all other sidebands lie within less than 1.2 fs from this value, indicating that, within the precision of our measurement, there is no noticeable chirp of the HHG pulse beyond the sub-femtosecond scale. Here it should be noted that in this work no attempt was made to maintain the synchronization between the XUV and NIR pulses on a time scale below one optical cycle of the NIR pulse. Correspondingly, a RABBITT-type periodic structure of the photoelectron spectrum, which is expected to appear in the delay-dependent two-color spectra because the temporal

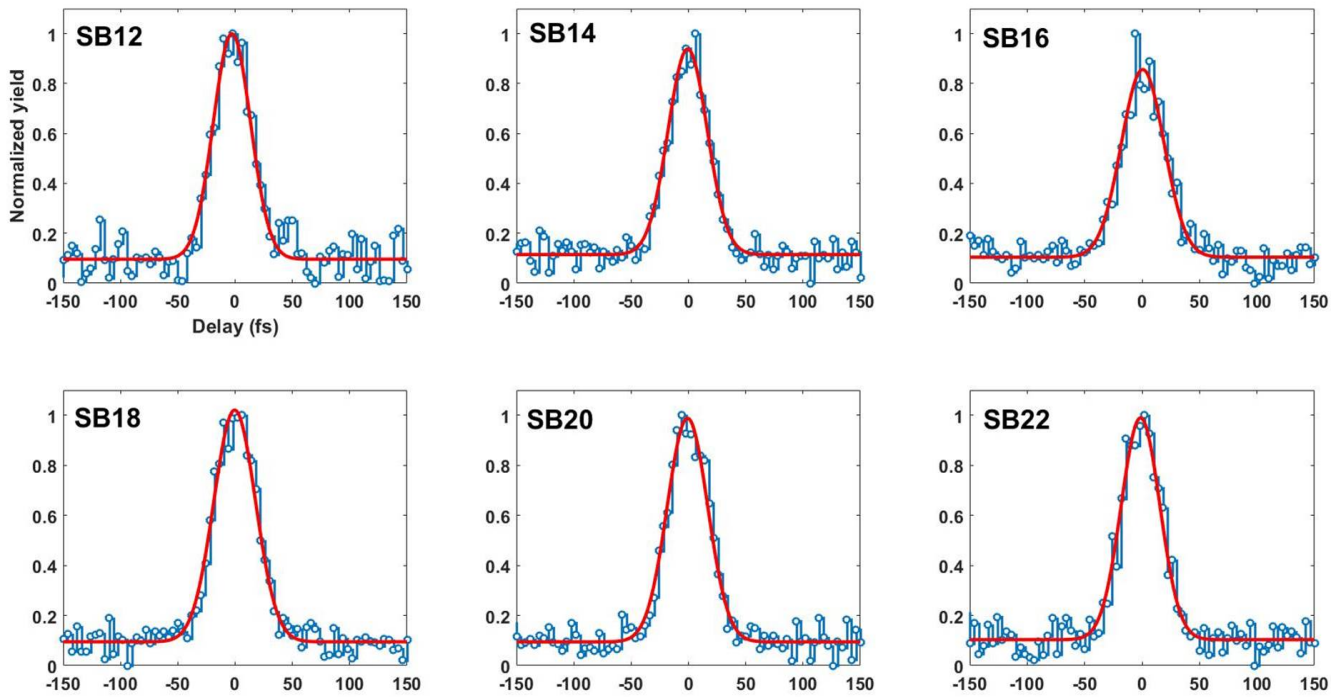

Figure 4.3: *Sideband yields as a function of XUV-NIR delay. All yields are normalized to the maximum yields in the absolute scale.*

SB	12	14	16	18	20	22
Cross-correlation width τ_{cc} in fs	38.2±1.6	40.2±1.3	43.8±1.8	42.6±1.6	41.5±1.4	39.6±1.2
XUV pulse duration τ_{XUV}/fs	23.6±3.9	26.8±3.1	31.9±3.4	30.5±3.2	28.7±3.1	25.8±3.0

Table 4.1: *Temporal width of the cross-correlation signals shown in Fig. 4.3 obtained from the Gaussian fits and the deduced XUV pulse durations. Both values are given as FWHM. The uncertainties shown represent the errors of the fits.*

structure of the HHG XUV pulse is an attosecond pulse train [62,67,31], is not resolved here (see Fig. 4.2a).

The measured FWHM of the cross-correlation signals in Fig. 4.3 obtained from the Gaussian fits are listed in Table 4.1, where FWHM=2.355*σ. The corresponding values lie between 38 and 44 fs. Assuming that the temporal profile of the sideband signal is given by the convolution of the two Gaussians corresponding to the XUV and NIR pulses,

the XUV pulse duration can be calculated from the relation $\tau_{XUV}^2 = \sqrt{\tau_{CC}^2 - \tau_{NIR}^2}$. With the NIR pulse duration $\tau_{NIR} = 30 \pm 1$ fs (measured using the FROG technique [68]), the corresponding XUV pulse lengths fall between 23.5 fs and 32 fs (see Table 4.1). As can be seen from the table, the deviation between the maximum and minimum obtained pulse durations lie slightly beyond the statistical error, with the longer pulses corresponding to the central part of the energy spectrum. While this can result from XUV pulse propagation effects, the deviation is too close to the error bar to reliably determine its origin. The XUV pulse duration obtained by averaging over the whole sideband spectrum yields $\tau_{XUV,ave} = 28.5 \pm 3.5$ fs.

4.3 Rydberg state excitation

The sideband structures discussed in the previous section can be measured for any XUV wavelength above the ionization threshold but appear only during the temporal overlap of XUV and NIR pulses. Here, we consider an example of a two-color signal that exists in a much broader delay range and can be traced in both photoelectron and photoion spectra. In this case, the XUV photon energy is tuned slightly lower than the ionization threshold of an atom or a molecule, such that one or more highly excited states is populated. Thus, following the interaction with the XUV pulse itself, no ionization signal is produced. However, in the presence of a weak NIR field, such excited states can be ionized, yielding a two-color signal whose temporal structure depends on the duration of the XUV and NIR pulses, their relative arrival time, and the lifetime of the excited state. If the latter is significantly longer than the width of the cross-correlation of both pulses, one can expect the ionization yield as a function of XUV-NIR delay to manifest a step function-like behavior, with the two-color signal appearing at the delays where the NIR pulse arrives after the XUV.

Since this scheme requires photon energies below the ionization threshold, higher-order harmonics only contribute as a delay-independent background and should be excluded from

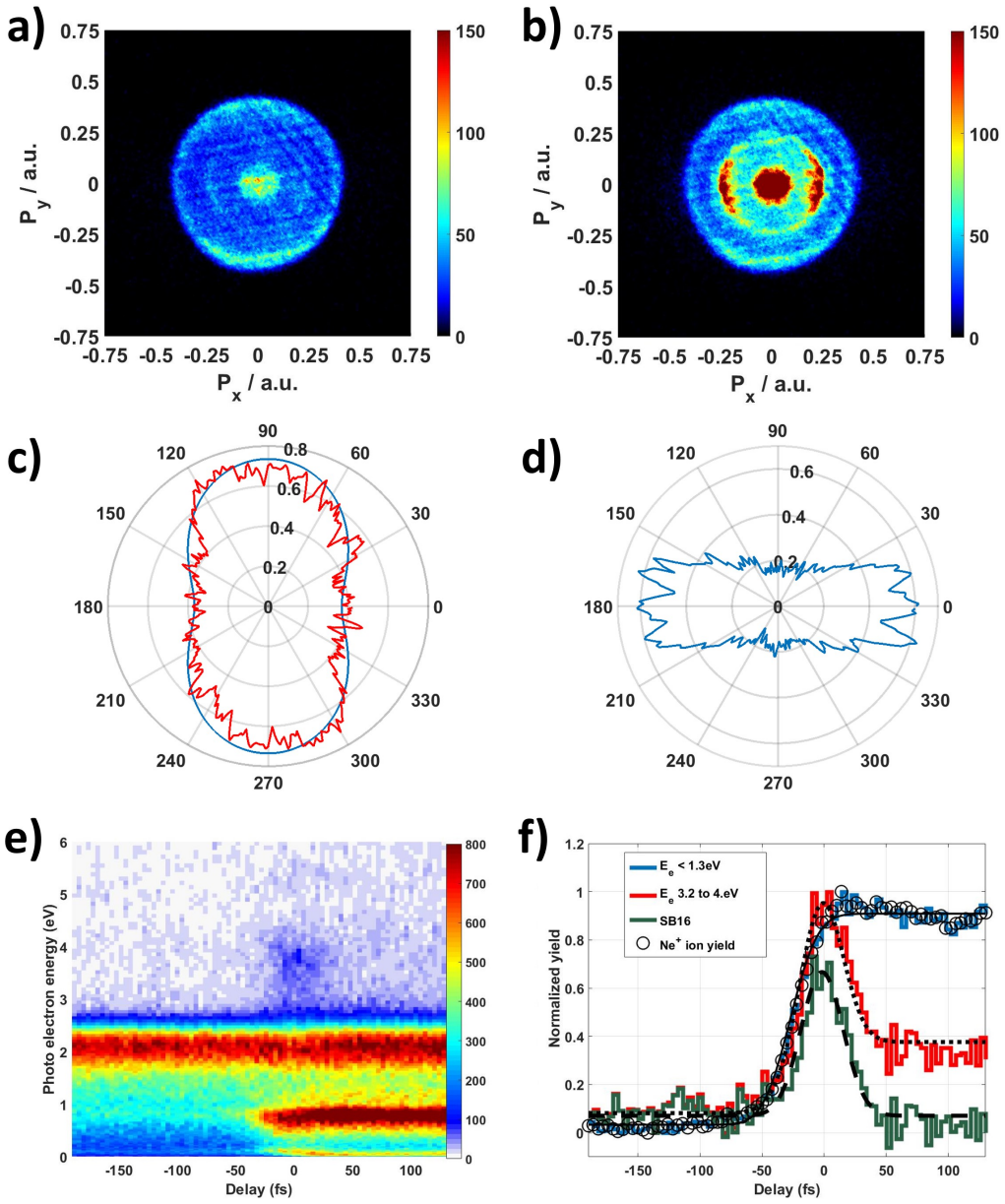

Figure 4.4: *Ne^+ photoelectron raw image for: a) NIR arriving before XUV and b) NIR arriving after XUV. c) The differential cross section of photoelectrons from the 2p state of Ne ionized by 24 eV photons (β_{2p} = -0.4 and σ_{2p} = 7.7 Mbn). Blue curve is the calculation and red curve shows the experimental results. θ is the angle between the (linear) polarization of light and the momentum of ejected electrons. d) The angular distribution of low energy Ne^+ photoelectrons, i.e., the inner ring features in (b). e) Ne^+ photoelectron energy vs delay. f) Normalized photoelectron yield vs delay for electron energies below 1.3 eV (blue curve), energies between 3.2 eV and 4 eV (red curve), Ne^+ ion yield (open circles), and the SB16 (green curve).*

the XUV spectrum. As was shown in Section 3.1, this can be realized, e.g., by using a Sn filter (see Fig. 3.3b), which predominantly transmits the 13th and 15th harmonics. The central photon energy of the former ($\sim$ 20.6 eV) lies slightly below the ionization potential of a Ne atom (21.56 eV), which was selected as a target for this experiment. Correspondingly, the phase matching conditions for this measurement are adjusted in order to maximize the 13th harmonic while suppressing the 15th. With the resulting XUV spectrum, the 13th harmonic maps the ground electronic state of Ne ($2p^6$) into highly excited states such as ($2p^5(^2P)4d$ and $2p^5(^2P)4p$)), whereas the remaining 15th harmonic photons result in ionization with the energy of emitted electrons of $\sim$ 2 eV.

The results of such XUV pump – NIR probe experiments on Ne atoms are depicted in Fig. 4.4. The intensity of the NIR pulse is kept below $10^{13} W/cm^2$ ($\sim 8 * 10^{12} W/cm^2$) , such that the ionization of Ne by the NIR pulse alone is negligible. Fig. 4.4a depicts the VMI image of the photoelectrons detected in coincidence with singly-charged Ne ions integrated over negative delays, i.e., over the region where the NIR pulse arrives before the XUV, whereas Fig. 4.4b shows the same image integrated over all positive delays (NIR arrives after XUV). The outer ring in both panels corresponds to the photoelectrons originating from Ne atoms ionized by the 15th harmonic. These photoelectrons are more likely emitted along the direction perpendicular to the light polarization (horizontal for both XUV and NIR pulses), which is due to the small negative value of the asymmetry parameter $\beta = -0.4$ for the 2p state of Ne[69,70,71] (see Fig. 4.4c). Both images also contain two structures due to lower-energy electrons, which are much more pronounced in Fig. 4.4b. Highly excited neutral Ne atoms prepared by the 13th harmonic are energetically less than one NIR photon below the ionization limit. Therefore, one NIR photon can ionize these highly excited states, ejecting an electron, which results in the inner ring and the central spot clearly observable in Fig. 4.4b. The angular distribution of the inner ring feature is peaked along the light polarization direction, resembling typical ATI peaks (see Fig. 4.4d).

The photoelectron energy spectrum as a function of XUV-NIR delay is plotted in Fig.

4.4e. Besides a pronounced photoelectron band centered slightly above 2 eV, two distinct delay-dependent features can be observed in this plot. First, there is an intense band of low-energy (< 1 eV) electrons, accompanied by a weaker structure very close to zero energy. Both of these bands are absent at negative delays smaller than -50 fs. These electrons result from the NIR ionization of highly excited neutral neon atoms. The dominant band is centered at 0.6 eV, which, assuming the central NIR photon energy of 1.57 eV (wavelength 790 nm), energetically corresponds to the absorption of a 20.59 eV XUV photon, perfectly matching the center of our 13th harmonic spectrum. A weaker band close to zero energy is due to the shoulder of the 13th harmonic spectrum just below 20 eV, which can be seen in Fig. 3.3b. An XUV photon at this energy populates somewhat lower excited states ($(2p^5(^2P)4s)$ and $(2p^5(^2P)3d)$, which are just one NIR photon below the ionization threshold. Second, a localized spot between 3 and 4 eV can be observed close to zero delay, mainly reflecting the electrons from sideband 16. In Fig. 4.4f, normalized electron yields in these two regions are plotted as a function of delay: the yield of all electrons with energies below 1.3eV is shown as a blue curve, whereas the region between 3.2eV and 4eV is depicted by the red curve. As expected, a step function behavior is observed for low-energy electrons (blue). Since the lifetime of the excited states (typically in nano-seconds) involved is much larger than the duration of both pulses, the rise time of the signal is determined by the XUV-NIR cross-correlation. The curve is fitted with a cumulative distribution function (CDF: $N(t) = \frac{h}{2}(1 + erf(\frac{t-c}{\sqrt{2\sigma^2}})) + l$, where h and l are constants and $FWHM_{cc} = 2.35 * \sigma$) [58], which yields a FWHM of the cross-correlation signal of 41±2 fs and a XUV pulse duration of 28±4 fs.

In contrast, the signal for electrons with energies between 3.2 to 4 eV (red curve) manifests a pronounced peak in the overlap region, which, however, does not drop back to the baseline at large positive delays, showing a noticeable enhancement compared to the negative delay region. We assume that these electrons result from two different processes. The peak at zero reflects the contribution from sideband 16, while the remaining enhancement

most likely reflects three-photon NIR ionization of the highly excited states populated by the 13th harmonic. (Note that the corresponding contribution from the two-photon NIR ionization falls into the intense band dominated by the 15th harmonic signal). By deconvolution of the red curve in Fig. 4.4f (assuming a Gaussian profile for the sideband and the CDF contribution for the rest of the signal), the SB16 yield as a function of delay is extracted (shown as a green curve). Fitting this yield by a Gaussian function, we obtain a FWHM of 40±2 fs (XUV pulse duration of 26.5±4 fs), which is in good agreement with the results obtained from the CDF fit of the low-energy electron yield. For comparison, the normalized delay-dependent yield of Ne^+ ions measured in the same experiment is also shown in Fig. 4.4f (open symbols). Remarkably, it is nearly identical to the low-energy electron yield curve, indicating that similar information can be obtained from the ion measurements. The sideband structure is not reflected in the ion yield curve, as can be expected, since the sideband effect merely redistributes the photoelectrons to different kinetic energies rather than changing the total ionization yield.

One issue that needs to be addressed is the determination of the exact "zero delay" position. In the current experiment, it is set to coincide with the maximum of the Gaussian fit to the SB16 yield. However, as can be seen from Fig. 4.4f, this position does not correspond to the center of the CDF distribution reflecting the long-lived two-color signal, but rather to the right edge of the rising part of the CDF curve. This finding might be relevant for many experiments, where the temporal overlap between the XUV (or soft X-ray) pulses with the synchronized laser pulse is characterized using ion signals from NIR ionization of highly excited states (see, e.g. [54,72]). Possible reasons behind such relative timing of both signals will be discussed in the next section.

4.4 Shake-up process

Direct XUV photoexcitation of high-lying excited states discussed in the previous section provides a long-lived two-color signal with high contrast, which can be detected in XUV-NIR pump-probe experiments measuring either electrons or ions. However, this approach requires the photon energy to be below the ionization threshold (ideally, within one NIR photon energy) and, thus, cannot be employed in many situations when the photon energies are well above the ionization limit. An alternative scheme relies on a two-color double ionization signal, where the absorption of an XUV photon results in an ionization process accompanied by the excitation of the ion, which can be further ionized by the NIR pulse. This scheme was used to study sub-femtosecond ionization dynamics of XUV-induced ionic states by monitoring doubly-charged ion yields as a function of XUV-NIR delay [73,74]. Here, two examples of such two-color double ionization experiments with femtosecond XUV and NIR pulses are presented.

We start with double ionization of Xe by a train of high harmonics with photon energies between 20 and 45 eV (13th to 29th harmonics, see Fig. 3.3a). In the neutral xenon atom, the ground state is $5p^6$. Depending on the photon energy, a single photoabsorption can result in single or double ionization of Xe atoms ($Ip_1 = 12.1eV$, and $Ip_2 = 33.1eV$). Fig. 4.5a and 4.5b show the VMI images of the photoelectrons detected in coincidence with singly- and doubly-ionized xenon ions, respectively. For Xe^+ ions, Fig. 4.5a, the majority of photoelectrons results from the absorption of harmonics 13, 15 and 17. The angular distribution of these electrons is peaked along the light polarization due to a positive asymmetry parameter for the 5p state in the energy range between 15 and 30 eV[75]. The electrons from double ionization (Fig. 4.5b) appear as a localized spot in the center of the image, indicating that a (weak) double ionization signal is dominated by very low energy electrons. Fig. 4.5c and 4.5d display the photolectrons detected in coincidence with Xe^{2+} ions in XUV-NIR pump-probe experiments with the same XUV pulse and the NIR pulse ($5*10^{12}W/cm^2$) arriving before (-150 fs) and after (+150 fs) the XUV, respectively. The

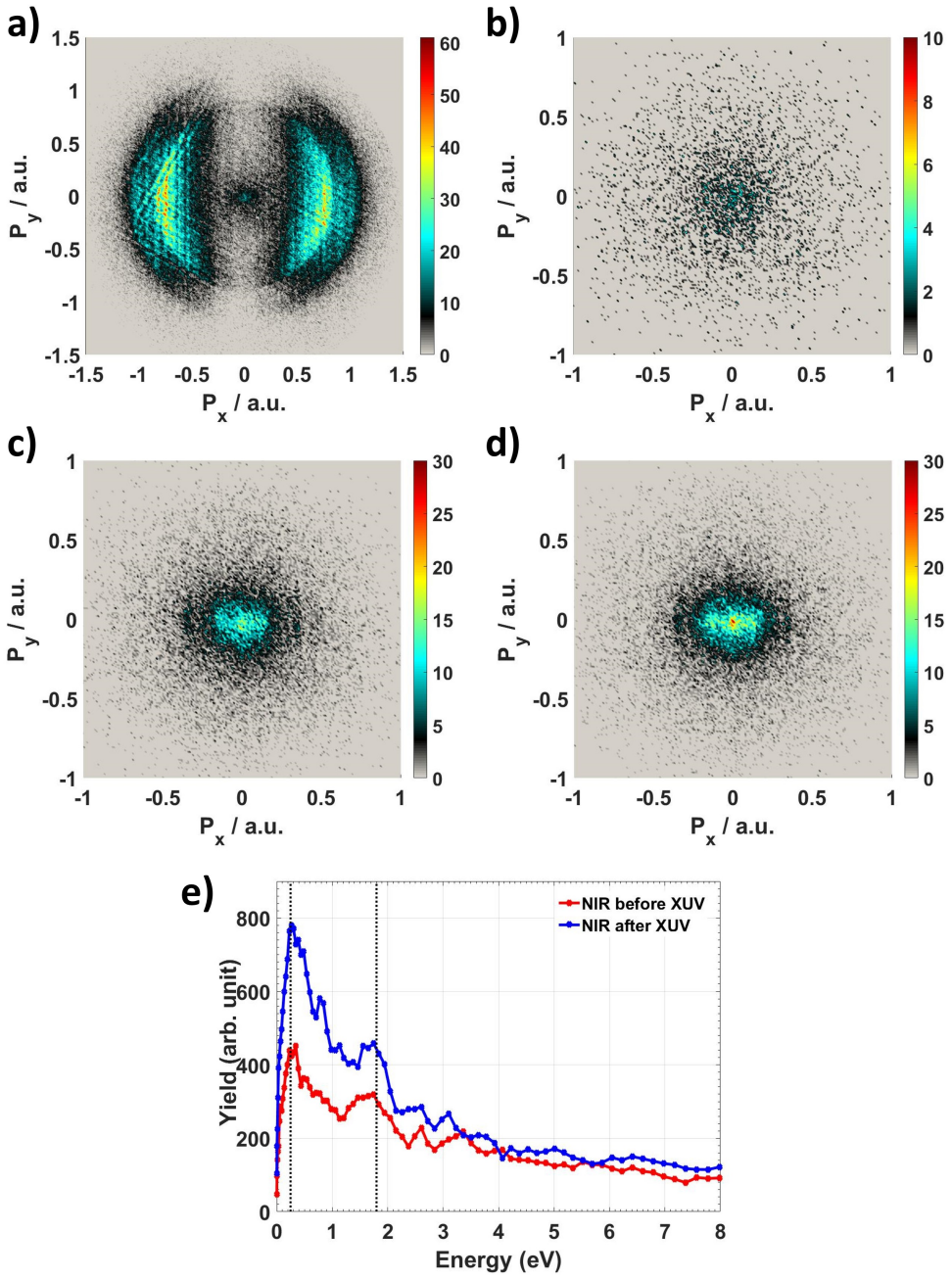

Figure 4.5: *a) and b) Photoelectron images for single and double ionization of Xe by a train of harmonics (13 to 29) (XUV only experiment). c) and d) Photoelectron images for double ionization of Xe at fixed XUV-NIR delays of -150fs and +150fs respectively (XUV-NIR experiment). e) Photoelectron energy spectrum for double ionization of Xe for NIR arriving before (-150fs, red curve) and after (+150fs, blue curve) the XUV pulse.*

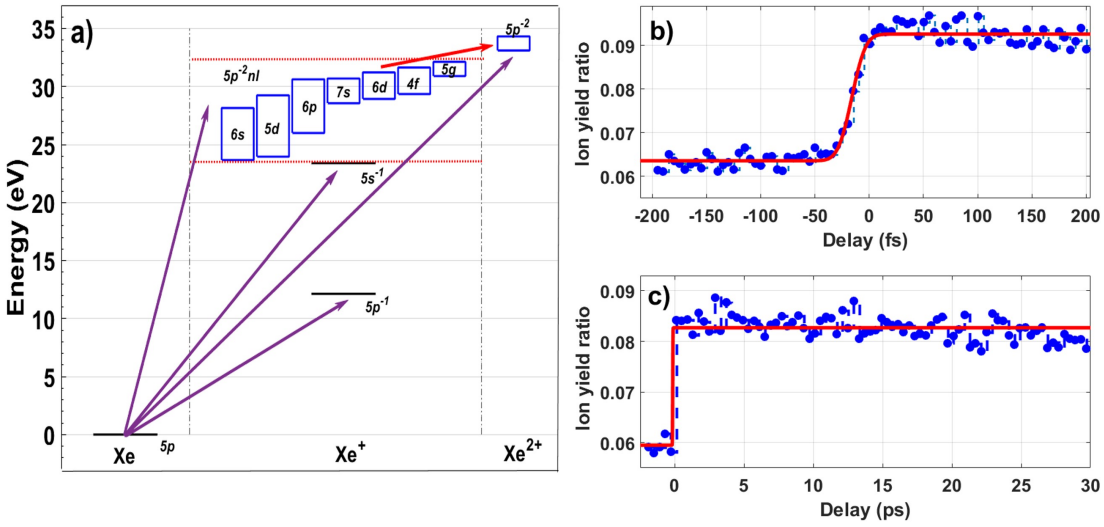

Figure 4.6: *a) Energy level diagram depicting possible transitions from Xe to Xe^+ to Xe^{2+}. Ratio of Xe^{2+} ion yield to Xe^+ as a function of delay between XUV and NIR pulses for a delay window of b) -200 fs to 200 fs (short delay) and c) -2ps to 30 ps (long delay).*

corresponding electron energy spectra are shown in Fig. 4.5e as red (-150 fs) and blue (+150 fs) lines. From this graphs, it is clear that significantly more doubly-charged ions are produced when the NIR pulse arrives after the XUV, and that the electrons with energies below 3 eV are responsible for this enhancement, with the curve at +150 fs showing two pronounced peaks separated by one NIR photon energy (marked by dashed vertical lines).

Fig. 4.6a shows the diagram of several possible transition from neutral Xe to Xe^+ and Xe^{2+}. As shown by purple arrows, if the XUV photon energy is above 23 eV, single ionization can leave the Xe^+ ion in one of its excited bound states due to shake-up processes (see section 2.3.4), while above 33.1 eV, direct double ionization is possible. The ground state of singly ionized xenon is $5p^{-1}$. The first excited state is $5s^{-1}$, and it is followed by $5p^{-2}nl$ states. The highly excited states $5p^{-2}4f$ and $5p^{-2}5g$ of Xe^+ ion are energetically 1.5 and 1 eV below the ground state of Xe^{2+} ($5p^{-2}$). Thus, the NIR pulse (with its central photon energy of 1.57 eV) can further ionize these states of Xe^+ by single photoabsorption (shown by red the arrow in the figure), resulting in the significant enhancement of the Xe^{2+} yield at positive delays observed in Fig. 4.5d,e. To quantify the time evolution of this

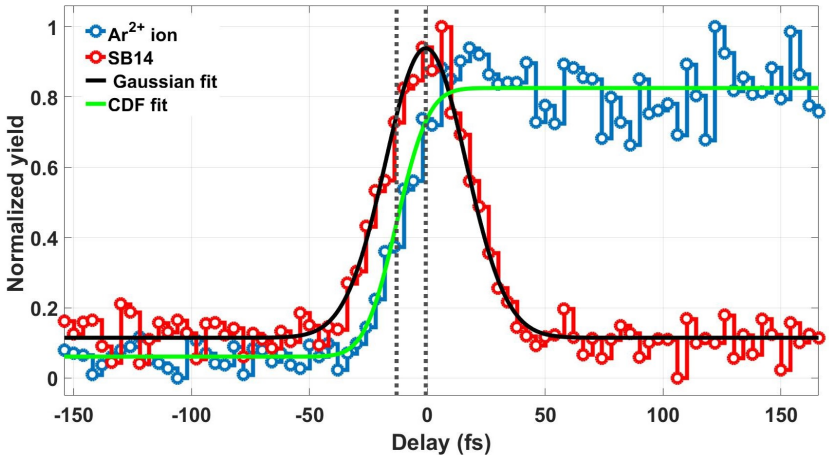

Figure 4.7: *Normalized yield of sideband 14 compared to the delay-dependent yield of Ar^{2+} ions.*

enhancement, Fig. 4.6b displays the measured ratio of double to single ionization yield as a function of XUV-NIR delay. Since, similar to the previous section, the lifetime of the excited states (here they are ionic) is significantly larger than the durations of both pulses, the signal exhibits a step function behavior. In Fig. 4.6c, the same ratio is plotted in a much larger delay range, up to 30 ps, showing very small decay of the signal. In Fig. 4.6b, the FWHM of the cross-correlation signal reconstructed from the CDF fit is measured to be 24 fs, which is significantly smaller than the FWHM of the sideband signal.

Similar delay-dependent enhancement of the two-color double ionization signal driven by XUV-induced shake-up processes can be also observed for argon. In this case, the XUV pulse ionizes neutral Ar leaving a singly-charged Ar^+ ion in one of many possible highly excited states, such as $3p^{-2}5g$, $3p^{-2}5f$, $3p^{-2}5d$ and $3p^{-2}5s$, which are less than one NIR photon energy below the Ar double ionization threshold (43.39 eV). These states can be efficiently reached by the 27th harmonic (centered at $\sim$ 42.4 eV). As discussed above for Xe, if the NIR pulse arrives after the XUV, it can efficiently ionize these excited ionic states with just one NIR photon. The corresponding delay-dependent yield of Ar^{2+} ions is plotted as a function of XUV-NIR delay in Fig. 4.7 (blue symbols). The signal exhibits a pronounced step function behavior, similar to Fig. 4.6b,c for Xe, and is also fitted with a

CDF (shown by a solid green line). For comparison, the delay-dependent yield of sideband 14 measured in the same experiment is shown in Fig. 4.7 (red symbols). It can be clearly seen that, similar to Fig. 4.4f in the previous section, the maximum of the Gaussian fit to the sideband signal (shown by the black line) is shifted with respect to the center of the CDF fit to the Ar^{2+} yield (see dashed vertical lines in Fig. 4.7), such that the Ar^{2+} ion yield is not increasing beyond zero delay. Note the zero delay position in the Ar measurements was set to the maximum of SB 14 from the experiment on Ar. However, in contrast to the results presented in Fig. 4.4f, here the FWHM of the cross-correlation signal reconstructed from the CDF fit is measured to be 25 fs, which is significantly smaller than the FWHM of the sideband signal, similar to the Xe^{2+} measurement.

The reasons for both the shift of the center of the CDF fit and the smaller cross-correlation signal compared to the sideband signal can be qualitatively understood by following the discussion in Ref. [73], where a similar experiment was performed with sub-femtosecond temporal resolution. In that study, where the Ne^{2+} yield was also shown to reach its maximum around zero XUV-NIR delay, it was demonstrated that the exact timing of this signal rise depends on (i) the population of the contributing shake-up states and (ii) on the transition probabilities for the NIR ionization from the individual states. In particular, the depletion of different contributing levels was shown to happen at different times. Although the same level of analysis is beyond the scope of this work, we assume that the observed reduction of the cross-correlation width as well as the CDF center shift with respect to the sideband maximum is due to depletion of highly excited states by the leading edge of the NIR pulse, before reaching its peak intensity. This also indicates that the observed temporal profile of the signal might be a function of the NIR intensity, since it can change the timing of the depletion effects. Thus, the main message here is that while the "steady", long-lived two-color signals that exhibit step function-like behavior and can be observed by measuring ion yields can be useful for measuring both XUV pulse duration and coarse relative timing between XUV and NIR pulses, a more precise determination of

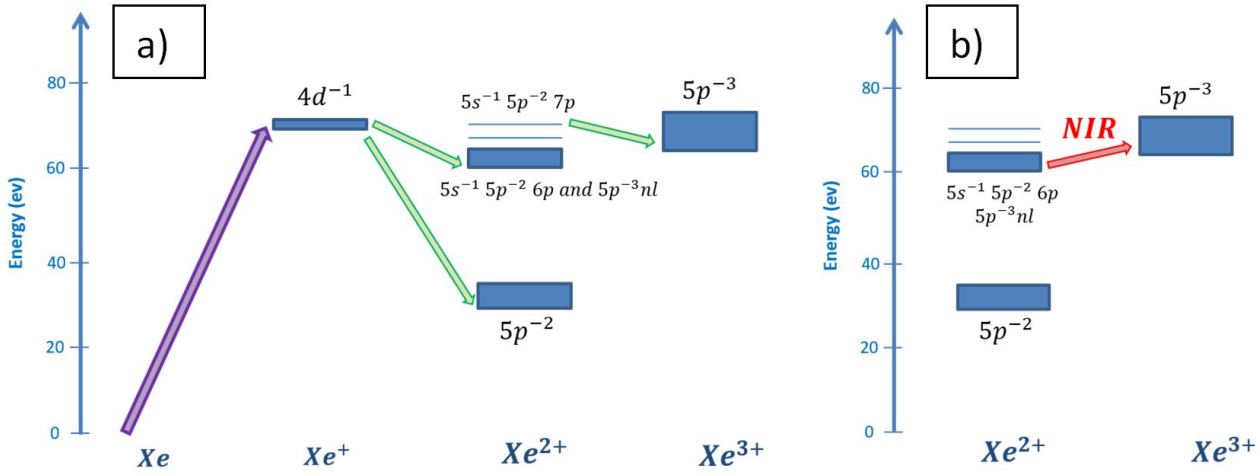

Figure 4.8: *Sketch of possible pathways leading to triple ionization of Xe after 4d shell ionization by the XUV pulse without (a) and with (b) the NIR probe pulse (adapted from [73]).*

the pulse duration and exact overlap position still requires an additional reference signal, like sidebands or reliable- all-optical schemes.

4.5 Inner-shell ionization

Up to now, we have discussed two-color signals produced after valence-shell photoabsorption. However, for many HHG and especially FEL experiments, the absorption of XUV or X-ray photons by the inner shells plays a crucial role. As was shown in Section 3.1, photons with energies up to 90 eV can be created in the XUUS setup used in this work, which is well above the first inner shells of heavy elements like Xe, I, Kr, Br, etc. In order to generate such high photon energies, the hollow core fiber needs to be filled with neon gas and the NIR beam with 1.2 mJ energy per pulse is coupled into the fiber with a coupling efficiency of more than 65 percent. A train of harmonics from the 13th up to the 57th can be generated. For the experiments requiring photon energies above 70 eV, a Zr filter needs to be used, yielding

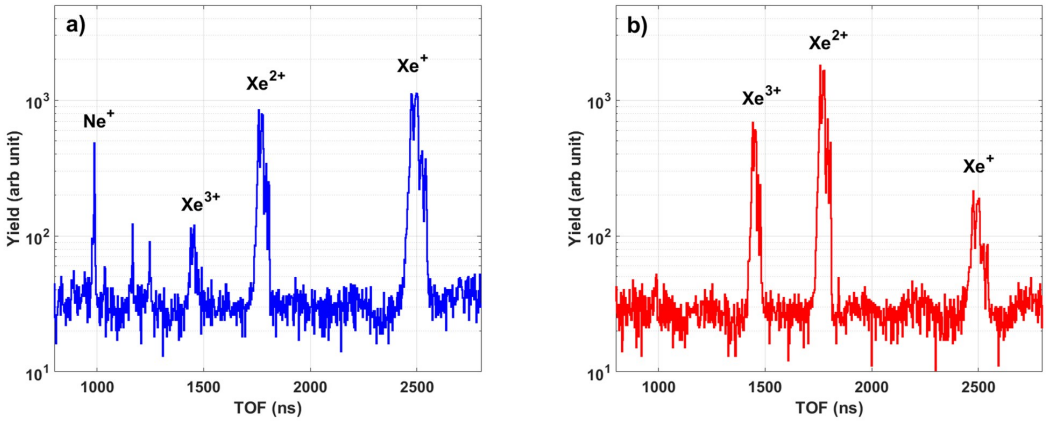

Figure 4.9: *Ion time of flight spectrum of Xe ionized by a) a train of harmonics selected by an Al filter, and b) a train of harmonics selected by a Zr filter.*

a harmonic spectrum similar to the one shown in Fig. 3.3d. Here, we present the results of a XUV-NIR pump-probe measurement on inner-shell ionization of Xe atoms employing such a train of high-energy harmonics.

In Xe atoms, within the photon energy range accessible with the XUUS setup, 5p and 5s electrons as well as the first inner shell, 4d, can be ionized. In the valence region, the 5p state has the largest cross section, while at the photon energies above the 4d ionization threshold (67.5 eV and 69.5 eV for for $4d_{5/2}$ and $4d_{3/2}$ states, respectively [76]) absorption by this 4d shell starts to dominate. For photon energies around 80 eV, the absorption cross section for the 4d shell is about two orders of magnitude higher than the cross section of 5p and 5s states combined [27]. As sketched in Fig. 4.8a, removing an electron from the $4d^{-1}$ or $4d^{-1}5p^{-1}nl$ shake-up satellites is typically followed by an Auger decay into the $5p^{-2}$, $5p^{-3}nl$, $5s^{-1}5p^{-2}6p$ or $5s^{-1}5p^{-2}7p$ states. While the first three of those states are energetically below the threshold for ionization of Xe^{2+}, leaving the ion doubly-charged, the $5s^{-1}5p^{-2}7p$ state lies above this threshold and, thus, can result in Xe^{3+} production by a second Auger decay ending up in the $5p^{-3}$ state. This cross section and energy level structure is reflected in the ion TOF spectra from Xe ionization by a train of harmonics, which are shown in Fig. 4.9. In Fig. 4.9a, the Al filter was used to select the low-energy part of the harmonic

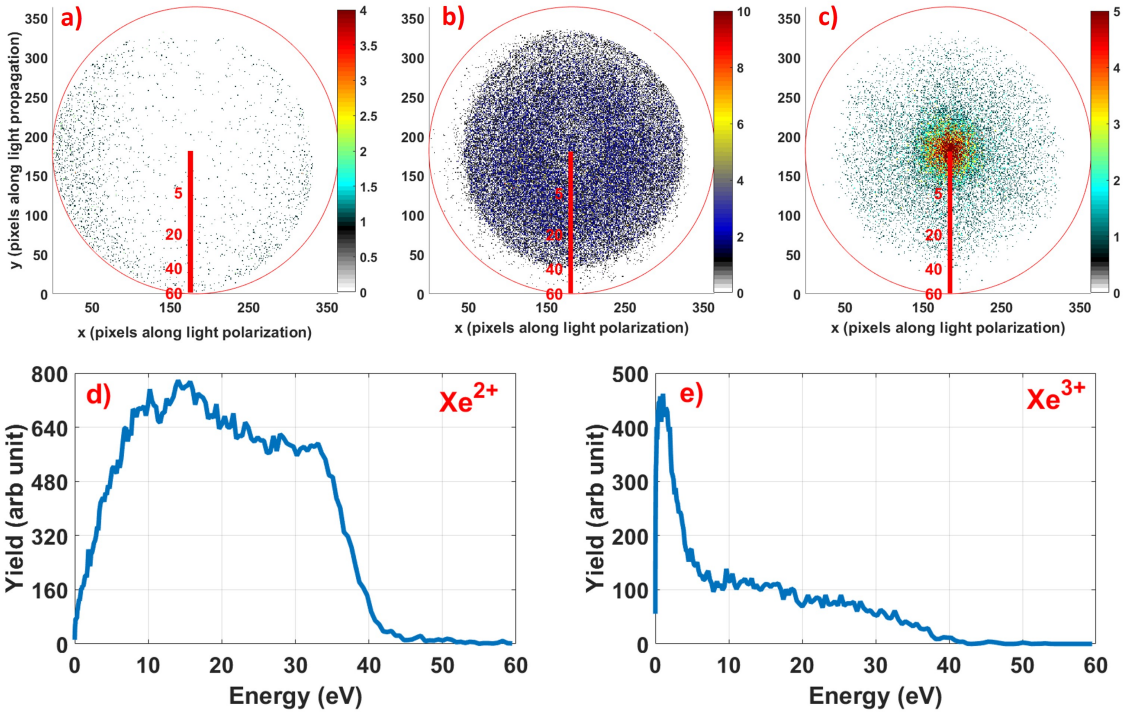

Figure 4.10: *Photoelectron images measured in coincidence with a) Xe^{+}, b) Xe^{2+}, and c) Xe^{3+} ionized by XUV high energy photons (60-90 eV). Photoelectron energy spectra measured in coincidence with d) Xe^{2+} and e) Xe^{3+}.*

train ($20 - 73$ eV), whereas the HHG spectrum used in Fig. 4.9b was obtained using the Zr filter and falls between 60 and 90 eV, with the most intense part around 77 eV. Both HHG spectra used to obtain the data of Fig. 4.9 are shown in Fig. 3.3d. In accordance with the above discussion, in the TOF spectrum obtained with the Al filter (Fig. 4.9a), the most abundant peak is Xe^{+}, which results from valence ionization. The TOF spectrum also contains a significant amount of Xe^{2+} ions, which are created either by shake-off processes after valence photoabsorption, or by the 4d shell ionization by the high-energy tail of the harmonic train followed by Auger decay. The latter process is also responsible for the rather weak Xe^{3+} peak. In contrast, the TOF spectrum obtained with the Zr filter (Fig. 4.9b) is dominated by Xe^{2+} and Xe^{3+} ions produced after inner-shell 4d photoabsorption, with a minor contribution of Xe^{+} from valence ionization.

By gating on times of flight and positions of ions, the photoelectrons coming from differ-

ent ionization channels can be separated. Fig. 4.10 displays the image of the photoelectrons detected in coincidence with Xe^+, Xe^{2+} and Xe^{3+} ions from the measurement with the Zr filter (corresponding to the TOF spectrum of Fig. 4.9b). The coincident photoelectron energy spectra for Xe^{2+} and Xe^{3+} are shown in Fig. 4.10d and 4.10e, respectively. Since the ions with an inner-shell (4d) vacancy almost always undergo Auger decay and end up in higher charge states, Xe^+ ions are nearly exclusively produced by removing an electron from 5p or 5s states, with the excess photon energy taken by the photoelectron. Accordingly, the resulting photoelectrons from single ionization typically have kinetic energy larger than 50 eV, such that most of them miss the detector (see Fig. 4.10a). In contrast, the electrons coincident with Xe^{2+} are a mixture of Auger electrons and photoelectrons removed from the 4d inner shell (Fig. 4.10b,d). With the harmonics spectrum selected by the Zr filter (see Fig. 3.3d), the 4d photoelectrons are expected to have kinetic energies ranging from 0 to 20 eV and peaked at 10-13 eV. The Auger electrons mostly originate from the decay of $4d^{-1}$ to $5p^{-2}$ states, which results in an electron kinetic energy between 30 and 37 eV [77]. Additional contributions come from shake-up satellite states $4d^{-1}5p^{-1}nl$ decaying to $5s^{-1}5p^{-2}nl$ or $5p^{-3}nl$, resulting in photoelectron energies between 15 and 25 eV [73]. These three groups of electrons form broad momentum and energy distributions observed in Fig. 4.10b and 4.10.d, respectively. For Xe^{3+} (Fig. 4.10.c,e), the signal is dominated by low-energy electrons that are coming from two subsequent Auger decay steps: $4d^{-1}$ to $5s^{-1}5p^{-2}7p$ and then to $5p^{-3}$ (see Fig. 4.8a). The high-energy tail in Fig. 4.10e is formed by the mixture of the 4d photoelectrons and energetic Auger electrons. The latter most likely originate from the triple ionization pathways not included in Fig. 4.8, where the photoabsorption by the 4d shell results in double ionization via shake-off-type processes, and the Auger electron energy is then comparable with Auger electrons from double ionization, extending to 35-40 eV.

As shown in Fig. 4.8, among the states populated by Auger decay upon 4d photoabsorption only the $5s^{-1}5p^{-2}7p$ state is energetically above the triple ionization threshold.

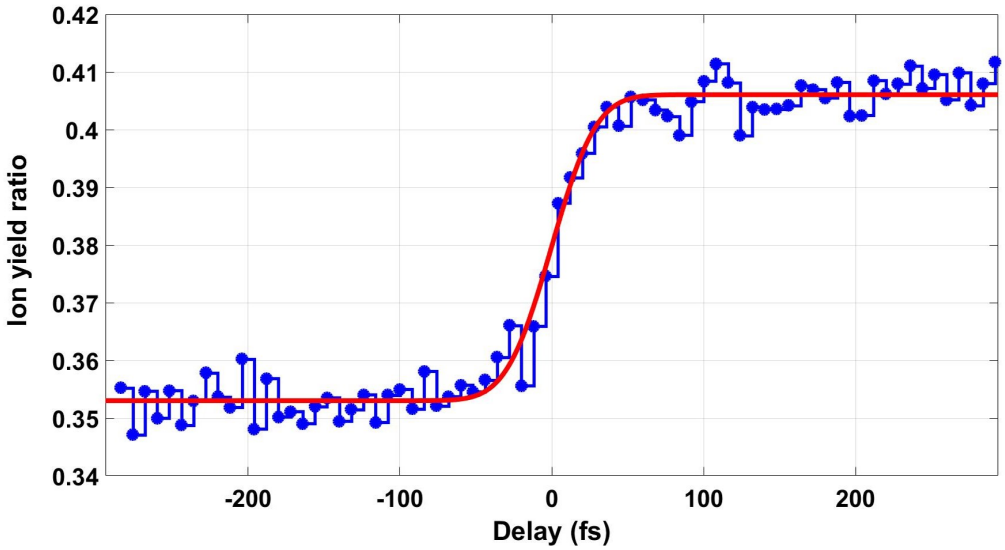

Figure 4.11: *Ratio of ion yield of Xe^{3+} to Xe^{2+} as a function of XUV-NIR delay.*

However, $5p^{-3}nl$ and $5s^{-1}5p^{-2}6p$ states lie just below this threshold and can be efficiently ionized by a single NIR photon. Accordingly, one can expect a significant enhancement of the Xe^{3+} signal if the XUV pulse is followed by the NIR probe pulse. Using the same train of high-order harmonics (selected by the Zr filter) in combination with a weak ($5 * 10^{12} W/cm^2$) NIR probe, we have carried out a pump-probe measurement aimed to map the population of the highly-excited states of Xe^{2+} discussed above into the triply-charged state. Fig. 4.11 depicts the ratio of Xe^{3+} to Xe^{2+} yields measured as a function of XUV-NIR delay. As expected, the signal exhibits a step function-type enhancement at positive delays and remains nearly constant within the measurement window. The CDF fit of this ratio yields the FWHM of 47 ± 5 fs. The time zero is set to the center of CDF function. Given rather large error bars, this value is consistent with that obtained from the Ne measurement discussed in Section 4.3, and with the broadest cross-correlation FWHM values obtained in side band measurements in Section 4.2, although it is nearly a factor of two larger than the corresponding values obtained for Xe^{2+} and Ar^{2+} signals produced via valence shake-up states discussed in Section 4.4. It should be noted that the cross-correlation signal here is expected to be slightly broadened because the pathway it is based on involves an Auger decay step

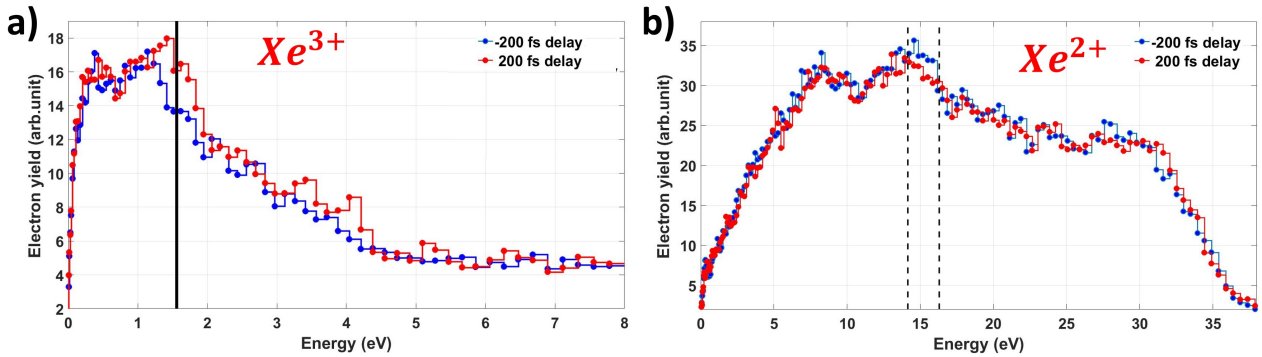

Figure 4.12: *Photoelectron energy spectra of a) Xe^{3+} and b) Xe^{2+} for the NIR pulse arriving before (blue) and after (red) the XUV pulse.*

with the characteristic lifetime of 6 fs [73]. A direct comparison with a simultaneous sideband measurement is not feasible here due to the broad, structureless shape of the emitted electron spectra, as can be seen from Fig. 4.10.

In order to confirm the origin of the observed enhancement, in Fig. 4.12 the photoelectron spectra coincident with Xe^{3+} (a) and Xe^{2+} (b) ions are plotted for two delays: one, where the NIR pulse precedes the XUV (-200 fs), and the other, where the NIR arrives after the XUV (+200 fs). As can be seen in Fig. 4.12.a, the electrons responsible for the additional Xe^{3+} production at positive delays are centered at the kinetic energy values corresponding to one NIR photon energy (marked by the black line). This indicates that the binding energy of these electrons is very close to zero, consistent with the scenario discussed above and illustrated in Fig. 4.8b. As can be seen from Fig. 4.12.b, the enhancement of Xe^{3+} yield is accompanied by the reduction of the Xe^{2+} photoelectron signal in a small kinetic energy window around 15 eV, marked by dashed vertical lines. This energy range corresponds to Auger electrons emitted in the transition populating the shake-up satellites (see Fig. 4.8), which are further ionized by the NIR pulse.

Since the delay-dependent Xe^{3+}/Xe^{2+} ratio shown in Fig. 4.11 behaves like a step function, it can be efficiently used for finding temporal overlap with an external laser at FEL facilities, as well as for coarse characterization of the XUV / soft X-ray pulse duration

and laser-FEL jitter. Earlier measurements at FLASH [74] employing a 400 nm probe showed that similar Xe^{3+} signal enhancement is still observable if the laser pulse arrives hundreds of picoseconds after the XUV pulse, suggesting 100 ps as the lowest limit for the lifetime of excited states involved. A more recent FLASH study aimed to establish timing determination protocol for experiments with a 800 nm probe [59] has shown that a noticeable enhancement of Xe^{3+} yield, as well as Xe^{2+} signal reduction, can be observed even at $1\mu s$ delay if the pulses are well-aligned and weak extraction fields are used, such that the ion does not leave the laser focus between them. Since this signal is based on the ionization of states populated by the Auger process, it is rather insensitive to the exact wavelength and can be used in a broad range of wavelengths above the 4d ionization threshold, up to at least 250 eV.

4.6 Double ionization of CO_2 molecules

The two-color signals discussed above either exist only in the region where XUV and NIR pulses overlap (like sideband features), or exhibit a step-function behavior, with the rise time of the signal broadened because of the non-zero duration of both pulses. Here, we consider another type of transient signal, which appears in the overlap region but rapidly decays with increasing delay. We found an illustrative example of such behavior in the ionization of a CO_2 molecule by a pair of XUV and NIR pulses. Since CO_2 is one of the best-studied polyatomic molecules, its double ionization by a single XUV photon has been extensively studied as a function of photon energy using synchrotron sources (see, e.g. [78,79,80]). Furthermore, CO_2 double ionization was a central subject of several recent NIR-NIR [81,82] and XUV-NIR [83] pump-probe experiments. Here, we aim to study two-color double ionization dynamics employing our combination of a high-repetition rate, short-pulsed XUV source with coincident detection of the fragments.

The ionization thresholds for the production of the four lowest states of the CO_2^{2+} dication

are 37.34 eV ($X^3\Sigma_g^-$), 38.55 eV ($a^1\Delta_g$), 39.22 eV ($b^1\Sigma_g^+$) and 40.1 eV ($c^1\Sigma_u^-$) [79,80]. All these states are metastable [79,80,84,85]. Depending on which vibrational levels of each electronic state are populated, they can either rapidly decay (on a femtosecond time scale), resulting in energetic CO^+ and O^+ ion pairs, or survive for a much longer time as a CO_2^{2+} dication, either being detected as a bound doubly-charged ion or dissociate underway to the detector on a nanosecond or even microsecond time scale [79,80,81]. Dissociative double ionization of CO_2 was also reported at photon energies below the above-mentioned thresholds and was assigned to indirect pathways involving the creation of dissociating $(CO_2^+)^*$ cationic states accompanied by the autoionization of oxygen atoms [78,79]. Since the latter occurs outside of the Franck-Condon region, two electrons can be emitted below the energetic limit for direct double ionization (37.34 eV).

The results of our experiment on two-color XUV-NIR double ionization of CO_2 are summarized in Fig. 4.13. Here, the harmonic train selected by the Al filter was used, resulting in a XUV spectrum similar to the one shown in Fig. 3.3a. Fig. 4.13a displays a photoion-photoion coincidence (PIPICO) spectrum obtained in this experiment, whereas the 1D insets along the horizontal and vertical axes show the corresponding portions of the non-coincident ion TOF distribution of the first and second detected ion, respectively. The data are integrated over all XUV-NIR delays (scanned from -110 fs to +240 fs). Besides a diffuse background due to false coincidences or the fragments from three-body breakup, a pronounced diagonal line (marked 1) with a long tail (marked 2, 3) can be observed in the figure, reflecting the CO^+ and O^+ detected in coincidence. While the main intense line (1) results from rapid breakup (Coulomb explosion) of the doubly-charged molecule, the long tail is due to the ions which travel part of the distance to the detector as a bound CO_2^{2+} dication and dissociate "in flight" (see [78,79,86,87] for detailed explanations). More specifically, regions (2) and (3) reflect the ions fragmented in the acceleration region and the drift region of the spectrometer (see section 3.2 for spectrometer details and ref. [78] for a detailed explanation of this shape of the line). Ions fragmented in drift the tube (field-

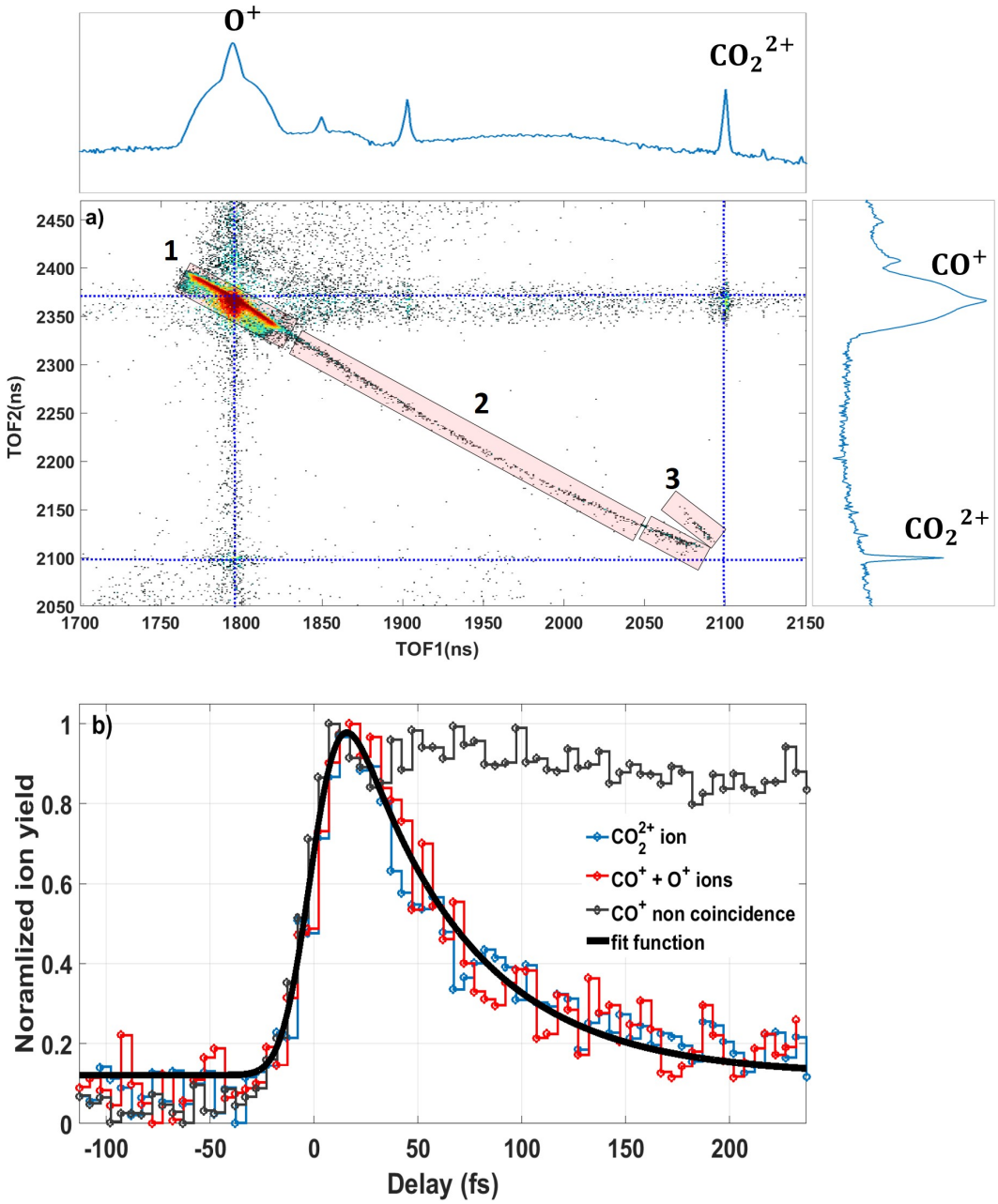

Figure 4.13: *a) PIPICO spectrum from XUV-NIR pump-probe experiment integrated over all delay steps. A clear line reflecting CO^+ and O^+ ions detected in coincidence can be seen. The 1D graphs represent the corresponding portions of the non-coincident ion TOF spectrum for the first (top) and the second (right) ions arriving at the detector. b) Delay dependent yields of CO_2^{2+} (blue line), $CO^+ + O^+$ coincidence channel (red) and non-coincident yield of CO^+ (grey).*

free region) can be ejected in all directions with respect to the center of mass of the CO_2 molecule. Therefore, in the upper arm of region 3, the CO^+ fragment is ejected toward the detector, and the O^+ fragment is ejected in the opposite direction with respect to the detector. In the lower arm, the O^+ fragment is ejected toward the detector, and the CO^+ fragment is ejected in the opposite direction with respect to the detector. The slope of the upper and lower arms are m_{CO}/m_O and m_O/m_{CO}, respectively. As can be seen from the 1D TOF spectra, a significant amount of bound CO_2^{2+} ions survives all the way to the detector and are measured at the corresponding TOF values (2100 ns).

Fig. 4.13b shows the measured yields of bound CO_2^{2+} ions (blue) and coincident CO^+ + O^+ ion pairs (red) as a function of XUV-NIR delay. The delay-dependent yield of non-coincident CO^+ ions, which is dominated by the low-energy fragments from the CO^+ + O dissociative ionization channel, is shown in grey for comparison. While all three signals exhibit nearly identical rise time, both double ionization channels decay to nearly the initial level within the measurement window, whereas the CO^+ signal from dissociative ionization remains nearly constant. The enhancement of the latter channel is due to the NIR dissociation of the CO_2^+ cationic states populated by the absorption of an XUV photon and will be discussed in detail in the next section. Hear, we focus on double ionization events. Nearly identical behavior of both the CO_2^{2+} and CO^+ + O^+ channels suggests that they do originate from the same set of metastable dicationic states discussed above. Besides directly populating those dicationic levels, at photon energies between 32 to 40eV, an inner-valence XUV ionization of neutral CO_2 can leave a molecular ion in one of the highly excited cationic states (e.g., $^2\Sigma_u^+$ or $^2\Sigma_g^+$) [88]. The potential energy curves of these $(CO_2^+)^*$ states are highly repulsive through an asymmetric C-O stretch [89]. The energy threshold for the $^2\Sigma_g^+$ state is 36.5 eV, which is very close to the peak of one of the most intense (23rd) harmonics in our XUV spectrum and is less than one NIR photon energy below the ground state of the CO_2^{2+} dication. Thus, these (or higher) highly excited $(CO_2^+)^*$ states, which are formed by XUV photon absorption (H23 and higher), can be further ionized into the low-lying dicationic

states by a single NIR photon, resulting in the enhancement of both double ionization channels at large delays visible in Fig. 4.13b. However, since all these $(CO_2^+)^*$ states are highly repulsive, the separation to the dicationic states increases with increasing C-CO distance and, thus, at large internuclear separations, one NIR photon is not enough to further ionize these states., As a result, a clear decay of both CO_2^{2+} and $CO^+ + O^+$ yields is observed with increasing delay in Fig. 4.13b. The signal is fitted by a convolution of Gaussian and decay functions [(exp($\frac{\sigma^2}{2\tau^2}$-$\frac{t}{\tau}$))*(1-erf($\frac{\sigma^2 - t\tau}{\sqrt{2}\sigma\tau}$)),90]. The fitting yields a Gaussian width of 27 ± 3 fs and a decay constants of 55 ± 5 fs.

It is interesting to compare the transient response of a molecule to a combined XUV-NIR field illustrated in Fig. 4.13b with the behavior of $CO^+ + O^+$ channel observed in a similar experiment (which employed a broader range of XUV photon energies) described in Ref. [83]. There, the observed $CO^+ + O^+$ signal also displayed a transient enhancement, but the shape of the delay-dependent yield was clearly symmetric, in contrast to the asymmetric shape observed in Fig. 4.13b. The likely reason for this difference is the time resolution of the experiment, which was comparable to the characteristic dissociation time scale of the $(CO_2^+)^*$ states responsible for the decay of both double ionization signals in Fig. 4.13b. Thus, the comparison of these two measurements clearly highlights the role of pulse duration in the analysis of XUV-NIR two-color signals.

4.7 Summary

In this chapter, a series of observables typical for ionization-based XUV-NIR pump-probe experiments has been analyzed making use of short (25-30 fs) HHG pulses at a 10 kHz repetition rate combined with a coincident ion-electron spectrometer. We have taken advantage of complementary experimental schemes and coincident measurements to trace the relative timing between the observed two-color signals and to reveal basic physics behind their formation. Several of these observables, in particular, those based on NIR ionization of

neutral or ionic excited states populated by XUV, are long-lived, i.e., they exist in a rather long delay range, limited only by the lifetime of the excited states involved. As can be seen from the examples considered in Sections 4.3-4.5, the range of wavelengths at which these signals can be found is rather broad and can be adjusted by choice of the process and the target. An example of a different, "transient" type of two-color effect, which exists only in the region where two pulses overlap, is given by the sideband measurements discussed in Section 4.2. Finally, delay-dependent ion signals obtained from double ionization of CO_2 molecules in Section 4.6 represent an intermediate situation, where the observed effect exists beyond the pulse overlap region but still decays rather rapidly due to the dynamics of the intermediate states involved (in this case, due the dissociation of the intermediate state).

As can be seen from the discussion in Sections 4.2-4.7, and from the comparison of the results obtained from different experimental schemes, although all these signals provide certain information about relative timing of the XUV and NIR pulses and about XUV pulse duration, for reliable interpretation of the data the calibration of the "steady", step function-like signals against a simultaneous sideband measurement is still highly desirable. In the experiments on time-resolved imaging of XUV-induced molecular dynamics described in the next two chapters, sideband signals were recorded simultaneously with the main observables and used for precise "zero delay" determination.

Chapter 5

State-selective analysis of electronic and nuclear dynamics in CO_2 molecules ionized by femtosecond XUV pulses

5.1 Background and motivations

After femtosecond or even attosecond XUV pulses delivered by FELs and HHG sources became available in the first decade of this century, they were soon applied to study the dynamics of high-lying molecular states previously inaccessible for time-resolved studies [56,57,91,92,93]. Most of these experiments used single-photon XUV ionization of a molecule to trigger the process of interest, creating a hole in a valence or inner-valence shell. Because of the relatively short durations of the XUV pulses used, not only nuclear but, in some instances, also electronic dynamics can be traced in time if a proper pump-probe arrangement can be found.

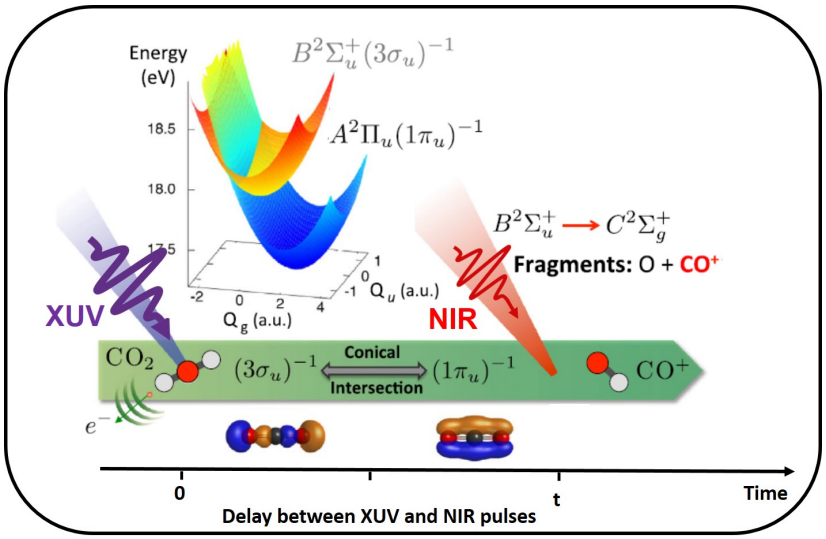

Figure 5.1: *Potential energy surfaces of the A and B states of CO_2^+ near a conical intersection and a scheme of an XUV-NIR pump-probe experiment (adapted from [52])*

One of the most interesting examples of tracing electronic dynamics driven by a conical intersection between two cationic states was reported for CO_2 molecules ionized by a train of harmonic pulses [52]. There, as illustrated in Fig. 5.1, the removal of an electron from the HOMO-2 orbital by an XUV pulse resulted in populating a cationic $B^2\Sigma_u^+$ state (see also Fig. 5.2). This state and a lower $A^2\Pi_u$ state form a conical intersection because of their "bilinear" vibronic coupling, driven by the bending and asymmetric stretch vibrations of the initially linear molecule [94]. Since these states are of different symmetries, the conical intersection can mediate the transfer of electron hole population between the σ_u symmetry of the $B^2\Sigma_u^+$ state and the π_u symmetry of the $A^2\Pi_u$. While both of these states are bound, a time-delayed NIR pulse can probe their population by coupling to a higher-lying state and dissociating the molecule. The most efficient dissociation processes, driven by one NIR photon, proceed via a predissociative $C^2\Sigma_g^+$ state [95,96]. Since the $B^2\Sigma_u^+$ is more efficiently coupled to the $C^2\Sigma_g^+$ state (see Fig. 5.2 and Ref. [52]), the yield of CO^+ ions resulting from the NIR-induced dissociation via $C^2\Sigma_g^+$ was exploited to monitor the $B^2\Sigma_u^+$ population as a function of time after the XUV photoabsorption. The measured CO^+ signal displayed an oscillation reflecting the periodic change of the hole density between σ and π character.

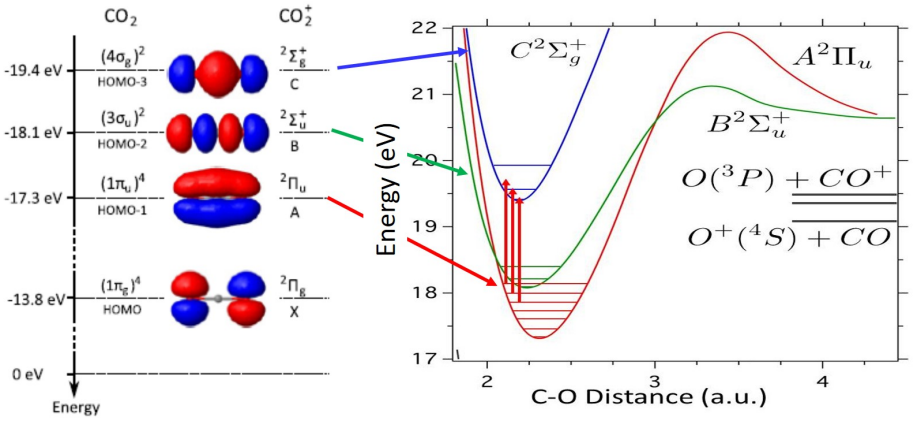

Figure 5.2: *Binding energy and orbital shape of HOMO, HOMO-1, HOMO-2, and HOMO-3 orbitals of the CO_2 molecule (left panel) and corresponding potential energy curves of CO_2^+ excited states (right panel). (Adapted from [95])*

In the CO_2 experiment described in Ref. [52] as well as in the other experiments, where the dynamics of interest are triggered by a short XUV pulse, the latter almost always populates many molecular states. Besides the broad bandwidth of the pulse, for ionizing transitions an emitted electron can take different amounts of excess energy, thus effectively populating all the ionic states which are energetically accessible. In [52] the dominance of the initial population in a specific state ($B^2\Sigma_u^+$) was achieved by a combination of partial cross section and the choice of the spectral range. However, the role of the other electronic states, which are necessarily populated by the train of harmonics used, and their contributions to different dissociation pathways of the created cation cannot be inferred from the experiments relying only on measuring the yields of ionic fragments.

In this Chapter, we describe an experiment aimed to shed light on the role of individual electronic states in the dynamics of the XUV-ionized CO_2 molecule using an electron-ion coincidence technique combined with the XUV-NIR pump-probe scheme. Due to its small size and well-known structure, a CO_2 (carbon dioxide) molecule represents an attractive target for studying molecular dynamics upon photoionization beyond diatomic systems. Accordingly, besides Ref. [52] mentioned above, CO_2 was a target on several recent pump-probe experiments studying the dynamics of its cationic or dicationic states using XUV

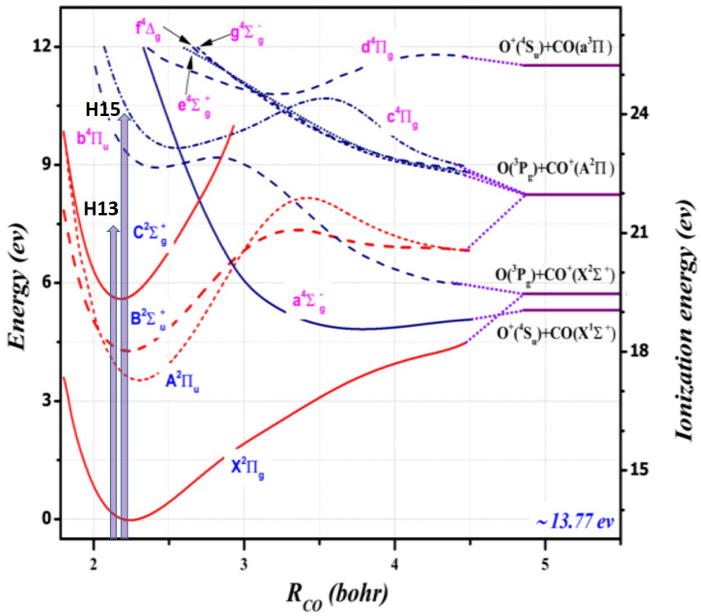

Figure 5.3: *Potential energy curves of CO_2^+ (adapted from [96]). Vertical arrows depict the photon energies of H13 and H15. Thus, electrons can be removed from HOMO-3 by H13 or H15 resulting in dissociation of the monocation by coupling between the predissociative $C^2\Sigma_g^+$ state and either $a^4\Sigma_g^-$ or $b^4\Pi_u$ states.*

[83,97] and optical laser [81,82,98,99] pulses. Furthermore, laser-induced dynamics in CO_2^+ served as a popular test ground for molecular HHG spectroscopy [100,101,102,103]. Finally, there is an extensive literature on single-pulse experiments characterizing the CO_2 response to XUV photoabsorption from synchrotron [78,79,96,104,105] and HHG [106] sources.

For most of the experiments described in this chapter, a Sn filter was used to restrict the XUV spectrum, which then mainly consists of 13th and 15th harmonics (see Fig. 3.3c). The phase-matching condition was further optimized to enhance the ratio between the 13th and 15th harmonic contributions, such that the dominant part of the resulting spectrum is centered at $\sim 20.4 - 20.6$ eV , with a smaller but non-negligible remaining contribution of the 15th harmonic ~ 3.1 eV higher in energy. The structure and energies of several low-lying electronic states of CO_2^+ relevant for this energy range are illustrated in Fig. 5.2 and 5.3. The three lowest ionic states of the CO_2 molecule, denoted as $X^2\Pi_g$, $A^2\Pi_u$, and $B^2\Sigma_u^+$, are bound since only very high vibrational levels of those states lie above the dissociation

limit. The lowest energies associated with these three electronic states are 13.8 eV, 17.3 eV, and 18.1 eV, respectively. In a Koopmans-type picture [107] these excited states of the created cation can be associated with the removal of an electron from the HOMO, HOMO-1, and HOMO-2 orbitals of a neutral CO_2 molecule, as sketched in Fig. 5.2 [95]. The first state with its low-lying vibrational levels above the dissociation limit is the $C^2\Sigma_g^+$ (19.4 eV), which corresponds to an electron removal from the HOMO-3 orbital. This state is a predissociative state and is known to fully dissociate on a nanosecond time scale, with the lowest limit for dissociation time above 1.2 ps [96]. The energy of the ground vibrational state of $C^2\Sigma_g^+$ is only above one dissociation limit, leading to dissociation of CO_2^+ molecular ions into $CO + O^+$. Therefore, the transitions ending up in a ground vibrational level of the C state produce only O^+ ionic fragments. In higher vibrational states, dissociation to $CO^+ + O$ becomes energetically accessible.

A more detailed sketch of cationic potential curves responsible for CO_2^+ dissociation is shown in Fig. 5.3 as a function of one C-O distance, while the other C-O distance and the O-C-O angle are kept fixed. Specific mechanisms leading to the dissociation of the $C^2\Sigma_g^+$ state proceed through internal couplings to some of the repulsive states sketched in this figure and have been discussed in [96,108,109,110,111]. In brief, the higher vibrational levels of the $C^2\Sigma_g^+$ state predominantly decay through the efficient spin-orbit coupling with the $b^4\Pi_u$ state:

$$CO_2^+(C^2\Sigma_g^+) \xrightarrow{\text{pred.}} CO_2^+(b^4\Pi_u^+) \rightarrow CO^+(X^2\Sigma^+) + O \tag{5.1}$$

resulting in CO^+ ion formation, whereas the ground vibrational state of $C^2\Sigma_g^+$ decays via the pathway:

$$CO_2^+(C^2\Sigma_g^+) \xrightarrow{\text{pred.}} CO_2^+(a^4\Sigma_g^-) \rightarrow CO + O^+(^4S_u) \tag{5.2}$$

producing O^+ ionic fragments [95,96]. According to Ref. [96], the latter pathway includes

Vibrational state	Energy	$O^+(^4S) + CO(X^1\Sigma^+)$	$O(^3P) + CO^+(X^2\Sigma^+)$
Threshold	19.07eV	1	0
Autoionization Ry state	19.15eV	1	0
(0 0 0)	19.39eV	1	0
(0 1 0)	19.47eV	0.88	0.12
(0 2 0)	19.54eV	0.35	0.65
(1 0 0)	19.56eV	0.22	0.78
(0 1 1)	19.76eV	0.18	0.82

Table 5.1: *Dissociation ratio for some vibrational levels of the predissociative $C^2\Sigma_g^+$ state [adapted from 96]*

an intermediate step driven by the vibronic coupling between the $C^2\Sigma_g^+$ and $A^2\Pi_u$ states, followed by the spin-orbit coupling of the latter to $a^4\Sigma_g^-$, since the spin–orbit integral for direct coupling between the $C^2\Sigma_g^+$ and $a^4\Sigma_g^-$ states gives no contribution to $\Delta m_s = 1$. Energy thresholds for different vibrational levels of the $C^2\Sigma_g^+$ state and the corresponding branching ratios for O^+ or CO^+ ion production are given in Table 5.1. As can be seen from this table, the dissociation of the cation can also occur slightly below the threshold $C^2\Sigma_g^+$ state. There, high-lying vibrational levels of $A^2\Pi_u$, and $B^2\Sigma_u^+$ can be populated, resulting in the dissociation towards the $CO + O^+(^4S_u)$ limit, e.g., due to relatively strong spin–orbit coupling between the $A^2\Pi_u$ and $a^4\Sigma_g^-$ states [96]. Specific energy values for relevant vibrational levels of $A^2\Pi_u$ and $B^2\Sigma_u^+$ states along with relative intensities of corresponding photo-induced transitions from the ground state of neutral CO_2 molecule are given in Tables A.1 and A.2 of Appendix A.

In the XUV-NIR pump-probe experiment, the predissociative $C^2\Sigma_g^+$ state can be either directly populated by a single XUV photon absorption from the neutral ground state or by coupling XUV-populated bound cationic states to the $C^2\Sigma_g^+$ state by the NIR probe pulse. At the NIR intensity chosen for the experiments described in this Chapter ($\leq 10^{13} W/cm^2$), the transitions from the ground cationic state ($X^2\Pi_g$), which require the absorption of at least three NIR photons (four photons for the low-lying vibrational states that are most likely populated by the photoionization), do not provide any distinguishable contribution

to the dissociation signal. The NIR pulse alone also does not produce any O^+ or CO^+ ions distinguishable from the background level. Under these conditions, the two-color contribution to the O^+ and CO^+ ion signals is dominated by one-photon NIR transitions from the XUV-populated $A^2\Pi_u$ and $B^2\Sigma_u^+$ to $C^2\Sigma_g^+$ (see Fig. 5.4). Since the fraction of the direct $C^2\Sigma_g^+$ state population at the photon energies between 20 and 21 eV, which dominate our XUV spectrum, is below 5 percent of the total photoionization cross section, whereas the population of each of the $A^2\Pi_u$, and $B^2\Sigma_u^+$ states is above 30 percent [112], such a two-color signal can be a dominant pathway for specific dissociation channels, providing efficient observables for studying dynamics in the cationic states. Partial ionization cross sections for the photoionization into the four lowest CO_2^+ states in a relevant energy range can be found in Table A.4 of Appendix A. Since the energy required to populate the ground vibrational level of the $B^2\Sigma_u^+$ is 18.07 eV, the absorption of an additional NIR photon from this state always ends up in one of the higher states of $C^2\Sigma_g^+$, leading to CO^+ ion production (see Table 5.1). In contrast, the two lowest vibrational levels of the $A^2\Pi_u$ state (below ∼17.5 eV) are more than one NIR photon energy below the dissociation threshold. The following few vibrational states (up to 17.9 eV) can be efficiently coupled only to the ground vibrational level of $C^2\Sigma_g^+$, mainly resulting in O^+ fragments. While the ionization to the $B^2\Sigma_u^+$ is dominated by the transition to its ground vibrational level, for the $A^2\Pi_u$ state, whose equilibrium C-O distance is shifted to somewhat higher values compared to the ground states of the ion and the neutral (which are very similar), the most intense transition from the neutral is $(0,0,0)^1\Sigma^+ \rightarrow (1,0,0)\ ^2\Pi_{3/2}$, where $(\nu1, \nu2, \nu3)$ represents symmetric stretching, bending, and asymmetric stretching respectively (see Table A.1 in Appendix A) [Ref. 104].

5.2 XUV-only measurements

Figure 5.4 displays "XUV-only" ion time-of-flight spectra obtained using a train of harmonics (H13 through H27, panel a) selected by the Al filter, and by H13 and H15 (panel

b) selected by the Sn filter (see Fig. 3.3a and b, respectively, for the XUV spectra used). The data in Fig. 5.4a stem from the same experiments as the results on double ionization discussed in Section 4.6. The energetic thresholds for observing CO_2^+, O^+, CO^+, C^+ and CO_2^{2+} ions are 13.8eV, 19.07eV, 19.46eV, 25eV, and 37.33eV respectively [96]. Correspondingly, while all five of these ionic fragments are present in Fig. 5.4a, only CO_2^+, O^+, and CO^+ fragments can be observed in Fig. 5.4b. The branching ratios are 0.943 ± 005 (CO_2^+), 0.044 ± 0.0006 (O^+), and 0.013 ± 0.0003 (CO^+). The total fraction of the ions resulting from CO_2 dissociation in Fig. 5.4b constitutes 0.057 ± 0.0009, which is in reasonable agreement with the expectations for the partial cross section of the ionization to the $C^2\Sigma_g^+$ state (0.04 at 21 eV and 0.07 at 24 eV [112], see Table A.4 in Appendix A). For comparison, the total fraction of the dissociating fragments in Fig. 5.4a (harmonic train) is much larger (0.345 ± 0.002), with the fraction of CO^+ ions increasing to 0.123 ± 0.0006, i.e., nearly an order of magnitude greater compared to H13 and H15 only. Thus, even though the CO^+ signal obtained with the train of harmonics in a pump-probe experiment does exhibit a clear enhancement in the presence of the NIR probe pulse, as was shown in Section 4.6 (see Fig. 4.13b), one can expect a much higher pump-probe contrast with the narrower XUV spectrum, such that the XUV-only contribution to the dissociation channel is limited and well understood. From now on, in this chapter, we will mainly focus on the experiments employing H13 and H15, corresponding to the conditions for Fig. 5.4b.

In order to confirm the contributions of individual cationic states to the ionization and dissociation of CO_2, and to identify corresponding electron emission patterns, in this section we analyze the VMI images of the photoelectrons detected in coincidence with ionic fragments shown in Fig. 5.4b. Since the photoionization of the CO_2 molecule has been extensively studied before, partial cross sections and asymmetry parameters for its four lowest cationic states (which we will be referring to simply as X, A, B, and C) are known, and a good agreement between experimental and theoretical values has been achieved [106,112,113]. Using these values, the differential photoionization cross section can be calculated using

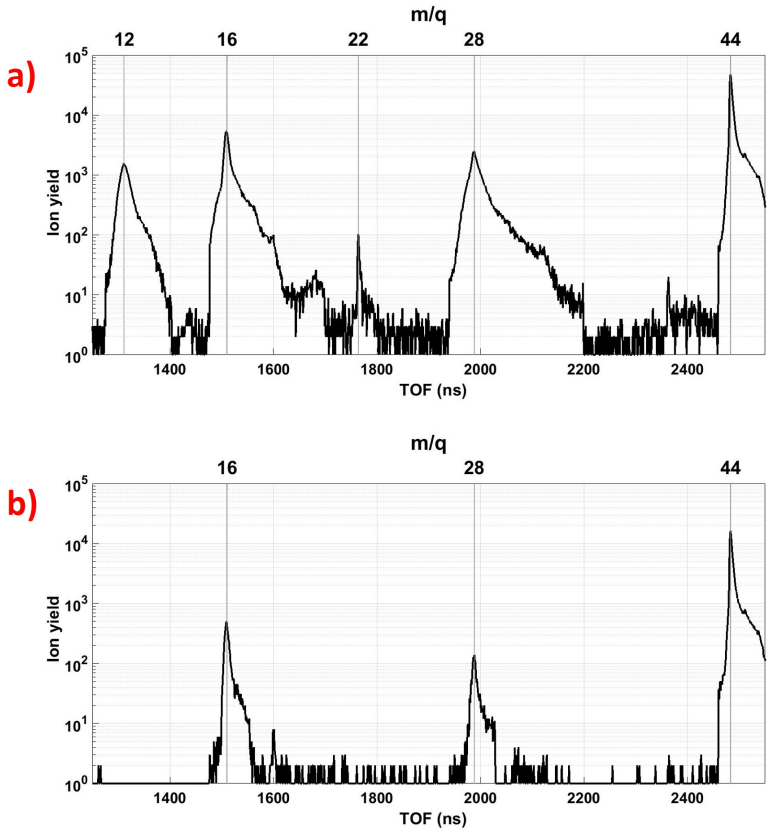

Figure 5.4: *Ion time of flight spectra from CO_2 molecule ionized by: a) a train of harmonics, b) H13-15.*

equation 2.20. The simulated differential cross sections for the X, A, B, and C states of CO_2^+ at 20.7 eV, the central photon energy of our H13, are plotted in Fig. 5.5. The angular distribution of the photoelectrons emitted from the ground X state is roughly isotropic. The photoelectrons from the A state are ejected in both parallel and perpendicular directions, with a slight preference for the former. The photoelectrons from the B state are more likely to be ejected in a direction perpendicular to the light polarization, whereas the angular distribution of the C state photoelectrons is strongly peaked parallel to the light polarization.

The VMI images of the photoelectrons detected in coincidence with O^+ and CO^+ ions are shown in Fig. 5.6a and 5.6c, respectively. According to the discussion in the previous

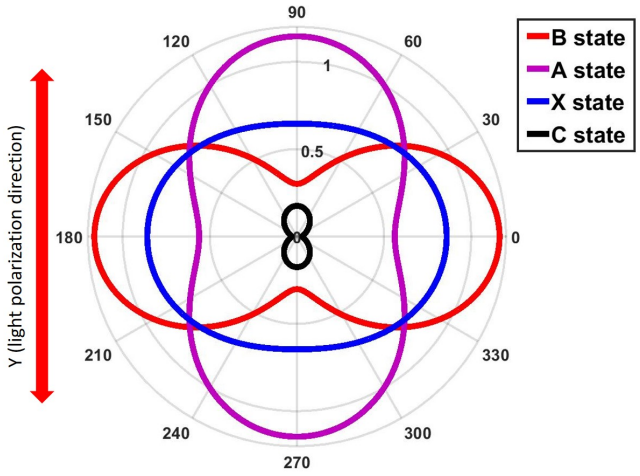

Figure 5.5: *The differential cross section for the first four electronic states of CO_2^+, plotted for an XUV photon energy of 20.7eV. The red arrow shows the light polarization direction.*

section, we expect that both of these ionic species result from the C state population. The electron emission patterns in Fig. 5.6a and 5.6c, which are both peaked along the XUV polarization direction, are consistent with this assignment. In order to make a more specific comparison with the expected emission pattern, the corresponding photoelectron images are simulated based on equation 2.20 [114]. For linearly polarized light with the polarization along the y direction and propagating along the x direction, the probability of electron ejection in a given direction with respect to the polarization with energy e1 is given by:

$$d\sigma = \sum_{i,j}[\sigma_{h\nu_j}\sqrt{2\pi} * exp(\frac{(h\nu_j - E_i - e1)^2}{-2(\sigma_{h\nu_j})^2}) * d(h\nu_j)] * [\frac{\sigma_i}{4\pi}[1+\beta_i P_2(sin(\theta)sin(\phi))] * [sin(\theta)d\theta d\phi]] \tag{5.3}$$

here the summation i is over all occupied final vibrational states of a chosen electronic state, and the summation j is over all harmonic orders (here only harmonics 13 and 15 corresponding to $h\nu_{13}$ and $h\nu_{15}$). E_i is the energy of the final state, σ_i is its partial cross section, θ and ϕ denote the polar and azimuthal angles, respectively. $\sigma_{h\nu}$ reflects the width of the photon spectrum and is calculated by fitting the H13 and H15 photon energy distribution

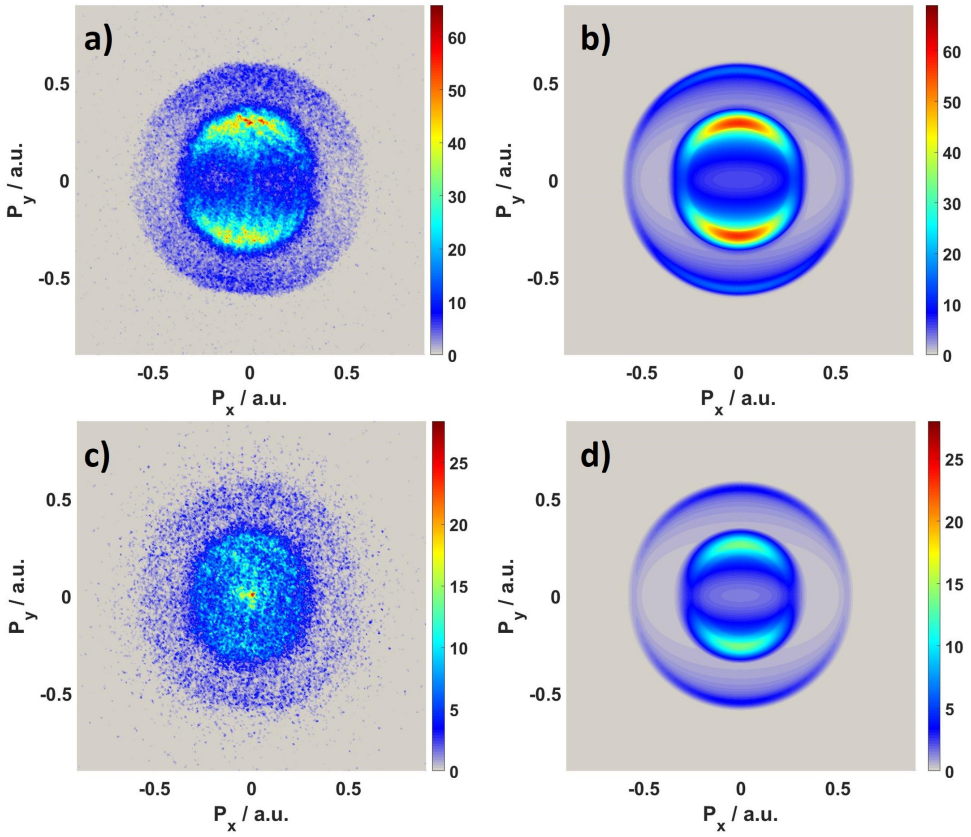

Figure 5.6: *Upper row: experimental (a) and simulated (b) photoelectron images measured in coincidence with O^+. Lower row: experimental (c) and simulated (d) photoelectron images measured in coincidence with CO^+.*

with a Gaussian function.

We use equation 5.3 to simulate the measured photoelectron images and corresponding kinetic energy distribution. While the simulation's output allows one to plot any differential observable describing the photoelectron emission, the experimental data in Fig. 5.6a and 5.6c are presented as non-inverted VMI images scaled in atomic units of momentum. As discussed in section 3.2.1, for low-statistics photoelectron images, appropriate VMI inversion is often not feasible. Correspondingly, we have chosen not to apply the inversion for any experimental data presented in this chapter. Instead, for comparison of the experimental results with modeling, we directly simulate the observables that correspond to the

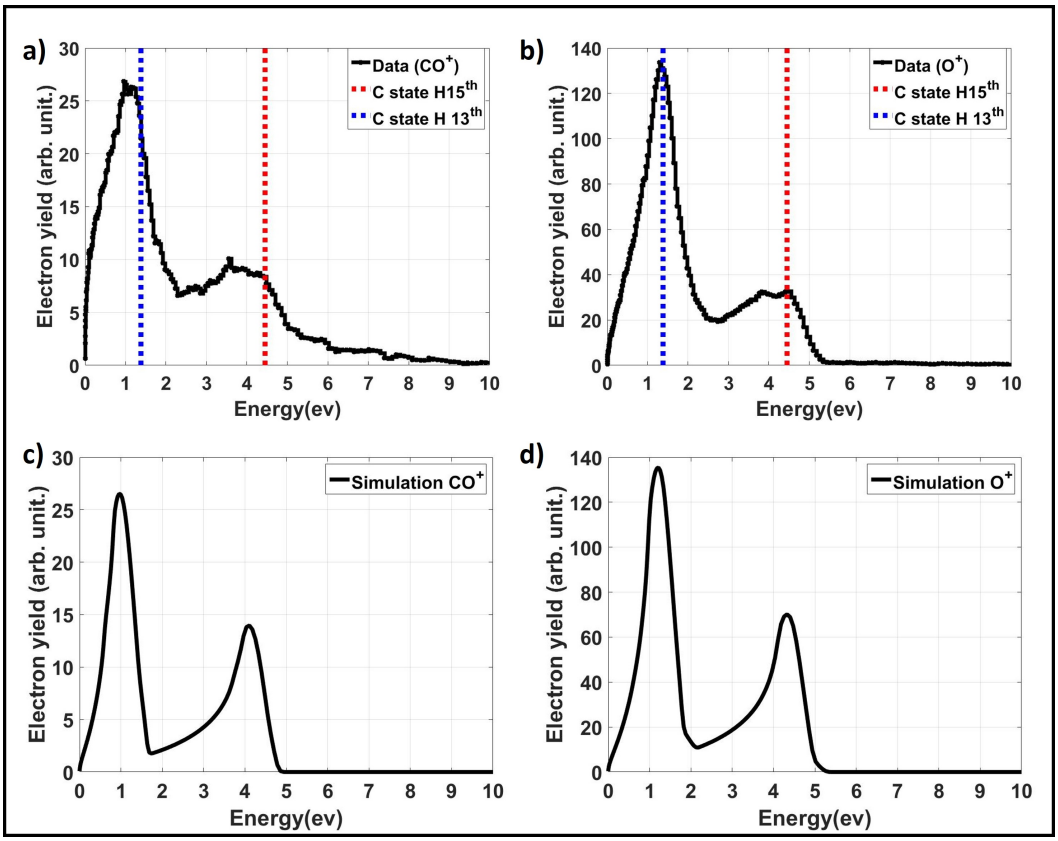

Figure 5.7: *Photoelectron energy spectra. a) the experimental data for CO^+, b) experimental data for O^+, c) simulation for CO^+, and d) simulation for O^+.*

chosen data representation. For VMI images like those shown Fig. 5.6 (and throughout this section), 3D photoelectron momentum distributions calculated based on equation 5.3 are projected onto a detector plane to produce 2D distributions that can be directly compared to the experimental results. The photoelectron energy spectra presented in this and the following chapter are, in fact, re-scaled squared radial distributions obtained from the raw VMI images and calibrated in energy.

The images simulated according to the procedure described above for photoelectron emission from the CO_2^+ C state are shown in Fig. 5.6 for the conditions expected to result in O^+ (b) and CO^+ (d) production. For both cases, the simulation is based on the energies of individual vibrational levels of the C state and the corresponding branching ratios for $O^+ + CO$ and $O + CO^+$ dissociation channels given in Table 5.1. A noticeable difference

between the CO^+ and O^+ photoelectron images can be observed in both experimental data and simulations. The electron emission patterns corresponding to O^+ ions are more intense. They appear somewhat broader, reflecting a more significant probability for this channel and larger access energy due to the lower vibrational states involved (see table 5.1). To quantify this difference, the photoelectron kinetic energy distributions obtained from the measured and simulated images of Fig. 5.6 are plotted in Fig. 5.7. A small but noticeable shift of the energy spectra towards lower values can be seen for the electrons corresponding to CO^+ production (panels a, c) as compared to O^+ (panels b, d), confirming that the CO^+ ions indeed result from the dissociation of higher vibrational levels of the C state. The simulated patterns qualitatively resemble the experimental data, with the main difference being the higher fraction of the events from H15 (peaks around 4 eV) in the theoretical plots. This most likely reflects the fact that the content of H15 in the experiment was reduced compared to the values assumed in the simulation.

The available excess photon energy can be shared between the photoelectron and the nuclei. Although under conditions of this experiment, little quantitative information can be obtained for very low-energy ions resulting from cationic dissociation, the ion VMI images can still be used for filtering the electron data. This is illustrated in Fig. 5.8, where the photoelectrons detected in coincidence with CO^+ ions are sorted according to the measured ion momenta. Selecting the ions with small but non-zero momenta (Fig. 5.8a) results in electron momentum and energy distributions peaked at very small values (Fig. 5.8b and 5.8c). In contrast, for ions with nearly zero momenta in the center of the VMI image (Fig. 5.8d), the electron emission pattern (Fig. 5.8e) and energy distribution (Fig. 5.8f) become very similar to the corresponding simulation results shown in Fig. 5.6d and 5.7c, respectively, obtained under the assumption that the photoelectron takes the whole excess energy. For a given electronic state, the situation when the noticeable fraction of the energy is carried by the ion (and by the neutral dissociation partner) reflects the population of higher-lying vibrational states, with a larger energy gap to the dissociation limit. This is

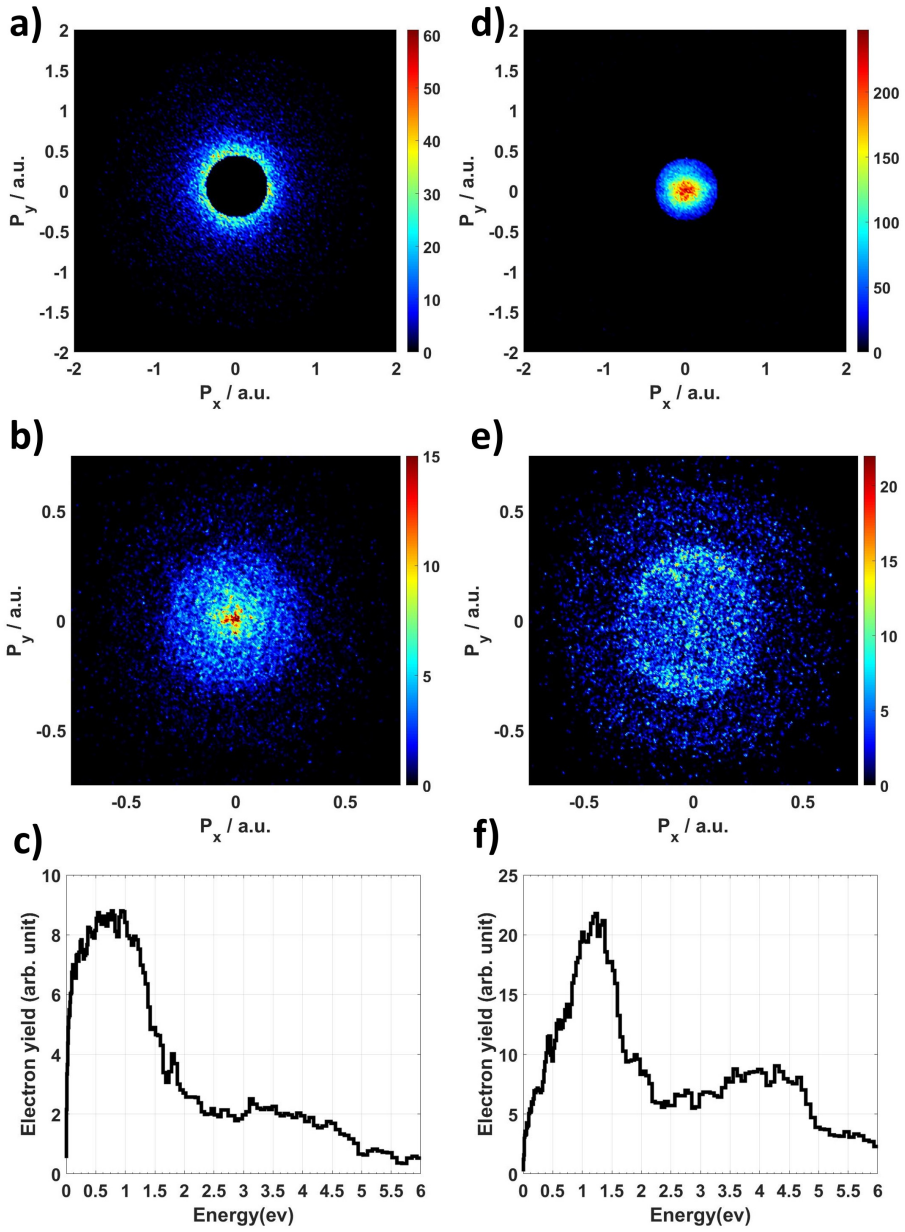

Figure 5.8: *Photoelectron images and energy spectra in coincidence with CO^+ corresponding to two different conditions on the ion momenta. a) Ion VMI image for ions with relatively high momenta (or energy). b), c) Photoelectron image and energy spectrum corresponding to the high-energy ions shown in a). d) VMI image for ions with low momenta (or energy). e), f) Photoelectron image and energy spectrum corresponding to the low-energy ions shown in d).*

consistent with the absence of the corresponding low-energy feature for the photoelectrons detected in coincidence with O^+ ions (Fig. 5.8a), since all the higher vibrational levels of the CO_2^+ C state predominantly dissociate via the $CO^+ + O$ pathway (see Table 5.1).

Fig. 5.9 shows the VMI image (a) and the kinetic energy distribution (b) of the photoelectrons detected in coincidence with CO_2^+ parent ions. Compared to the electrons resulting from dissociation channels discussed above, the CO_2^+ photoelectrons are more energetic and exhibit a noticeable enhancement in the direction perpendicular to the light polarization. Since the C state of CO_2^+ is predissociative, it is not expected to contribute to the CO_2^+ photoelectron emission pattern, which then contains the photoelectrons from the three lower, bound CO_2^+ states (X, A and B). In order to visualize the expected contributions from each of these states, their simulated photoelectron images are plotted in 5.9d (B state), 5.9e (A state), and 5.9f (X state), whereas the sum of all these images weighted with the corresponding partial cross sections is plotted in Fig. 5.9c. The image resembles the experimental data reasonably well. From the analysis of the individual contributions in Fig. 5.9d-f, one can see that, in accordance with the negative asymmetry parameter value, the electrons emitted perpendicular to the polarization direction dominate the emission pattern for the B state (Fig. 5.9d). Thus, the B state is responsible for the enhancement along the x-axis observed in the measured and simulated electron patterns for all CO_2^+ electrons shown in Fig. 5.9a and 5.9c. The energy distributions obtained from the calculated images in Fig. 5.9c-f are shown in Fig. 5.9. Each spectrum for individual electronic states (Fig. 5.9b-d) contains pronounced peaks reflecting the photoelectrons from H13 and H15. The energy distribution integrated over all three contributing electronic states, which is shown in Fig. 5.9a, is in reasonable agreement with the corresponding experimental spectrum shown in Fig. 5.9b.

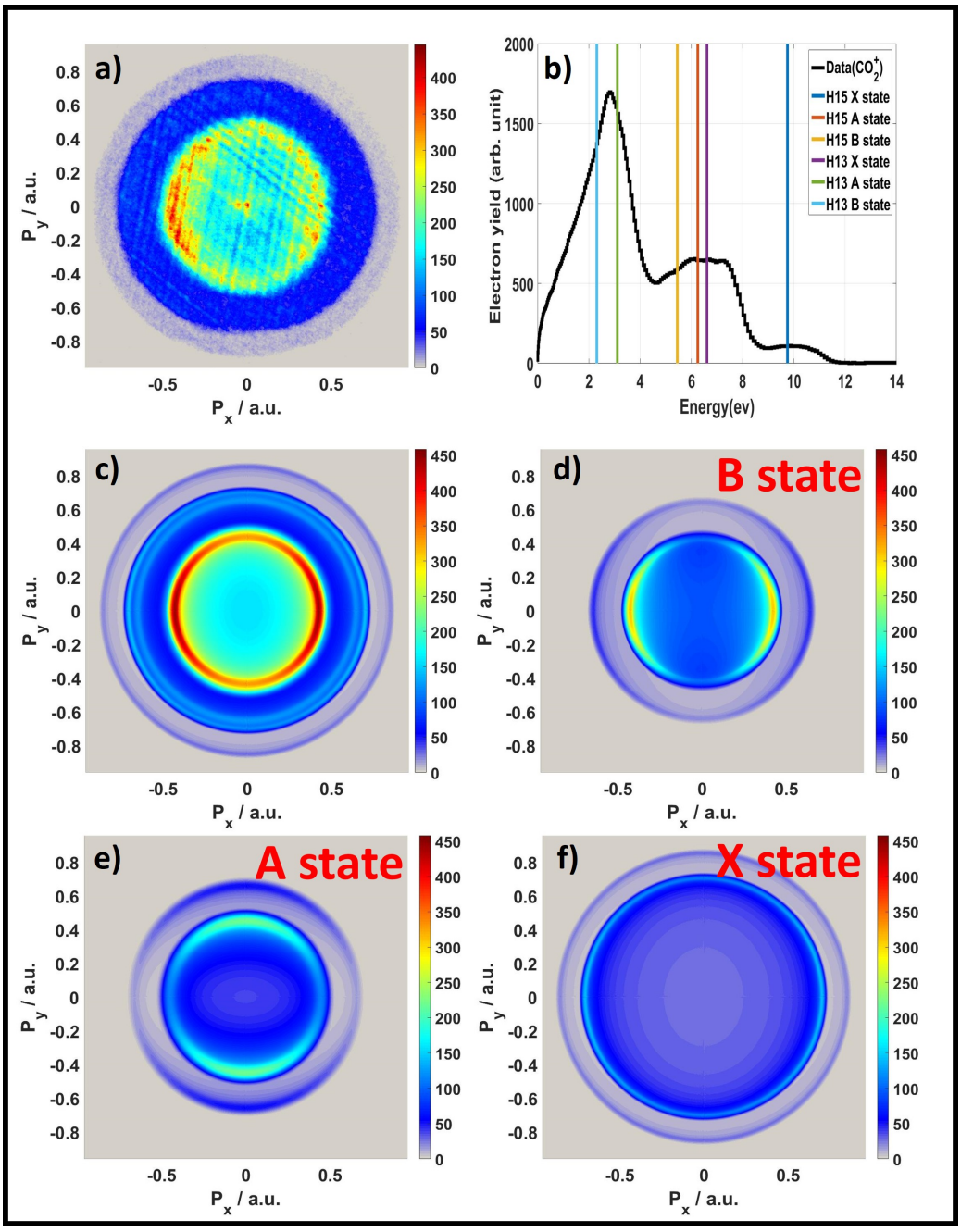

Figure 5.9: *a), b) Experimentally recorded photoelectron image and energy spectrum in coincidence with CO_2^+. c) Simulated photoelectron image for CO_2^+ (summed over all contributing states). d), e) and f): simulated individual photoelectron images for the B state, A state and X state of CO_2^+, respectively.*

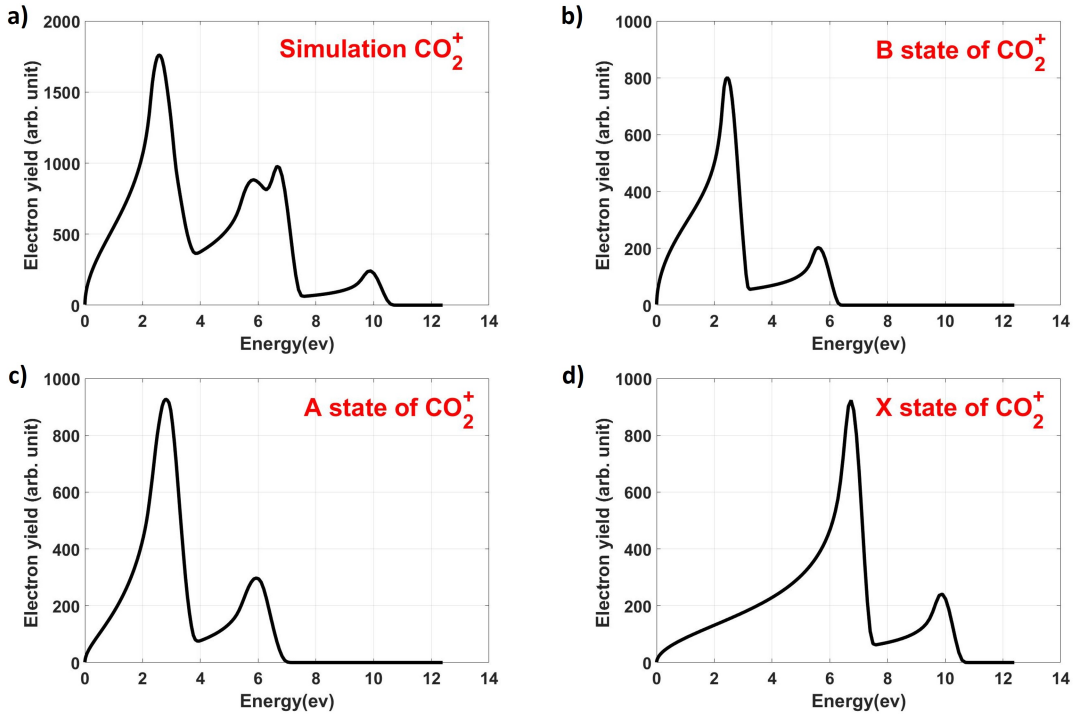

Figure 5.10: *a) Simulated photoelectron energy spectrum for CO_2^+ summed over all contributing states. b), c) and d): simulated individual photoelectron energy spectra for the B state, A state and X state of CO_2^+, respectively.*

5.3 Probing the dynamics of CO_2^+ cationic states in an XUV-pump NIR-probe experiment

This section describes the results of a pump-probe experiment, where the dynamics of CO_2^+ cationic states prepared by the XUV photoionization of a neutral CO_2 molecule are mapped by dissociating the ion with a NIR pulse arriving at varying time delays. The NIR beam is linearly polarized in the direction parallel to the XUV polarization. As in the previous section, the Sn filter is used to select only harmonics 13 and 15 (H13 and H15) from the harmonic train, and the phase-matching conditions are set such that the H13 contribution is considerably stronger than H15. The NIR intensity is set to $7 * 10^{12} W/cm^2$, such that no dissociative ionization signal (i.e., no O^+ or CO^+ ions) can be observed with the NIR pulse alone. Although this does result in multiphoton ionization producing CO_2^+ ions, the count

rate of the ionization signal due to NIR pulses is at least an order of magnitude lower than for the XUV pulse, indicating that ionization can happen only at the peak NIR intensity reached in a small central region of the focal volume.

We mainly monitor the dynamics by tracing the delay-dependent yields of the ionic dissociation products, CO^+ and O^+, and analyzing the emission pattern of the photoelectrons detected in coincidence with these ions. The basic underlying assumption for this analysis is that all the pathways we focus on here result from the electron emission induced by the absorption of the XUV photon, and that the NIR probe pulse does not significantly disturb the energy of the emitted electron and its measured emission angle with respect to the light polarization direction. While not strictly true, this appears to be a reasonable assumption at the chosen moderate NIR intensity. The ponderomotive potential of such a NIR field is ~ 0.42 eV, such that ponderomotive effects can at most broaden the electron energy distribution by this value. The absorption of an additional NIR photon can result in photoelectron sidebands, as discussed in section 4.2. However, since the channels we consider here require the absorption of at least one NIR photon to couple different ionic states, the simultaneous sideband appearance would mean at least a second-order process, which, at the chosen intensity, can provide only a minor contribution compared to the main two-color channels. Correspondingly, we use specific regions in the energy and angular distributions of the photoelectrons detected in coincidence with the specific ions to link these events to the population of a specific cationic state by the XUV pulse and to plot the dependence of the corresponding channels as a function of XUV-NIR delay.

5.3.1 CO_2^+ results

Although the main specific objective of this pump-probe experiment is to trace the evolution of the cationic states by observing the products of dissociation, we start with the measured parent ion signal, which we use as a reference. Fig. 5.11 depicts the measured yield of CO_2^+ ions as a function of XUV-NIR delay. The yield curve is nearly flat (on a level of

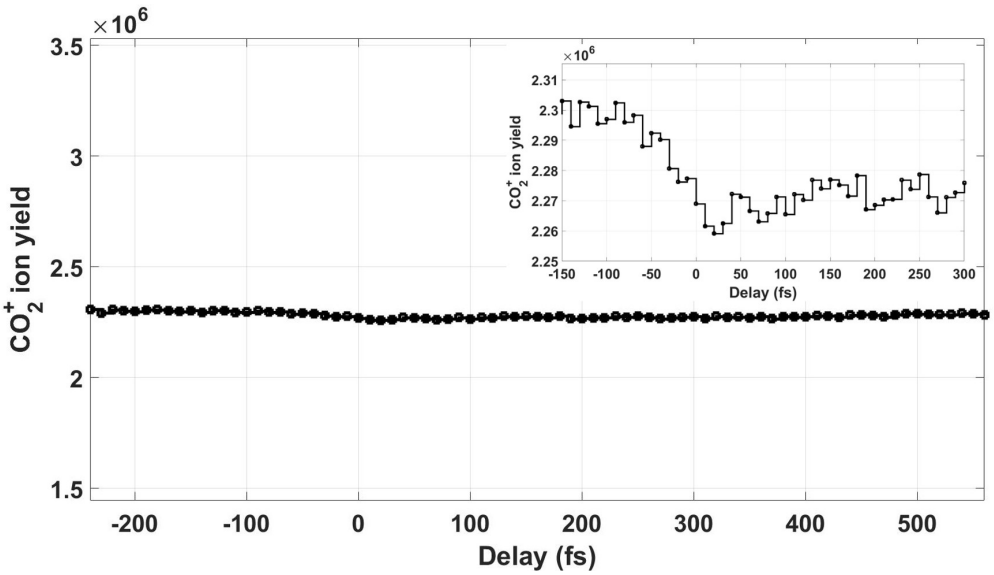

Figure 5.11: *The CO_2^+ ion yield as function of XUV-NIR delay. Inset shows the region of small delays strongly zoomed-in along the vertical axis.*

$<$ 2 percent). However, from the inset, which shows the region of small delays strongly zoomed-in along the vertical axis, there is a small but noticeable reduction of CO_2^+ signal at small positive delays, which partially recovers at larger delay values. This reduction is due to the depletion of the cationic target resulting from the dissociation of the CO_2^+ ions by the NIR probe pulse, which will be discussed in detail below.

The VMI image of all photoelectrons detected in coincidence with the CO_2^+ ions is plotted in Fig. 5.12. The data shown in this figure are integrated over the whole delay range of Fig. 5.11. The most obvious difference compared to a similar image obtained without the NIR probe pulse (Fig. 5.9a) is the appearance of the ATI features in the middle part of the image, which is more pronounced along the polarization direction. These structures result from CO_2 ionization by the NIR pulse. In order to explore the delay dependence of the processes leading to CO_2^+ ion formation, we analyze different regions of this pattern by plotting the portions of the corresponding photoelectron spectra as a function of XUV-NIR delay in Fig. 5.13 (electron energies from 2.1 to 4 eV) and Fig. 5.14 (4 -7.4 eV). In the left panels of both figures, (a) corresponds to the electrons detected within $\pm 30^o$ angle with

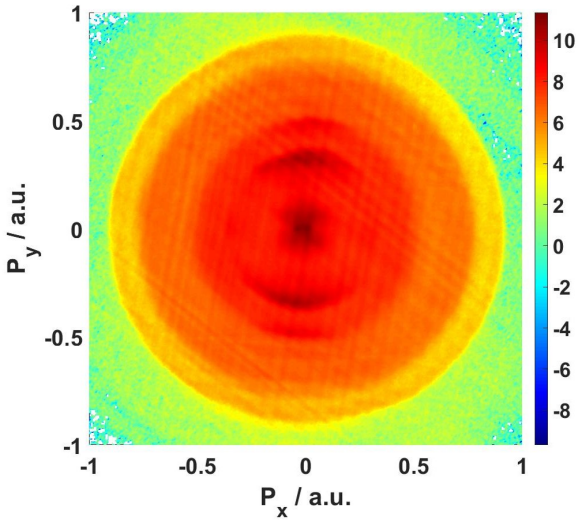

Figure 5.12: *The CO_2^+ photoelectron image integrated over all delays plotted in log scale*

respect to the polarization direction (vertical in all photoelectron images in this chapter), and (b) the electrons within $\pm 30^o$ angle with respect to the direction perpendicular to polarization and parallel to the light propagation direction (horizontal in all photoelectron images here). Throughout the rest of this chapter, these two angular regions will be referred to as "parallel" and "perpendicular" to the polarization direction, respectively. The right columns in both Fig. 5.13 and 5.14 show the delay-dependent yield of all electrons included in shaded rectangular areas marked on the left. In both rows of Fig. 5.13, the photoelectron spectrum shows a small but noticeable decrease of the signal between 2 and 4 eV at small delays, which is more pronounced and shifted to somewhat later times for the perpendicular emission direction. As can be seen by comparison with Fig. 5.10, this is the energy range where the XUV pulse populates A and B states of the CO_2^+ cation, and the reduction of the signal at positive delays in Fig. 5.13 reflects the NIR depletion of these states. In contrast, in Fig. 5.14a (electrons emitted parallel to the light polarization), a clear maximum in the photoelectron yield at zero delay can be observed in the lower part of the energy range shown in this figure (4.2 – 5.4 eV), whereas no clear effect can be observed for the electrons emitted in the perpendicular direction (Fig. 5.14b). This feature reflects the sideband effect, with the

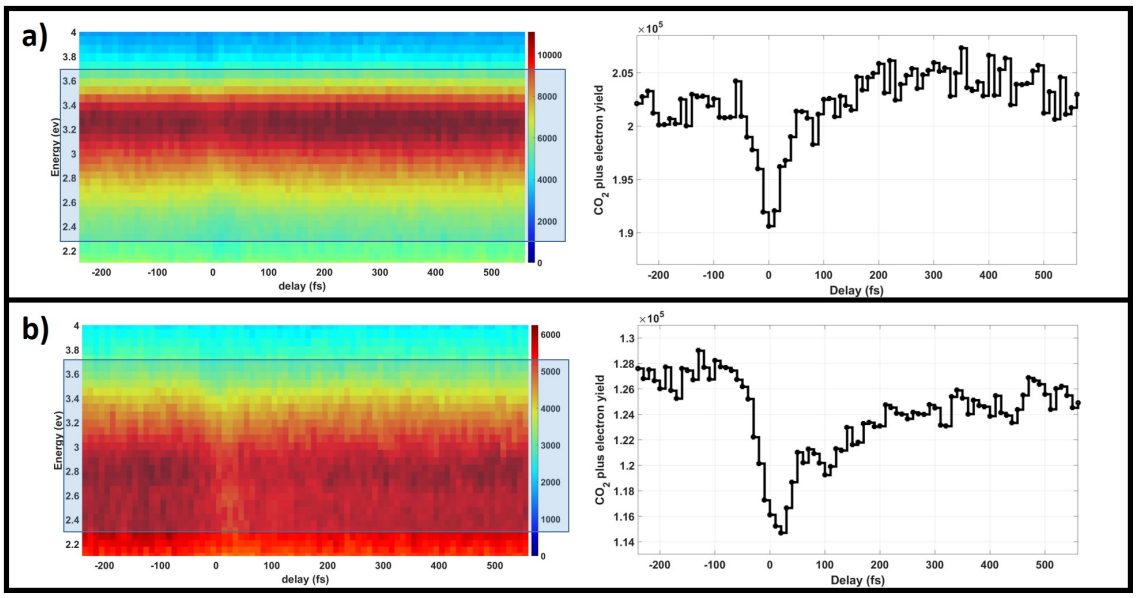

Figure 5.13: *Left: photoelectron energy spectrum vs delay for electrons emitted in a (a) parallel and (b) perpendicular direction with respect to the XUV and NIR polarization. Right panels are the 1D projections of the electron yield vs delay in the energy range of 2.3eV to 3.7eV (marked as rectangular shaded areas on the left).*

peak in Fig. 5.14a arising mainly from sideband 14 of the electrons corresponding to the A state of CO_2^+ (with the main line from H13 centered at 3.3 eV), with some contribution from sideband 12 from the X state electrons. The width of the XUV-NIR cross-correlation signal obtained from the sideband peak in Fig. 5.14 is 51 ± 5 fs. This is somewhat larger than the values obtained for sidebands in Sections 4.2-4.4, most likely because of the phase-matching conditions used to optimize H13 content.

The enhancement at certain photoelectron energies due to sidebands should be accompanied by a corresponding reduction of the main XUV line. Although we do observe a decrease of a signal between 2 and 4 eV (see Fig. 5.13), which, for the direction parallel to polarization, can be partly caused by sidebands, the primary source of this depletion cannot be a sideband effect. First, sidebands do not change the overall ionization yield, which can be observed in Fig. 5.11. Second, an even stronger reduction of the signal in Fig. 5.13 is observed for the perpendicular direction, where sidebands do not play a role.

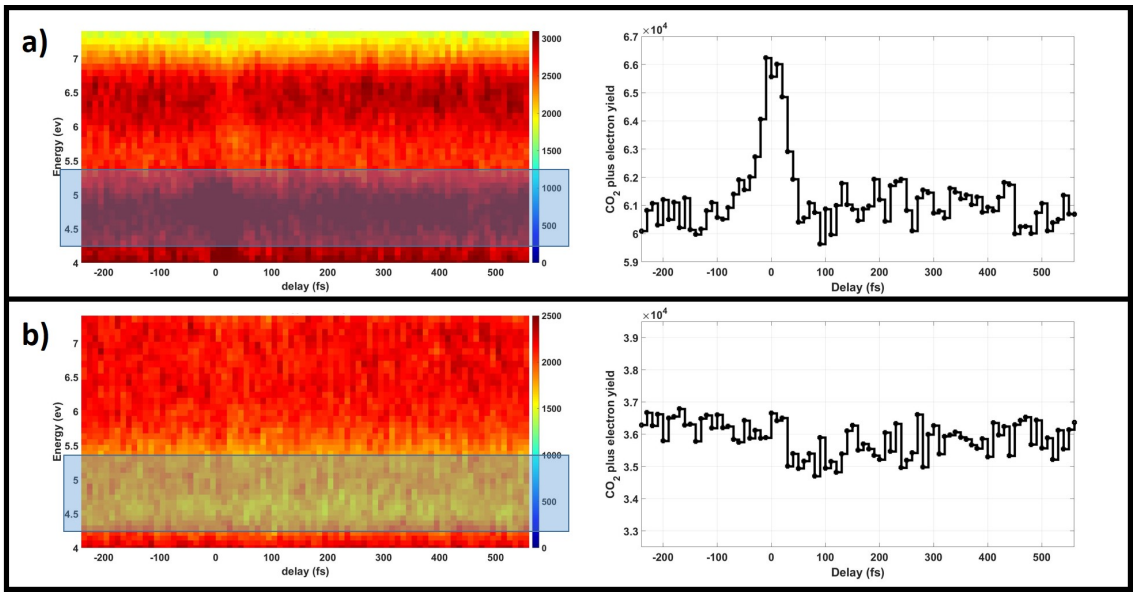

Figure 5.14: *Left: photoelectron energy spectrum vs. delay for electrons emitted in (a) parallel and (b) perpendicular direction. Right panels are the 1D projections of the electron yield vs delay in energy range of 4.2eV to 5.4eV (marked as rectangular shaded areas on the left).*

5.3.2 CO^+ results

In this section, we focus on the pump-probe effects resulting in CO^+ ion production. We start the analysis of this channel by considering the CO^+ yield measured as a function of XUV – NIR delay shown in Fig. 5.15a. Three distinct delay-dependent features can be observed in this graph: 1) a sharp increase of the measured CO^+ signal around zero delay; 2) a slower decrease of the signal at larger positive delays (throughout the scanned delay range up to 520 fs; (3) a pronounced oscillation of the CO^+ ion yield on top of the decaying curve. In order to visualize the latter feature, in Fig. 5.15b, the delay-dependent CO^+ yield is shown after filtering out a non-oscillating decay component. A clear oscillation with a period of 117 ± 10 fs can be observed.

Despite a noticeably different XUV spectrum used in this work, the results shown in Fig. 5.15 are very similar to the time evolution of the CO^+ ion signal observed in the earlier work of Timmers et al. [52]. There, the sharp rise of the CO^+ yield was attributed

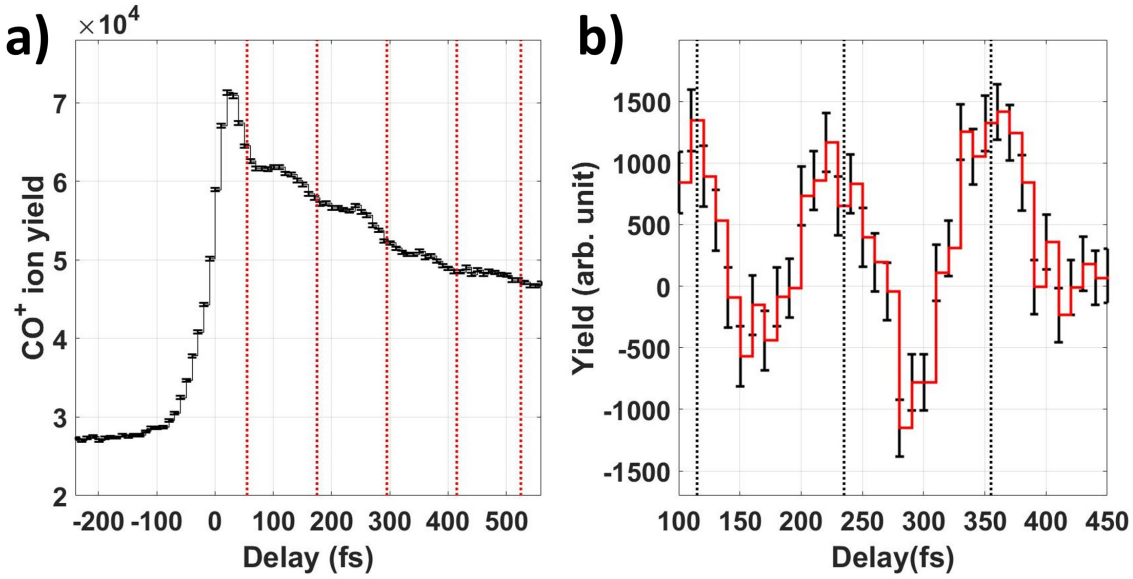

Figure 5.15: *a) CO^+ ion yield as function of XUV-NIR delay. b) Oscillatory part of CO^+ signal extracted by filtering out the non-oscillating decay component.*

to the contribution from the B-state of the CO^+ cation, which was populated by the XUV ionization of the neutral molecule and dissociated by the subsequent NIR pulse. As discussed in Section 5.1, the B and A states of CO_2^+ form a conical intersection relatively close to the equilibrium distance of neutral CO_2. The B state population is periodically transferred to the A state, driven by strong vibronic coupling between these two states. Since the B state can be more efficiently coupled to the higher vibrational states of the predissociative CO_2^+ C state, which results in CO^+ ion formation, the corresponding signal exhibits a periodic oscillation with the minima corresponding to the population transferred to the A state. Finally, a decrease of the CO^+ ion yield, observed in Fig. 5.15 as well as in Ref. [52], was explained as a signature of rotational dynamics of the cation. Since the ground state of the CO_2 molecule is $X^1\Sigma_g^+$, the ionization of its HOMO-2 or HOMO-3 orbitals leading to the formation of the cationic $B^2\Sigma_u^+$ or $C^2\Sigma_g^+$ states (see Fig. 5.1)is more likely for the molecules aligned parallel to the XUV polarization, thus inducing the so-called "geometric alignment" of the cationic molecular ensemble. The coupling between the cationic B and C states with one NIR photon also strongly favors the molecules aligned parallel to the NIR polarization

(here the same as the XUV). Right after the XUV pulse, the NIR probe interacts with the aligned ensemble of molecular ions, and the probability of coupling the ions in the B state to the predissociative C state is large. However, since the molecular ensemble is prepared in a broad range of rotational levels, after the initial "geometric" alignment by the ionizing XUV pulse, the molecules will incoherently rotate out of alignment, leading to a decrease of the signal in Fig. 5.15.

Although the delay-dependent CO^+ yield presented here, as well as the same observable measured in Ref. [52], is consistent with the picture of rotational dynamics discussed above (which was also quantitatively simulated in [52]), the decrease of a signal alone, even combined with the observed oscillation, cannot be treated as unique evidence of the initial population of the cationic B-state. For example, the ionization from the HOMO-1 orbital of neutral CO_2, associated with the transition to the $A^2\Pi_u$ state of CO_2^+, favors the molecules aligned perpendicular to the XUV polarization. This orientation then matches well with the symmetry of the NIR-induced transition between the $A^2\Pi_u$ and $C^2\Sigma_g^+$ states of CO_2^+, which is also a perpendicular transition. This scenario would also cause the initial rise of the CO^+ signal and its subsequent decrease because of the loss of alignment with time.

In order to explore in more detail which states contribute to the time evolution of the CO^+ ion signal observed in Fig. 5.15, we analyze the emission patterns of the photoelectrons detected in coincidence with these ions. In Fig. 5.16, the VMI images of the photoelectrons coincident with CO^+ ions are presented for three different XUV-NIR delays marked on the ion yield curve. In panel (a), the NIR pulse precedes the XUV (negative delays); (b) corresponds to the maximum of the CO^+ signal, where the two pulses still overlap (0-100 fs); and in (c) the NIR pulse arrives $\sim$ 500 fs after the XUV. Since the NIR pulse alone does not cause any dissociative ionization, the CO^+ ions observed at negative delays originate from the direct population of the predissociative C state of CO_2^+ by the XUV pulse. Correspondingly, the photoelectron emission pattern in Fig. 5.16a closely resembles the image obtained with XUV-only (5.6c), with most of the electrons emitted along the

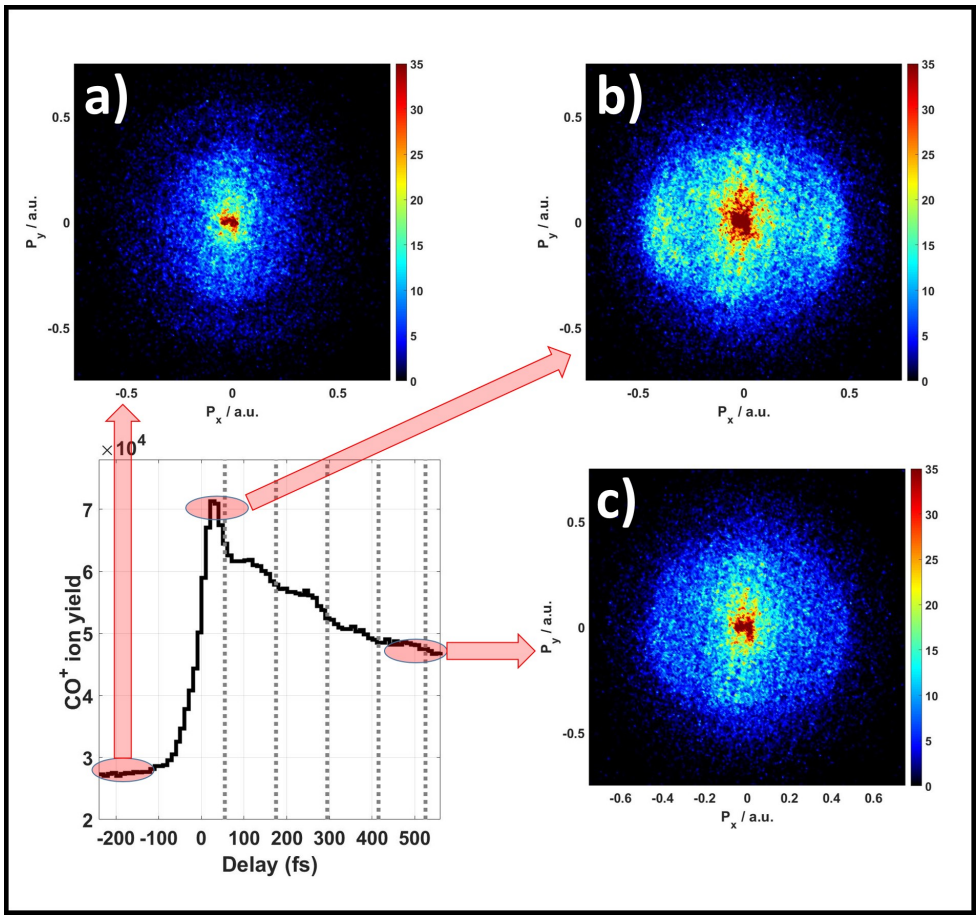

Figure 5.16: *Photoelectron images in coincidence with* CO^+ *for three different delay steps*

polarization direction. In contrast, in Fig. 5.16bc, a clear photoelectron contribution in the perpendicular direction (along the x-axis) appears in the images, resembling the simulation for the electrons resulting from the B state (see Fig. 5.9d). In Fig. 5.17 (a) and (b), the angular distributions extracted from the images in Fig. 5.16a (NIR before the XUV) and Fig. 5.16b (NIR right after XUV) are plotted as a function of the hit position on the detector and compared with the simulations for the C state photoelectrons (a) and the mixture of B and C states (b). The simulations reproduce the main features of the experimental data reasonably well, except for the intense spot in the center of the detector, corresponding to low-energy electrons. As was shown in Fig. 5.8, those primarily result from the events where a significant fraction of the excess photon energy is taken by the ion, whereas the simulation

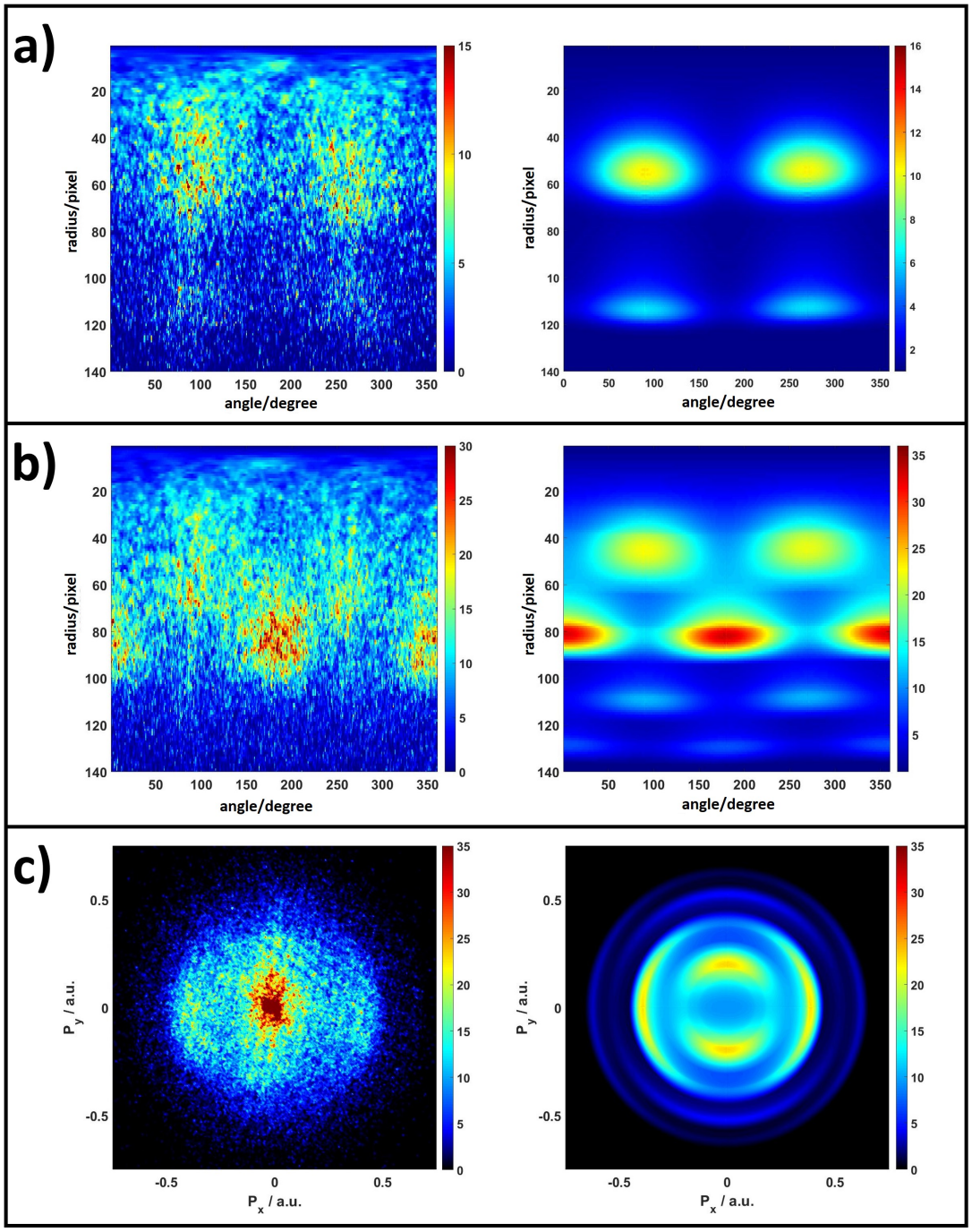

Figure 5.17: *a) Left panel: the measured angular distribution of photoelectrons for NIR arriving before XUV. Right panel: the simulated angular distribution of photoelectrons for the C state. b) Left panel: the measured angular distribution of photoelectrons for NIR arriving slightly after XUV. Right panel: the simulated angular distribution of photoelectrons from simulation combining the C state and 10 % contribution from the B state. All angular distributions are shown as a function of an electron hit position on the detector. c) Measured (left) and simulated (right) photoelectron images corresponding to the angular distributions in b).*

assumes that all the excess energy is given to the electron.

While the dominant contributions in the experimental images shown in Fig. 5.16-5.17 seem to match our expectations for the XUV-only population of the predissociative C state and the population of the B state with subsequent coupling to the C state by one NIR photon, based on these images, we cannot exclude potential contributions from the A state. Since the lowest vibrational level of the C state that can result in CO^+ production is at 19.47 eV with respect to the ground state of the neutral molecule, the lowest few vibrational levels of the A state (below 17.9 eV) cannot be dissociated into the $CO^+ + O$ channel with one NIR photon. Nevertheless, as can be seen from table A.1 in Appendix 1, a few higher-lying vibrational levels of the A state can also be populated, potentially contributing to the pump-probe enhancement observed in Fig. 5.15.

Fig. 5.18a displays the energy distributions of the photoelectrons detected in coincidence with CO^+ ions as a function of XUV-NIR delay. The enhanced signal at positive delays is dominated by a broad structure below 3 eV, with the low-energy part of this feature more visible at large delays (beyond 300 fs). Horizontal black lines mark the energy value of the electron emitted from the ground vibrational levels of the A and B state of CO_2^+ at the central energy of H13. However, as discussed above, the A state contribution to the CO^+ signal would be restricted to higher vibrational levels, which yields a practical energy threshold very close to the value expected for the electrons from the ground vibrational level of the C state ($\sim$2.5 eV, lower line in Fig. 5.18a). The angular distributions of the electrons corresponding to the A, B, and C cationic states are rather different (see Fig. 5.5). In order to disentangle the contributions from different states to the total pump-probe signal we plot the same electron energy distribution, in panels (b) and (c) of Fig. 5.18, as in panel (a), but for the electrons emitted perpendicular (b) or parallel (c) to the polarization direction of both pulses. As defined in Section 5.3, "parallel" or "perpendicular" emission corresponds to the angular range of $\pm 30^o$ with respect to the corresponding direction. Comparing these graphs, one can see that while the oscillatory structure is dominated by the events corresponding to

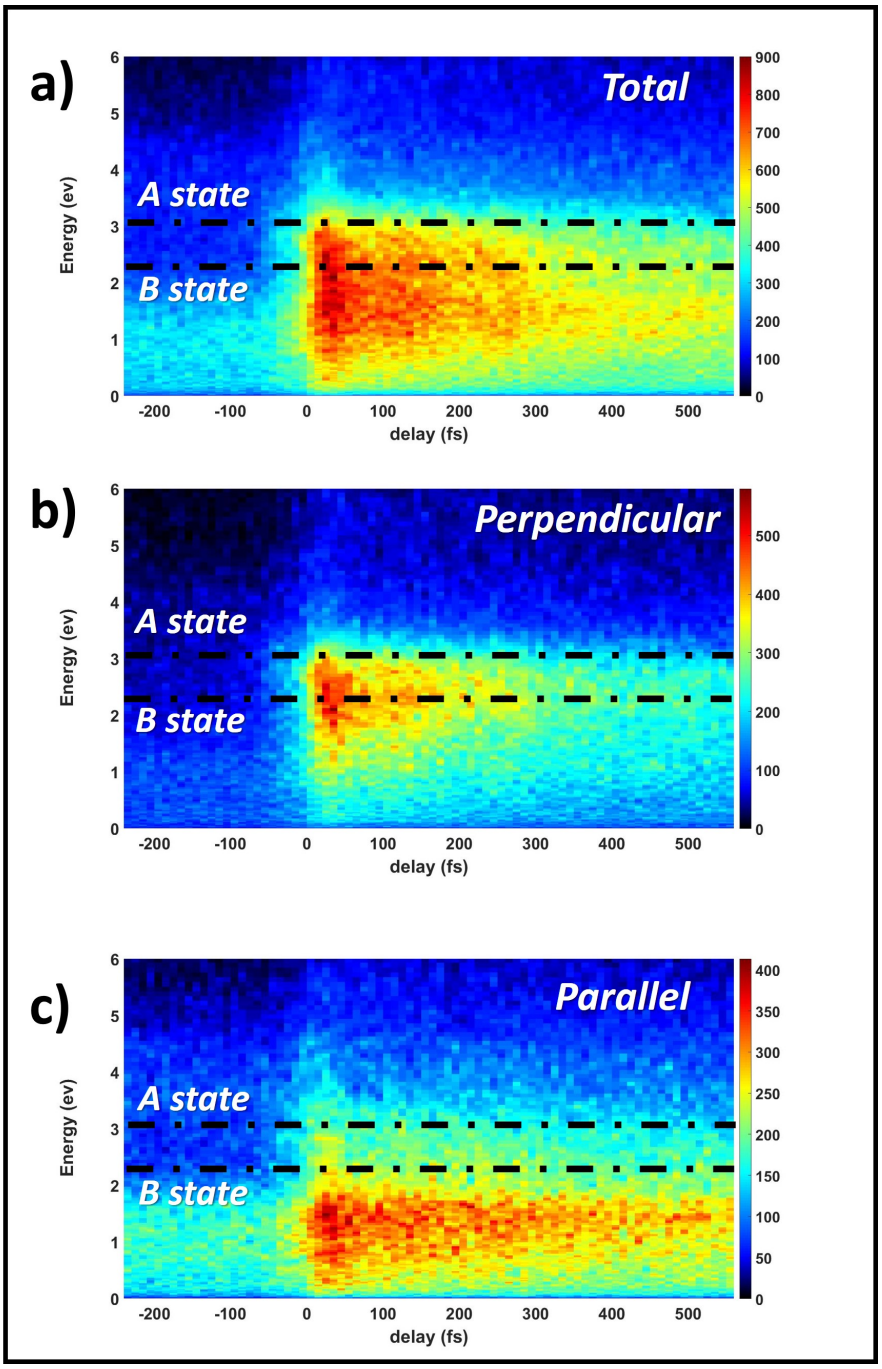

Figure 5.18: *CO^+ photoelectron energy vs delay: a) Integrated over all angles, b) perpendicular direction, c) parallel direction*

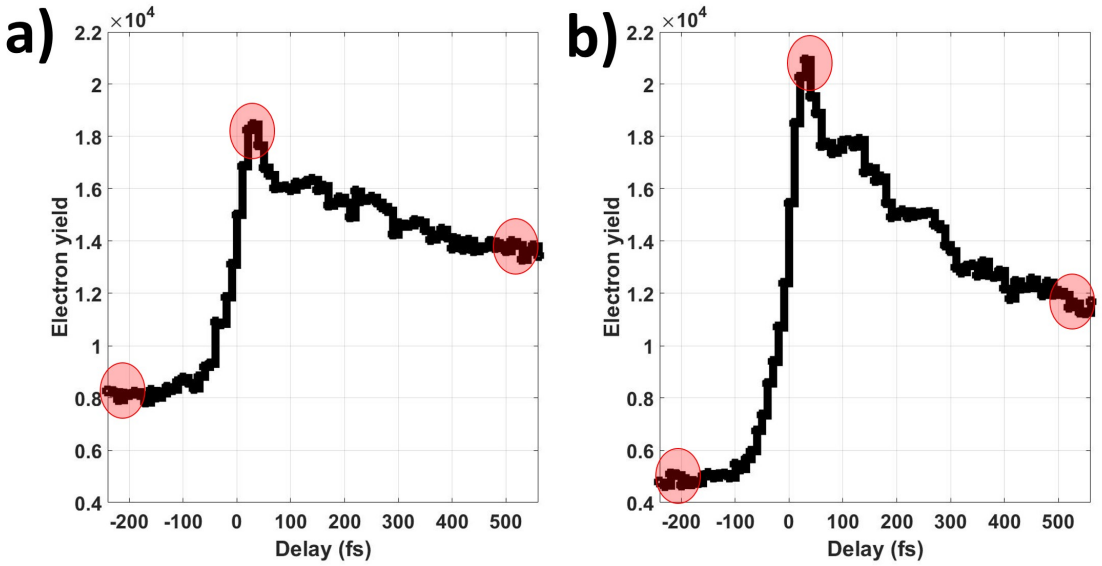

Figure 5.19: *CO^+ photoelectron yield vs. delay for energies below 2.7 eV: a) parallel direction, b) perpendicular direction. Shaded areas are NIR before, overlap, and NIR after regions used to produce the photoelectron spectra in the next figure.*

the electrons emitted in the perpendicular direction, with energies around 2.3 eV, the signal at lower energies is mostly due to events where the electrons are emitted parallel to the light polarization. In order to quantify it further, in Fig. 5.19, the yield of the electrons emitted in parallel (a) and perpendicular (b) directions with energies below 2.7 eV (close to the upper limit expected for B state electrons) is plotted as a function of the delay. While the signal for the parallel direction is stronger at negative delays, the situation reverses when the NIR pulse arrives just after the XUV. The signal for the perpendicular direction grows to a larger value at small positive delays but then exhibits a sharper decrease, becoming again smaller than the yield for the parallel direction after 400 fs. The signal for the perpendicular electron emission in Fig. 5.19b also manifests much cleaner oscillatory structure, which is hardy visible for the parallel direction (Fig. 5.19a).

The observed behavior can be rationalized considering the electron angular distributions expected for different cationic states (see Fig. 5.5, 5.6, and 5.9). At negative delays, where the NIR pulse arrives first, the CO^+ signal is dominated by the direct XUV photoionization

to the predissociative C state, for which the electrons are mostly emitted along the polarization direction. At positive delays, the XUV-populated B state starts to contribute to the signal by coupling to the C state with a single NIR photon. Since the B-state electrons are preferentially emitted in the perpendicular direction, the corresponding signal dominates the total yield at small positive delays and results in a pronounced oscillation due to the vibronic coupling population transfer to the A state discussed above. However, since this channel requires the molecular ions to be aligned with the NIR polarization, the corresponding contribution to the signal decays rather fast due to largely decoherent rotational motion. As can be seen from Fig. 5.5, the B state also has a non-negligible fraction of electrons emitted in the direction parallel to the polarization. These events contribute to the corresponding CO^+ ion yield plotted in Fig. 5.19a, and are likely responsible for the remaining oscillatory signal observed in that graph. However, from the delay-dependent electron energy distribution graph presented in Fig. 5.18c, it is clear that the signal for the parallel direction is dominated by electrons with energies between 1 and 1.5 eV, significantly smaller than what is expected for the B state. This band is also responsible for the slower decay of the CO^+ signal for the parallel direction observed in Fig. 5.19a.

In order to further inspect formation mechanisms of the delay-dependent CO^+ signal, in Fig. 5.20, the electron energy distributions for three different delay regions marked in Fig. 5.19 are plotted for parallel (a) and perpendicular (b) emission directions. Panels (c) and (d) of Fig. 5.20 show the difference between the signal measured when both pulses nearly overlap (blue curves in (a,b), corresponding to the maximum of the signal in Fig. 5.19), and when the NIR pulse precedes the XUV (red curves in (a,b), negative delays in Fig. 5.19), plotted for parallel and perpendicular electron emission, respectively. As expected, in the perpendicular direction, the signal is dominated by the contribution from the B state. The electron energy distribution simulated to match the actual experimental conditions assuming the population of the ground vibrational level of the B state is shown in Fig. 5.20e and 5.20f for parallel and perpendicular directions, respectively. The simulation for the perpendicular

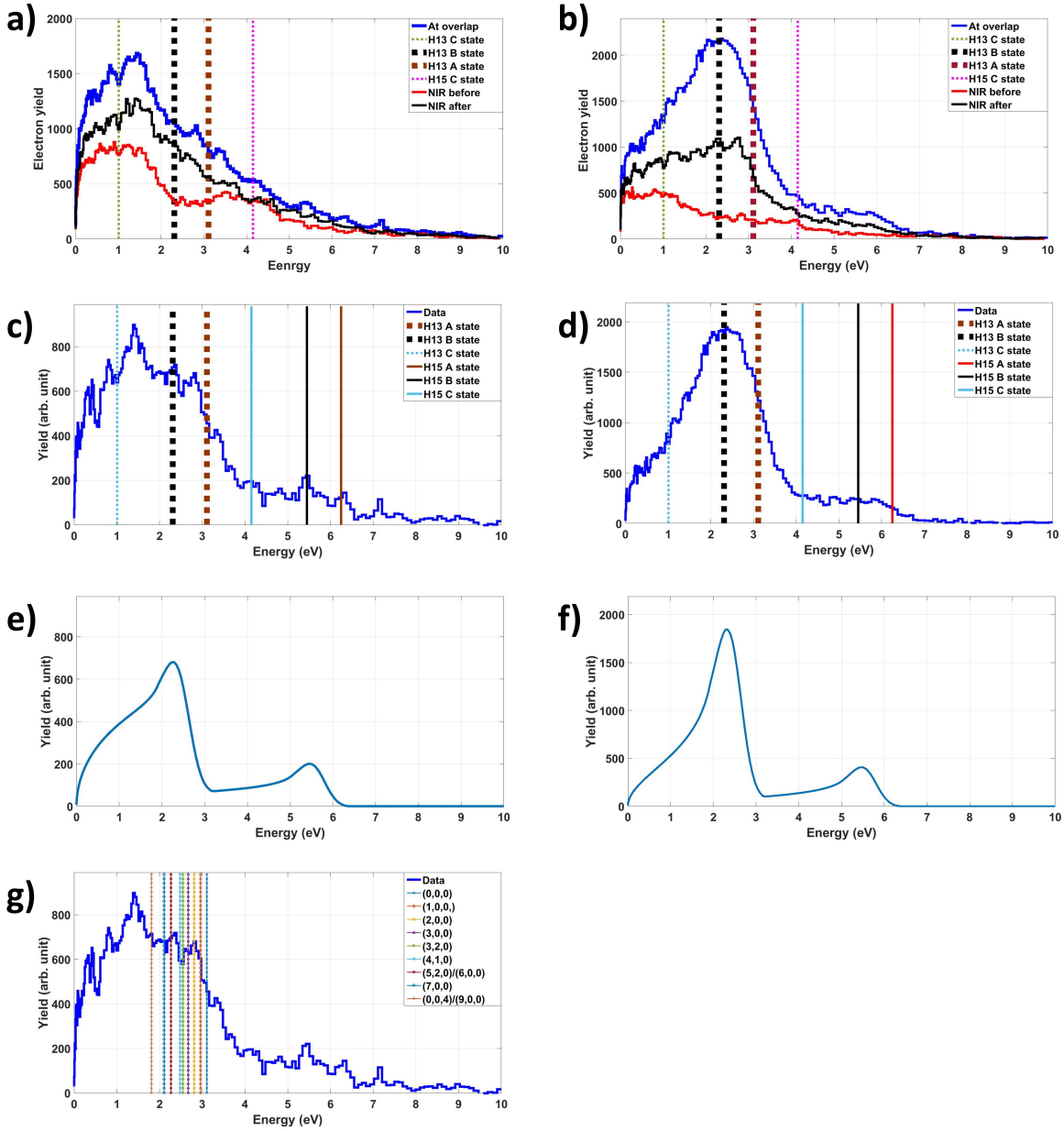

Figure 5.20: *The photoelectron energy spectra in coincidence with CO^+ for parallel (left panels) and perpendicular (right panels) directions. Panels a) and b) show the energy spectra at three delays marked in Fig. 5.19a. Panels c) and d) show the difference between the spectra obtained in the overlap region and for the NIR arriving before the XUV. Panels e) and f) show the simulated spectra for the B state in the parallel (e) and perpendicular (f) direction. Panel g) is the same as c), but with the expected contributions from the individual vibrational levels of the A state marked as vertical lines.*

direction matches the experimental distributions well, with some contributions at the high-energy shoulder likely coming from the A state.

However, for the parallel direction, the contribution of the B state cannot explain the observed energy spectra, where the enhancement peaks at ∼1.4 eV electron energy (Fig. 5.20a,c). It is also outside of the range of energies expected for the A state contributions, which are explicitly shown in Fig. 5.20g for individual vibrational levels(dashed lines). Even taking into account that the spectra shown in Fig. 5.20 are reconstructed from the non-inverted VMI images, such that the low-energy regions always contain "tails" from the higher-energy features (see, e.g., Fig. 5.20e,f), the contributions from A and B cationic states cannot explain the pronounced peak centered at 1.4 eV. This peak is slightly above the energies expected from the C-state electrons, which, for the lowest vibrational level contributing to CO^+ production, lies at ∼1eV (assuming the central photon energy of the H13 used). The C state is expected to fully dissociate after the XUV pulse, irrespective of whether the NIR pulse will arrive later or not, and, thus, is not supposed to contribute to the two-color pump-probe signal. However, as can be seen from table 5.1, the lowest vibrational levels of the C state as well as autoionizing Rydberg states just below it are expected to dissociate towards the $O^+ + CO$ limit, thus not creating any CO^+ ions. The redistribution of the population from these states to the higher vibrational levels of the C state can explain the peak at 1.4 eV, which energetically corresponds to the range between the lowest vibrational states resulting in CO^+ formation down to the lowest dissociation threshold. Such redistribution can likely result from an off-resonance two-photon stimulated Raman scattering driven by the NIR pulse (see e.g., [115,116,82] and references therein). If this is the reason for the observed structure, it should be accompanied by the corresponding reduction of O^+ yields for the same electron energy. Our observations for O^+ ions, which will be presented in the next section, to a large extent support this scenario.

We also employ our coincident electron spectra to examine in more detail the origin of the oscillatory structure, which can be clearly seen in Fig. 5.15, 5.18 and 5.19. In Fig.

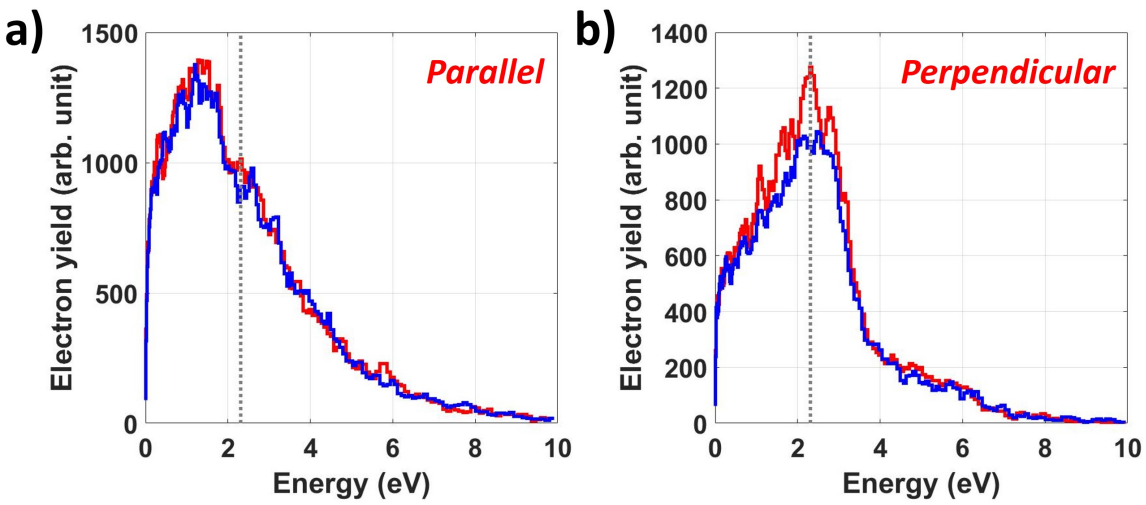

Figure 5.21: *Photoelectron energy spectra for the delay regions where the oscillatory CO^+ ion yield curve reaches its maxima (red) and minima (blue).*

5.21, the photoelectron spectrum for parallel (a) and perpendicular (b) emission direction is plotted at the delays corresponding to the maxima (red) and minima (blue) of the oscillation highlighted in Fig. 5.15. At the maxima of this structure, where the hole density is expected to be mostly of the σ_g character (i.e., the population mostly in the B state), the spectrum in Fig. 5.21b exhibits an apparent enhancement exactly at the energies corresponding to the ionization to the lowest vibrational level of the B state. The effect is much less pronounced in the parallel direction (Fig. 5.21a), reflecting the characteristic angular pattern for the B-state electrons. This peak is suppressed in the minima of the oscillation, where the hole density is expected to be mostly of the π_u character, corresponding to the population transfer to the A state.

While the data presented so far cover a rather small delay range (up to 600 fs), we have also performed a similar experiment over a much longer delay range, focusing on ion detection. The CO^+ yield obtained covering a 0 to 9 ps range is shown as a function of XUV-NIR delay in Fig. 5.22. While the signal exhibits a sharp rise and then considerable drop, similar to the short scans discussed above, it also exhibits a pronounced periodic oscillation with a $\sim$ 3.3 ps period. Although the picosecond time scale implies a possibility

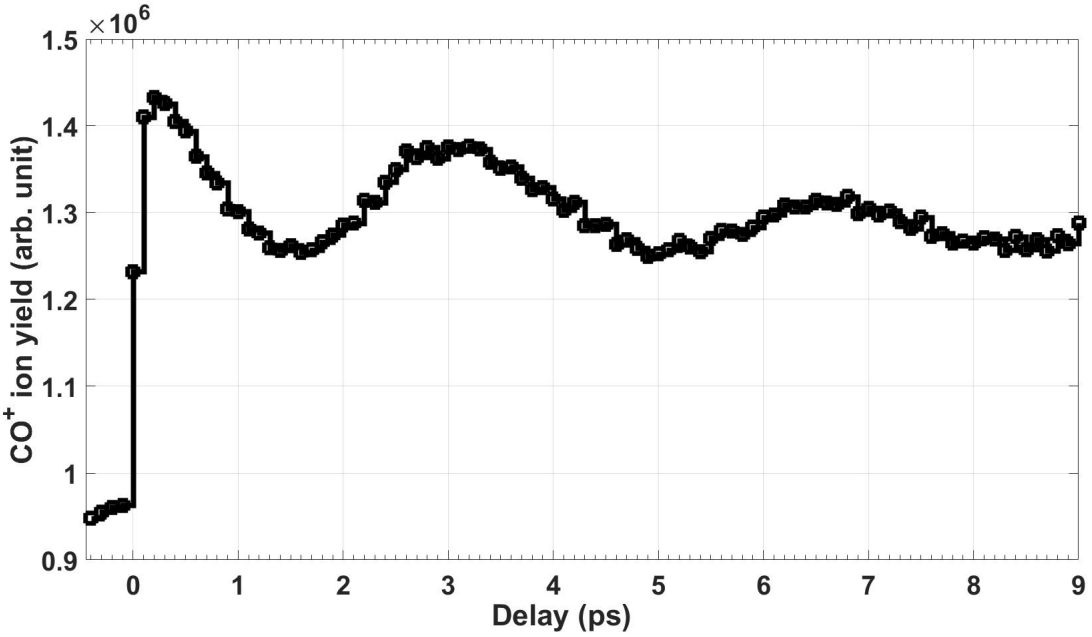

Figure 5.22: *CO^+ ion yield vs XUV-NIR delay for a long delay scan (up to 9ps).*

of some rotational dynamics behind this oscillatory behavior, at this moment we are not aware of any rotational constants, or any other spectroscopic data which can be directly associated with the observed oscillation.

5.3.3 O^+ results

While the $CO^+ + O$ dissociation channel considered in the previous section provides an efficient tool for probing the XUV-induced cationic dynamics, most of the dissociation events observed in the experiments described here result from the $O^+ + CO$ channel (see, e.g., Fig. 5.4). In this section, we focus on the pathways leading to O^+ ion production. As in previous sections, the analysis includes both delay-dependent O^+ ion yields and ion-electron coincident data.

The dissociative ionization thresholds for O^+ and CO^+ production are at 19.07 eV and 19.46eV. The ionization energy for the ground vibrational level of the CO_2^+ C-state is 19.39eV and, thus, lies below the threshold for CO^+ production. Therefore, as discussed in the

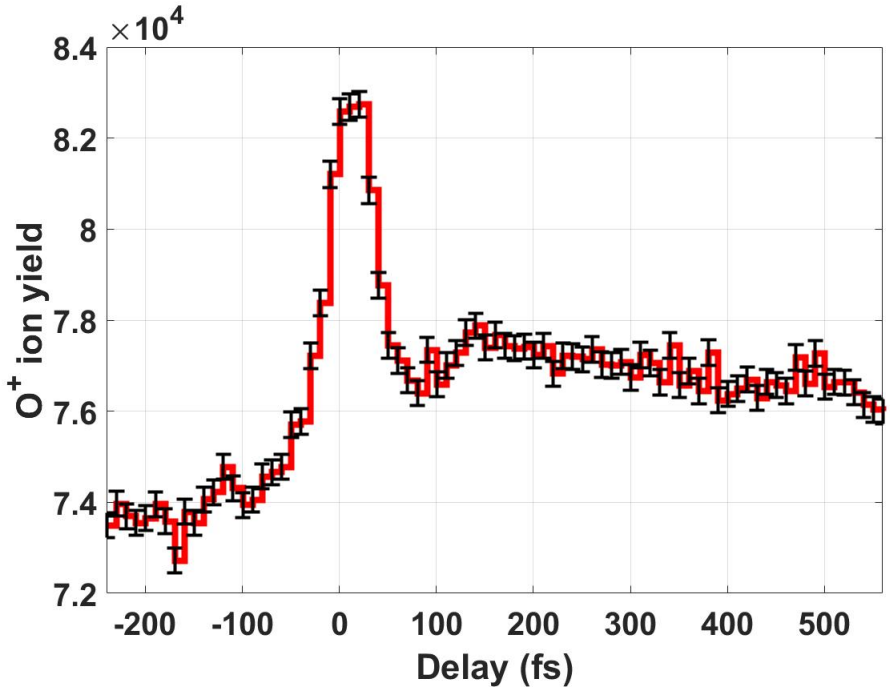

Figure 5.23: O^+ *ion yield as a function of XUV-NIR delay*

previous sections, the ground state vibrational state of the C state, as well as the autoionizing Rydberg states just below it (but above the lowest dissociation threshold), only dissociate into $O^+ + CO$. The next vibrational state (0,1,0) at 19.47 eV still mostly dissociates via the $O^+ + CO$ pathway, although ∼12 percent of the population ends up in the $CO^+ + O$ channel. For higher vibrational levels, the dissociation branching ratio strongly favors the $CO^+ + O$ channel, though a non-negligible amount of O^+ ions is still produced (see table 5.1).

The measured total O^+ ion yield is plotted in Fig. 5.23 as a function of XUV-NIR delay. The overall effect of the NIR probe pulse here is smaller than in CO^+ channel (compare with Fig. 5.15a). One apparent reason for this is that the cationic B state, which is responsible for the dominant fraction of the pump-probe enhancement observed in the CO^+ (see the previous section), cannot be coupled to the lowest vibrational level of the C state by the NIR field. The vertical ionization threshold for the B state is 18.07 eV. Since the transitions to the C state are non-ionizing, because of energy conservation, the absorption of a NIR

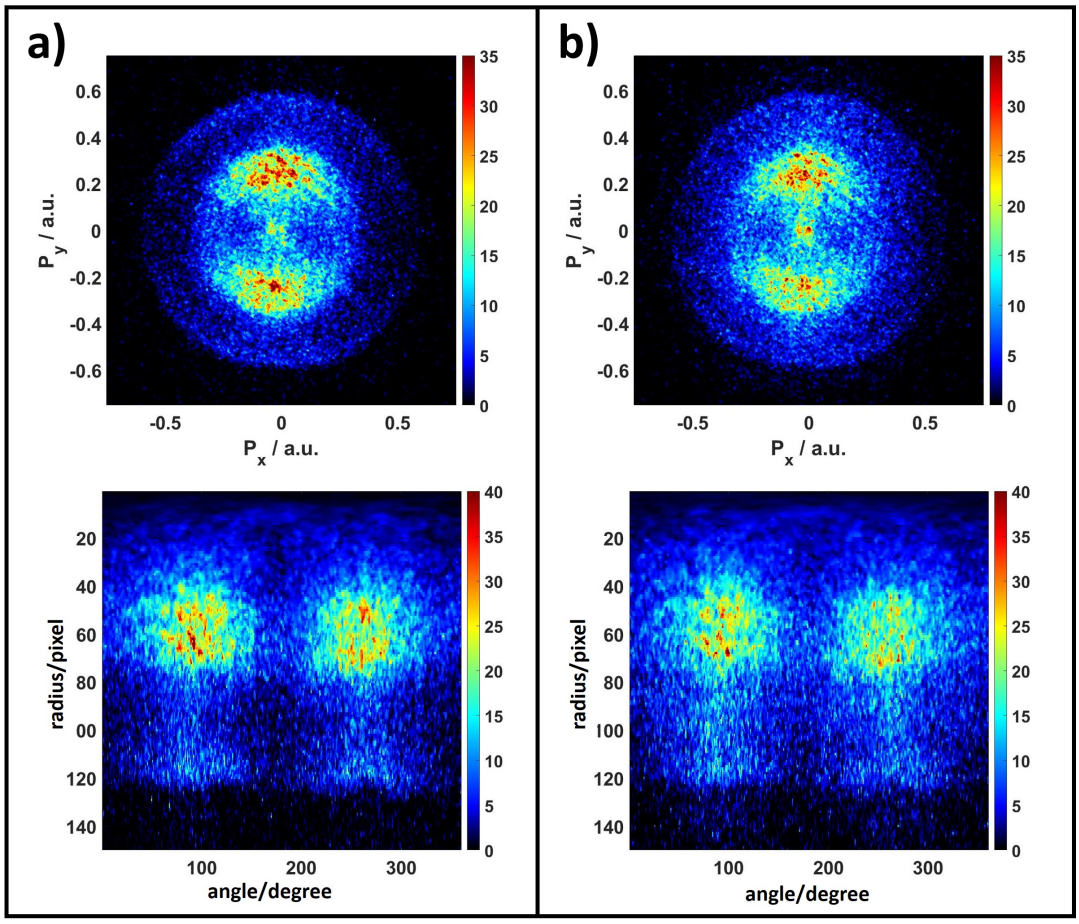

Figure 5.24: *O^+ photoelectron images (top) and extracted angular distributions (bottom) for the NIR pulse arriving (a) before the XUV and (b) in the overlap region.*

photon populates vibrational states above 19.5 eV, which mostly dissociate via the $CO^+ + O$ channel. Nevertheless, the O^+ signal in Fig. 5.23 exhibits a pronounced delay dependence, with a sharp rise in the overlap region, followed by a rapid decrease to a level 4-5 precent higher than at negative delays, where the NIR pulse arrives before the XUV. In order to understand the origin of this behavior, in the following, the observed ion signal is analyzed exploiting the coincident electron spectra.

In the upper row of Fig. 5.24, the VMI images for the electrons detected in coincidence with O^+ ions are plotted for negative delays (a) and for the XUV-NIR overlap region where the O^+ reaches its maximum (b). There are no obvious differences between the two images,

and both of them resemble the emission pattern obtained for the C-state photoelectron with only the XUV pulse (see Fig. 5.6a), with most of the electrons emitted parallel to the light polarization. A closer inspection of the photoelectron angular distributions extracted from these images, which are plotted in the bottom row of Fig. 5.24 as a function of the hit position on the detector, reveals some diffuse signal enhancement in the overlap region (right column) between 80 and 120 pixels (radius). In Fig. 5.25, the energy distribution of the photoelectrons detected in coincidence with O^+ fragments is plotted as a function of the delay for all coincident events (a), as well as for electrons emitted parallel (b) or perpendicular (c) to the light polarization direction (each selection covering the angular range of $\pm 30^o$). The most pronounced delay-dependent features observed in these spectra are (1) transient enhancement in the energy range of 2eV to 3.5eV in both parallel and perpendicular directions which appears as a tilted band; (2) a transient depletion in the parallel direction in the energy range of 0.8 eV to 1.8 eV; and (3) a weak transient enhancement between 5 and 7 eV, which appears mostly in the parallel direction. The latter structure can be assigned to sideband 16 of the electrons resulting from the C state of CO_2^+. One would expect a comparable signature of the corresponding sideband 14 to appear $\sim$ 3.1 eV lower in energy. However, the structure (1) observed between 2 and 3.5 eV cannot originate from the sideband effect (at least not entirely) because it appears with comparable strength in the perpendicular direction.

To assign the observed effects to the dynamics in particular cationic states, in Fig. 5.26 the electron energy distributions for three different delay regions are plotted for parallel (a) and perpendicular (b) emission directions. In each panel, a black curve corresponds to negative delays, where the NIR pulse precedes the XUV, a blue curve results from the overlap region, and the red one is obtained at large positive delays, where the NIR pulse arrives well after the XUV. Panels (c) and (d) of Fig. 5.26 show the difference between the signal measured when both pulses overlap and when the NIR pulse precedes the XUV, plotted for parallel and perpendicular electron emission, respectively. From these graphs, it becomes

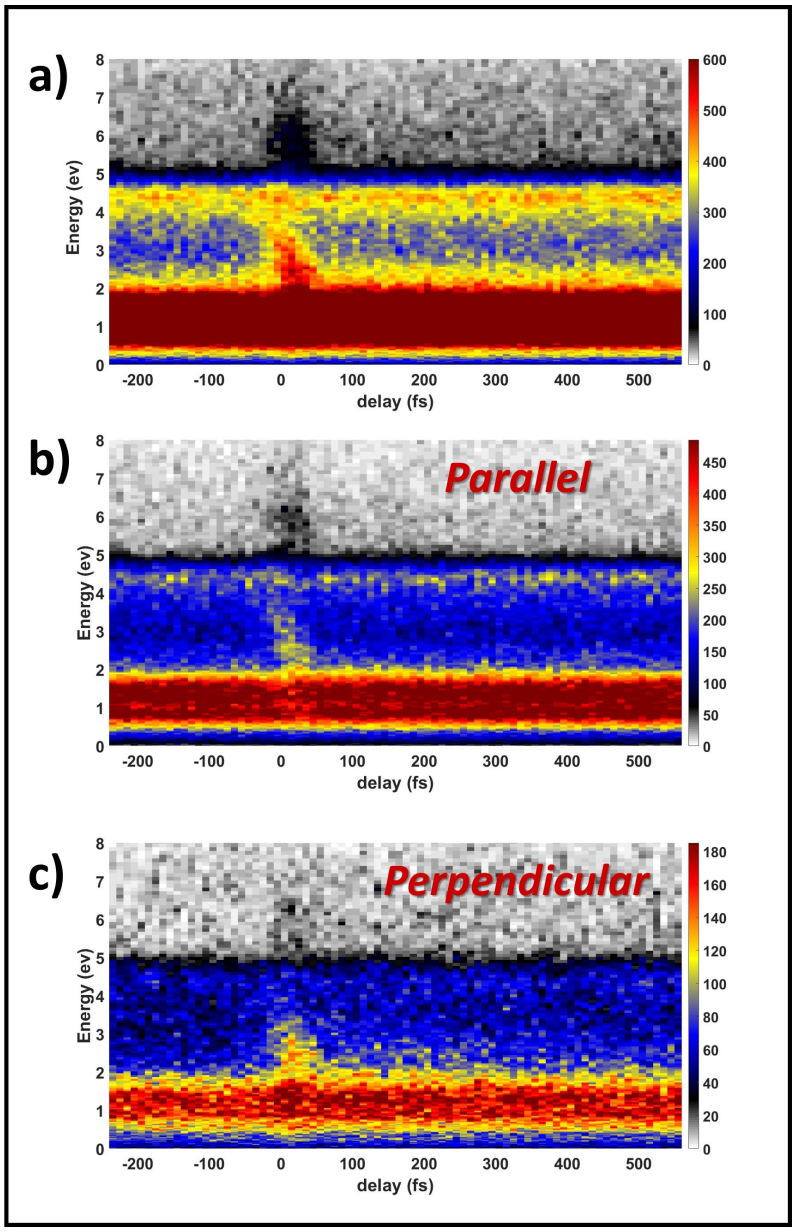

Figure 5.25: *O^+ photoelectron energy spectra vs delay: a) Integrated over all emission angles; b) parallel direction; c) perpendicular direction.*

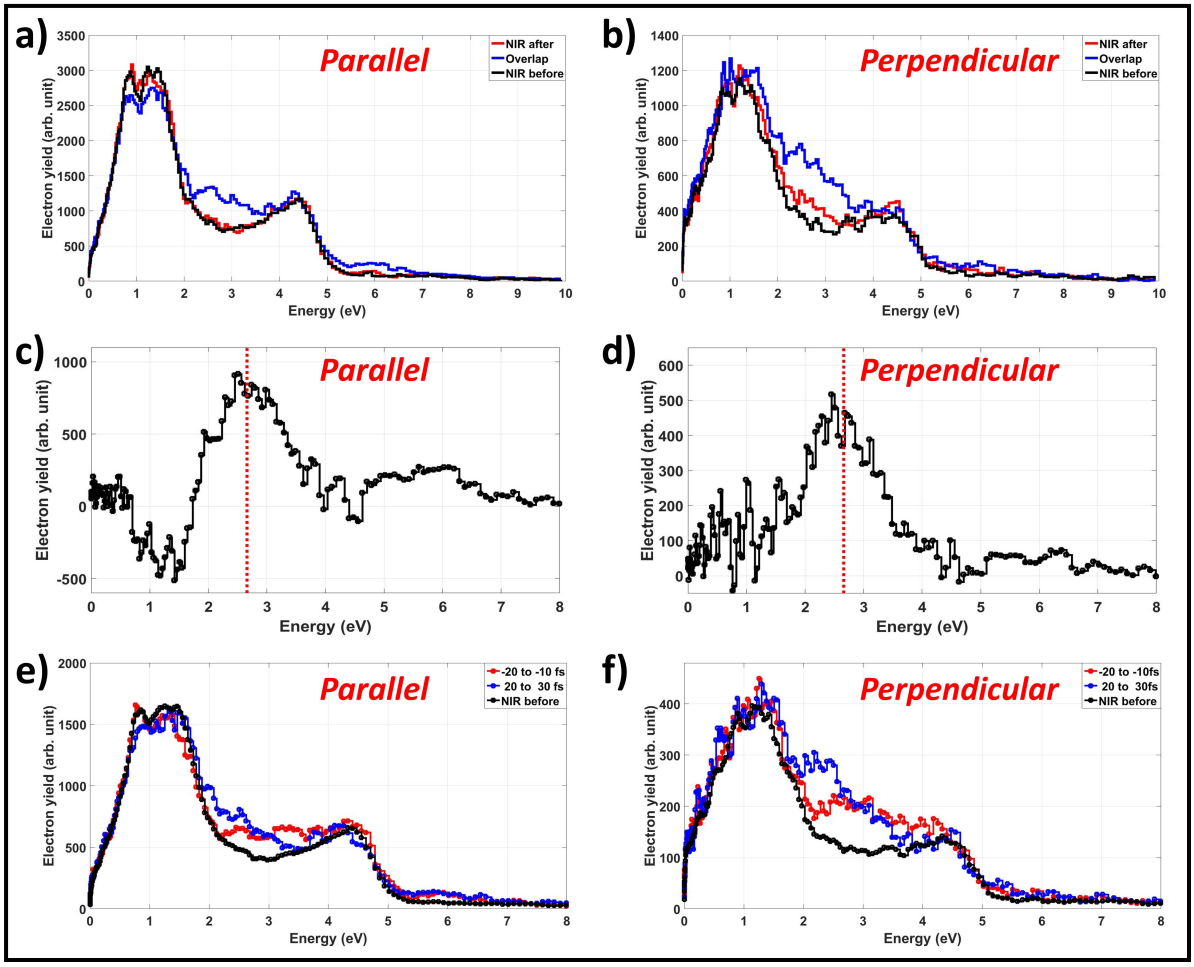

Figure 5.26: *The photoelectron energy spectra in coincidence with O^+ ions for parallel (left panels), and perpendicular (right panels) directions. Panels a) and b) show the energy spectra at three different delays (blue: overlap region; black: NIR before XUV; red: NIR after XUV). Panels c) and d) show the difference between the spectra obtained in the overlap region and for the NIR arriving before the XUV. Panels e) and f) show the spectra in the overlap region for small negative (red) and small positive (blue) delays, as indicated in the figure. The spectrum for NIR before XUV, the same as in a) and b), is shown in black.*

clear that sharp enhancement of the O^+ signal in the overlap region is mainly driven by events with electron energies between 2 and 3.5 eV, with somewhat higher contribution from the parallel direction. Both the electron energy range and the dependence on the emission angle are consistent with the values expected for a single-photon NIR transition from the cationic A state. The dissociation threshold for O^+ production lies at 19.07 eV, and the lowest vibrational level of the C state is at 19.39 eV. Assuming the central NIR photon energy of 1.57 eV, one would expect that corresponding cationic states that can result in O^+ production lie between 17.5 and 17.83 eV. Given the bandwidth of our NIR pulse, the corresponding energy range covers several vibrational levels of the cationic A-state (see table A.1 in Appendix 1). The angular distribution expected for the A-state electrons is slightly peaked in the parallel direction, as shown in Fig. 5.5.

The assumption that the pronounced enhancement of the O^+ yield in the overlap region results from the XUV population of the A-state also provides a qualitative explanation for the sharp decrease of this signal beyond the overlap region. As can be seen from the 1D potential curves shown in Fig. 5.2 and 5.3, the minimum of the A state is shifted towards larger C-O distances with respect to both neutral and cationic ground states (which have very similar geometry), as well as with respect to the C state of the cation. Correspondingly, upon photoionization, several vibrational states of the A state are populated, and the created wave packet propagates toward larger C-O separations. Since the minimum of the C state roughly coincides with the Franck-Condon region, a selection of vibrational states that could be coupled to the bottom of the C-state at a given NIR photon energy decreases at larger C-O distances, shifting towards higher vibrational states (and, thus, resulting in the lower energy of the corresponding photoelectrons). In the outer part of the A state potential well, right from its equilibrium distance, only the highest, barely populated vibrational states can be coupled to the C state. Initially, the whole A-state vibrational wave packet in the levels above 17.5 eV, which are populated by the XUV photoionization in the Franck-Condon region, can be dissociated via a single NIR photon transition to the C state, resulting in

a sharp rise of the O^+ yield when both pulses overlap. At later times, only a fraction of the vibrational wave packet in the highest vibrational states can be dissociated, causing the sharp decrease of the signal and the tilt of the corresponding photoelectron structure between 2 and 3.5 eV in Fig. 5.25. Although a portion of the wave packet comes back to the inner turning point after each vibrational cycle ($\sim$ 30 fs for an A-state symmetric stretch), because of the dephasing of the wave packet and the distortions due to the other vibrational modes, the wave packet probability density never reaches its maximum initial value.

In order to quantify the photoelectron energy shift due to the closing of single-photon NIR coupling to the C state for lower vibrational levels of the A state, in Fig. 5.26 e,f, we also plot the electron energy distributions for two small delay windows within the overlap region, for the electrons emitted in the parallel and perpendicular direction, respectively. At small negative delays, where the NIR pulse overlaps with the leading edge of the XUV pulse (red curves), the enhancement due to the probe pulse appears in a broad energy window from 2 to nearly 4 eV. At small positive delays, where the NIR pulse is in the trailing edge of the XUV (blue curves), we observe a clear shift towards lower electron energies for both emission directions, with the maximum enhancement shifting to 2.5 eV. This reflects the preference for higher vibrational levels of the A-state at increasing XUV-NIR delays and, thus, at larger C-O separations.

As can be seen from Fig. 5.26 a,b, at large positive delays (red curves) only very little enhancement is left compared to the situation where the NIR pulse arrives earlier than XUV. The remaining enhancement shows up only for perpendicular electron emission at 2.5 -3.2 eV and most likely reflects the small fraction of events for which the XUV ionization to the B state, followed by the NIR-induced transition to one of the higher vibrational level of the C state, ends up producing an O^+ ion. As can be seen from table 5.1, this fraction is on the order of $\sim$ 20 percent, depending on a particular vibrational state.

Besides the features discussed above, the O^+ coincident electron spectra for the overlap region show a pronounced depletion of around 1.4 eV for the parallel direction (see Fig.

5.26a,c). Since this is accompanied by the increase of the CO^+ ion production at the same electron energy and angular range as shown in Fig. 5.20a,c, we interpret this depletion as a confirmation of the redistribution of the C state population from its lowest vibrational levels to one of the higher-lying vibrational states, which predominantly dissociate via the $CO^+ + O$ channel. As mentioned above, such redistribution likely occurs via the stimulated Raman transitions driven by the NIR pulse, similar to the processes discussed in Ref. [115,116,82]. It should be noted that the depletion of the C state signal in the parallel direction can also occur due to the appearance of sideband 14 at 3 eV. However, the sideband effect alone cannot explain our observations. First, the enhancement observed around 3 eV also appears in the perpendicular direction, which means that the sideband cannot be the dominant contribution in that region. Second, more importantly, the depletion of the C state electrons due to sideband 14 formation would also influence the photoelectrons coincident with CO^+ ions in the same energy region, and we see an enhancement at those photon energies in CO^+ data shown in Fig. 5.20. Thus, even though the sideband effect likely contributes to the depletion of a signal around 1.4 eV (and to the enhancement observed at 3eV) for the parallel direction, it does not appear to be the main reason for the observed behavior.

In order to highlight the delay dependence of our coincidence signal for different regions of the photoelectron spectrum, Fig. 5.27 displays the delay-dependent yields of the O^+ ions detected in coincidence with 0.4-1.5 eV (a,b) and 1.9-3.5 eV (c,d) electrons emitted in parallel (a,c) and perpendicular (b,d) to the light polarization. The lower-energy band exhibits a clear drop in signal in the overlap region for the parallel direction (Fig. 5.27a), which, as discussed above, is most likely due to a combination of the sideband effect and the NIR-induced redistribution of the vibrational population of the C state to higher levels that mainly result in CO^+ production. In all other panels of Fig. 5.27 (b-d), a clear maximum is observed for the overlap region. For the 1.9-3.5 eV band in the parallel direction, the signal level after the overlap drops back to nearly the same level as at negative delays. Since this

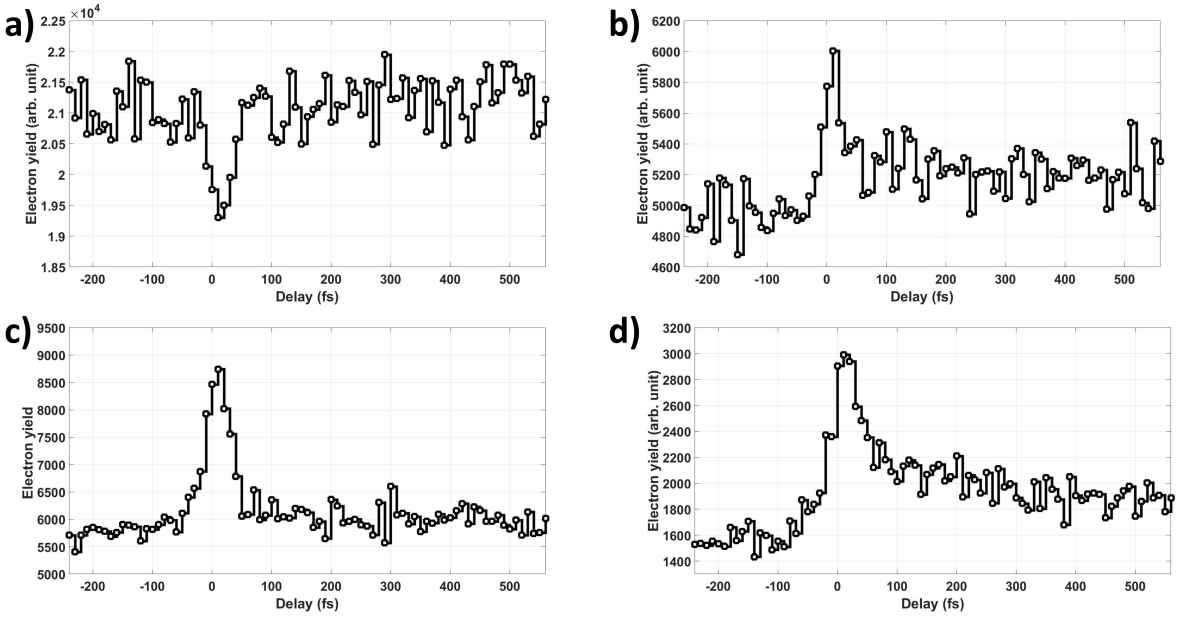

Figure 5.27: *O^+ photoelectron yield vs delay. a) parallel direction, electron energy range 0.4-1.5eV; b) perpendicular direction, electron energy range 0.4-1.5eV; c) parallel direction, electron energy range 1.9-3.5eV; d) perpendicular direction, electron energy range 1.9-3.5eV.*

region is expected to be mostly due to the events where the XUV populates the cationic A-state, this behavior most likely reflects the dynamics in the A-state discussed above. Both graphs for the perpendicular direction exhibit some "residual" level of enhancement at large delays, which is due to the contribution from the B-state, similar to the results shown for CO^+ signals in the previous section.

5.4 Summary and discussion

The results presented in this chapter provide a comprehensive picture of the dynamics in CO_2^+ molecular ions prepared by photoionization and exposed to a NIR field of moderate intensity. Taking advantage of a coincident ion-electron VMI spectrometer, we disentangle the contributions of individual cationic states to NIR-induced dissociation and use the latter to monitor the time-dependent evolution of the population in these cationic states.

More specifically, three main results have been obtained in this experiment. First, we

reproduce the earlier observation of the coherent electron hole density oscillation between the two lowest cationic excited states, $B^2\Sigma_u^+$ and $A^2\Pi_u$, driven by the vibronic coupling between these states in the vicinity of their conical intersection. This charge motion is resolved in time by monitoring the population of the upper state (B), which is probed by the NIR-induced dissociation via the $CO^+ + O$ channel. In the initial work [52], the assignment of the transition initiating these dynamics was made based on the measured and calculated photoionization cross sections. Analyzing energy and angular distributions of the photoelectrons detected in coincidence with the CO^+ ions, here we experimentally prove that the events forming this oscillatory structure almost exclusively result from the XUV ionization to the cationic B state. We found that this channel is strongly favored if the photoelectron is emitted perpendicular to the light polarization.

Second, we found that while the dynamics triggered by the population of the B state are responsible for both the oscillatory structure in the delay-dependent CO^+ yield and its rather sharp decrease due to rotational decoherence, a dominant fraction of the pump-probe enhancement of the CO^+ signal is due to some other mechanism, which results in rather low-energy photoelectrons (1 - 1.5 eV), predominantly emitted parallel to polarization. The most realistic scenario behind this observation is the redistribution of the vibrational population from the ground vibrational level of the predissociative C state to its higher vibrational states induced by the NIR field via a Raman-type process. This hypothesis is supported by the depletion of the O^+ signal observed for the same photoelectron energy range, since the dissociation of the ground vibrational level of the C state results exclusively in O^+ ion ejection. The delay dependence of both of these phenomena is not exactly identical: the depletion of the O^+ signal occurs mainly when both XUV and NIR pulses overlap, while the enhancement of the corresponding CO^+ signal is observed at larger delays as well. The sideband appearance is also likely to contribute to the observed depletion. Nevertheless, a strong correlation between the increase of CO^+ and the decrease of O^+ ion yield for the electrons in the same energy range strongly suggests that vibrational redistribution of the

C state populations plays a central role in these observations.

Finally, the NIR-induced enhancement of overall O^+ ion production is found to originate from the XUV ionization to the ionic A state. The short-lived nature of this enhancement is most likely due to the motion of the vibrational wave packet in the A state, which can be efficiently coupled to the predissociative C state only in the Frank-Condon region, around its inner turning point

Chapter 6

Ion-electron coincident study of XUV ionization and fragmentation of alcohol molecules

6.1 Background and motivation

Intramolecular hydrogen or proton motion plays a vital role for many processes in physics, chemistry, and biology [117,118,119,120]. In particular, it is important for the chemistry of hydrocarbons, considerably influencing their chemical functions [121]. With the development of femtosecond light pulses, various processes driven by ultrafast hydrogen motion became popular targets for time-resolved measurements [122,91,123,124,125,126,127,128]. These efforts strongly benefited from continuous improvements in charged-particle detection and imaging techniques, including coincidence measurement schemes. The choice of experimental method is often motivated by the fact that scattering-based imaging methods like ultrafast electron [129,130,131] or X-ray diffraction [53,55,132], which have been very successful for many time-resolved applications, have inherently limited sensitivity to the location of individual hydrogen atoms, mainly because the scattering amplitude is propor-

tional to the atomic number. In contrast, ionization-based momentum imaging approaches are usually almost equally sensitive to both light and heavy atoms.

One of the most intriguing processes involving ultrafast hydrogen migration or proton transfer is the formation of tri-hydrogen cations (H_3^+) in small polyatomic molecules [133]. Such H_3^+ formation necessarily requires breaking and consecutive formation of three molecular bonds and, thus represents attractive and challenging test grounds for our fundamental understanding of intramolecular reaction mechanisms. It can be initiated by a variety of excitation methods, including ion collisions [134,135,136], electron impact [137,138], single-photon absorption [139,133,140,141] or interaction with intense laser fields [142,143,144,145] [146,147,148]. The latter approach has received particular attention because it is capable of resolving the underlying dynamics in time. Recent developments of short-pulsed XUV sources paved the way for extending time-resolved experiments on H_3^+ formation toward shorter wavelength [127]. In particular, it was argued that the experiments where the dynamics of interest are triggered by a single-photon XUV excitation are easier to interpret and model compared to strong-field-induced processes [127].

Remarkably, almost all of these studies addressed the tri-hydrogen ion formation in dicationic molecular states. This also applies to a recent pump-probe experiment [146], where the measured H_3^+ signal was used to trace vibrational motion in methanol monocations, since the actual reaction steps leading to H_3^+ production occurred in the doubly charged state. To the best of our knowledge, the only clear exception here is a methane molecule, where earlier studies performed with proton impact [134] or intense NIR laser fields [149] have found significant H_3^+ production from both dicationic and monocationic states. In addition, in a recent joint theoretical and experimental study on methanol [147], the observation of the pathways leading to the H_3^+ formation in the monocationic states has been reported. However, while the modeling performed in that work clearly identified H_3^+ production from the methanol monocation, in the corresponding experimental data (obtained with intense 800 nm laser pulses), the contribution assigned to the monocation appeared

only as a structureless low-energy shoulder around 1 eV in the overall weak H_3^+ VMI spectrum dominated by the fragments from the dication. A more recent study [148], which also employed strong-field excitation at 800 nm, did not find any H_3^+ fragments in that energy range.

The main goal of the work presented in this chapter is to adapt the experimental approach described in two previous chapters for studies of molecular dynamics driven by ultrafast hydrogen or proton motion upon XUV ionization of medium-size polyatomic systems like alcohols. The main idea here is to exploit the advantages of a single-photon excitation in combination with ion-electron coincidence measurements to restrict and identify the range of states in which the dynamics to be studied are initiated. Even though one cannot expect to achieve the same level of state-specificity as in the CO_2 experiment described in Chapter 5, mainly because of a much larger number of accessible states, channel-resolved electron spectra obtained at several different XUV wavelengths still carry information on the ionic states involved and can provide a very detailed set of constraints for theory. The latter aspect is very important because most of the studies on H_3^+ formation [127,143,144,145;147] as well as other hydrogen migration phenomena [125,126] heavily rely on theoretical modeling. More specifically, we focus on exploring H_2^+ and H_3^+ formation in methanol (CH_3OH) monocations triggered by XUV photoabsorption and use its deuterated isotopologue (CD_3OH) to distinguish the contributions from methyl and hydroxyl hydrogens. Varying the XUV photon energy below, just at, and above the double-ionization threshold, we can reliably isolate the contributions from the singly charged state and compare the results with the model calculations. We follow the description of this XUV-only experiment with a brief overview of two exemplary XUV pump – NIR probe measurements on methanol and ethanol.

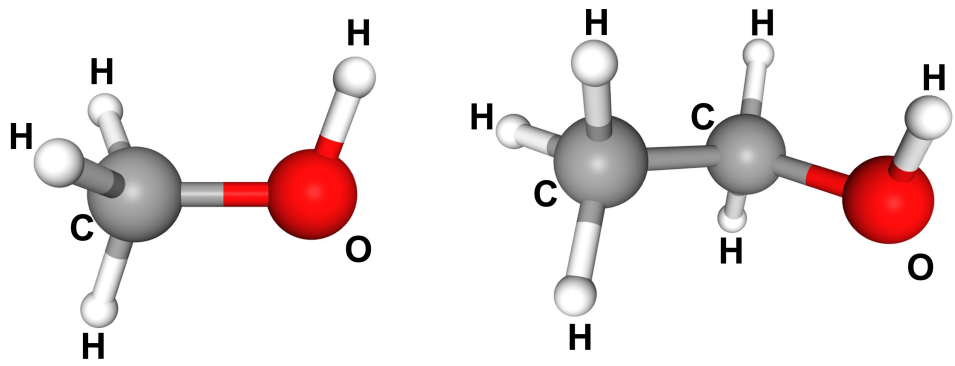

Figure 6.1: *3D interactive chemical structure model of methanol (CH_3OH), and ethanol (CH_3CH_2OH)[150]*

6.2 H_2^+ and H_3^+ ejection from methanol

Owing to its relatively small size, large abundance and broad range of practical uses, methanol, (also called methyl alcohol) represents an attractive target for various molecular dynamics studies. In particular, it has been chosen as model system for many of H_3^+ formation experiments discussed above (see, e.g., [127,133,135,138,139,141,142,144,145,146,147,-140]). As sketched in Fig. 6.1, a methanol molecule contains a methyl group (CH_3 - R) linked to a hydroxyl group (OH - R). The single- and double-ionization threshold of methanol are 10.85 eV and 32.1 eV, respectively. Thus, XUV photons with energies between 10.85 eV to 32.1 eV can only result in single ionization of methanol. Harmonics 13 up to 19 from our XUV setup fall into this range. However, higher-order harmonics, 21st and higher, can also doubly ionize the methanol molecule, triggering various dicationic dissociation pathways. For this experiment, we have used three different combinations of XUV filters: Sn, Ge + Al or Al only. As can be seen from Fig. 3.3a-c, the resulting XUV spectra contain 13th and 15th harmonics, 15th through 19th harmonics, or a rather broad train of harmonics, respectively. The spectra used for the experiments in this section are not exactly identical to those shown in Fig. 3.3, having a smaller contribution of H15 for both Sn and Ge + Al filter configurations.

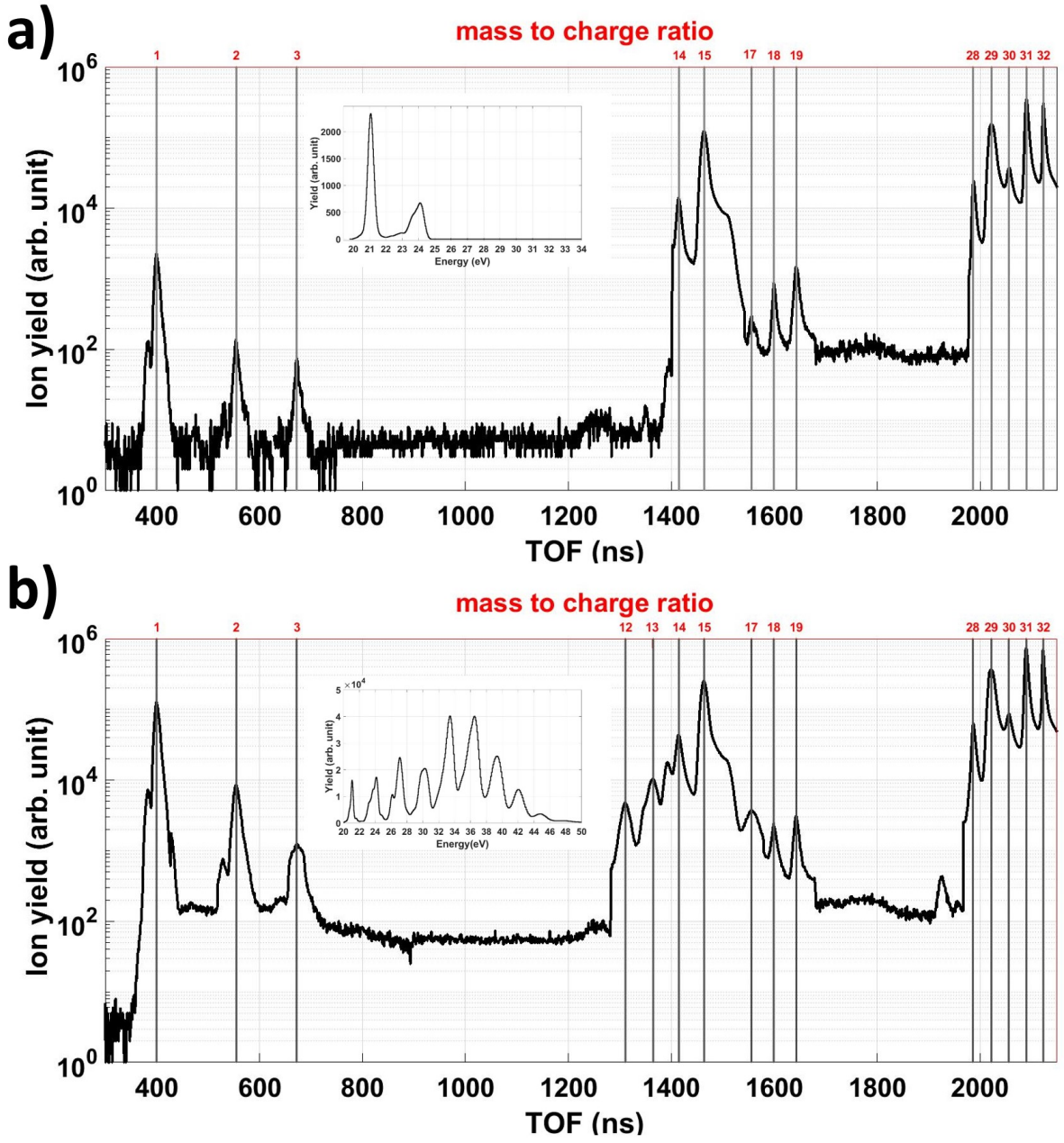

Figure 6.2: *Time-of-flight spectra of methanol ionized by a) H13-15, b) a train of high harmonics.*

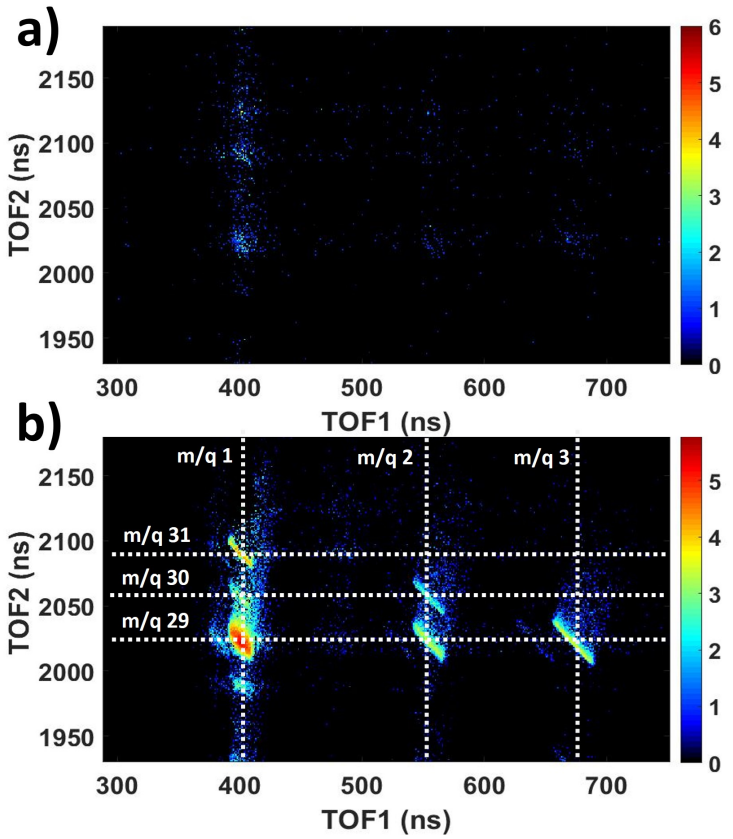

Figure 6.3: *PIPICO spectra of CH_3OH ionized by: a) H13-15, b) a train of high harmonics.*

6.2.1 Experiment on CH_3OH

The ion TOF spectrum from methanol ionization and fragmentation obtained in the XUV-only measurement with a Sn filter (transmitting mainly H13, with a certain fraction of H15 still present) is shown in Fig. 6.2a (log scale). While the spectrum is dominated by heavy fragments in the parent ion group (mass to charge ratio m/q = 32) or in the methyl group (m/q = 15), weak but clear peaks can also be observed at m/q = 2 and 3, reflecting H_2^+ and H_3^+ production, respectively. Since the photon energy for both H13 and H15 is well below the double-ionization threshold, and no traces of true ion-ion coincidence events are observed in the corresponding PIPICO spectrum (see Fig. 6.3a), we conclude that both H_2^+ and H_3^+ ions are formed in one of the singly charged (monocationic) states. In the next step, we measured the mass spectra of methanol ionized by a train of harmonics, some of

which (starting from H21) have the photon energies above the double-ionization threshold. The corresponding ion TOF spectrum is shown in Fig. 6.2b, whereas Fig. 6.3b displays the portion of the PIPICO spectrum zoomed in on the region containing light fragments. We observe a significant increase in the fractional yield of H_3^+ and especially H_2^+ fragments as well as the appearance of clear coincidence lines containing these ions in Fig. 6.3b, both reflecting the opening of the dicationic channels for H_2^+ / H_3^+ production at larger photon energies. This is also reflected in the change of the shape of the H_3^+ TOF peak between Fig. 6.2a and 6.2b, with the significant broadening of the peak due to energetic H_3^+ ions appearing with a charged partner. A comparison between the yield of non-coincident H_3^+ ions and the yield of all coincidence events containing this fragment suggests that about 80% of all H_3^+ ions result from double-ionization events (H_3^+ + CHO^+), with the remaining 20% still originating from the dissociation of monocationic states (most likely via the H_3^+ + CHO channel).

Similar to the previous chapter, here we will mainly focus on the results obtained using a narrower XUV spectrum obtained with a Sn (and later on with a Ge) filter, such that the range of cationic states involved in the production of a particular ionic fragment can be inferred from coincident photoelectron spectra. Exemplary photoelectron images and extracted kinetic energy distributions for several different ion peaks of Fig. 6.2a are shown in Fig. 6.4, starting with the parent ion in the top row. (Note that the VMI images are not inverted, and the "energy spectra" shown in Fig. 6.4, as well as all other photoelectron distributions throughout chapters 5 and 6, are in fact squared radial distributions scaled in units of energy). Based on this graph, one can trace the relation between various dissociation pathways and the vertical ionization energy of the states involved. For example, the proton spectrum, which peaked very close to zero energy, suggests that the main portion of the XUV spectrum used lies below the energy needed for deprotonation. A full set of photoelectron images and kinetic energy distributions measured in coincidence with most abundant ion peaks in Fig. 6.2 can be found in Appendix 2.

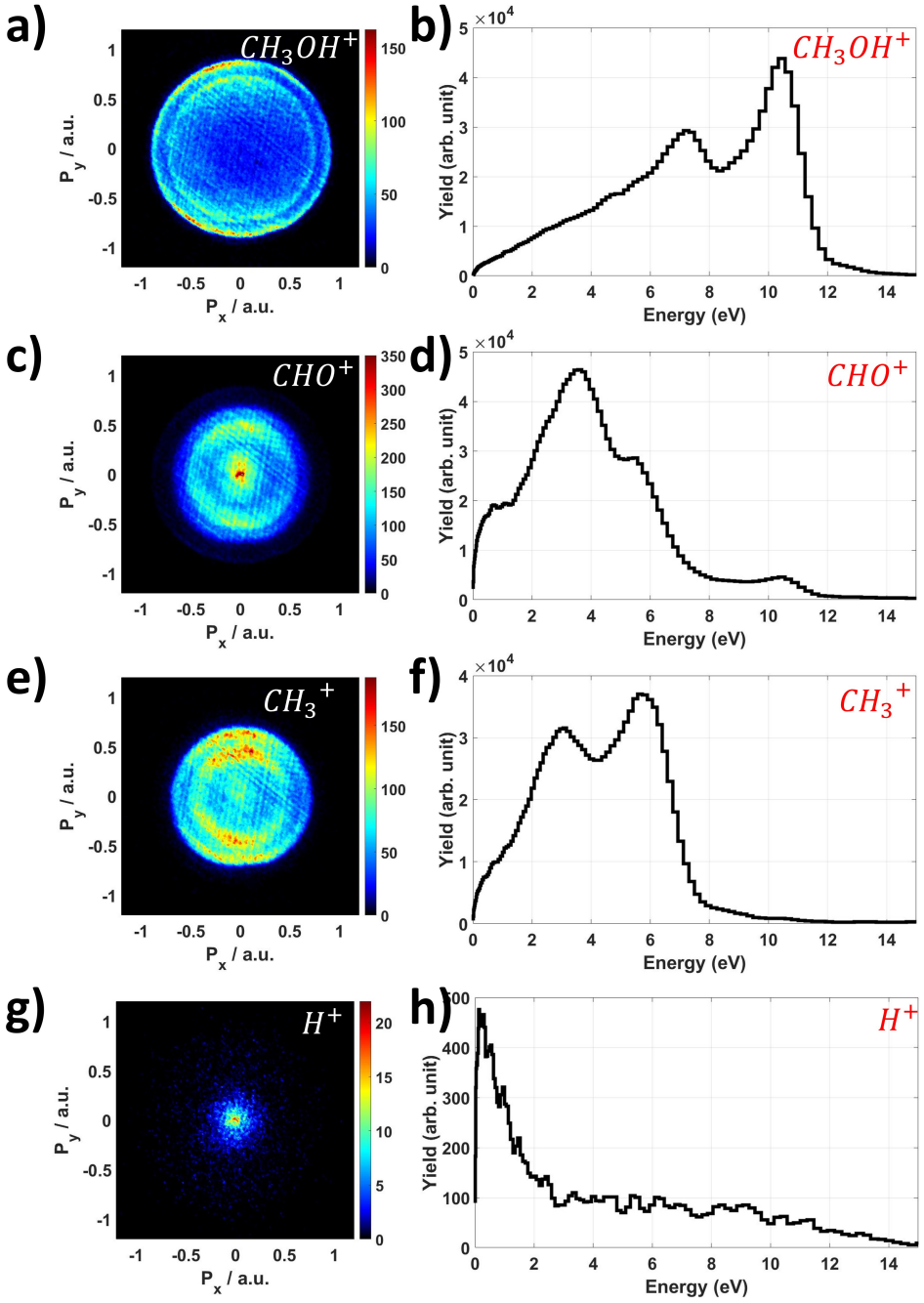

Figure 6.4: *Exemplary photoelectron images and extracted kinetic energy distributions measured in coincidence with several different ionic fragments from methanol ionized by H13-15.*

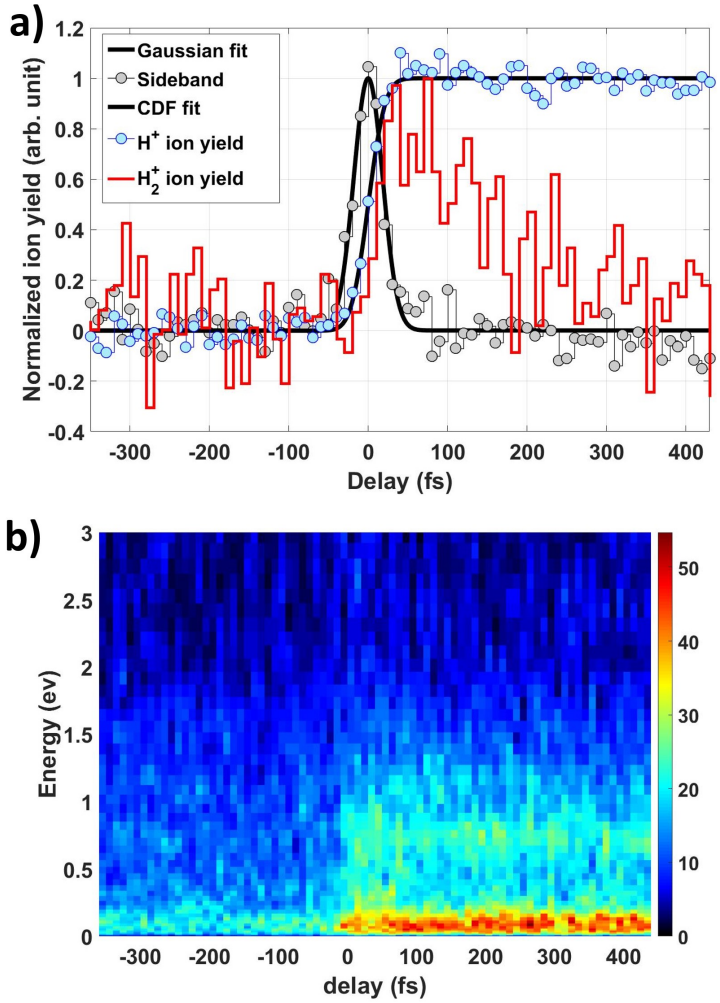

Figure 6.5: *a) Normalized delay dependent yields of the H^+ (blue circles), H_2^+ (red line), and sideband from parent ion (gray circles). b) photoelectron energy spectrum in coincidence with H^+ ion fragment vs delay.*

Fig. 6.5 summarizes the results of a pump-probe experiment on CH_3OH employing H13/ H15 as a pump, followed by a weak ($4 * 10^{12} W/cm^2$) NIR probe. Fig. 6.5 displays the measured H^+ and H_2^+ yields as a function of XUV-NIR delay, normalized for comparison. The delay-dependent profile of a sideband feature for the photoelectrons measured in coincidence with the parent ion is shown for comparison, providing a cross check for the "time zero" position. The proton yield exhibits a clear step-function-like enhancement at positive delays, such that the signal is nearly a factor of two larger than if the NIR pulse arrives before

the XUV (negative delays). The corresponding delay-dependent photoelectron spectrum shown in Fig. 6.5b reveals that this enhancement is associated with low-energy electrons within the main peak of the XUV-only spectrum of Fig. 6.4h. This suggests that the XUV photoionization by our combination of H13 and H15 populates some cationic states within one NIR photon from the deprotonation threshold. The delay-dependent H_2^+ yield in Fig. 6.5a rises very similar to the proton signal but then seems to decay within 300 fs. The possible explanation for this behavior will be discussed in the next section.

6.2.2 Experiments on CD_3OH

Earlier theoretical and experimental studies on methanol dications [144,145,151] suggested that the dominant mechanism of tri-hydrogen ejection from doubly charged methanol is driven by roaming of the neutral H_2 moiety following double-ionization, where a neutral hydrogen molecule from the methyl side roams around the methanol dication until it captures an additional proton to form H_3^+. The proton can then come either from the methyl or from the hydroxyl side of the dication, referred to as "local" and "extended" roaming, respectively [148]. An alternative mechanism, which involves single ionization of a molecule and subsequent ionization of the monocation to lower-lying transition states in the dication, was suggested based on the results of pump-probe experiments [146]. This scheme also implies the creation of a neutral H_2 moiety, which abstracts the proton from either the methyl or hydroxyl side. To experimentally quantify the contributions of these "local" and "extended" formation mechanisms, in [144,145,148] deuterated isotopomers of methanol have been used. Here, we follow this general scheme and use a CD_3OH target to study molecular hydrogen and tri-hydrogen formation in monocationic states.

Fig. 6.6 shows the ion TOF spectra obtained from CD_3OH ionization and fragmentation by three different sets of harmonics: H13 and H15 (a); H17 and H19 (b); and a train of harmonics from H13 to H29 (c). As can be seen in the insets showing the corresponding XUV spectra, the dominant fraction of XUV photon energies are well below (a), just below

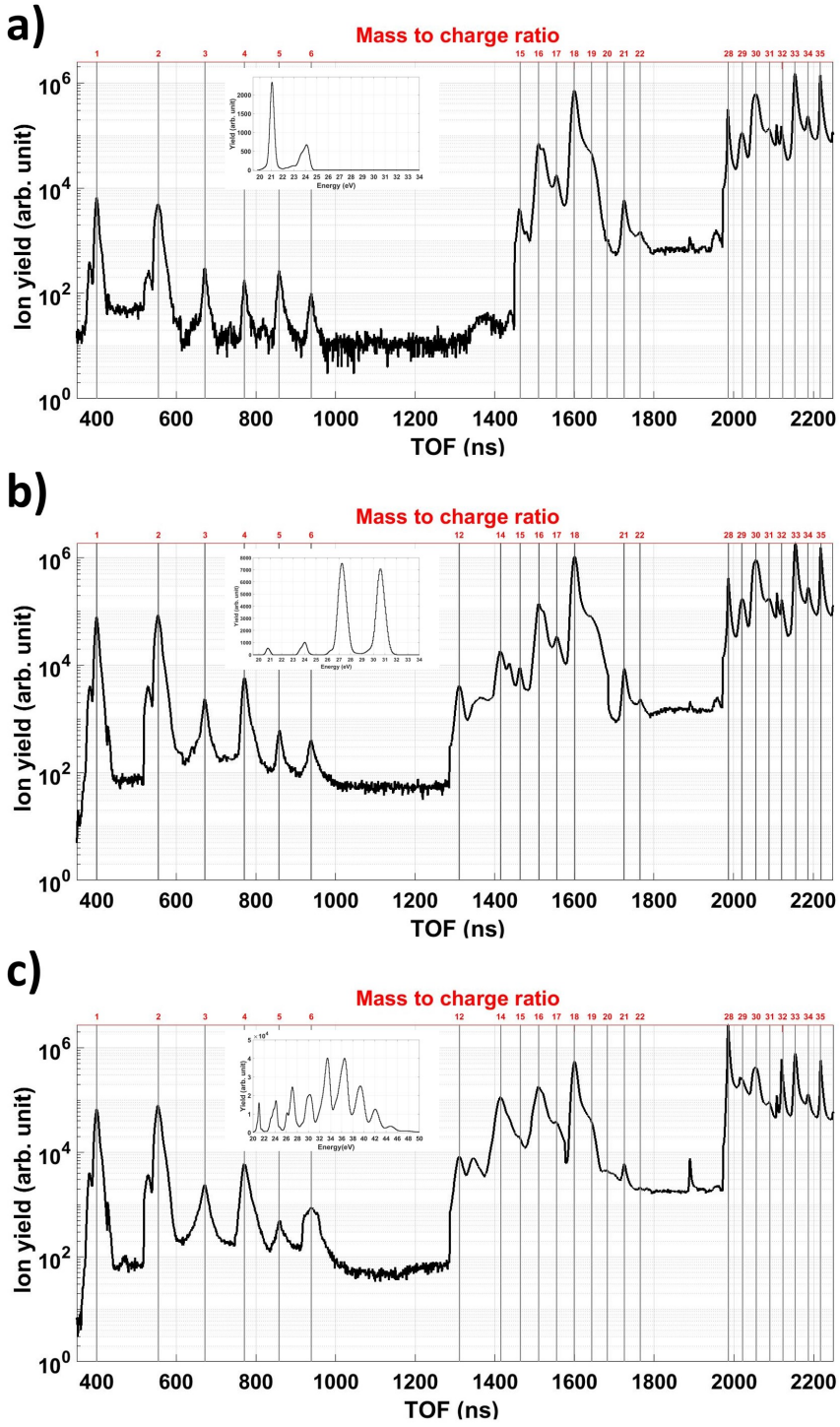

Figure 6.6: *Time-of-flight spectra of CD_3OH ionized by a) H13-15, b) H17-19, and c) a train of high harmonics.*

Harmonic spectrum	H^+ and D^+ ratio	DH^+ and D_2^+ ratio	D_2H^+ and D_3^+ ratio
H13-15	0.42(7.4E-3)-0.58(9.9E-3)	0.65(4.3E-4)-0.35(2.3E-4)	0.69(4.1E-4)-0.29(1.7E-4)
H17-19	0.38(8.0E-2)-0.62(1.3E-1)	0.31(3.7E-3)-0.69(8.1E-3)	0.56(9.3E-4)-0.44(7.3E-4)
H13-29	0.37(2.2E-1)-0.63(3.7E-1)	0.30(1.3E-2)-0.70(3.0E-2)	0.32(3.1E-3)-0.68(6.7E-3)

Table 6.1: *The ratios between each pair of ions (H^+ and D^+), (H_2^+ and HD^+), and (D_2H^+ and D_3^+).*

(b), and mostly above (c) the double-ionization threshold of 32.1 eV. In the following, we mainly focus on the analysis of different hydrogen or deuterium fragments. In all three spectra, all combinations of hydrogen and deuterium masses possible for CD_3OH can be observed, resulting in six peaks with mass to charge ratios from 1 to 6. The fraction of atomic hydrogen (H^+ / D^+), molecular hydrogen (H_2^+ / HD^+) and tri-hydrogen (D_2H^+ / D_3^+) ions, which either include or do not include the hydroxyl hydrogen, are shown in table 6.1. The ratios between each pair of ions are calculated by, for example, $H^+_{ratio} = \frac{H^+_{yield}}{H^+_{yield}+D^+_{yield}}$. The values in parenthesis give the yield of each ionic fragment divided by the yield of the parent ion. Below, we discuss basic trends observed for each of these ion groups.

Atomic hydrogen (H^+ and D^+):

Although the ratio between the yield of H^+ or D^+ ions does not significantly change for different XUV wavelengths, the fractional yield of each of these species increases by an order of magnitude when changing from H13-15 to H17-19 (see Fig. 6.6a,b and table 6.1). Here, it should be noted that the analysis of the PIPICO spectra shows that in the experiment with H17-19, there is only a very small contribution from double-ionization events, in agreement with the expectations based on the photon energies. This, the enhancement of the proton/deuteron yield for H17-19, results from the monocationic states that are not (or

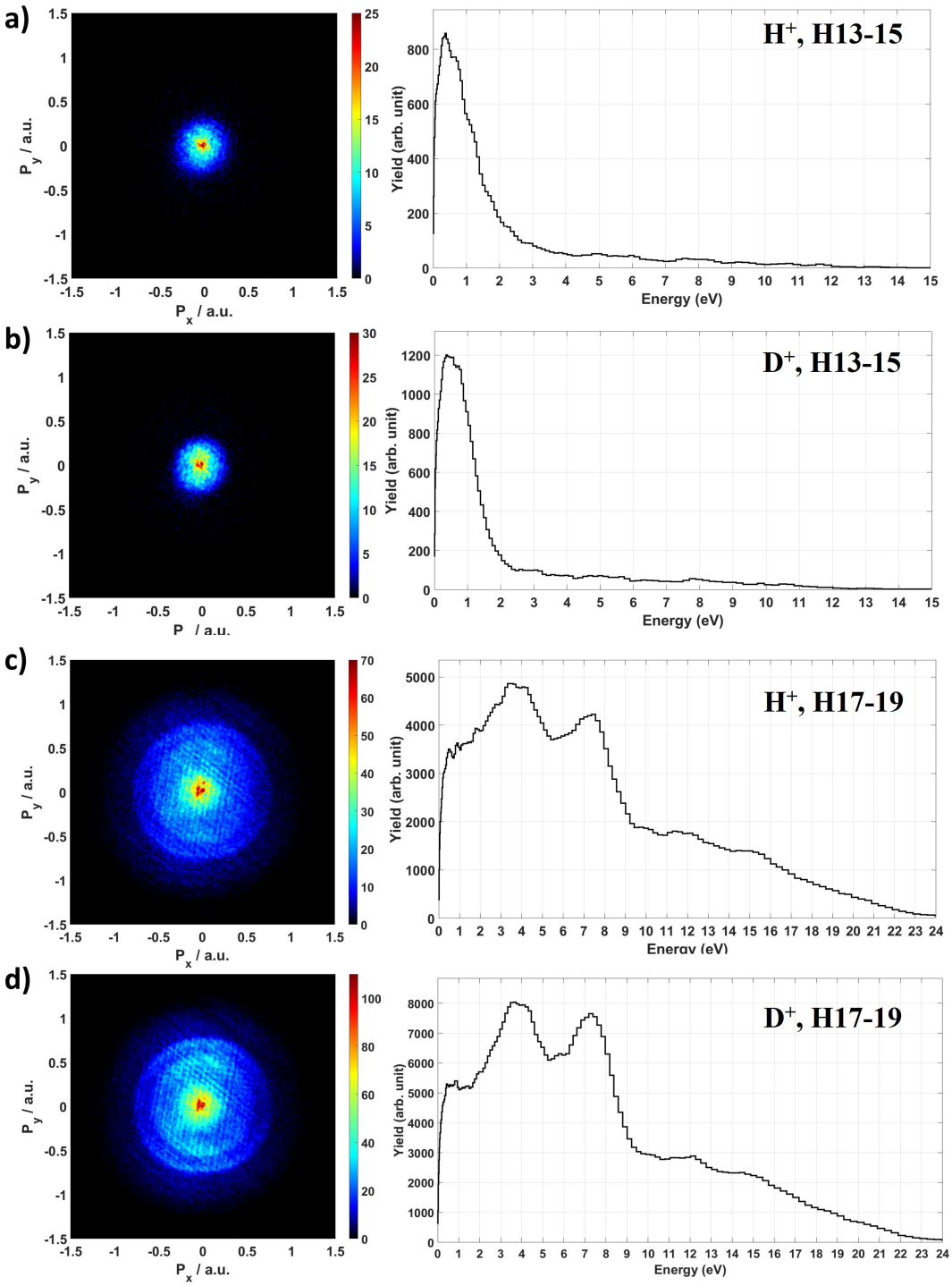

Figure 6.7: *Photoelectron images (left panel) and energy spectra (right panel) measured in coincidence with H^+ and D^+. a)H^+ ionized by H13-15, b)D^+ ionized by H13-15, c)H^+ ionized by H17-19, and d)D^+ ionized by H17-19.*

barely) accessible with H13-15. This is consistent with the photoelectron and pump-probe data for CH_3OH discussed in the previous section. To shed further light on this, we consider the photoelectron images and spectra measured in coincidence with H^+ and D^+ ions from CD_3OH shown in Fig. 6.7. The results obtained with H13-15 are very similar for protons and deuterons (Fig. 6.7a,b), and also similar to the data obtained with H13-15 for protons from CH_3OH (see Fig. 6.4g,h), with all spectra dominated by nearly zero-energy ions. This suggests that the energetics for the deprotonation/deuteron detachment are rather similar for both sides of the molecule and are not changed by isotope effects. A comparison with the data obtained with H17-19 (Fig. 6.7c,d), where two clear peaks at 4 eV and 7.3 eV can be assigned to ionization by H17 (with central photon energy 27.2 eV) and H19 (centered at 30.5 eV), respectively, shows that the binding energy of the corresponding state lies slightly above 23 eV. Thus, the protons observed with H13-15 for both molecules (Fig. 6.4g,h and 6.7a,b) originate from the weak contribution of H15, with many events ending up below (but close to) the deprotonation threshold. Those events are responsible for the step-function-like increase of the delay-dependent H^+ signal observed in the pump-probe data shown in Fig. 6.5.

Molecular hydrogen (DH^+ and D_2^+):

Important qualitative conclusions can be deduced from the wavelength dependence of molecular hydrogen and tri-hydrogen ion yields shown in Fig. 6.6 (see also table 6.1). The enlarged view of the corresponding region of the ion TOF spectra is shown in Fig. 6.8 on a linear scale. The advantage of using CD_3OH as a target is that for either of the fragments shown here, one can uniquely determine whether it resulted from "local" or "extended" pathways discussed above. There are two things of immediate interest in Fig. 6.8a, which shows the TOF spectrum obtained with H13-15. First, for both molecular hydrogen and tri-hydrogen formation, the channels involving a mixture of hydrogens from the methyl and hydroxyl groups ("extended" pathways) provide a dominant contribution. Second, the

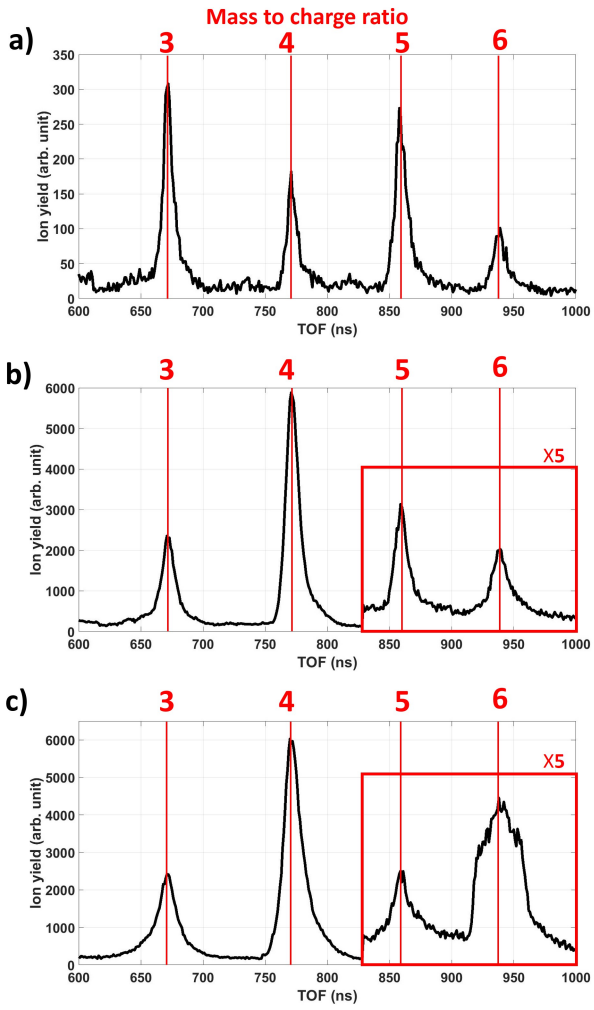

Figure 6.8: *Time-of-flight spectra of CD_3OH, for a selected region of m/q between 3 to 6, ionized by a)H13-15, b)H17-19, and c) a train of high harmonics.*

contribution from molecular hydrogen and tri-hydrogen to the spectrum are close to each other, in stark contrast with the data obtained using 800 nm lasers (see, e.g.,142,144,145,147] or with ion impact [135]. This ratio changes in favor of D_2^+ by more than an order of magnitude when using H17-19 (Fig. 6.8b). In particular, a "local" production of D_2^+ from the methyl site becomes a dominant channel. It should be noted that this effect still results from the dynamics in monocationic states since the contribution from double-ionization when using H17-19 is negligibly small. Similar to the CH_3OH results discussed in section 6.2.2, double-ionization starts to contribute significantly when the train of harmonics is used

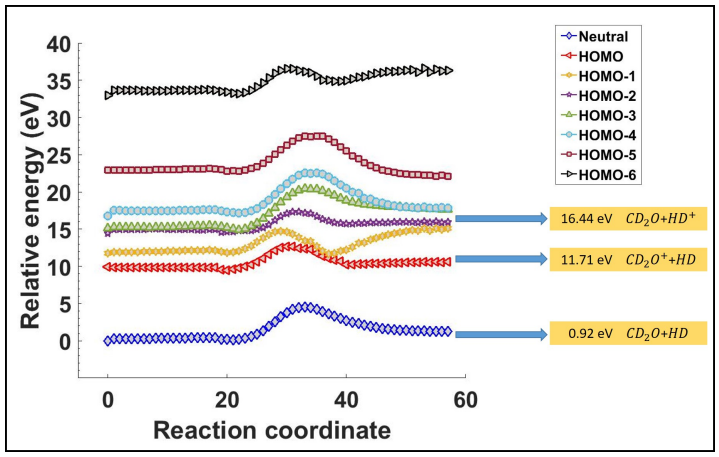

Figure 6.9: *Calculated potential energy surfaces, cut along a chosen reaction coordinate, showcasing reaction pathways leading to DH and DH^+ production*

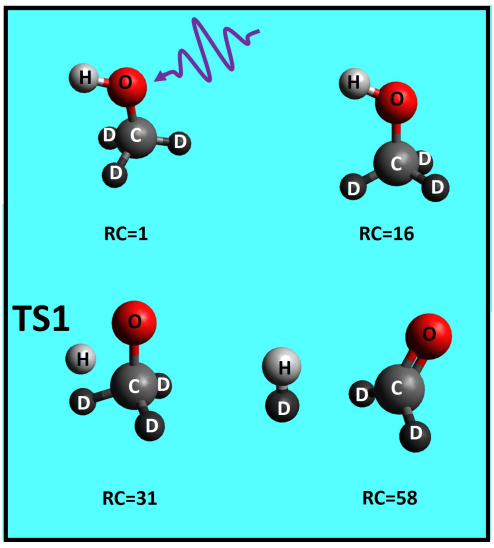

Figure 6.10: *DH^+ formation pathway from deuterated methanol (CD_3OH)*

(Fig. 6.8c).

In order to better understand mechanisms behind DH^+ and D_2^+ production from the CH_3OH monocation, the experimental results are compared with a set of recent theoretical simulations performed by Enliang Wang [152].

The simulations follow basic principles and methodology used recently in Ref. [138,153]. In brief, the reaction coordinate calculation was performed on the ground electronic state of the cationic state. First, the transition states were optimized by the density functional

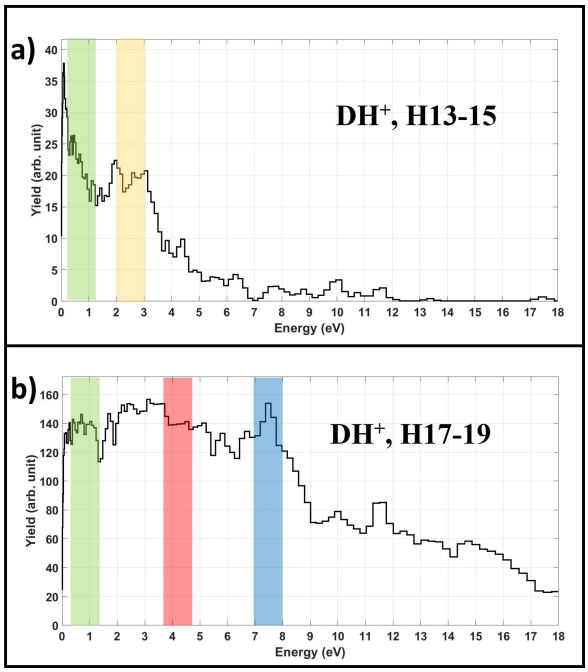

Figure 6.11: *Photoelectron energy spectra measured in coincidence with DH^+ from ionization of CD_3OH by a) H13-15, b) H17-19.*

theory method (B3LYP) with the aug-cc-pVTZ basis set [154,155,156]. The reaction path was confirmed by an intrinsic reaction coordinate (IRC) calculation. Second, the same reaction path was adapted in the neutral ground state and excited-states potential energy calculation. To obtain the potential energy corresponding to the removal of an electron from a "pure" molecular orbital, the potential energy was determined by the ionization energy of the corresponding orbital relative to the neutral ground state. The absolute potential energy of the neutral ground state was calculated using the CCSD(T)/cc-pVTZ method [157]. The ionization potential was calculated using the extended Koopmans' theorem [158].

The calculated potential energy surface for reaction pathways leading to DH^+ production is plotted in Fig. 6.9, while Fig. 6.10 shows several snapshots of the calculated molecular geometry at the values of the reaction coordinate illustrated in the figure. Based on the calculation, HOMO-4 and HOMO-5 orbitals can lead to DH^+ production. The vertical ionization energies from the ground state of the neutral CD_3OH molecule for HOMO-4 and HOMO-5 orbitals are 17.5 and 23 eV, respectively. Thus, the HOMO-4 orbital can

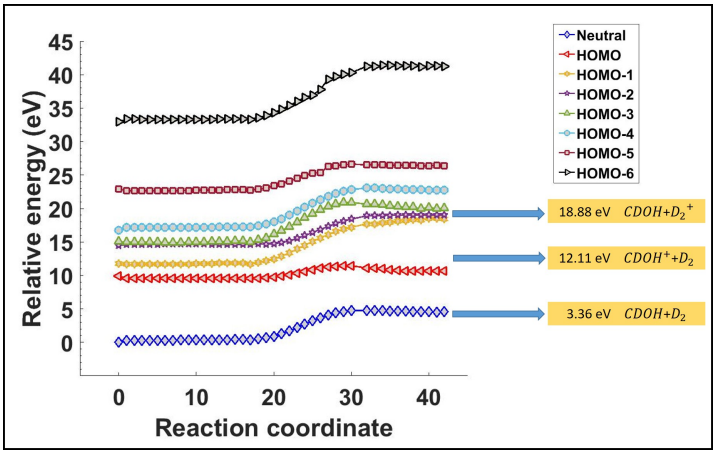

Figure 6.12: *Potential energy surfaces, cut along a chosen reaction coordinate, for reaction pathways leading to D_2 and D_2^+ formation.*

be energetically accessible by both H13 and H15. However, the HOMO-5 orbital is only accessible by H15 (23.9 eV). The theoretical calculation for the DH^+ dissociation pathway agrees well with our PEPICO results shown in Fig. 6.11. In Fig. 6.11a the photoelectron energy spectrum measured in coincidence with DH^+ ions for the experiment employing H13 and H15 is shown. The green and yellow shaded areas correspond to photoelectrons resulting from H15 ionizing HOMO-5 and from H13 ionizing HOMO-4, respectively. In order to confirm these assignments, the photoelectron energy spectrum of DH^+ mainly ionized by H17 and H19 is plotted in Fig. 6.11b. The red and blue shaded areas in the graph correspond to photoelectrons from H17 and H19 ionizing the HOMO-5 orbital. In view of the good agreement between the calculation and experimental results, we conclude that the dominant dissociation pathways leading to DH^+ formation are triggered by the ionization events leaving a hole in HOMO-4 or HOMO-5 of the molecule.

The calculated potential energy surface for reaction pathways leading to D_2^+ production is plotted in Fig. 6.12, whereas Fig. 6.13 shows several snapshots of the calculated molecular geometry at several fixed positions along the reaction coordinate. Based on the simulation, only the HOMO-5 orbital can lead to D_2^+ production. As discussed above, the ionization out of the HOMO-4 orbital could lead to DH^+ production since the vertical ionization energy

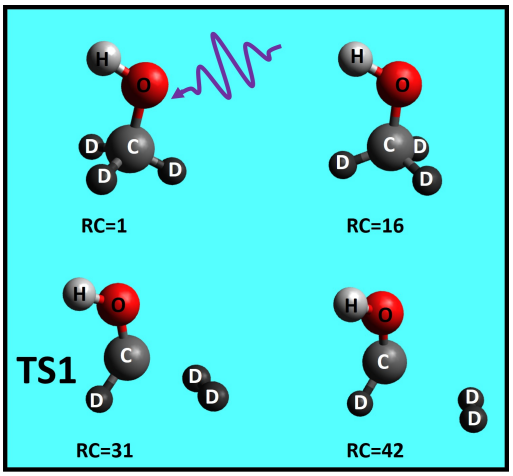

Figure 6.13: *D_2^+ formation pathway from deuterated methanol (CD_3OH).*

of that state (17.5 eV) was above the dissociation energy threshold of the $DH^+ + CD_2O$ channel, which is 16.44 eV. However, the dissociation energy threshold of the $D_2^+ + CDOH$ channel (18.88 eV) is above the vertical ionization energy of HOMO-4. The HOMO-5 vertical ionization energy is 23 eV, which is not energetically accessible by H13. Thus, H13 cannot produce D_2^+ fragments, and the corresponding fragments in the H13-15 data (Fig. 6.6a, 6.8a) originate from a weak contribution of H15. However, in the H17-19 experiment, the HOMO-5 orbital is energetically accessible by both harmonics, thus resulting in a large (a factor of 35) increase of the fractional yield of the D_2^+ contribution compared to the H13-15 results (see table 6.1). Under these conditions, the D_2^+ contribution becomes larger than that of HD^+, indicating that the "local" pathway illustrated in Fig. 6.13 becomes a dominant channel of molecular hydrogen formation.

A similar "local" channel is also likely responsible for the transient enhancement of the delay-dependent H_2^+ ion yield from CH_3OH observed in Fig. 6.5a. Although we performed only a short, exploratory pump-probe measurement on CD_3OH (with H13-15 used as a pump), which is not shown here because of its limited statistical significance, these data do suggest that similar enhancement is observed for D_2^+ but not for the DH^+ channel. A possible underlying mechanism here is the ionization of the HOMO-4 orbital (vertical

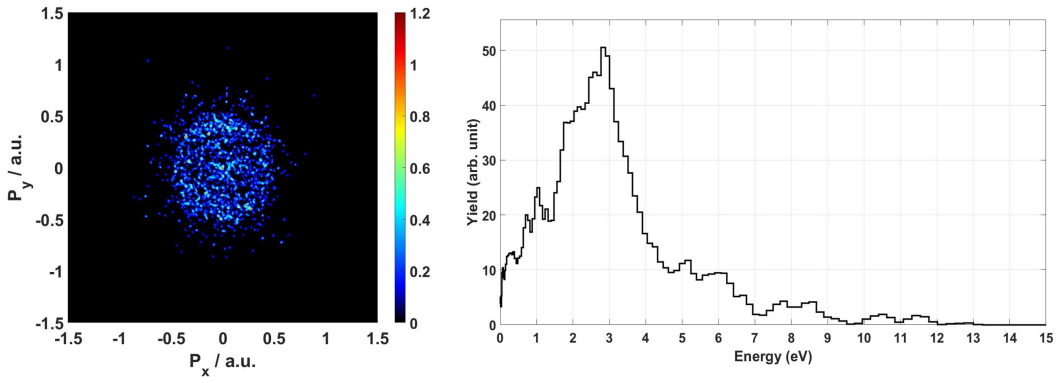

Figure 6.14: *Photoelectron image (left panel) and energy spectrum measured in coincidence with the ionic fragment D_2H^+ from the CD_3OH molecule ionized by H13.*

ionization energy 17.5 eV), which, by itself, does not result in D_2^+ ejection but can be brought above the corresponding threshold (18.88 eV) with one NIR photon. The fact that the H_2^+ signal in Fig. 6.5a decays to almost its initial level within 200-300 fs suggests that in this time, the ionic state involved can dissociate via some other channel, conceptually similar to the scenario responsible for CO_2^{2+} signal enhancement discussed in Section 4.6 (compare Fig. 6.5a and 4.13b).

Tri-hydrogen channels ($\mathbf{D_2H^+}$ and $\mathbf{D_3^+}$):

The data shown in Fig. 6.2a, 6.6a,b, and 6.8a,b clearly demonstrate tri-hydrogen ion formation in monocationic states of methanol. As shown in table 6.1, the ratio between D_2H^+ and D_3^+ production smoothly decreases with the transition from longer to shorter XUV wavelengths, with the fractional yield of both of the two channels smoothly increasing. For ionization by H13-15, the "extended" mechanism leading to D_2H^+ formation is clearly a dominant one (69% compared to 31% for D_3^+), while the ratio becomes closer to unity for H17-19, and finally reverses for the harmonic train, where tri-hydrogen formation from dicationic states becomes dominant. While the statistics for the photoelectrons measured in coincidence with D_3^+ ions are rather low, the binding energy associated with D_2H^+ formation can be extracted from the corresponding PEPICO measurement. The photoelectron image and energy spectrum of photoelectrons measured in coincidence with D_2H^+ ions produced

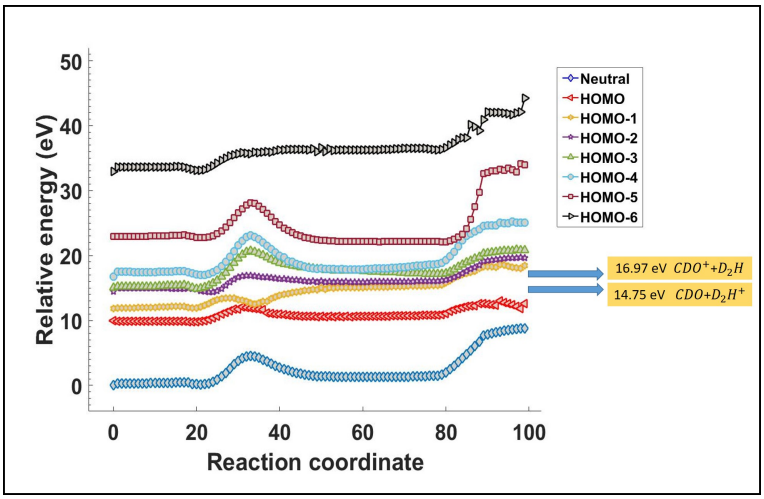

Figure 6.15: *Potential energy surfaces, cut along a chosen reaction coordinate, for reaction pathways leading to D_2H^+ formation.*

by H13-15 are plotted in Fig. 6.14. We observe a clear peak in the photoelectron energy spectrum of D_2H^+ at 3 ev, corresponding to 17.5 eV binding energy. This photoelectron energy corresponds to the vertical ionization energy of the HOMO-4 orbital. The calculated potential energy surface for reaction pathways leading to D_2H^+ production is plotted in Fig. 6.15. Based on the calculation [152], a contribution from HOMO-4 can lead to D_2H^+ ejection. The dissociation energy threshold of the $D_2H^+ + CDO$ channel, based on our calculation, is 14.75 eV. A series of snapshots of the calculated molecular geometry at several fixed positions along the reaction coordinate leading to D_2H^+ formation is shown in the cartoon presented in Fig. 6.16. Here, the H atom on the hydroxyl site first aligns with one of the deuterium atoms from the methyl group. Then, H and D atoms form a neutral DH moiety. It roams around the C-D bond and abstracts a deuteron from the methyl site to form D_2H^+. The simulation results are in good agreement with the modeling performed in Ref. [147].

The calculations [152] also suggest that direct, local D_3^+ formation is very unlikely for monocationic states because of the very large energies required. Based on our experimental results, the probability of D_2H^+ is 2.7 times higher than the D_3^+ at these photon energies. Further modeling hints the pathways responsible for the observed D_3^+ signal. When the

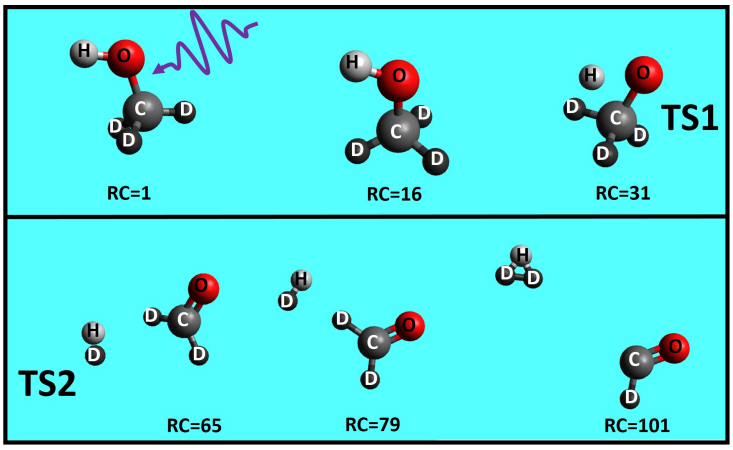

Figure 6.16: *D_2H^+ formation pathway from deuterated methanol (CD_3OH).*

molecule is ionized by H17 and H19, the ratio between D_2H^+ and D_3^+ decreases (to 56% vs. 44%, see table 6.1). However, at least part of this enhancement is driven by the weak double-ionization signal, which can be observed in the corresponding PIPICO spectrum. Finally, when the molecule is ionized by a train of harmonics, we observe a significant increase in D_3^+ signal, dominated by its formation in dicationic states.

Besides hydrogenic fragments, signatures of many other important processes can be found in the data presented above. As an example, channels resulting in H_3O^+, D_2HO^+, and D_3O^+ ion formation can be observed in TOF mass spectra of CH_3OH (Fig 6.2) and CD_3OH (Fig 6.3a) ionized by H13-15. Here, two or even three hydrogen or deuterium atoms migrate from the methyl group to the hydroxyl group to form D_2HO^+ and D_3O^+ (or H_3O^+ in the case of CD_3OH) fragments (see also 125). The analysis of these channels will be the subject of future work. The photoelectron images and energy spectra coincident with fragments can be found in Appendix 2.

6.3 Experiments on ethanol

In the last section of this thesis, we complement the discussion of XUV and XUV-NIR experiments on methanol with a brief overview of a similar study on ethanol. Among extensive

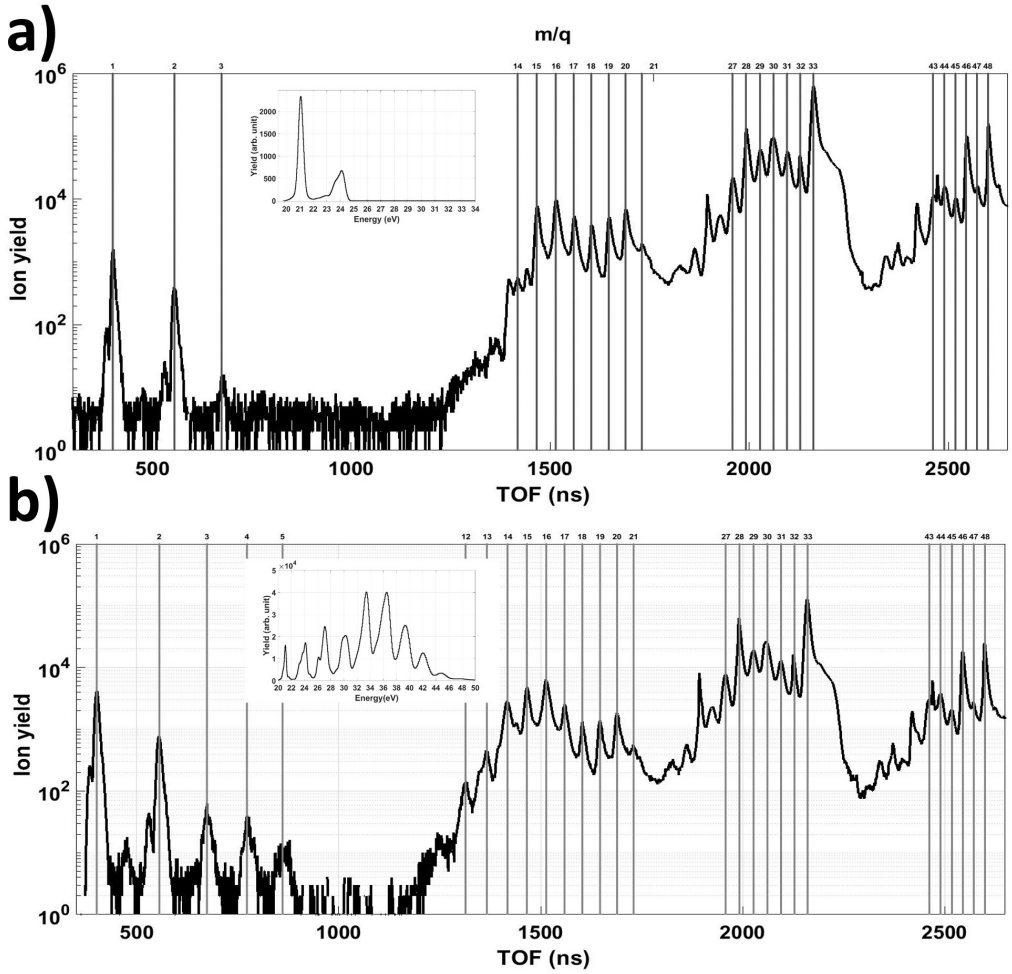

Figure 6.17: *CH_3CD_2OH time-of-flight spectra ionized by: a) H13-15, b) a train of high harmonics.*

literature on different aspects of molecular dynamics in this system, closely related to this work are recent measurements and simulations of single and double hydrogen migration [125] and tri-hydrogen elimination [145] driven by intense laser fields, as well as ultrafast proton transfer triggered by electron impact [153]. In particular, a recent study [145] demonstrated that the fractional yield of tri-hydrogen formation from doubly ionized states decreases by more than a factor of 3 in ethanol compared to methanol and is reduced even further in larger alcohol molecules. The first goal of our experiment on ethanol was to verify this somewhat counterintuitive trend for singly charged states of ethanol. To achieve this, we

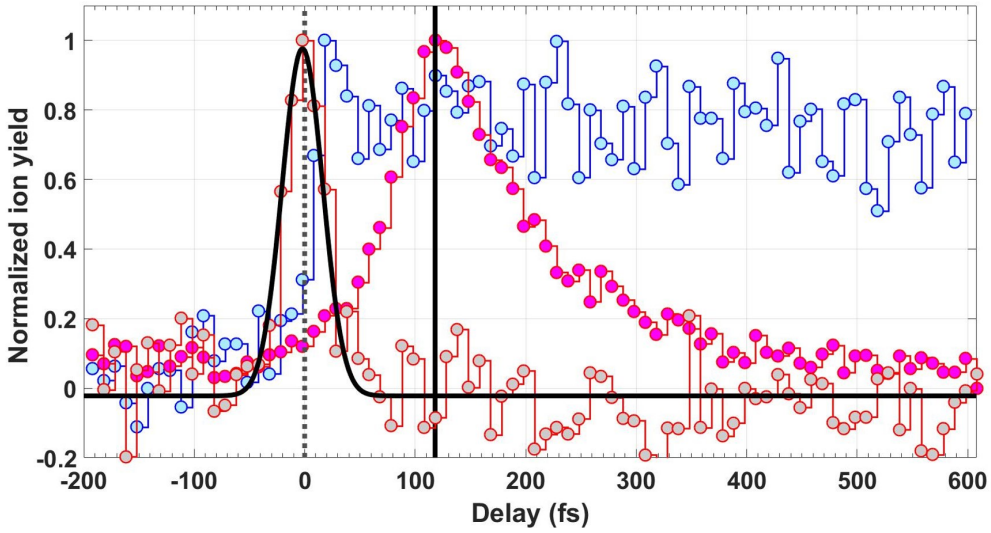

Figure 6.18: *Normalized ion yields of H^+ (blue circles), CH_3^+/CHD^+ (magneta circles) as function of XUV(H13-15)-NIR delay. The sideband from electrons measured in coincidence with the parent ion (brown circles) as function of XUV(H13-15)-NIR delay.*

performed several experiments on the ionization and fragmentation of ethanol at different XUV wavelengths.

Two exemplary ion TOF spectra from a deuterated isotopomer of ethanol, CH_3CD_2OH, are shown in Fig. 6.17. The spectrum in Fig. 6.17a is obtained with H13-15, with photon energies well below the vertical double-ionization threshold (29.6 eV for ethanol [159]). Fig. 6.17b shows the TOF spectrum obtained with a train of harmonics (H13-29, see inset), with H19 and all higher orders lying above the double-ionization threshold. The spectrum for H13-15 in panel (a) does not show any noticeable amount of tri-hydrogen fragments (with a tiny contribution at m/q = 3, most likely from HD formation). In contrast, the spectrum obtained with the train of harmonics does show non-negligible contributions at m/q =3-5, reflecting the tri-hydrogen production from different dicationic channels. However, the fractional yield of these products is more than an order of magnitude smaller than for methanol (compare with Fig. 6.2c and table 6.1). Thus, our measurements confirm a general trend reported in [145] for doubly charged states populated by intense laser fields: the tri-hydrogen production is less important for larger alcohols with more carbon atoms.

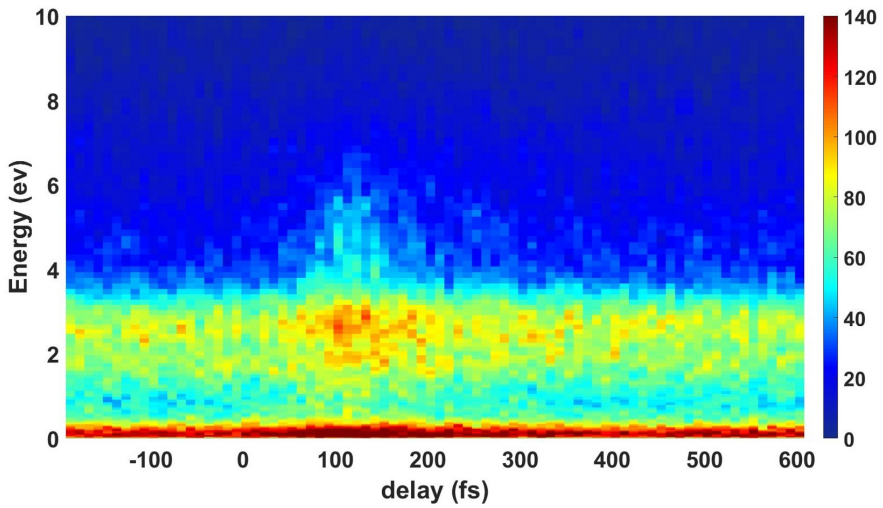

Figure 6.19: *CH_3^+/CHD^+ photoelectron energy as a function XUV(H13)-NIR delay.*

In this experiment, we do not observe any noticeable signatures of tri-hydrogen formation in the ethanol monocation.

We have also performed XUV-NIR pump-probe experiments on ethanol(CH_3CD_2OH), employing both of the XUV pulse configurations used to obtain the data of Fig. 6.17. Fig. 6.18 shows an excerpt from the pump-probe results obtained using H13-15 as a pump. There, the measured yields of H^+ and CH_3^+ /(or CHD^+) ions are shown as a function of XUV-NIR delay. A sideband structure obtained from the electrons detected in coincidence with parent ions is also plotted for comparison. The delay-dependent proton yield manifests a step-function-type increase at positive delays, very similar to the results for methanol shown in Fig. 6.5a. However, the most striking feature that we observe in this pump-probe experiment on ethanol is a transient enhancement of the delay-dependent yield of CH_3^+/CHD^+ ions (magenta symbols in Fig. 6.18). This signal starts to grow around zero delay, reaches a clear, pronounced maximum at 120 fs, and decays back to its initial level within 400 fs, a behavior very different compared to all two-color signals considered so far in this work. The energy distribution of the photoelectrons detected in coincidence with these ions is plotted as a function of delay in Fig. 6.19, whereas the photoelectron spectra

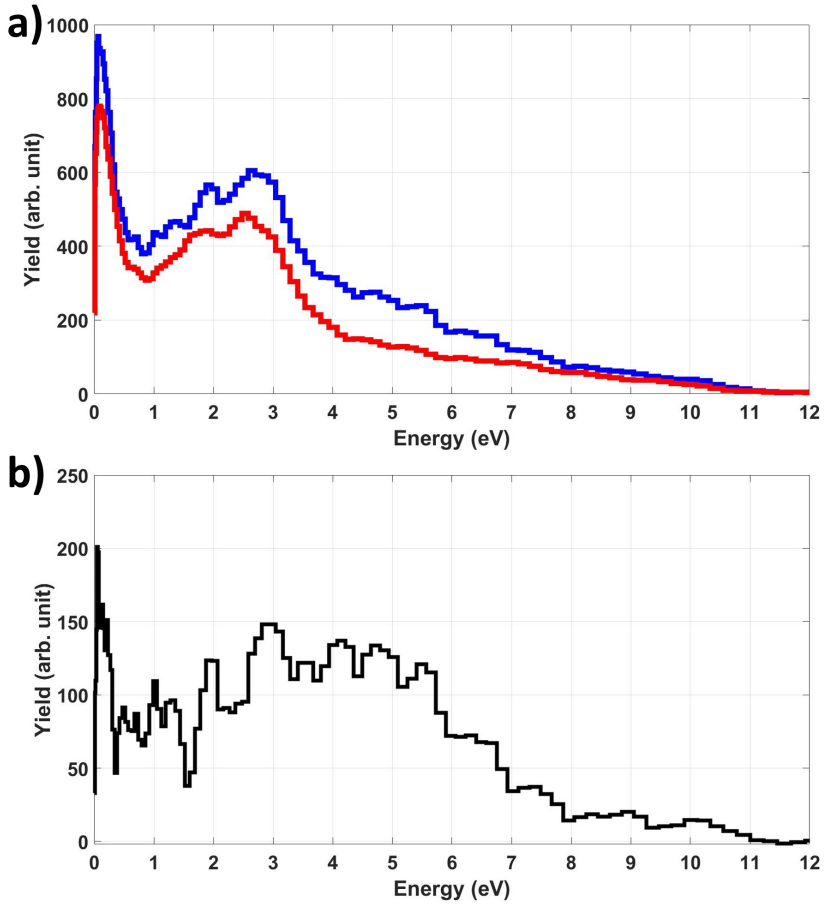

Figure 6.20: *a)Photoelectron spectra at two fixed delays (+120 fs, red and -150 fs, blue). b)the difference between blue and red curves*

at two fixed delays (+120 fs, red and -150 fs, blue) as well as their difference are shown in Fig. 6.20a and b, respectively. From these graphs, one can see that the enhancement covers a broad range of electron energies, with the difference spectrum mainly covering the range from 2 to 6 eV.

We observe a similar behavior of the m/q = 15 channel in the pump-probe results obtained using a train of harmonics, which is summarized in Fig. 6.21. Fig. 6.21a-c display three different regions of the PIPICO spectrum measured in this experiment (integrated over all XUV-NIR delays). While the most intense coincidence lines are $CH_3^+ + CD_2OH^+$ and its satellites, where the heavy fragment loses deuteron(s) and a proton (Fig. 6.21b), one

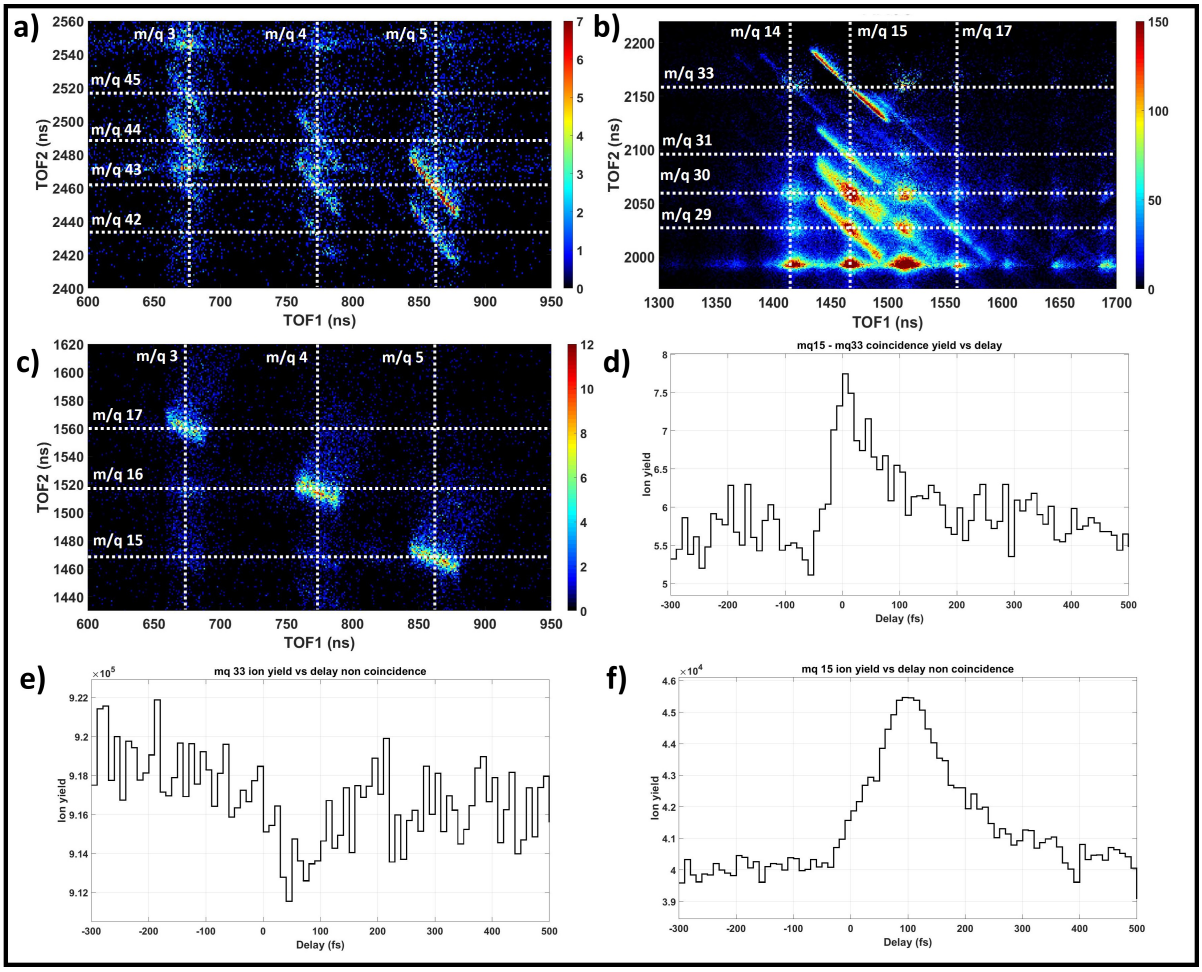

Figure 6.21: *a), b), and c) Selected regions of the PIPICO spectra from CH_3CD_2OH ionized by a train of high harmonics. Delay-dependent yields of d) m/q 15 and m/q 33 in coincidence, e) m/q 33 in non-coincidence, and f) m/q 15 in non-coincidence.*

can also clearly see two-body breakup channels involving HD^+, D_2^+ and D_2H^+ formation (Fig. 6.21a). However, quite surprisingly, the most intense contribution for each of these fragments appears to come from the "incomplete" channels, i.e., from a three-body breakup with a neutral partner. As can be seen from Fig. 6.21c, for all three features ($[D_2H^+ + CH_3^+ + CO]$, $[D_2^+ + CH_4^+ + CO]$ and $[HD^+ + CH_3D^+ + CO]$), a neutral fragment is CO.

Fig. 6.21d displays the yield of the most intense coincidence line ($CH_3^+ + CD_2OH^+$) as a function of XUV-NIR delay. The signal shows a clear enhancement shortly after zero delay, which then decays within 200 fs. This behavior, which is also typical for several other

coincidence lines observed in this experiment, closely resembles the enhancement for the CO_2^{2+} signal discussed in section 4.6 (see Fig. 4.13b). This suggests that the enhancement observed here is also driven by the excitation to high-lying cationic states, which can be coupled to a double-ionization continuum with one NIR photon. The decay of the signal then corresponds to the dynamics of such repulsive states, with their separation to the double-ionization limit increasing in time. The time evolution of this double-ionization signal is very different from the corresponding CH_3^+ results in Fig. 6.18 obtained with H13-15, which originate from the dynamics unfolding on singly charged states. However, the yields of the individual non-coincident CH_3^+ fragments shown in Fig. 6.21f exhibit the behavior very similar to what we observe in the H13-H15 experiment, with a clear transient peak shortly after 100 fs. Fragments with m/q = 14-17 as well as m/q = 28, 29 (not shown here) all exhibit similar delay dependence. Interestingly, the CD_2OH signal shown in Fig. 6.21e manifests a pronounced depletion in the same delay range, suggesting that the two signals in Fig. 6.21e,f are correlated with each other.

At this point, the origin of this transient enhancement of the CH_3^+ ion yield remains unclear. However, in view of a simultaneous decrease of the CD_2OH signal, a scenario proposed in Ref. [153] for dicationic states of ethanol can be considered as a possible mechanism behind our observations. There, it was suggested that several pathways of hydrogen/proton transfer or exchange guide the dynamics of the dication fragmentation via a roaming-type motion. In our case, one can imagine a situation where a proton roams between the dissociating CH_3 and CD_2OH fragments, resulting in an increase in one and a decrease in the other signal at a particular time.

While the data presented above are meant to provide a glimpse into basic fragmentation processes triggered by photoionization of ethanol in the XUV domain, real understanding of the underlying dynamics requires theoretical modeling, as well as further, more elaborate data analysis, including the analysis of individual photoelectron spectra measured in coincidence with different ionic fragments. While such analysis is the subject of future work, a

brief overview of the VMI images and corresponding electron energy spectra for a selection of ionic fragments from ethanol is presented in Appendix B.

Chapter 7

Summary and outlook

In this thesis, an experimental setup combining a femtosecond light source in the extreme ultraviolet spectral range, a synchronized near-infrared laser, and a coincident electron-ion velocity map imaging spectrometer has been developed, commissioned, and applied to experiments on atomic and molecular photoionization. The XUV source, built around a commercial fiber-based high harmonics generation setup operated at 10 kHz, delivered 25-30 fs XUV pulses with photon energies from 20 to 90 eV, which could be restricted by using a proper combination of filters. Combined with the NIR probe pulses of similar duration, it enabled a variety of XUV pump – NIR probe experiments on atomic and molecular cationic (or highly excited neutral) states with 30-40 fs temporal resolution. Among those, three basic groups of experiments are discussed in this work.

In the first part of this work (discussed in chapter 4), a set of two-color pump-probe experiments on single, double, or triple ionization of atoms has been performed. The goal of this effort was two-fold. First, we intended to provide an overview of several characteristic two-color signals typical for femtosecond HHG or FEL experiments in the XUV domain and analyze the information on the temporal characteristic of the pulses (XUV temporal profile envelope and XUV-NIR relative arrival time) that can be extracted from different experimental observables. Second, we attempted to achieve a detailed understanding of

the physical mechanisms responsible for the formation of such two-color signals. It was shown that both the "transient" signals, which require the simultaneous presence of both pulses (like electron sidebands), and the steady ones, which exist in a broad range of delays between the XUV and NIR pulses, can be used for a coarse determination of the "time zero" as well as the temporal duration of the XUV pulse envelope. We have shown that the photoelectron sidebands do yield consistent and reliable information on both parameters in question (provided the NIR laser intensity is kept low enough) within the limits of our experimental capabilities. However, we found that the same information obtained from the "step-function-type", "steady" signals, which often are much easier for practical use in less than perfect environmental conditions (like, for example, at FEL facilities), can vary depending on the experimental parameters and specific atomic or molecular states involved. Therefore, if both parameters are needed with a precision of a few femtoseconds, additional calibration is desirable (e.g., against the sideband signal, as often employed in this work).

In this work, no attempt has been made to ensure the sub-cycle (with respect to the NIR) synchronization of both pulses, which is routinely done in attosecond HHG experiments. The main reason for this is that for the main applications envisioned for this setup, focused on femtosecond molecular dynamics, the achievable temporal resolution is limited by the length of both pulses, which is on the order of 10-12 NIR optical cycles. However, the coincident electron-ion detection employed here might also be useful for some applications relying on the sub-cycle phase relation between both pulses (like, for example, the RABBITT technique [32,31] Since such measurements require < 1 fs temporal stability, they are much more sensitive to changes in environmental conditions and normally cannot run for days like the experiments described here. Thus, in order to make practical use of coincidence techniques applied here, in attosecond physics, a higher repetition rate of the light source would be extremely helpful.

The CO_2 results presented in chapter 5 demonstrate the potential of the employed combination of short-pulsed XUV excitation and electron-ion coincidences for studies of molecular

dynamics in ionic or highly excited states. Tracing a coherent electron-hole oscillation driven by the vibronic coupling between the first two cationic excited states in the vicinity of their conical intersection (initially reported and modeled in Ref. [52]), this study provides unambiguous experimental evidence for the role of individual states involved in the formation of this signal. While the signature of this ultrafast hole motion is imprinted in the delay-dependent CO^+ ion signal, we also show that the lowest excited state of CO_2^+, the $A^2\Pi_u$ state, is responsible for a competing dissociating channel, which produces O^+ ions. This signal is strongly influenced by the vibrational wave packet motion upon XUV photoionization. Finally, we observe the NIR-induced change in the branching ratio between these two dissociation channels, which is tentatively attributed to the redistribution of the vibrational population in the predissociative $C^2\Sigma_g^+$ state caused by the NIR pulse.

This detailed experimental analysis provides benchmark data for theoretical modelling, which should be feasible for this prototypical triatomic system. Such comparison with theory is one of the main directions for future work. From a more technical point of view, this study is somewhat limited by two factors. First, because of the limitations of a double-sided VMI spectrometer and stray light issues, the chosen spectrometer field configuration restricted the quality of ion imaging, such that the differential data (momenta, energies, emission angles) recorded for the ions were of limited use. Second, the VMI data shown in this work were not inverted, mainly because of the limited statistics for coincident channels. This made the direct identification of the contributions from individual states much more challenging. While the second limitation can be to some extent lifted if the experiment can be performed at a higher repetition rate, the inversion procedure would still restrict "event by event" analysis of individual particle correlations. An alternative solution, which would address both of these limitations, is using a COLTRIMS-type spectrometer with Helmholtz coils for the electron [44]. However, this solution has its own limitations: regions of the phase space with no transverse resolution, and difficulties handling high-energy electrons. Thus, one of the important directions for future developments is a coincident spectrometer

design, which would allow one to avoid the above-mentioned issues.

The results presented in chapter 6 clearly demonstrate the production of tri-hydrogen cations in singly charged states of methanol, which was not unambiguously identified before. Ion-electron coincident measurements combined with variable XUV wavelength, use of deuterium markers, and comparison with quantum chemistry calculations enable efficient identification of pathways leading to both "local" and "extended" formation of molecular hydrogen and tri-hydrogen. Although this measurement suffers from the same limitations as the CO_2 experiment discussed above, it provides an efficient path for joint experimental and theoretical studies of ultrafast molecular dynamics. Coincident data similar to those presented here provide a set of detailed constraints for different levels of theory, from basic exploratory quantum chemistry calculations similar to those used here for comparison with the data, to a direct modeling of final experimental observables. This is especially important for studies where the interpretation of the results heavily relies on modeling, which is a typical case for many ultrafast experiments on polyatomic molecules.

One limitation that becomes clear from the exploratory pump-probe experiments on methanol and ethanol, also discussed in chapter 6, is the choice of the probe scheme. A weak NIR pulse, which can serve as a very efficient probe for CO_2^+, where it couples different intermediate states to a well-defined predissociative state, is much less efficient for complex polyatomic molecules. A scheme involving a stronger NIR probe and Coulomb explosion imaging, a popular choice for similar applications [91,123,125,126], is hardly compatible with coincident photoelectron measurements. A valid alternative is provided by a flexible combination of XUV / VUV / UV wavelengths, enabling a single photon pump - single photon probe scheme (see, e.g. [160,161,162] for a few recent examples). In our configuration, such a probe might actually bring the system to a doubly charged state. Combined with electron-ion and ion-ion coincident measurements, this might be a scheme of choice for the experiments similar to those discussed in chapter 6.

Finally, as mentioned above, an increase in the repetition rate of the XUV / laser sources

employed might be a decisive factor for broader applications of the methodology developed here. In practical terms, this is envisioned to become available in the very near future. As an example, a 100 kHz laser system with a tunable UV arm and an XUV HHG setup is expected to be installed at the J.R. Macdonal Laboratory within next two years. This will enable similar measurements on more complex molecules, or even more detailed and rigorous studies of small prototypical systems. In combination with further theoretical developments, this is a very promising direction for research in ultrafast molecular dynamics.

Bibliography

[1] R. F. Mould. The early history of x-ray diagnosis with emphasis on the contributions of physics. *Phys Med Biol.*, 40:1895–1915, 1995.

[2] J. D. Watson and F. H. C. Crick. Molecular structure of nucleic acids: A structure for deoxyribose nucleic acid. *Nature.*, 171:737, 1953.

[3] J. H. D. Eland. *An Introduction to Ultraviolet Photoelectron Spectroscopy in the Gas Phase.* Butterworth-Heinemann, 1984.

[4] S. Hüfner. *Very High Resolution Photoelectron Spectroscopy.* Springer-Verlag Berlin Heidelberg, 2007.

[5] P. G. Flesch. *Light and Light Sources High-Intensity Discharge Lamps.* Springer-Verlag Berlin Heidelberg, 2006.

[6] S. Mobilio, F. Boscherini, and C. Meneghini. *Synchrotron Radiation.* Springer-Verlag Berlin Heidelberg, 2015.

[7] W. Ackermann , G. Asova et al. Operation of a free-electron laser from the extreme ultraviolet to the water window. *Nature Photonics.*, 1:336, 2007.

[8] E. Allaria, R. Appio et al. Highly coherent and stable pulses from the fermi seeded free-electron laser in the extreme ultraviolet. *Nature Photonics.*, 6:669–704, 2012.

[9] X. F. Li, A. L Huillier et al. Multiple-harmonic generation in rare gases at high laser intensity. *Phys. Rev. A.*, 39:5751, 1989.

[10] P. Agostini and L. F. DiMauro. The physics of attosecond light pulses. *Rep. Prog. Phys.*, 67:813, 2004.

[11] A. H. Zewail. Femtochemistry: atomic-scale dynamics of the chemical bond. *The Journal of Physical Chemistry A.*, 104:24:5660, 2000.

[12] S. R. Leone, C. W. McCurdy et al. What will it take to observe processes in 'real time'. *Nature Photonics.*, 8:162–166, 2014.

[13] J. Ullrich, A. Rudenko, R. Moshammer. Free-electron lasers: new avenues in molecular physics and photochemistry. *Annu. Rev. Phys. Chem.*, 63:635–660, 2012.

[14] W. Cao, G. Laurent et al. Identification of a previously unobserved dissociative ionization pathway in time-resolved photospectroscopy of the deuterium molecule. *Phys. Rev. Lett.*, 114:13001, 2015.

[15] L. V. Keldysh. Ionization in the field of a strong electromagnetic wave. *Sov. Phys. JETP.*, 20:1307, 1965.

[16] T. B. Miladinovic, V. M. Petrovic. Laser field ionization rates in the barrier-supression regime. *Journal of Russian Laser Research.*, 36:312, 2015.

[17] T. Ditmire, E. Gumbrell et al. Spatial coherence measurement of soft x-ray radiation produced by high order harmonic generation. *Phys. Rev. Lett.*, 77:23:4576, 1996.

[18] M. Bellini, C. Lynga et al. Temporal coherence of ultrashort high-order harmonic pulses. *Phys. Rev. Lett.*, 81:2:297, 1998.

[19] C. Lynga, M. Gaarde et al. Temporal coherence of high-order harmonics. *Phys. Rev. A.*, 60:4823, 1999.

[20] D. Lee, J. Park et al. Wave-front phase measurements of high-order harmonic beams by use of point-diffraction interferometry. *Optics Letters.*, 26:480, 2003.

[21] P. B. Corkum. Plasma perspective on strong field multiphoton ionization. *Phys. Rev. Lett.*, 71:13:1994, 1993.

[22] C.D. Lin, A.T. Le, C. Jin and H. Wei. *Attosecond and Strong-Field Physics Principles and Applications*. Cambridge, 2018.

[23] M. Lewenstein, P. Balcou et al. Theory of high-harmonic generation by low-frequency laser fields. *Phys. Rev. A.*, 49:2117, 1994.

[24] P. Salieres, B. Carre et al. Feynman's path-integral approach for intense-laser-atom interactions. *Science.*, 292:902, 2001.

[25] M. Grishin. *Advances in Solid State Lasers Development and Applications*. InTech, 2010.

[26] C. G. Durfee III, A. R. Rundquist et al. Phase matching of high-order harmonics in hollow waveguides. *Phys. Rev. Lett.*, 83:2187, 1999.

[27] J. J. Yeh. Atomic calculation of photoionization cross-sections and asymmetry parameters, 1993. URL https://vuo.elettra.eu/services/elements/WebElements.html.

[28] B. Teo. EXAFS: basic principles and data analysis. Inorganic chemistry concepts (Springer-Verlag, 1986).

[29] J. H. Hubbell, P. N. Trehan et al. A review, bibliography, and tabulation of k, l, and higher atomic shell x-ray fluorescence yields. *Journal of Physical and Chemical Reference Data.*, 23:2, 1994.

[30] J. Itatani, F. Quéré et al. Attosecond streak camera. *Phys. Rev. Lett.*, 88:17, 2002.

[31] H. G. Muller. Reconstruction of attosecond harmonic beating by interference of two-photon transitions. *Appl. Phys. B.*, 74:17–21, 2002.

[32] M. Isinger, D. Busto et al. Accuracy and precision of the rabbit technique. *Phil. Trans. R. Soc. A*, 377:20170475, 2019.

[33] M. Meyer, J. T. Costello et al. Two-colour experiments in the gas phase. *J. Phys. B: At. Mol. Opt. Phys.*, 43:194006, 2010.

[34] P. Maine, D.Strickland et al. Generation of ultrahigh peak power pulses by chirped pulse amplification. *IEEE.*, 24:393, 1988.

[35] X. Ren, A. M Summers et al. Single-shot carrier-envelope-phase tagging using an f–2f interferometer and a phase meter: a comparison. *Journal of Optics.*, 19:124017, 2017.

[36] KMLABS. Xuus™ extreme ultraviolet ultrafast source and beamline, 2018. URL https://www.kmlabs.com/sxr-xuus.

[37] L. Struder, S. Epp et al. Large-format,high-speed,x-ray pnccds combined with electron and ion imaging spectrometers in a multipurpose chamber for experiments at 4th generation light sources. *Nuclear Instruments and Methods in Physics Research A.*, 614:483–496, 2010.

[38] B. Erk, J. P. Muller et al. Camp@flash: an end-station for imaging, electron- and ion-spectroscopy, and pump–probe experiments at the flash free-electron laser. *J. Synchrotron Rad.*, 25:1529–1540, 2018.

[39] T. Osipov, C. Bostedt et al. The lamp instrument at the linac coherent light source free-electron laser. *Rev. Sci. Instrum.*, 89:035112, 2018.

[40] RoentDek Handels GmbH. Mcp delay line detector manual, 2021. URL https://www.roentdek.com/manuals/MCP%20Delay%20Line%20manual.pdf.

[41] C. Bordas, F. Paulig. Photoelectron imaging spectrometry: Principle and inversion method. *Rev. Sci. Instrum.*, 67:2257, 1996.

[42] J. Winterhalter and D. Maier. Imaging of charged atomic reaction products: Inversion by a two-dimensional regularization method. *J. Chem. Phys.*, 110:11187, 1999.

[43] M. J. J. Vrakking. An iterative procedure for the inversion of two-dimensional ion/photoelectron imaging experiments. *Rev. Sci. Instrum.*, 72:4084, 2001.

[44] J. Ullrich, R. Moshammer et al. Recoil-ion and electron momentum spectroscopy: reaction-microscopes. *Rep. Prog. Phys.*, 66:1463, 2003.

[45] J. Feldhaus. Flash—the first soft x-ray free electron laser (fel) user facility. *J. Phys. B: At. Mol. Opt. Phys.*, 43:194002, 2010.

[46] P. Emma, R. Akre et al. First lasing and operation of an angstrom-wavelength free-electron laser. *Nature Photonics.*, 4:641, 2010.

[47] Z. Huang and K. J. Kim. Review of x-ray free-electron laser theory. *Physical Review Special Topics.*, 10:034801, 2007.

[48] G. Margaritondo and P. R. Ribic. A simplified description of x-ray free-electron lasers. *J. Synchrotron Rad.*, 18:101, 2010.

[49] K Midorikawa. Ultrafast dynamic imaging. *Nature Photonics.*, 5:640, 2011.

[50] C. D. Lin, X. M. Tong et al. Direct experimental visualization of atomic and electron dynamics with attosecond pulses. *J. Phys. B: At. Mol. Opt. Phys.*, 39:419–426, 2006.

[51] M. Born and R. Oppenheimer. Zur quantentheorie der molekeln. *Annalen der Physik.*, 389:457, 1927.

[52] H. Timmers, Z. Li et al. Coherent electron hole dynamics near a conical intersection. *Phys. Rev. Lett.*, 113:113003, 2014.

[53] M. P. Minitti, J. M. Budarz et al. Imaging molecular motion: Femtosecond x-ray scattering of an electrocyclic chemical reaction. *Phys. Rev. Lett.*, 114:255501, 2015.

[54] J. M. Glownia, J. Cryan et al. Time-resolved pump-probe experiments at the LCLS. *Optics Express.*, 18:17620, 2010.

[55] B. Stankus, H. Yong et al. Ultrafast x-ray scattering reveals vibrational coherence following rydberg excitation. *Nature Chem.*, 11:716, 2019.

[56] E. Gagnon, P. Ranitovic et al. Soft x-ray–driven femtosecond molecular dynamics. *Science.*, 317:1374, 2007.

[57] A. S. Sandhu, E. Gagnon et al. Observing the creation of electronic feshbach resonances in soft x-ray–induced o2 dissociation. *Science.*, 322:1081, 2008.

[58] B. Erk, R. Boll et al. Imaging charge transfer in iodomethane upon x-ray photoabsorption. *Science.*, 345:6194, 2014.

[59] D. Rolles, R. Boll et al. An experimental protocol for femtosecond $NIR/UV - XUV$ pump-probe experiments with free-electron lasers. *Journal of Visualized Experiments.*, 140:e57055, 2018.

[60] M. Schultze, M. Fieß et al. Delay in photoemission. *Science.*, 328:1658, 2010.

[61] W. Cao, G. Laurent et al. Spectral splitting and quantum path study of high-harmonic generation from a semi-infinite gas cell. *J. Phys. B: At. Mol. Opt. Phys.*, 45:074013, 2012.

[62] Y. Mairesse, A. de Bohan et al. Attosecond synchronization of high-harmonic soft x-rays. *Science.*, 302:1540, 2003.

[63] D. Anielsky. Untersuchung der photoelektronen-winkelverteilungen von ausgerichteten molekülen in der gasphase, 2020. URL https://bib-pubdb1.desy.de/record/441908. PhD thesis.

[64] N. D. Loh, C. Y. Hampton et al. Fractal morphology, imaging and mass spectrometry of single aerosol particles in flight. *Nature.*, 486:513, 2012.

[65] J. Andreasson, A. V. Martin et al. Automated identification and classification of single particle serial femtosecond x-ray diffraction data. *Optics Express.*, 22:2497, 2014.

[66] S. Schorb, T. Gorkhover et al. X-ray–optical cross-correlator for gas-phase experiments at the linac coherent light source free-electron laser. *Applied Physics Letters.*, 100:121107, 2012.

[67] P. M. Paul, E. S. Toma et al. Observation of a train of attosecond pulses from high harmonic generation. *Science.*, 292:1689, 2001.

[68] R. Trebino, K. W. DeLong et al. Measuring ultrashort laser pulses in the time-frequency domain using frequency-resolved optical gating. *Rev. Sci. Instrum.*, 68: 3277, 1997.

[69] W. R. Johnson and K. T. Cheng. Photoionization of the outer shells of neon, argon, krypton, and xenon using the relativistic random-phase approximation. *Phys. Rev. A.*, 20:3, 1979.

[70] K. T. Taylor. Photoelectron angular-distribution ß parameters for neon and argon. *J. Phys. B: Atom. Molec. Phys.*, 10:18, 1977.

[71] K. Codling, R. G. Houlgate et al. Angular distribution and photoionization measurements on the 2p and 2s electrons in neon. *J. Phys. B: Atom. Molec. Phys.*, 9:5, 1976.

[72] P. Johnsson, A. Rouzée et al. Characterization of a two-color pump–probe setup at flash using a velocity map imaging spectrometer. *Optics Letters.*, 35:4163, 2010.

[73] M. Uiberacker, T. Uphues et al. Attosecond real-time observation of electron tunnelling in atoms. *Nature.*, 446:627, 2007.

[74] M. Krikunova, T. Maltezopoulos et al. Time-resolved ion spectrometry on xenon with the jitter-compensated soft x-ray pulses of a free-electron laser. *New Journal of Physics.*, 11:123019, 2009.

[75] L. W. Pi, A. S. Landsman. Attosecond time delay in photoionization of noble-gas and halogen atoms. *Appl. Sci.*, 8:322, 2018.

[76] A. Thompson, D. Attwood et al. *X-ray Data Booklet*, volume 3nd Ed. Lawrence Berkeley National Laboratory, 2009.

[77] S. Kosugi, M. Iizawa et al. *PCI* effects and the gradual formation of *R*ydberg series due to photoelectron recapture, in the *A*uger satellite lines upon *X*e 4d 5/2 photoionization. *J. Phys. B: At. Mol. Opt. Phys.*, 48:115003, 2015.

[78] M. Alagia, P. Candori et al. Double photoionization of CO_2 molecules in the 34-50 ev energy range. *The Journal of Physical Chemistry A.*, 113:14755–14759, 2009.

[79] A. E. Slattery, T. A. Field et al. Spectroscopy and metastability of CO_2^{2+} molecular ions. *J. Chem. Phys.*, 122:084317, 2005.

[80] P. Millie, I. Nenner et al. Theoretical and experimental studies of the triatomic doubly charged ions CO_2^{2+}, OCS^{2+}, and CD_2^{2+}. *J. Chem. Phys.*, 89:1259, 1986.

[81] S. Erattupuzha, S. Larimian et al. Two-pulse control over double ionization pathways in CO_2. *J. Chem. Phys.*, 144:024306, 2016.

[82] A. Rudenko, V. Makhija et al. Strong-field-induced wave packet dynamics in carbon dioxide molecule. *Faraday Discuss.*, 194:463, 2016.

[83] D. M. Bittner, K. Gope et al. Time-resolved dissociative ionization and double photoionization of CO_2. *J. Chem. Phys.*, 153:194201, 2020.

[84] M. Hochlaf, F. R. Bennett et al. Theoretical study of the electronic states of $CO2^{2+}$. *J. Phys. B: At. Mol. Opt. Phys.*, 31:2163–2175, 1998.

[85] H. Hogreve. Stability properties of CO_2^{2+}. *J. Phys. B: At. Mol. Opt. Phys.*, 28:L263, 1995.

[86] B. Jochim, R. Erdwien et al. Three-dimensional momentum imaging of dissociation in flight of metastable molecules. *New J. Phys.*, 19:103006, 2017.

[87] S. Larimian, S. Erattupuzha et al. Fragmentation of long-lived hydrocarbons after strong field ionization. *Phys. Rev. A.*, 93:053405, 2016.

[88] Q. Tian, J. Yang et al. Outer- and inner-valence satellites of carbon dioxide: Electron momentum spectroscopy compared with symmetry adapted- cluster configuration interaction general-r calculations. *J. Chem. Phys.*, 136:094306, 2012.

[89] W. Iskandar, A. S. Gatton et al. Tracing intermolecular coulombic decay of carbon-dioxide dimers and oxygen dimers after valence photoionization. *Phys. Rev. A.*, 99: 043414, 2019.

[90] C. Hastings Jr, J. T. Wayward and J. P. Wang. *Approximations for Digital Computers.* Princeton University Press, 1955.

[91] Y. H. Jiang, A. Rudenko et al. Ultrafast extreme ultraviolet induced isomerization of acetylene cations. *Phys. Rev. Lett.*, 105:263002, 2010.

[92] G. Sansone, F. Kelkensberg et al. Electron localization following attosecond molecular photoionization. *Nature.*, 465:763, 2010.

[93] M. Krikunova, T. Maltezopoulos et al. Ultrafast photofragmentation dynamics of molecular iodine driven with timed xuv and near-infrared light pulses. *J. Chem. Phys.*, 134:024313, 2011.

[94] T. Zimmermann, H. Köppel and L. Cederbaum. On the bilinear vibronic coupling mechanism. *J. Chem. Phys.*, 83:4697, 1985.

[95] M. Oppermann, S. J. Weber et al. Control and identification of strong field dissociative channels in CO_2^+ via molecular alignment. *J. Phys. B: At. Mol. Opt. Phys.*, 47:124025, 2014.

[96] J. Liu, W. Chen et al. Unimolecular decay pathways of state selected CO_2^+ in the internal energy range of 5.2– 6.2 ev an experimental and theoretical study.. *J. Chem. Phys.*, 118:149, 2003.

[97] C. Neidel, J. Klei et al. Probing time-dependent molecular dipoles on the attosecond time scale. *Phys. Rev. Lett.*, 111:033001, 2013.

[98] J. Yao, G. Li et al. Alignment-dependent fluorescence emission induced by tunnel ionization of carbon dioxide from lower-lying orbitals. *Phys. Rev. Lett.*, 111:133001, 2013.

[99] H. Hu, S. Larimian et al. Laser-induced dissociative recombination of carbon dioxide. *Physical Review Research.*, 1:033152, 2019.

[100] T. Kanai, S. Minemoto et al. Quantum interference during high-order harmonic generation from aligned molecules. *Nature.*, 435:470, 2005.

[101] C. Vozzi, F. Calegari et al. Controlling two-center interference in molecular high harmonic generation. *Phys. Rev. Lett.*, 95:153902, 2005.

[102] X. Zhou, R. Lock et al. Molecular recollision interferometry in high harmonic generation. *Phys. Rev. Lett.*, 100:073902, 2008.

[103] O. Smirnova, Y. Mairesse et al. High harmonic interferometry of multi-electron dynamics in molecules. *Nature.*, 460:972, 2009.

[104] J. Liu, M. Hochlaf et al. Pulsed field ionization–photoelectron bands for CO_2^+ ($A^2\Pi_u$ and $B^2\Sigma_u^+$) in the energy range of 17.2–19.0 ev: An experimental and theoretical study. *J. Chem. Phys.*, 113:18, 2000.

[105] J. Liu, W. Chen et al. High resolution pulsed field ionization–photoelectron study of CO_2^+ ($\mathbf{x}\ ^2\ \Pi_g$) in the energy range of 13.6–14.7. *J. Chem. Phys.*, 112:24, 2000.

[106] F. J. Furch, S. Birkner et al. Photoelectron imaging of xuv photoionization of CO_2 by 13–40 ev synchrotron radiation. *J. Chem. Phys.*, 139:124309, 2013.

[107] T. Koopmans. Über die *Z*uordnung von *W*ellenfunktionen und *E*igenwerten zu den einzelnen *E*lektronen eines *A*toms. *Physica.*, 1:104–113, 1934.

[108] M. T. Praet, J. C. Lorquet and G. Raşeev. Unimolecular reaction paths of electronically excited species the $C^2\Sigma_g$ state of CO_2^+. *J. Chem. Phys.*, 77:4611, 1982.

[109] R. Bombach, J. Dannacher et al. Branching ratios and partition of the excess energy for the predissociation of CO_2^+ $C^2\Sigma_g$ molecular cations. *J. Chem. Phys.*, 79:4214, 1983.

[110] R. Locht and M. Davister. The dissociative electroionization of carbon dioxide by low-energy electron impact. the C^+, O^+ and CO^+ dissociation channels. *International Journal of Mass Spectrometry and Ion Processes.*, 144:105–129, 1995.

[111] M. Yang, L. Zhang et al. Study on the [1 + 1] photodissociation spectra of CO_2^+ via ${C^2\Sigma_g}^+$ $B^2\Sigma_u^+$, $A^2\Pi_u$, and $X^2\Pi_g$ transitions. *Chemical Physics Letters.*, 480:41–45, 2009.

[112] M. R. F. Siggel, J. B. West et al. Shape-resonance-enhanced continuum– continuum coupling in photoionization of CO_2. *J. Chem. Phys.*, 99:1556, 1993.

[113] R R. Lucchese and V. McKoy. Studies of differential and total photoionization cross sections of carbon dioxide. *Phys. Rev. A.*, 26:1406, 1982.

[114] C. M. Oana and A. I. Krylov. Cross sections and photoelectron angular distributions in photodetachment from negative ions using equation-of-motion coupled-cluster dyson orbitals. *J. Chem. Phys.*, 131:124114, 2009.

[115] S. Chelkowski and A. D. Bandrauk. Raman chirped adiabatic passage: a new method for selective excitation of high vibrational states. *J. Raman. Spectr.*, 28:459–466, 1997.

[116] E. Goll, G. Wunner and A. Saenz. Formation of ground-state vibrational wave packets in intense ultrashort laser pulses. *Phys. Rev. Lett.*, 97:103003, 2006.

[117] Z. H. Loh, G. Doumy et al. Observation of the fastest chemical processes in the radiolysis of water. *Science.*, 367:179, 2020.

[118] S. Xu, D. Guo et al. Damaging intermolecular energy and proton transfer processes in alpha-particle-irradiated hydrogen-bonded systems. *Angew. Chem. Int. Ed.*, 57: 17023, 2018.

[119] J. Heberle, J. Riesle et al. Proton migration along the membrane surface and retarded surface to bulk transfer. *Nature.*, 370:379, 1994.

[120] J. Zhao, T. Song et al. Intramolecular hydrogen atom migration along the backbone of cationic and neutral radical tripeptides and subsequent radical-induced dissociations. *Phys. Chem. Chem. Phys.*, 14:8723, 2012.

[121] P. D. Estes, C. Copéret. The role of proton transfer in heterogeneous transformations of hydrocarbons. *Chimia (Aarau).*, 69:321, 2015.

[122] A. Hishikawa, A. Matsuda et al. Visualizing recurrently migrating hydrogen in acetylene dication by intense ultrashort laser pulses. *Phys. Rev. Lett.*, 99:258302, 2007.

[123] H. Ibrahim, B. Wales et al. Tabletop imaging of structural evolutions in chemical reactions demonstrated for the acetylene cation. *Nature Chem.*, 5:4422, 2014.

[124] C. E. Liekhus-Schmaltz, I. Tenney et al. Ultrafast isomerization initiated by X-ray core ionization. *Nature Chem.*, 6:8189, 2015.

[125] N. G. Kling, S. D. Tendero et al. Time-resolved molecular dynamics of single and double hydrogen migration in ethanol. *Nature Comm.*, 10:2813, 2019.

[126] M. McDonnel, A. C. LaForge et al. Ultrafast laser-induced isomerization dynamics in acetonitrile. *J. Phys. Chem. Lett.*, 11:6724, 2020.

[127] E. Livshits, I. Luzon et al. Time-resolving the ultrafast H_2 roaming chemistry and H_3^+ formation using extreme-ultraviolet pulses. *Communications Chemistry.*, 3:49, 2020.

[128] T. Endo, S. P. Neville et al. Capturing roaming molecular fragments in real time. *Science.*, 370:1072, 2020.

[129] S. P. Weathersby, G. Brown et al. Mega-electron-volt ultrafast electron diffraction at slac national accelerator laboratory. *Rev. Sci. Instrum.*, 86:073702, 2015.

[130] J. Yang, X. Zhu et al. Imaging CF_3I conical intersection and photodissociation dynamics with ultrafast electron diffraction. *Science.*, 361:64, 2018.

[131] T. J. A. Wolf, D. M. Sanchez et al. The photochemical ring-opening of 1,3-cyclohexadiene imaged by ultrafast electron diffraction. *Nature Chem.*, 11:504, 2019.

[132] J. M. Glownia, A Natan et al. Self-referenced coherent diffraction x-ray movie of angstrom- and femtosecond-scale atomic motion. *Phys. Rev. Lett.*, 117:153003, 2016.

[133] J. Eland. The origin of primary H_3^+ ions in mass spectra. *Rapid Communications In Mass Spectrometery.*, 10:1560, 1996.

[134] I. Ben-Itzhak, K. D. Carnes et al. Fragmentation of CH_4 caused by fast-proton impact. *Phys. Rev. A.*, 47:3478, 1993.

[135] S. De, J. Rajput et al. Formation of H_3^+ in methanol : an intramolecular bond rearrangement study. *Phys. Rev. Lett.*, 97:213201, 2006.

[136] B. Jochim, A. Lueking et al. Rapid formation of H_3^+ from ammonia and methane following 4 mev proton impact. *J. Phys. B: At. Mol. Opt. Phys.*, 42:091002, 2009.

[137] Y. Zhang, B. Ren et al. Formation of H_3^+ from ethane dication induced by electron impact. *Communications Chemistry.*, 3:160, 2020.

[138] E. Wang, X. Ren and A. Dorn. Role of the environment in quenching the production of H_3^+ from dicationic clusters of methanol. *Phys. Rev. Lett.*, 126:103402, 2021.

[139] J. Eland B. J. Treves-Brown. The fragmentation of doubly charged methanol. *J. Mass Spectrom. Ion Processes.*, 113:167, 1992.

[140] I. Luzon, K. Jagtap et al. Single-photon coulomb explosion of methanol using broad bandwidth ultrafast *EUV* pulses. *Phys. Chem. Chem. Phys.*, 19:13488, 2017.

[141] I. Luzon, E. Livshits et al. Making sense of *C*oulomb explosion imaging. *J. Phys. Chem. Lett.*, 10:1361, 2019.

[142] K. Hoshina, Y. Furukawa et al. Efficient ejection of H_3^+ from hydrocarbon molecules induced by ultrashort intense laser fields. *J. Chem. Phys.*, 129:104302, 2008.

[143] P. M. Kraus, M. C. Schwarzer et al. Unusual mechanism for H_3^+ formation from ethane as obtained by femtosecond laser pulse ionization and quantum chemical calculations. *J. Chem. Phys.*, 134:114302, 2011.

[144] N. Ekanayake, M. Nairat et al. Mechanisms and time-resolved dynamics for trihydrogen cation (H_3^+) formation from organic molecules in strong laser fields. *Scientific Reports.*, 7:4703, 2017.

[145] N. Ekanayake, T. Severt et al. H_2 roaming chemistry and the formation of H_3^+ from organic molecules in strong laser fields. *Nature Comm.*, 9:5186, 2018.

[146] T. Ando, A. Shimamoto et al. Coherent vibrations in methanol cation probed by periodic H_3^+ ejection after double ionization. *Communications Chemistry.*, 1:7, 2018.

[147] H. Wu, Y. Xue et al. Theoretical and experimental studies on hydrogen migration in dissociative ionization of the methanol monocation to molecular ions H_3^+ and H_2O^+. *Royal Society of Chemistry Advances.*, 9:16683, 2019.

[148] N. Iwamoto, C. J. Schwartz et al. Strong-field control of H_3^+ production from methanol dications: Selecting between local and extended formation mechanisms. *J. Chem. Phys.*, 152:054302, 2020.

[149] Y. Malakar, W. L. Pearson and A. Rudenko. Tracing H_2^+ and H_3^+ formation in methane molecules irradiated with intense femtosecond laser pulses. *Unpublished.*, 2018.

[150] National Center for Biotechnology Information. $3D$ interactive structure model, 2021. URL https://pubchem.ncbi.nlm.nih.gov/.

[151] K. Nakai, T. Kato et al. Communication: Long-lived neutral h_2 in hydrogen migration within methanol dication. *J. Chem. Phys.*, 139:181103, 2013.

[152] E. Wang. Modelling orbital-resolved H_2^+ and H_3^+ formation pathways from singly charged states of methanol. *Unpublished.*, 2021.

[153] E. Wang, X. Shan et al. Ultrafast proton transfer dynamics on the repulsive potential of the ethanol dication: Roaming-mediated isomerization versus coulomb explosion. *The Journal of Physical Chemistry A.*, 124:2785–2791, 2020.

[154] A. L. Hickey, C. N. Rowleyand et al. Benchmarking quantum chemical methods for the calculation of molecular dipole moments and polarizabilities. *The Journal of Physical Chemistry A.*, 118:20:3678, 2014.

[155] J. M. L. Martin, J. El-Yazal et al. Basis set convergence and performance of density functional theory including exact exchange contributions for geometries and harmonic frequencies. *Mol. Phys.*, 86:6:1437, 1995.

[156] A. D. Becke. Density-functional thermochemistry. iii. the role of exact exchange. *J. Chem. Phys.*, 98:5648, 1993.

[157] P. R. Nagy, D. Samu et al. Optimization of the linear-scaling local natural orbital $CCSD(T)$ method: Improved algorithm and benchmark applications. *J. Chem. Theory Comput.*, 14:8, 2018.

[158] U. Bozkaya and A. Unal. State-of-the-art computations of vertical ionization potentials with the extended koopmans' theorem integrated with the $CCSD(T)$ method. *The Journal of Physical Chemistry A.*, 122:17:4375, 2018.

[159] P. Linusson, M. Stenrup et al. Double photoionization of alcohol molecules. *Phys. Rev. A.*, 80:032516, 2009.

[160] Y. Liu, T. Rozgonyi et al. Excited-state dynamics of CH_2I_2 and CH_2IBr studied with UV-pump VUV-probe momentum-resolved photoion spectroscopy. *J. Chem. Phys.*, 153:184304, 2020.

[161] E. G. Champenois, L. Greenman et al. Ultrafast photodissociation dynamics and nonadiabatic coupling between excited electronic states of methanol probed by time-resolved photoelectron spectroscopy. *J. Chem. Phys.*, 150:114301, 2019.

[162] T. K. Allison, H. Tao et al. Ultrafast internal conversion in ethylene. ii. Mechanisms and pathways for quenching and hydrogen elimination. *J. Chem. Phys.*, 136:124317, 2012.

Appendix A

CO_2 spectroscopy database

Transition	Intensity	Ionization energy
(0,0,0)-(0,0,0)	36	17.32 eV
(0,0,0)-(1,0,0)	160	17.46 eV
(0,0,0)-(2,0,0)	76	17.60 eV
(0,0,0)-(2,2,0)	20	17.72 eV
(0,0,0)-(3,0,0)	67	17.74 eV
(0,0,0)-(4,0,0)	24	17.87 eV
(0,0,0)-(4,1,0)	79	17.94 eV
(0,0,0)-(4,2,0)	23	18.00 eV
(0,0,0)-(5,0,0)	22	18.01 eV
(0,0,0)-(6,0,0)	17	18.15 eV
(0,0,0)-(7,0,0)	8	18.29 eV

Table A.1: *Most probable transitions into vibrational states of A state, [adapted from 104]*

Transition	Intensity	Ionization energy
(1,0,0)-(1,0,0)	12	18.06 eV
(0,0,0)-(0,0,0)	100	18.07 eV
(0,0,0)-(0,1,0)	1.9	18.15 eV
(0,0,0)-(1,0,0)	7.2	18.23 eV
(0,0,0)-(1,1,0)	1.1	18.30 eV
(0,0,0)-(1,2,0)	0.9	18.39 eV
(0,0,0)-(0,0,2)	0.9	18.53 eV

Table A.2: *Most probable transitions into vibrational states of B state, [adapted from 104]*

$h\nu$	$X^2\Pi_g$	$A^2\Pi_u$	$B^2\Sigma_u^+$	$C^2\Sigma_g^+$
20	0.343 ± 0.026	0.301 ± 0.028	0.327 ± 0.044	0.029 ± 0.002
21	0.313 ± 0.023	0.301 ± 0.027	0.346 ± 0.044	0.039 ± 0.003
22	0.284 ± 0.020	0.318 ± 0.024	0.348 ± 0.038	0.050 ± 0.004
23	0.288 ± 0.019	0.329 ± 0.022	0.323 ± 0.031	0.060 ± 0.004
24	0.292 ± 0.019	0.338 ± 0.021	0.300 ± 0.027	0.069 ± 0.005
25	0.309 ± 0.019	0.339 ± 0.020	0.270 ± 0.023	0.082 ± 0.006

Table A.3: *Photoionization branching ratio of CO_2 molecules into $X^2\Pi_g$, $A^2\Pi_u$, $A^2\Sigma_u^+$, and $C^2\Sigma_g^+$ electronic states of CO_2^+. [adapted from 112]*

$h\nu$	$X^2\Pi_g$	$A^2\Pi_u$	$B^2\Sigma_u^+$	$C^2\Sigma_g^+$
20	-0.219 ± 0.045	0.373 ± 0.031	-0.666 ± 0.095	1.329 ± 0.191
21	-0.143 ± 0.045	0.657 ± 0.037	-0.644 ± 0.086	1.081 ± 0.131
22	-0.010 ± 0.046	0.870 ± 0.044	-0.580 ± 0.074	0.989 ± 0.124
23	0.138 ± 0.052	0.943 ± 0.045	-0.484 ± 0.058	1.060 ± 0.116
24	0.300 ± 0.060	0.975 ± 0.047	-0.404 ± 0.052	1.196 ± 0.123
25	0.410 ± 0.067	1.026 ± 0.049	-0.268 ± 0.048	1.326 ± 0.139

Table A.4: *Photoionization asymmetry parameters of CO_2 molecules resulting in $X^2\Pi_g$, $A^2\Pi_u$, $A^2\Sigma_u^+$, and $C^2\Sigma_g^+$ electronic states of CO_2^+. [adapted from 112]*

Appendix B

Photoelectron images and energy spectra

In the following pages a selection of photoelectron images and photoelectron energy spectra of CH_3OH, CD_3OH, and CH_3CD_2OH ionized by H13-15 are plotted.

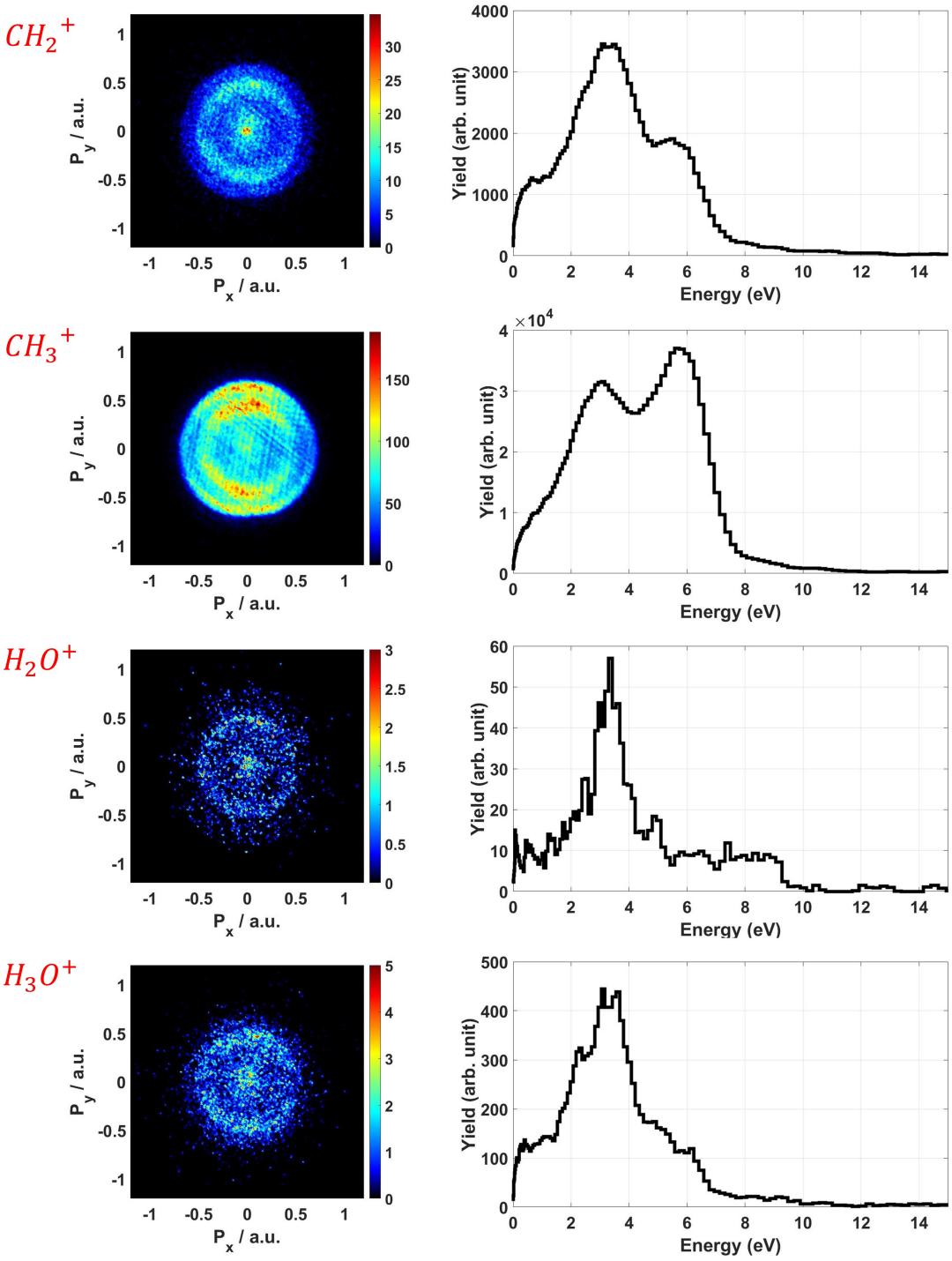

Figure B.1: *Photoelectron images and energy spectra in coincidence with CH_2^+, CH_3^+, H_2O^+, and H_3O^+ from CH_3OH ionized by H13-15*

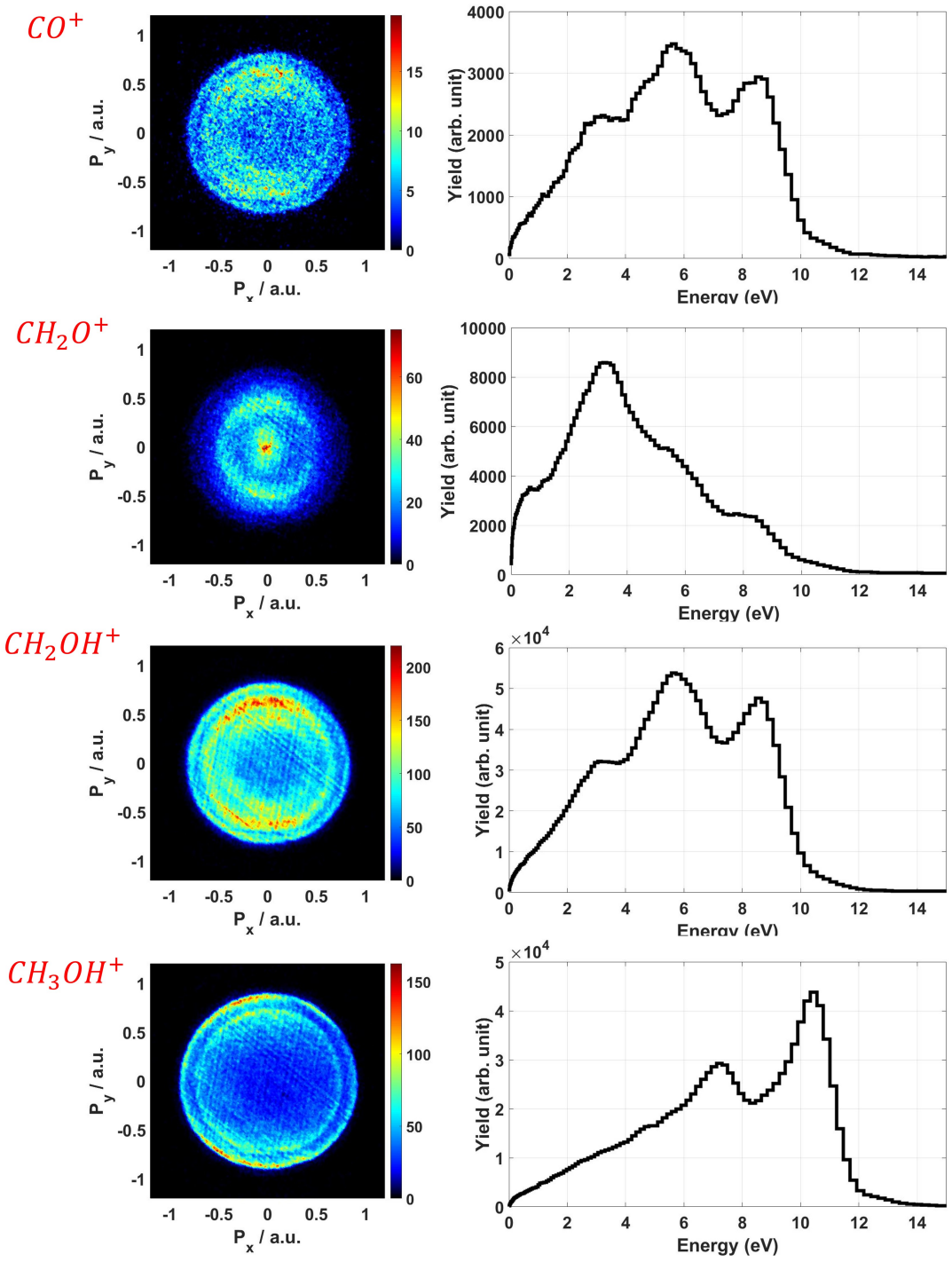

Figure B.2: *Photoelectron images and energy spectra in coincidence with CO^+, CH_2O^+, CH_2OH^+, and CH_3OH^+ from CH_3OH ionized by H13-15*

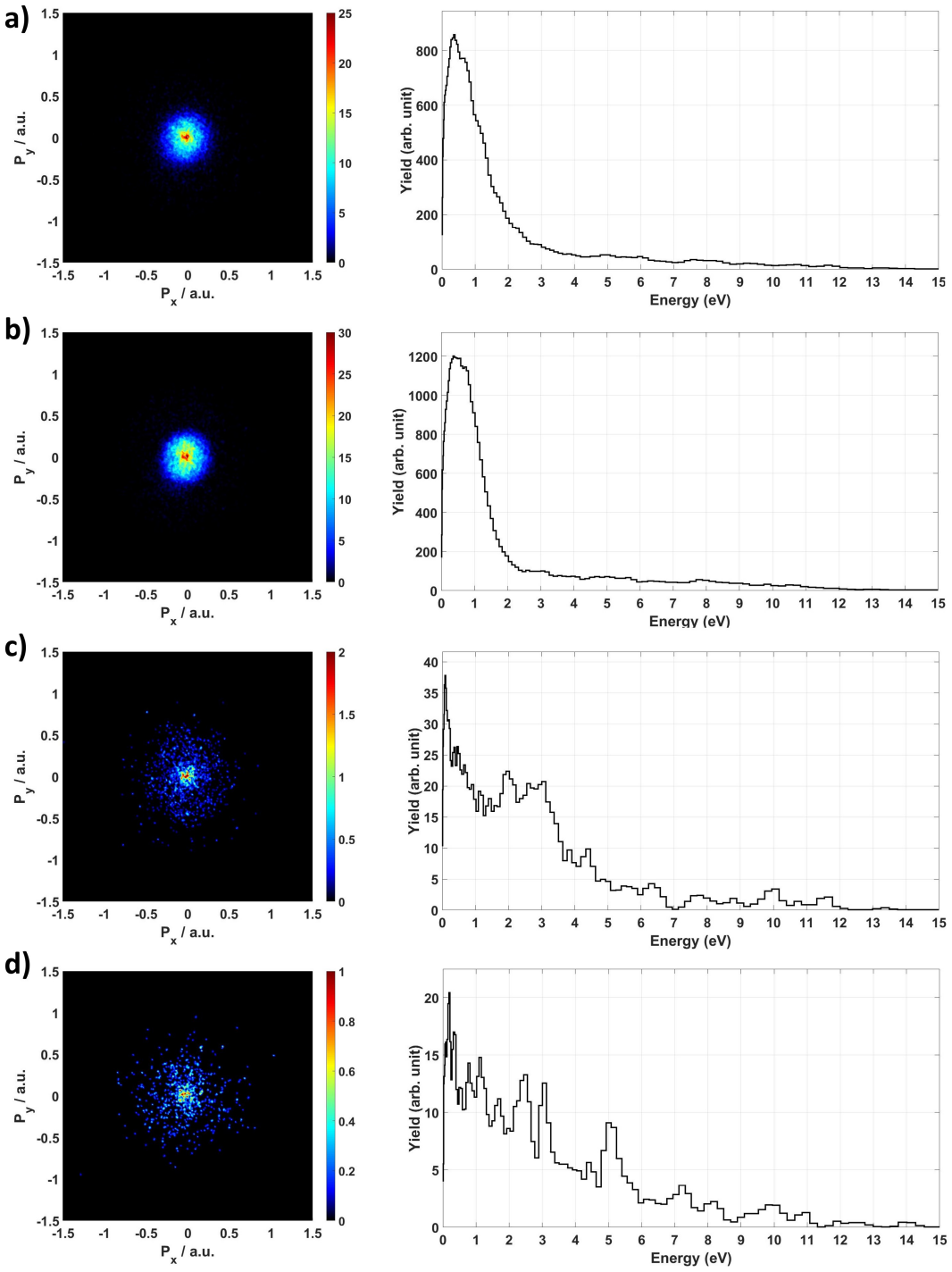

Figure B.3: *Photoelectron images (left panels) and energy spectra (right panels) in coincidence with: a)H^+, b)D^+, c)DH^+, d)D_2^+ from CD_3OH ionized by H13-15.*

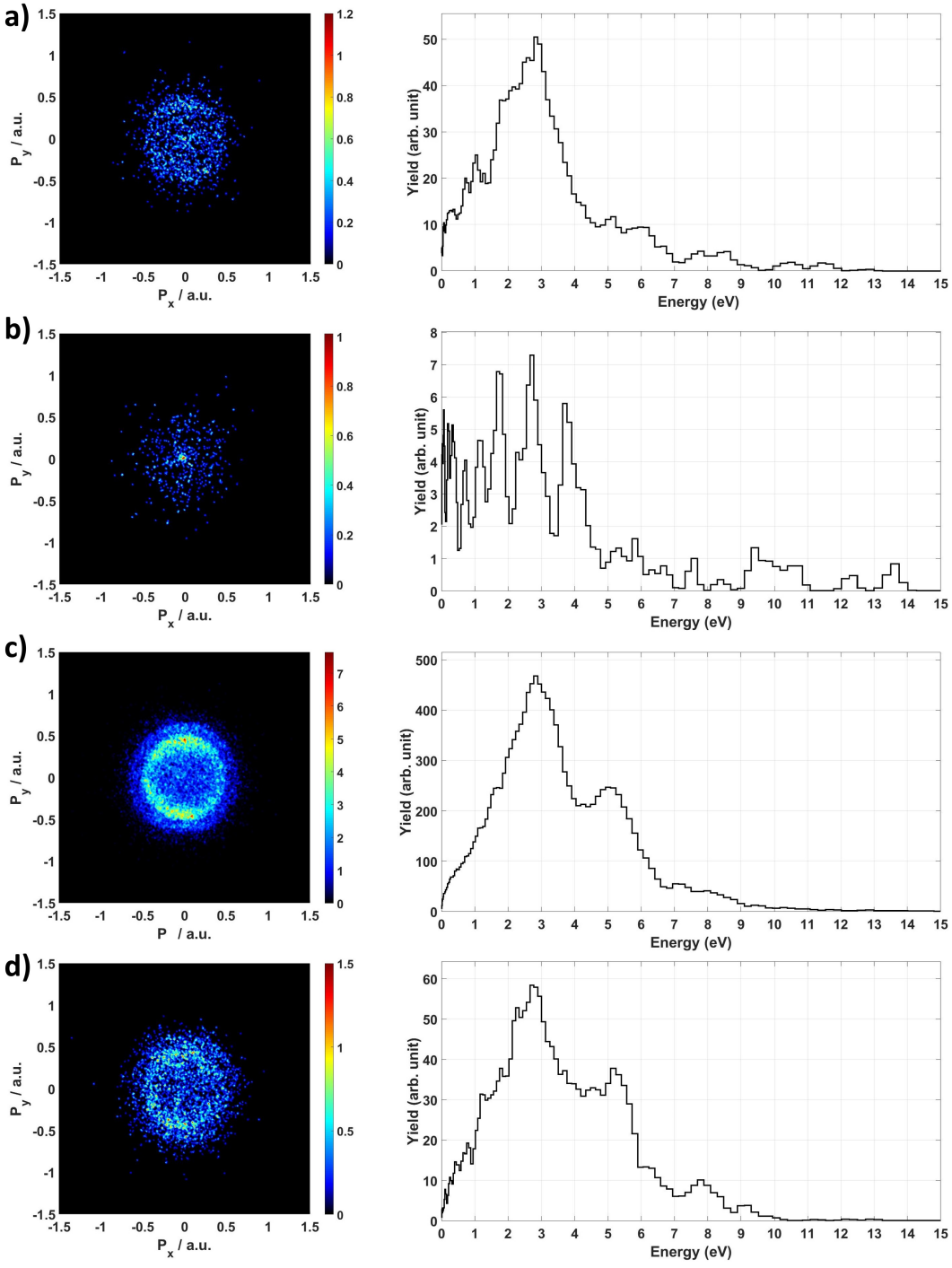

Figure B.4: *Photoelectron images (left panels) and energy spectra (right panels) in coincidence with: a)D_2H^+, b)D_3^+, c)OD_2H^+, d)OD_3^+ from CD_3OH ionized by H13-15.*

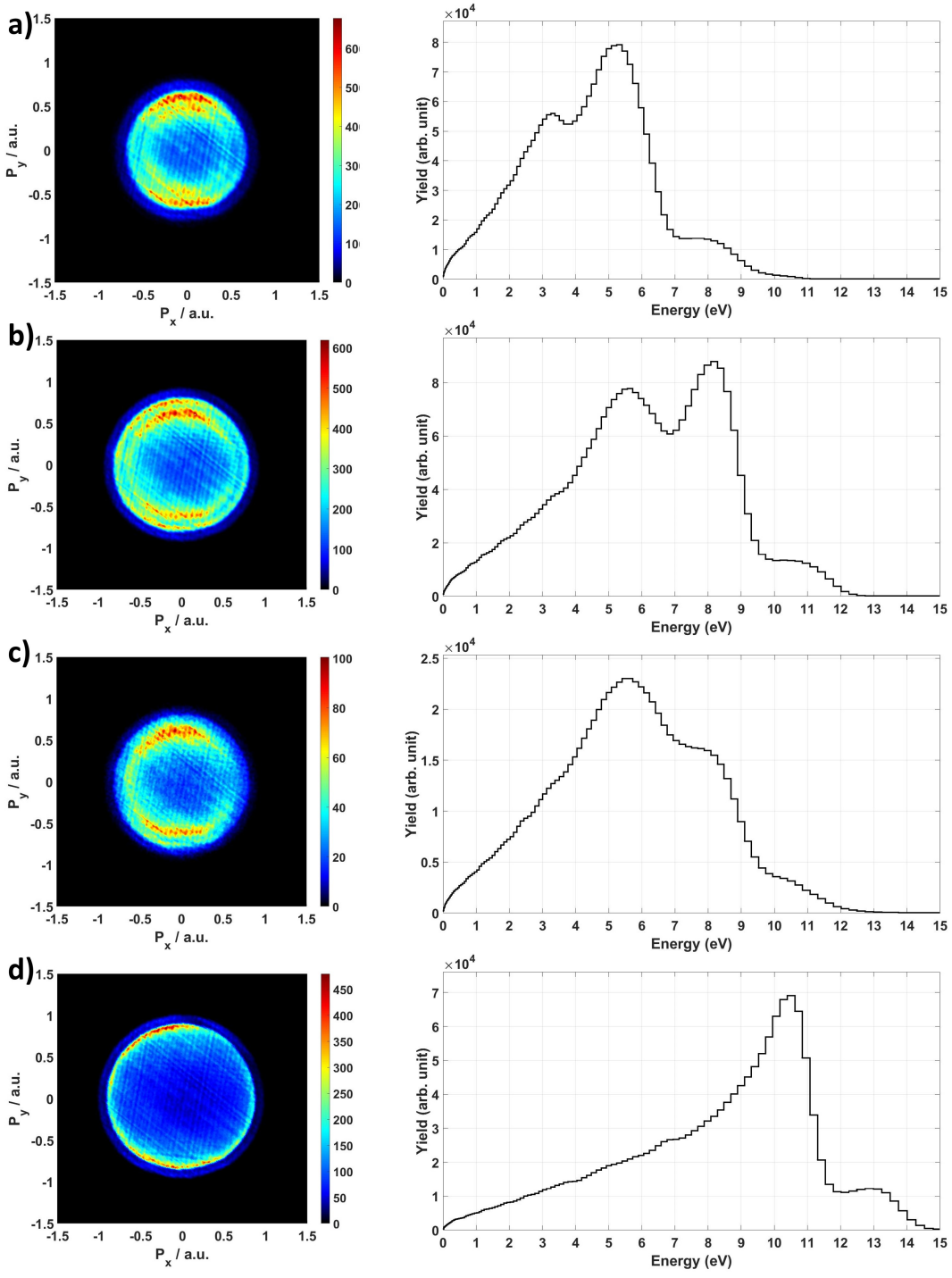

Figure B.5: *Photoelectron images (left panels) and energy spectra (right panels) in coincidence with: a)CD_3^+, b)CD_2OH^+, c)CD_3O^+, d)CD_3OH^+ from CD_3OH ionized by H13-15.*

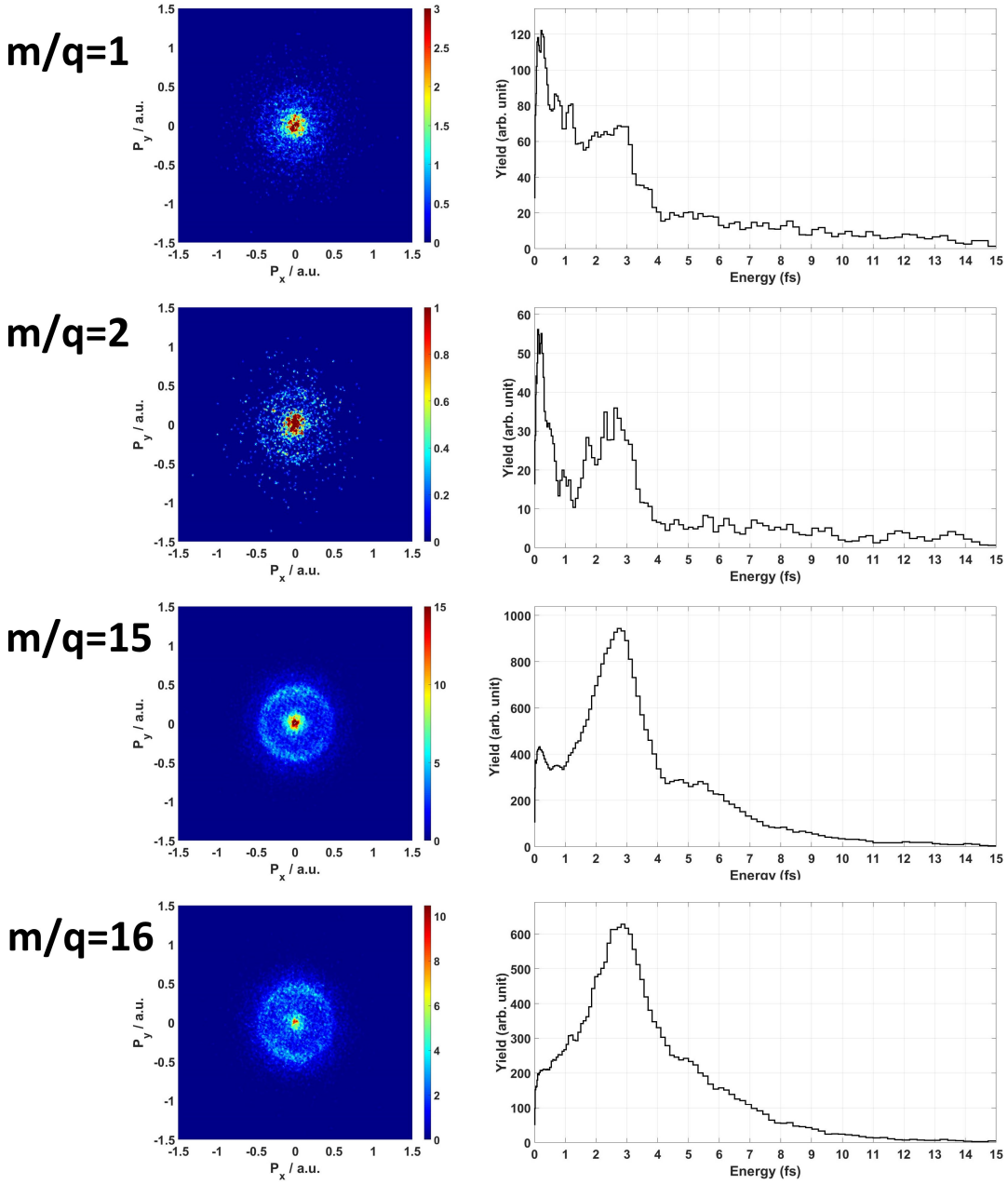

Figure B.6: *Photoelectron images (left panels) and energy spectra (right panels) in coincidence with: m/q=1, m/q=2, m/q=15, and m/q=16 from CH_3CD_2OH ionized by H13-15.*

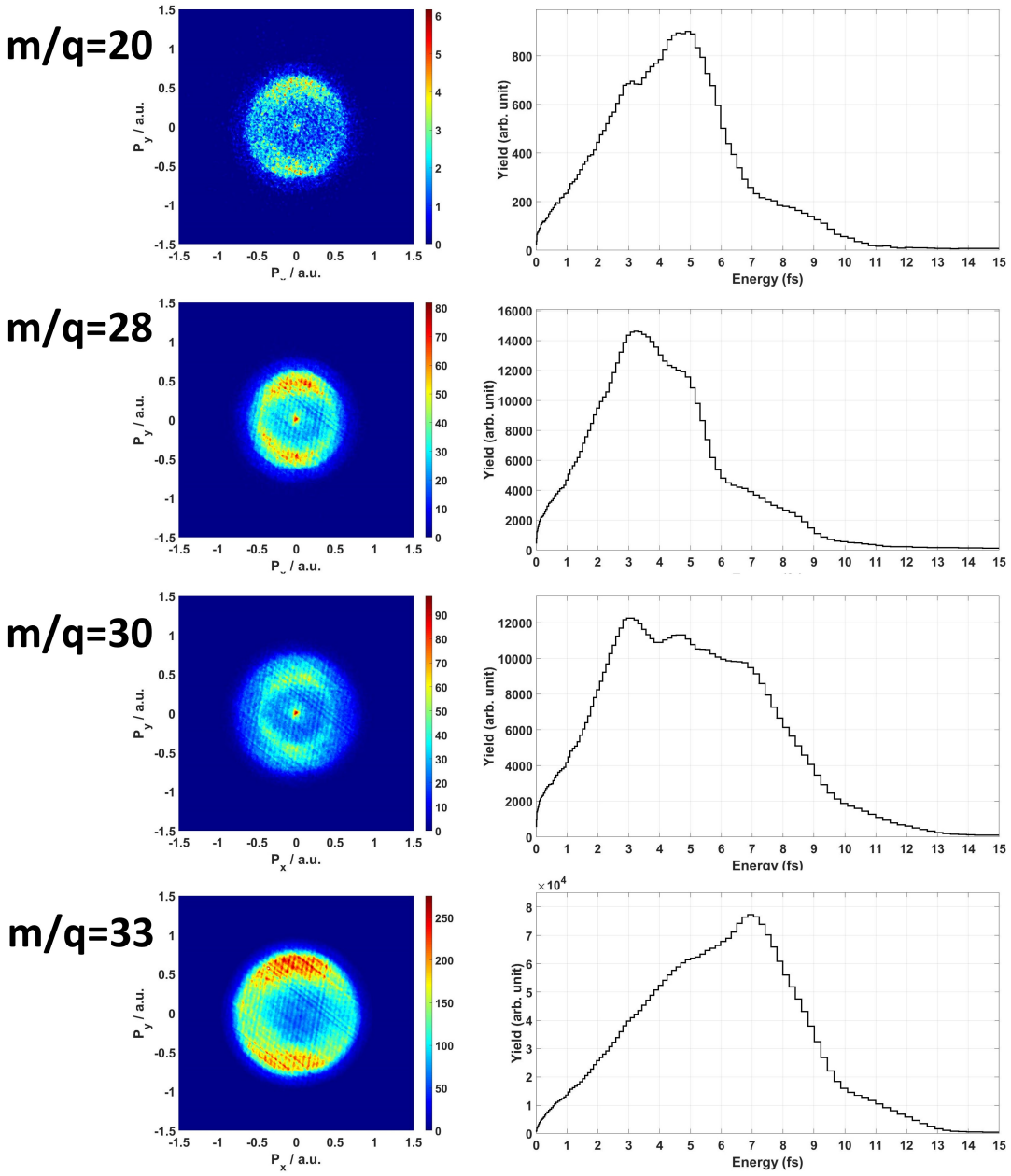

Figure B.7: *Photoelectron images (left panels) and energy spectra (right panels) in co-incidence with: m/q=20, m/q=28, m/q=30, and m/q=33 from CH_3CD_2OH ionized by H13-15.*

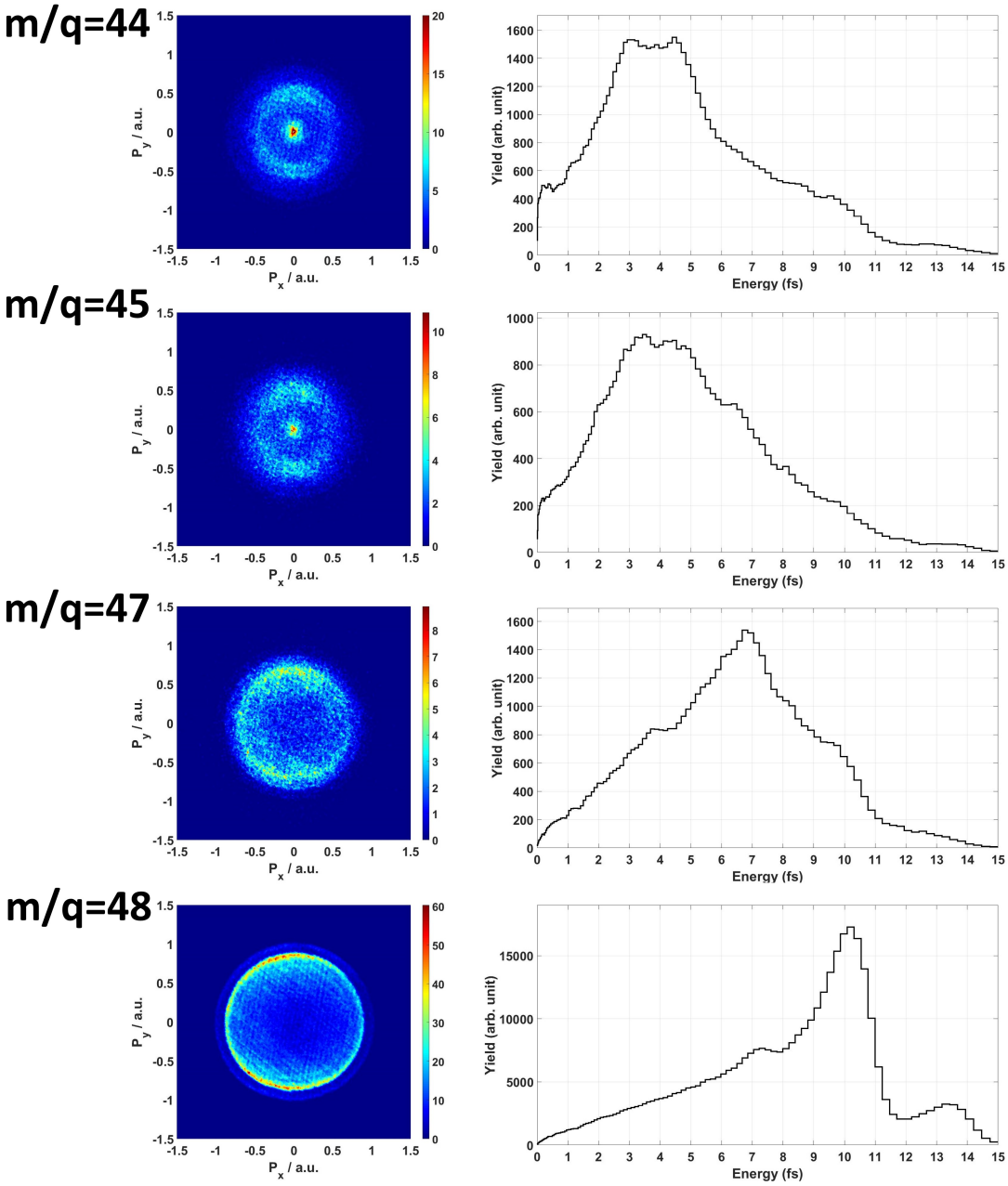

Figure B.8: *Photoelectron images (left panels) and energy spectra (right panels) in coincidence with: m/q=44, m/q=45, m/q=47, and m/q=48 from CH_3CD_2OH ionized by H13-15.*